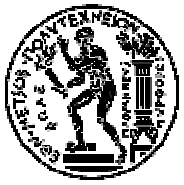

ΕΘΝΙΚΟ ΜΕΤΣΟΒΙΟ ΠΟΛΥΤΕΧΝΕΙΟ

ΣΧΟΛΗ ΕΦΑΡΜΟΣΜΕΝΩΝ ΜΑΘΗΜΑΤΙΚΩΝ

ΚΑΙ ΦΥΣΙΚΩΝ ΕΠΙΣΤΗΜΩΝ

ΔΙΕΠΙΦΑΝΕΙΑΚΕΣ ΑΛΛΗΛΕΠΙΔΡΑΣΕΙΣ ΚΑΙ ΜΟΡΙΑΚΗ ΔΥΝΑΜΙΚΗ ΣΕ ΟΡΓΑΝΙΚΑ-ΑΝΟΡΓΑΝΑ ΝΑΝΟΣΥΝΘΕΤΑ ΠΟΛΥΜΕΡΙΚΑ ΥΛΙΚΑ

ΔΙΔΑΚΤΟΡΙΚΗ ΔΙΑΤΡΙΒΗ

ΠΑΝΑΓΙΩΤΗΣ Α. ΚΛΩΝΟΣ

Φυσικός Εφαρμογών, ΜΔΕ

ΕΠΙΒΛΕΠΩΝ:

ΠΟΛΥΚΑΡΠΟΣ ΠΙΣΣΗΣ

Καθηγητής ΕΜΠ

ΑΘΗΝΑ, Σεπτέμβριος 2015

Ευρωπαϊκή Ένωση
Ευρωπαϊκό Κοινωνικό Ταμείο

ΕΠΙΧΕΙΡΗΣΙΑΚΟ ΠΡΟΓΡΑΜΜΑ
ΕΚΠΑΙΔΕΥΣΗ ΚΑΙ ΔΙΑ ΒΙΟΥ ΜΑΘΗΣΗ
επένδυση στην κοινωνία της γνώσης
ΥΠΟΥΡΓΕΙΟ ΠΑΙΔΕΙΑΣ ΚΑΙ ΘΡΗΣΚΕΥΜΑΤΩΝ
ΕΙΔΙΚΗ ΥΠΗΡΕΣΙΑ ΔΙΑΧΕΙΡΙΣΗΣ

ΕΣΠΑ 2007-2013
πρόγραμμα για την ανάπτυξη
ΕΥΡΩΠΑΪΚΟ ΚΟΙΝΩΝΙΚΟ ΤΑΜΕΙΟ

Με τη συγχρηματοδότηση της Ελλάδας και της Ευρωπαϊκής Ένωσης

NATIONAL TECHNICAL UNIVERSITY OF ATHENS

SCHOOL OF APPLIED MATHEMATICAL

AND PHYSICAL SCIENCES

INTERFACIAL INTERACTIONS AND MOLECULAR DYNAMICS IN ORGANIC-INORGANIC NANOCOMPOSITE POLYMERIC MATERIALS

PHD THESIS

PANAGIOTIS A. KLONOS

Applications Physicist NTUA, MSc

SUPERVISOR:

POLYCARPOS PISSIS

Professor NTUA

ATHENS, September 2015

European Union
European Social Fund

OPERATIONAL PROGRAMME
EDUCATION AND LIFELONG LEARNING
investing in knowledge society
MINISTRY OF EDUCATION & RELIGIOUS AFFAIRS
MANAGING AUTHORITY

NSRF 2007-2013
programme for development
EUROPEAN SOCIAL FUND

Co- financed by Greece and the European Union

ΕΘΝΙΚΟ ΜΕΤΣΟΒΙΟ ΠΟΛΥΤΕΧΝΕΙΟ

ΣΧΟΛΗ ΕΦΑΡΜΟΣΜΕΝΩΝ ΜΑΘΗΜΑΤΙΚΩΝ

ΚΑΙ ΦΥΣΙΚΩΝ ΕΠΙΣΤΗΜΩΝ

ΔΙΕΠΙΦΑΝΕΙΑΚΕΣ ΑΛΛΗΛΕΠΙΔΡΑΣΕΙΣ ΚΑΙ ΜΟΡΙΑΚΗ ΔΥΝΑΜΙΚΗ ΣΕ ΟΡΓΑΝΙΚΑ-ΑΝΟΡΓΑΝΑ ΝΑΝΟΣΥΝΘΕΤΑ ΠΟΛΥΜΕΡΙΚΑ ΥΛΙΚΑ

ΔΙΔΑΚΤΟΡΙΚΗ ΔΙΑΤΡΙΒΗ

ΠΑΝΑΓΙΩΤΗΣ Α. ΚΛΩΝΟΣ

Φυσικός Εφαρμογών, ΜΔΕ

ΣΥΜΒΟΥΛΕΥΤΙΚΗ ΕΠΙΤΡΟΠΗ:

1. Π. ΠΙΣΣΗΣ, Καθηγητής (Επιβλέπων)
2. Α. ΚΑΝΑΠΙΤΣΑΣ, Καθηγητής
3. M. MONLEON PRADAS, Καθηγητής

ΕΞΕΤΑΣΤΙΚΗ ΕΠΙΤΡΟΠΗ:

1. Π. ΠΙΣΣΗΣ, Καθηγητής
2. Α. ΚΑΝΑΠΙΤΣΑΣ, Καθηγητής
3. M. MONLEON PRADAS, Καθηγητής
4. Ε. ΚΟΝΤΟΥ, Καθηγήτρια
5. J.L. GOMEZ RIBELLES, Καθηγητής
6. Π. ΤΑΡΑΝΤΙΛΗ, Αν. Καθηγήτρια
7. Α. ΚΥΡΙΤΣΗΣ, Επ. Καθηγητής

ΑΘΗΝΑ, Σεπτέμβριος 2015

Ευρωπαϊκή Ένωση
Ευρωπαϊκό Κοινωνικό Ταμείο

ΕΠΙΧΕΙΡΗΣΙΑΚΟ ΠΡΟΓΡΑΜΜΑ
ΕΚΠΑΙΔΕΥΣΗ ΚΑΙ ΔΙΑ ΒΙΟΥ ΜΑΘΗΣΗ
επένδυση στην κοινωνία της γνώσης
ΥΠΟΥΡΓΕΙΟ ΠΑΙΔΕΙΑΣ ΚΑΙ ΘΡΗΣΚΕΥΜΑΤΩΝ
ΕΙΔΙΚΗ ΥΠΗΡΕΣΙΑ ΔΙΑΧΕΙΡΙΣΗΣ

ΕΣΠΑ 2007-2013
πρόγραμμα για την ανάπτυξη
ΕΥΡΩΠΑΪΚΟ ΚΟΙΝΩΝΙΚΟ ΤΑΜΕΙΟ

Με τη συγχρηματοδότηση της Ελλάδας και της Ευρωπαϊκής Ένωσης

NATIONAL TECHNICAL UNIVERSITY OF ATHENS

SCHOOL OF APPLIED MATHEMATICAL

AND PHYSICAL SCIENCES

INTERFACIAL INTERACTIONS AND MOLECULAR DYNAMICS IN ORGANIC-INORGANIC NANOCOMPOSITE POLYMERIC MATERIALS

PHD THESIS

PANAGIOTIS A. KLONOS

Applications Physicist NTUA, MSc Microsystems and Nanodevices

ADVISORY COMMITEE:

1. P. PISSIS, Professor (Supervisor)
2. A. KANAPITSAS, Professor
3. M. MONLEON PRADAS, Professor

EXAMINATION BOARD:

1. P. PISSIS, Professor
2. A. KANAPITSAS, Professor
3. M. MONLEON PRADAS, Professor
4. E. KONTOU, Professor
5. J.L. GOMEZ RIBELLES, Professor
6. P. TARANTILI, As. Professor
7. A. KYRITSIS, As. Professor

ATHENS, September 2015

European Union
European Social Fund

OPERATIONAL PROGRAMME
EDUCATION AND LIFELONG LEARNING
investing in knowledge society
MINISTRY OF EDUCATION & RELIGIOUS AFFAIRS
MANAGING AUTHORITY

NSRF 2007-2013
programme for development
EUROPEAN SOCIAL FUND

Co- financed by Greece and the European Union

Contents

Acknowledgements

First of all, I would like to express my sincerest gratitude to Professor Polycarpos Pissis, my supervisor, for giving me the opportunity to work with this project. He was always there to offer me his help and advices. During our collaboration, my scientific knowledge and way of thinking were strongly enhanced. Except for offering his support at all levels, he has also taught me to be honest in relation to science and in my life, in general, to be helpful and kind to my colleagues, and to be a hard working and open minded scientist.

Secondly, I would like to thank the other two members of my thesis advisory committee, Professor Manuel Monleón Pradas and Professor Athanasios Kanapitsas, for their help and support. Next, I would like to thank Professor José Louis Gómez Ribelles, Professor Evagelia Kontou, As. Professor Petroula Tarantili and As. Professor Apostolos Kyritsis for being members of my thesis advisory committee and for closely following my work.

I would like to express my thanks to Professor Liliane Bokobza from the Laboratoire PPMD, E.S.P.C.I. (Paris, France) and Professor Vladimir M. Gun'ko from the Chuiko Institute of Surface Chemistry, National Academy of Sciences of Ukraine (Kiev, Ukraine), for preparing and providing me with the materials under investigation, for the very useful discussions and their help. Additionally, I thank the rest of Professor Gun'ko's team for the excellent collaboration and discussions, Professor Valentin A. Tertykh, Dr. Mykola V. Borysenko, Dr. Iryna Ya. Sulym, Dr. Yuliia Bolbukh, Dr. Nataliia V. Guzenko, and Dr. Mariia V. Galaburda. Throughout the last years we had very interesting and fruitful discussions, also, in the frame of many scientific visits.

I owe special thanks to Professor Dr. Christoph Schick, Dr. Andreas Wurm, and Mr. Gunnar Schulz, from the Institute of Physics, of University of Rostock (Germany), for giving me the opportunity to visit their group and expand my knowledge on Differential Scanning Calorimetry (DSC) technique, in particular, and polymer physics, in general. I also thank Dr.

Doris Pospiech from the IPF – Leibniz Institute of Polymer Research (Dresden, Germany) for offering me the opportunity to visit her Laboratory and for the collaboration that followed. Next, I thank Professor Yevgen P. Mamunya and Professor Lyudmyla Karabanova, from the Institute of Macromolecular Chemistry (National Academy of Sciences of Ukraine, Kiev) for hosting me in their laboratories.

I would like to thank the members (past and present) of the Dielectrics Research Group of the National Technical University of Athens (NTUA), Professor Costas Christodoulides, Professor Lazaros Apekis, As. Professor Vasileios Peoglos, As. Professor Alexandros Georgakilas, Dr. Sotiria Kripotou, Dr. Daniel Fragiadakis, Dr. Konstantinos N. Raftopoulos, Dr. Emmanuel Logakis, Dr. Christos Pandis, Dr. Andreas Stathopoulos, Dr. Panagiotis Maroulas, Dr. Anna Panagopoulou, Ms Dionisia Aravopoulou, Mr. Stefanos Koutsoumpis, Mr. Dimosthenis Georgopoulos, and Mr. Christos Chatzimanolis-Moustakas, for having nice and productive time together and, most of all, very friendly relationships for the last nine years.

Follows, many thanks to Dr. Konstantinos Kyriakos, Ms. Constantina Stamatopoulou, Ms. Vasileia Chatzidogiannaki, Ms. Maria Souli, Mr. Elias Giannoulidis, Ms. Giorgia Dapei, Mr. Konstantinos Roumpos, Mr. Stelios Kaprinis, Mr. Ioannis Vangelidis, and Mr. Konstantinos Vlachodimos, for working with them in the framework of their MSc and Diploma theses. In addition, I would like to thank the scientists from abroad, Dr. Pavel Yakushev (Saint Petersburg, Russian Federation), Dr. Franziskus Näther (Dresden, Germany), Dr. Evgenia Minko (Prague, Czech Republic), Dr. Muhammad Sajjad (Wien, Austria), Dr. Liana Azizova, Dr. Lyudmyla Nosach, Dr. Anna Turova, and Dr. Tanya Podust (Kiev, Ukraine), for the cooperation and discussions in the frame of their visits to NTUA.

I should not forget to express my gratitude to the employees of NTUA, Mrs. Marika Piperigou, Mrs. Margarita Papada, Mrs. Ifigeneia Moraiti, Mrs. Ioanna Syka, and Mrs. Alkistis Dimakopoulou, for their help with paperwork. I also feel obliged to thank and congratulate Mrs. Ypatia Karagiozopoulou and Mr. Emmanuel Tsimas, from the ESPA office of NTUA, for offering perfect services, immediate help whenever asked for, and for their exceptional kindness.

Last but not least, I would like to express my gratitude to my family for their love, support and encouragement.

As far as the financial support of my thesis is concerned, I acknowledge the Research Funding Program Heracleitus II as follows. This research has been co–financed by the European Union (European Social Fund – ESF) and Greek national funds through the

Operational Program “Education and Lifelong Learning” of the National Strategic Reference Framework (NSRF) – Research Funding Programs: Heracleitus II. Investing in knowledge society through the European Social Fund.

Summary

This PhD Thesis, entitled '*Interfacial interactions and molecular dynamics in organic-inirganic nanocomposites polymeric materials*', deals with the systematic investigation of the effects of interfacial interactions between a polymer (polydimethylsiloxane, PDMS) and the solid surface of various metal oxide (silica, titania) nanoparticles on molecular dynamics and thermal transitions of the polymer. The main effort is paid on the study of the characteristics of the fraction of polymer interacting directly with the nanoparticles. This fraction is called '*interfacial polymer fraction*' and is widely thought to be responsible for the tremendous improvements in desired properties of polymer nanocomposites (NCs), as compared to those of traditional composites. Throughout the last decades it has been suggested that the modified properties of polymer NCs are dominated by those of the interfacial polymer fraction. Next to the physical properties of the polymer, also the characteristics of the interacting solid surface are of significance for interfacial interactions. It has been recently reported that the size and surface curvature of the solid surface strongly affect the strength of interaction. So far, the dependence of the characteristics of the interfacial polymer fraction (dynamics, cooperativity, chain segment conformations) on surface roughness has not been sufficiently considered in the literature. In the present work we show results which suggest that, at least for PDMS based NCs, the surface roughness of the particles in combination with the flexibility of the polymer chains dominate interfacial interactions, over other factors, such as the type and size of the primary particles.

This study involves morphological, thermal and dielectric measurements on PDMS/silica and PDMS/titania NCs (i) of various filler loadings, (ii) with a broad range of surface roughness and variety in size of the primary particles, (iii) with different molecular weight and structure (linear/crosslinked) of PDMS, and (iv) at various levels of NCs hydration. In order to quantify hydration level, water equilibrium sorption–desorption

measurements at room temperature were also performed. The materials studied can be classified into two series. The first series is that of '*conventional*' polymer NCs type consisting of silica (SiO_2) and titania (TiO_2) nanoparticles, 5 and 20–40 nm in diameter, respectively, *in situ* synthesized and well dispersed (via sol–gel technique) in PDMS (*MW* ~18000) networks. The second series is that of '*core–shell*' NCs type, as linear PDMS (*MW* ~ 2000 and ~8000) is adsorbed via hydrogen bonding on aggregates of fumed metal oxide particles of a wide range of surface roughness, S_{BET}. The metal oxides used are titania (~70 nm in diameter for primary particles, ~800 nm in size for aggregates, S_{BET} ~ 25 m^2/g) and various silicas (8–85 nm in diameter for primary particles, 300–600 nm in size for aggregates, S_{BET} ~ 55–342 m^2/g). Finally, we studied confinement effects of PDMS adsorbed in the cylindrical-like pores (of 6-20 nm in diameter) of silica–gel of high S_{BET} (~384 m^2/g, affiliated mainly to intraparticle porosity). In selected samples, before adsorption of PDMS, the initial silica particle surfaces were partly modified by the chemical development of small zirconia nanoparticles, in an attempt to manipulate polymer adsorption.

Morphology was examined by scanning electron microscopy (SEM). Thermal transitions (focusing on glass transition) were monitored employing differential scanning calorimetry (DSC), while molecular dynamics was investigated in detail using two dielectric techniques, thermally stimulated depolarization currents (TSDC) and broadband dielectric relaxation spectroscopy (DRS), in wide frequency (10^{-4} to 10^6 Hz) and temperature (–150 to 60 ^oC) ranges. All measurements were performed using instruments at the Physics Department of the National Technical University of Athens. Our results are discussed in relation to those obtained with Nitrogen adsorption-desorption isotherms (IPSD analysis), wide angle X-ray diffraction (WAXD), and Fourier transform infrared spectroscopy (FTIR), performed on the same materials in the laboratory where they have been synthesized.

The most important results that came out of this PhD Thesis may be described, in relation to hot soft matter issues in the literature, as follows. Extended measurements using different thermal treatments show that the good dispersion and strong interactions of the nanonaparticles with PDMS restrict crystallization and segmental mobility of the polymer. In addition to calorimetry, the dielectric DRS and TSDC techniques provide significant information on the overall mobility, mostly on the segmental dynamics of the polymer (dynamic glass transition), which was found to consist of three discrete and well defined relaxations. These relaxations arise from the bulk (unaffected) polymer (α relaxation), the mobility of polymer chains restricted between condensed crystalline regions (α_c relaxation)

and the segmental dynamics in an interfacial polymer layer around (or, in general, close to) the nanoparticles (α_{int} relaxation).

Compared with PDMS/silica, a shift of α_{int} to lower frequencies / higher temperatures and a larger thickness of the interfacial layer in the series of PDMS/titania conventional NCs, arise possibly from stronger polymer-titania hydrogen bonds as compared to PDMS-silica. This explanation is based on the different electrochemical properties of the surface hydroxyls of titania as compared to those of silica (-OH more acidic in titania). Taking into account recent literature, our results can be alternatively explained on the basis of the larger size of titania nanoparticles, as compared to silica. However, results obtained with core-shell NCs of titania and silica, both of low S_{BET} (surface roughness), demonstrate similar characteristics of α_{int} (dynamics, strength, cooperativity), being almost identical to those of PDMS/titania of the conventional type, independently of the initial particles dimension. Moreover, results by thermal annealing and dehydration of PDMS/silica show a slowing down and weakening of α_{int}. Additionally, the presence of the interfacial polymer fraction in the NCs results in increased internal polarization (e.g. high real part of dielectric permittivity, ε', at very low temperatures) beyond additivity, while $\Delta\varepsilon$ decreases systematically with temperature for low S_{BET} and increases for high S_{BET}. We recall that $\Delta\varepsilon$ represents the population of the mobile (relaxing) molecular groups. Regarding the effects of molecular weight (MW) of PDMS, the interfacial polymer fraction is larger for the shorter polymer chains (lower MW), while α_{int} is slower, as compared to longer polymer chains (higher MW). Thus, combining all effects on the overall dielectric response (which is often not the case in the literature) we discuss results by employing a model that involves the formation of two types of segment conformations of the highly flexible PDMS chains at interfaces, namely (a) extended tails with bulk–like density but reduced mobility, and (b) loop–like chain segments with multiple contact points with the silica surface resulting in increased density and cooperativity. Obviously, both types of segments are characterized by increased orientation (order) and polarizability, as compared to segments in the bulk, which explains the increased dielectric response in the NCs beyond additivity. The loops / tails ratio increases with increasing S_{BET}. In addition, increase in surface roughness in the present work leads to increased number of contact points and, therefore, gradually denser interfacial layer. This implies reduction of the cooperativity length, thus, in the frame of Adam–Gibbs theory, faster and more cooperative segmental dynamics is expected, in agreement with results for α_{int} in the present thesis. Next to that, our results suggest that the tails to loops ratio should be larger for shorter PDMS chains (lower molecular weight), as compared to longer chains, due to increased concentration of free

polymer chain ends. Thus, we conclude that number and accessibility of contact points (surface properties of the particles) and structure and flexibility of polymer chain (polymer topology at the interfaces) dominate interfacial interactions.

Finally, measurements on PDMS adsorbed into the cylindrical-like pores of silica-gel (6-20 nm in diameter) show an additional glass transition step in DSC at lower temperature than that of bulk, while an additional segmental relaxation (α_p) faster than that in bulk was recorded by DRS. Both additional responses represent the spatially 2-D confined dynamics of PDMS, demonstrating, also, that the latter is sensitive to nanometric changes on spatial restriction of the polymer. On the contrary, thermal (crystallization) annealing did not impose any significant change on the respective glass transition (DSC) and dielectric process (α_p, DRS).

This research has been co–financed by the European Union (European Social Fund – ESF) and Greek national funds through the Operational Program "Education and Lifelong Learning" of the National Strategic Reference Framework (NSRF) – Research Funding Programs: Heracleitus II. Investing in knowledge society through the European Social Fund.

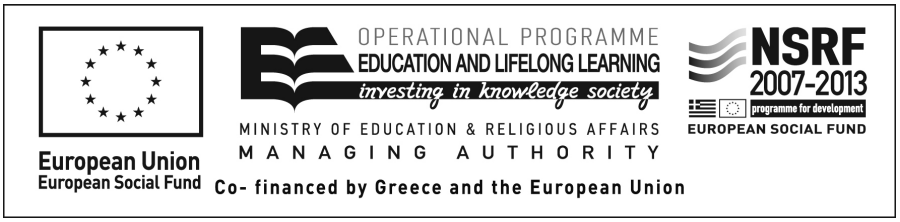

Περίληψη

Αντικείμενο της παρούσας διδακτορικής διατριβής, υπό τον τίτλο '*Διεπιφανειακές αλληλεπιδράσεις και μοριακή δυναμική σε οργανικά-ανόργανα νανοσύνθετα πολυμερικά υλικά*', είναι η συστηματική μελέτη της επίδρασης των διεπιφανειακών αλληλεπιδράσεων μεταξύ ενός πολυμερούς (συγκεκριμένα, του πολυδιμεθυλοσιλοξανίου, PDMS) και της στερεάς επιφάνειας διαφόρων τύπων νανοσωματιδίων μεταλλικών οξειδίων (πυριτίας, τιτανίας) στη μοριακή δυναμική και της θερμικές μεταβάσεις του πολυμερούς. Μελετώνται κυρίως τα χαρακτηριστικά του πολυμερούς που αλληλεπιδρά απευθείας με τα νανοσωματίδια. Το κλάσμα αυτό του πολυμερούς ονομάζεται '*διεπιφανειακό πολυμερές*' ή '*διεπιφανειακό στρώμα*' και θεωρείται ευρέως ότι η παρουσία του ευθύνεται για τις σημαντικά βελτιωμένες ιδιότητες που χαρακτηρίζουν τα νανοσύνθετα (ΝΣ) πολυμερικά υλικά, σε σύγκριση με τα παραδοσιακά σύνθετα υλικά. Έχει προταθεί τα τελευταία χρόνια ότι οι τροποιημένες ιδιότητες του διεπιφανειακού πολυμερούς κυριαρχούν στον καθορισμό των τελικών ιδιοτήτων του ΝΣ. Εκτός των φυσικών ιδιοτήτων του εκάστοτε πολυμερούς (π.χ. τη δομή του), τα χαρακτηριστικά της προς αλληλεπίδραση στερεής επιφάνειας παίζουν σημαντικό ρόλο στην ανάπτυξη διεπιφανειακών αλληλεπιδράσεων. Έχει επίσης αναφερθεί ότι το μέγεθος και η επιφανειακή καμπυλότητα των νανοσωματιδίων επηρεάζουν την ισχύ της αλληλεπίδρασης. Στην παρούσα μελέτη, παρουσιάζουμε αποτελέσματα που αναδεικνύουν πώς, τουλάχιστον για τα ΝΣ που βασίζονται στο PDMS, η επιφανειακή τραχύτητα (νανομετρικής κλίμακας) των νανοσωματιδίων και η ευκαμψία της πολυμερικής αλυσίδας κυριαρχούν στον καθορισμό των διεπιφανειακών αλληλεπιδράσεων συγκριτικά με άλλες παραμέτρους, όπως ο τύπος και το μέγεθος των νανοσωματιδίων. Η εξάρτηση των ιδιοτήτων του διεπιφανειακού πολυμερούς (δυναμική των πολυμερικών αλυσίδων, συνεργασιμότητα στην κίνηση, διαμορφώσεις των αλυσίδων) από την επιφανειακή

τραχύτητα των σωματιδίων δεν είχε μέχρι τώρα μελετηθεί σε σημαντικό βαθμό στη βιβλιογραφία.

Η παρούσα μελέτη περιλαμβάνει μετρήσεις μορφολογίας, θερμικών μεταβάσεων και διηλεκτρικής συμπεριφοράς σε ΝΣ συστήματα PDMS/πυριτίας και PDMS/τιτανίας (α) διαφόρων περιεκτικοτήτων σε έγκλεισμα (σωματίδια), (β) μεγάλου εύρους επιφανειακής τραχύτητας και μεγέθους σωματιδίων, (γ) διαφόρων μοριακών βαρών και δομής του πολυμερούς (γραμμικό/σταυροδεμένο), και (δ) σε διάφορα επίπεδα υδάτωσης των υλικών. Για την αποτίμηση των επιπέδων υδάτωσης εφαρμόσθηκαν τεχνικές ισόθερμης υδάτωσης–αφυδάτωσης σε ισορροπία (σε θερμοκρασία δωματίου). Τα προς μελέτη υλικά μπορούν να κατηγοριοποιηθούν σε δύο σειρές. Τα υλικά της πρώτης σειράς θεωρούνται '*συμβατικά*' νανοσύνθετα (ΝΣ) και είναι δοκίμια στα οποία έχουν συντεθεί και διασπαρεί νανοσωματίδια πυριτιας (SiO_2) και τιτανίας (TiO_2), διαμέτρου 5 και 20–40 nm, αντιστοίχως, παρουσία (*in situ*) δικτύων PDMS (μοριακού βάρους *MB* ~18000) μέσω τεχνικών λύματος πηκτής (sol–gel technique). Τα υλικά της δεύτερης σειράς θεωρούνται ΝΣ τύπου '*πυρήνα–φλοιού*' και είναι δοκίμια στα οποία γραμμικό PDMS (*MB* ~2000 και ~8000) έχει προσροφηθεί με φυσικό τρόπο (ανάπτυξη δεσμών υδρογόνου) σε συσσωματώματα νανοσωματίδιων μεταλλικών οξειδίων, οι επιφάνειες των οποίων χαρακτηρίζονται από μεγάλο εύρος νανομετρικής τραχύτητας (ειδική επιφάνεια, S_{BET}). Τα νανοσωματίδια είναι τιτανία (αρχικά σωματίδια διαμέτρου ~70 nm, συσσωματώματα ~800 nm, S_{BET} ~25 m^2/g) και διαφόροι τύποι πυριτίας (αρχικά σωματίδια 8–85 nm, συσσωματώματα 300–600 nm, S_{BET} ~55–342 m^2/g). Επισης, μελετήθηκαν φαινόμενα χωρικού περιορισμού του πολυμερούς (confinement effects) σε δοκίμια στα οποία το PDMS είναι προσφοφημένο σε πόρους κυλινδρικού τύπου (διαμέτρων 6-20 nm) silica–gel υψηλής S_{BET} (~384 m^2/g). Για επιλεγμένα δοκίμια, οι επιφάνειες τροποποιήθηκαν μερικώς μέσω χημικής ανάπτυξης μικρών νανοσωματιδίων ζιρκονίας (ZrO_2) με σκοπό την χειραγώγηση της αλληλεπίδρασης σωματιδίου-πολυμερούς.

Η μορφολογία των υλικών εξετάσθηκε με χρήση μικροσκοπίας ηλεκτρονιακής σάρωσης (SEM). Οι θερμικές μεταβάσεις (με έμφαση στην υαλώδη μετάβαση) καταγράφηκαν εφαρμόζοντας την τεχνική της διαφορικής θερμιδομετρίας σάρωσης (DSC), ενώ η μοριακή δυναμική εξετάσθηκε λεπτομερώς με τη χρήση δύο τεχνικών διηλεκτρικής φασματοσκοπίας, των θερμικώς διεγειρόμενων ρευμάτων αποπόλωσης (TSDC) και της διηλεκτρικής φασματοσκοπίας εναλλασομένου πεδίου (DRS), σε ευρεία περιοχή συχνοτήτων (10^{-4} to 10^6 Hz) και θερμοκρασιών (–150 to 60 ^oC). Οι παραπάνω μετρήσεις διεξήχθησαν χρησιμοποιώντας πειραματικές διατάξεις στον Τομέα Φυσικής του Εθνικού Μετσόβιου Πολυτεχνείου (ΕΜΠ). Τα αποτελέσματά μας διερευνώνται και σε σχέση με αποτελέσματα

μετρήσεων ισόθερμης ρόφησης-εκρόφησης αερίου αζώτου (Incremental Pore Size Distribution analysis, IPSD), σκέδασης ακτίνων-Χ υπό ευρεία γωνία (WAXD) και φασματοσκοπίας υπερύθρου (FTIR), οι οποίες πραγματοποιήθηκαν στα ίδια υλικά στα εργαστήρια που παρασκευάσθηκαν.

Τα σημαντικότερα αποτελέσματα αυτής της διδακτορικής διατριβής συζητούνται αναλυτικά, σε συσχέτιση με σημαντικά ανοιχτά θέματα της πρόσφατης βιβλιογραφίας. Διεξοδικές μετρήσεις υπό διάφορα θερμικά πρωτόκολλα δείχνουν ότι η καλή διασπορά των νανοσωματιδίων εντός της πολυμερικής μήτρας και οι ισχυρές αλληλεπιδράσεις πολυμερούς/νανοσωματιδίων περιορίζουν την κρυστάλλωση αλλά και τις συνεργασιακές κινήσεις (υαλώδης μεταβαση) του πολυμερούς. Παράλληλα με τη θερμιδομετρία, οι διηλεκτρικές τεχνικές προσφέρουν σημαντικές πληροφορίες σχετικά με την συνολική συνεργασιακή δυναμική του πολυμερούς (δυναμική υαλώδους μετάβασης), η οποία βρέθηκε να εκφράζεται από τρεις διακριτές συνεισφορές (τρεις μηχανισμοί διηλεκτρικής χαλάρωσης). Αυτές οι συνεισφορές προέρχονται από το τμήμα (α) του άμορφου ανεπηρέαστου (bulk) πολυμερούς (μηχανισμός α), (β) του πολυμερούς περιορισμένης κινητικότητας μεταξύ κρυσταλλικών περιοχών (μηχανισμός α_c) και (γ) του διεπιφανειακού πολυμερούς με συνεργασιακή δυναμική (μηχανισμός α_{int}).

Σε σύγκριση με τα συστήματα PDMS/πυριτίας, στα συμβατικά ΝΣ PDMS/τιτανίας ο μηχανισμός α_{int} καταγράφεται σε χαμηλότερες συχνότητες / υψηλότερες θερμοκρασίες, ενώ το πάχος του διεπιφανειακού στρώματος είναι μεγαλύτερο. Οι μεταβολές σχετίζονται, πιθανώς, με την ανάπτυξη δεσμών υδρογόνου που είναι ισχυρότεροι μεταξύ PDMS και τιτανίας σε σχέση με τους αντίστοιχους δεσμούς PDMS–πυριτίας. Αυτή η πρώτη προσέγγιση μπορεί να αιτιολογηθεί με βάση τη διαφορετική ηλεκτροχημική κατάσταση των επιφανειακών υδροξυλίων στα δύο οξείδια (τα –OH της τιτανίας είναι πιο όξινα). Συγκρίνοντας με την πρόσφατη βιβλιογραφία, τα αποτελέσματά μας μπορούν να εξηγηθούν επίσης με βάση το μεγαλύτερο μέγεθος των νανοσωματιδίων τιτανίας. Ωστόσο, τα αποτελέσματα σε ΝΣ τύπου πυρήνα–φλοιού τιτανίας και πυριτίας, χαμηλής τραχύτητας (S_{BET}) δείχνουν ομοιότητες μεταξύ τους στα χαρακτηριστικά του μηχανισμού α_{int} (δυναμική, ισχύς, συνεργασιμότητα) και είναι, επίσης, όμοια με εκείνα των συμβατικών ΝΣ PDMS/τιτανίας, ανεξαρτήτως του μεγέθους των αρχικών σωματιδίων. Επιπροσθέτως, τα αποτελέσματα σε δοκίμια που είχαν υποστεί θερμική ανόπτηση (προς ενίσχυση της κρυσταλλικότητας) και αυτών που υπέστησαν αφυδάτωση έδειξαν υποβάθμιση της δυναμικής και της ισχύος του μηχανισμού α_{int}. Επίσης, η παρουσία του διεπιφανειακού πολυμερούς στα ΝΣ έχει ως αποτέλεσμα την ενίσχυση της ενδογενούς πόλωσης των υλικών

(π.χ. αυξημένες τιμές του πραγματικού μέρους της διηλεκτρικής διαπερατότητας, ε', σε χαμηλές θερμοκρασίες) πέραν της προσθετικότητας, ενώ η διηλεκτρική ισχύς των μηχανισμών, Δε, ελαττώνεται συστηματικά με τη θερμοκρασία για χαμήλες τιμές S_{BET} και αυξάνει για υψηλές τιμές S_{BET}. Υπενθυμίζουμε ότι η Δε περιγράφει τον πληθυσμό των αντίστοιχων ευκίνητων μοριακών ομάδων. Σχετικά με την επίδραση του μοριακού βάρους (*MB*, μέσο μήκος μακρομορίων) του PDMS, το διεπιφανειακό πολυμερές είναι λιγότερο στην περίπτωση των βραχύτερων πολυμερικών αλυσίδων (μικρότερο *MB*), ενώ η δυναμική του καταγράφεται καθυστερημένη, σε σχέση με την περίπτωση μακρύτερων αλυσίδων (υψηλότερο *MB*). Έτσι, συνδυάζοντας όλες τις επιδράσεις στη συνολική διηλεκτρική συμπεριφορά των υλικών (κάτι που δεν γίνεται συνήθως στη βιβλιογραφία), ερμηνεύουμε τα αποτελέσματα επιστρατεύοντας ένα σύγχρονο μοντέλο. Σύμφωνα με το μοντέλο αυτό, το PDMS (πολυμερές με πολύ εύκαμπτες πολυμερικές αλυσίδες) μπορεί να διαμορφωθεί με 2 (τουλάχιστον) τρόπους στη διεπιφάνεια με τα σωματιδια, συγκεκριμένα μέσω (α) διαμορφώσεων τύπου εκτεταμένης ουράς (tail), και (β) διαμορφώσεων τύπου βρόχου (loop) με πολλαπλά σημεία επαφής με τη διεπιφάνεια. Οι διαμορφώσεις αυτές, ιδίως οι τύπου βρόχου, οδηγούν σε υψηλότερη πυκνότητα και συνεργασιμότητα του διεπιφανειακού πολυμερούς. Είναι προφανές ότι και οι δύο τύποι διαμορφώσεων χαρακτηρίζονται από αυξημένο προσανατολισμό (τάξη) και πολωσιμότητα, συγκρινόμενοι με τις διαμορφώσεις του πολυμερούς μακρυά από τη διεπιφάνεια (bulk). Αυτό εξηγεί πιθανώς την παρατηρούμενη αυξημένη διηλεκτρική απόκριση των ΝΣ πέραν της προσθετικότητας. Ο λόγος των πληθυσμών βρόχοι / ουρές αυξάνει με την τραχύτητα (S_{BET}). Επίσης, η αύξηση στην επιφανειακή τραχύτητα οδηγεί, στην παρούσα μελέτη, στην αύξηση του αριθμού των προσβάσιμων θέσεων πρόσδεσης / αλληλεπίδρασης μεταξύ πολυμερούς και νανοσωματιδίων, και, έτσι, στην σταδιακά αυξανόμενη πυκνότητα του διεπιφανειακού πολυμερικού στρώματος. Αυτό έχει ως αποτέλεσμα τη μείωση του μήκους συνεργασιμότητας των διεπιφανειακών αλυσίδων, άρα, στο πλαίσιο της θεωρίας Adam–Gibbs, η διεπιφανειακή δυναμική επιταχύνεται και η συνεργασιμότητα αυξάνει, σε συμφωνία με τα αποτελέσματά μας για το μηχανισμό α_{int}. Επίσης, τα αποτελέσματα δείχνουν ότι ο λόγος ουρές / βρόχοι είναι, πιθανώς, μεγαλύτερος στην περίπτωση κοντών πολυμερικών αλυσίδων PDMS (μικρό μοριακό βάρος του πολυμερούς), σε σχέση με τις μακρύτερες αλυσίδες, λόγω της μεγαλύτερης συγκέντρωσης ελεύθερων άκρων. Συμπερασματικά, καταλήγουμε στο ότι ο αριθμός και η προσβασιμότητα των σημείων επαφής (επιφανειακές ιδιότητες των σωματιδίων) και η δομή και ευκαμψία των πολυμερικών αλυσίδων (τοπολογία του

πολυμερούς στις επιφάνειες των σωματιδίων) κυριαρχούν στη διαμόρφωση των διεπιφανειακών αλληλεπιδράσεων.

Τέλος, οι μετρήσεις του πολυμερούς υπό 2-D χωρικό περιορισμό (διασωματιδιακοί πόροι τύπου κυλίδρου, διαμέτρου 6-20 nm), ανέδειξαν ένα επιπλέον βήμα υαλώδους μετάβασης (DSC) σε χαμηλές θερμοκρασίες και έναν γρήγορο επιπλέον μηχανισμό διηλεκρικής χαλάρωσης (α_p, DRS). Οι δύο αυτές συνεισφορές φαίνονται να είναι ευαίσθητες στον επιπλέον χωρικό περιορισμό του πολυμερούς, όμως, δεν επηρεάζονται καθόλου από την θερμική ανόπτηση του υλικού (που έχει ως αποτέλεσμα την αύξηση του βαθμού κρυσταλλικότητας).

Η παρούσα έρευνα έχει συγχρηματοδοτηθεί από την Ευρωπαϊκή Ένωση (Ευρωπαϊκό Κοινωνικό Ταμείο - ΕΚΤ) και από εθνικούς πόρους μέσω του Επιχειρησιακού Προγράμματος «Εκπαίδευση και Δια Βίου Μάθηση» του Εθνικού Στρατηγικού Πλαισίου Αναφοράς (ΕΣΠΑ) – Ερευνητικό Χρηματοδοτούμενο Έργο: Ηράκλειτος ΙΙ . Επένδυση στην κοινωνία της γνώσης μέσω του Ευρωπαϊκού Κοινωνικού Ταμείου.

1. Introduction

1.1. Polymer nanocomposites (NCs)

Polymer nanocomposites (NCs) are in the center of the interest of materials science and industry in the last decades [Ray03, Paul08, Pavlidou08, Allegra08, Kumar10, Jancar10, Okada06, Sperling06, Kumar13]. The use of fillers with dimensions varying between 1 and 100 nm (such as spherical nanoparticles [Zou08, Akcora10, Giannelis11, Kumar13], carbon nanotubes (CNTs) [Moniruzzaman06, Huang14], nanofibers [Sohrabi13, Redeker13], nanosheets [Ray03, Okada06, Pavlidou08, Kripotou10, Giannelis11, Chryssopoulou11, Papageorgiou14]) in composite materials offers the great benefit that small amount of filler content is sufficient to induce tremendous improvements in desired properties [Tuteja07, Sen07]. A common reason for adding small inclusions to polymers is to increase the Young's modulus of elasticity and improve the mechanical properties, in general, via well known reinforcement mechanisms [Chow78, Fornes03, Lee05, Sen07]. For example, Bokobza and Chauvin [Bokobza05] showed mechanical reinforcement of natural rubber (NR) in the presence of well dispersed small silica nanoparticles, this reinforcement being better than that predicted by models successfully employed for conventional polymer composites (microcomposites). Such effects are ascribed, mainly, to the large surface to volume ratio of the nano–fillers and, consequently, to a significant fraction of polymer at the interfaces with the nanoparticles. In addition to the large interaction (interfacial) area, the development of interactions (physical and chemical) between the polymer and the fillers has been found of significance in modification of NCs properties [Si06, Wang03, Allegra08], while computer simulations have predicted dependences between improvement of NCs properties and the range of the strength of the respective interfacial interactions [Mansfiled89, Allegra08].

During the last decades much attention has been drawn to the relation between the improved 'macroscopic' properties of polymer NCs and the modification of structure of the

polymer in the nanometric range in the interfacial layer, namely a few nanometers from the surface of the nanoparticles [Harton10, Zou08, Okada06, Akcora10, Kumar10, Giannelis11 and references therein]. Parallel to interfacial polymer in NCs, polymers in the form of thin films adsorbed on flat solid surfaces are being studied [Kumar99N, Capponi12, Vanroy13 and references therein], as the adsorption mechanisms and the nature of developed interactions, in both cases, are practically the same [Guselin91]. Based on the large amount of respective publications on these topics, we can easily conclude that this '*interfacial polymer fraction*' [Wurm10] is widely thought to be characterized by a modified structure [Mansfield89, Kumar99N, Sen07, Koga12, Vogiatzis13, Harmandaris14] and dynamics [Fragiadakis05, Fragiadakis07, Fragiadakis11, Lacabanne11, Fullbrant13, Holt14, Leng15, Lin15] as compared to the bulk [Akcora09, Koga12], which can affect significantly or even dominate the properties of the system [Schmidt10, Akcora09]. The main focus of this thesis is on effects of various parameters on dynamics and structure of interfacial polymer in NCs [Klonos10A, Klonos11, Klonos12, Klonos15A-C]. These effects are discussed in more detail in the next section. Therefore, the knowledge about the polymer–particle interactions and the factors which govern the polymer structure and dynamics at the interfaces is of high importance for understanding the long–term performance of materials in engineering applications and in materials design issues.

Regarding the procedure of NCs preparation, polymer NCs could be categorized to (a) *conventional* and (b) *core–shell* based NCs (Fig. 1.1). We note that the present study deals with materials of both classes and the chapters of the thesis are accordingly organized. *Conventional* NCs were developed historically first, aiming at the improvement of a polymer matrix in polymer NCs by introducing and well dispersing organic or, mostly, inorganic particles (Fig. 1.1a) [Bokobza05, Fornes03, Lee05, Sen07]. For better control of the interfacial properties and optimization of the dispersion of filler in the polymer matrix and, in general, of the macroscopic properties of the materials, *core–shell* NCs were developed (Fig. 1.1b) [Liu10]. This term is used to define the development of composite nanoparticles, consisted of a *core*, which may be either an inorganic particle [Bershtein09, Giannelis10, Redeker13, Sohrabi13, Kumar13] or even a polymeric particle [Wang06, Quan15, Chen15], on which one or more extra layers are adsorbed covering its surface and forming the *shell*. The extra layer(s) can be consisted either of inorganic [Kofinas11] or organic substances (e.g. polymers) [Dong11]. Various polymeric materials based on *core–shell* structure have already been developed, targeting industrial [Nan12, Quan15], optics [Nakabayashi12] and

optoelectronics [Liao12, Redeker13, Kofinas11, Giannelis10], chemistry, biological [Wang06, Bershtein09 Dong11, Sohrabi13] and biomedicine [Wang06] applications.

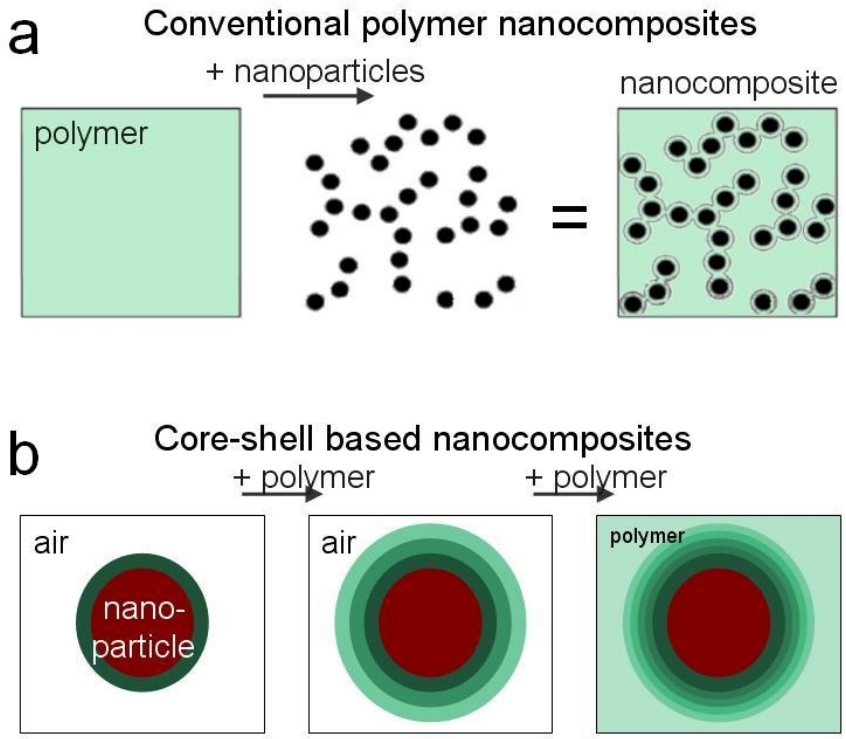

Fig. 1.1. Schematic representation of the preparation procedure for (a) *conventional* and (b) *core–shell* based polymer NCs.

Focusing now on metal oxide/polymeric systems, such as silica/polymer [Zou08], and comparing the *conventional* NCs, where the nanoparticles are embedded [Jancar10] and/or generated [Fragiadakis07] within a polymer matrix, with *core–shell* NCs, we can mention that in the latter category the polymer–particle interaction can be better controlled. Indeed, the encapsulation of the particles can be achieved by applying more mild chemical procedures [Giannelis10, Sulim09] and, at the same time, by fine tuning of the physical bonding between polymer and nanoparticles [Giannelis11, Akcora09, Kumar13]. Such advantages can lead to easier preparation of materials [Kofinas11] and, moreover, to higher quality of filler dispersion [Nan12, Ackora09, Kalathi14]. Additionally, the ability of preparation of materials with higher silica/polymer ratios (as close to unity as possible) is also an important advantage for certain applications (e.g. drug delivery).

1.2. Characteristics of the interfacial polymer fraction in polymer NCs

The fraction of interfacial polymer in NCs (Fig. 1.2) has been attempted to be evaluated by various experimental techniques, such as by monitoring the structure [Mixa04, Miwa06, Harton10, Papon11, Koga12, Jouault13, Fullbrant13, Holt14, Leng15, Antonelli15, Lin15], the thermal behavior (thermal transitions) [Dobbertin96, Sargsyan07, Wurm10, Chen10, Moll12, Merino13, Purohit14], and polymer molecular dynamics [Fragiadakis05, Lacabanne11, Fullbrant13, Purohit14, Gong14, Holt14, Leng15, Lin15].

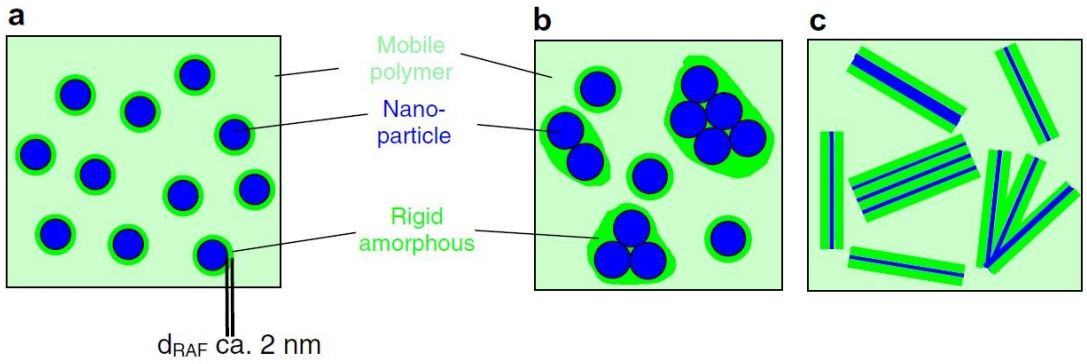

Fig. 1.2. Sketch of spherical (a, b) and layered (c) nanoparticles (blue) covered by a layer of immobilized polymer (*RAF*) (dark green) in a mobile amorphous matrix (light green), taken from [Sargsyan07].

Depending on the physical property followed [Eslami13], results suggest that the range of interfacial polymer properties domination may vary in the range of a few nm (although larger values of many tens of nm have also been reported [Miwa04, Miwa06]) from the surface of the nanoparticles (Fig. 1.2). The density of interfacial polymer has been found, in general, increased as compared to that in bulk, in addition to changes imposed on interfacial polymer chain conformations at the same polymer/particles interfaces [Koga12, Voyatzis13, Johnston13R]. Regarding molecular mobility, in most cases in the literature, the polymer in the interfacial layer is thought completely immobile, as it does not demonstrate any additive contribution to segmental mobility, for example to glass transition. Among others, Schick and coworkers [Dobbertin96, Wurm03, Sargsyan07, Wurm10, Purohit14, Zhuravlev14] have demonstrated such contribution of the interfacial polymer to glass transition, in particular a reduction in the heat capacity step during glass transition, ΔC_p (Fig. 1.3). Thus, simple multi-phase models and mathematical formulas have been proposed and have been already employed for the calculation of the fraction of interfacial polymer, by comparing the response (ΔC_p) of the mobile polymer fraction, *MAF*, with the missing part in the response in NCs, i.e. the reduction in ΔC_p, which represents the rigid (immobile) polymer

fraction, *RAF*, at interfaces (Fig. 1.3). Much attention has been also paid to the effects imposed on T_g by the presence of nanoparticles, results demonstrating, however, controversial changes [Paul08, Jancar10 and references therein].

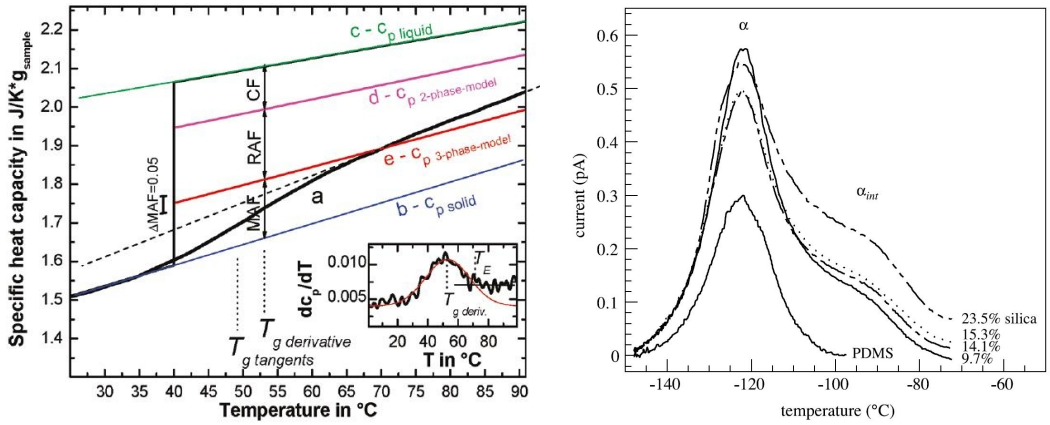

Fig. 1.3. (Left) Specific heat capacity, C_p, of polyamide-6 (PA6) in the glass transition region as recorded by differential scanning calorimetry (DSC) and illustration of estimation of *RAF* from the missing response (details in the text), taken from [Wurm10]. (Right) segmental polymer response for PDMS and PDMS/silica NCs as recorded by a dielectric relaxation spectroscopy technique (details in text), showing the bulk (α relaxation peak) and interfacial (additional α_{int} peak) polymer responses, taken from [Fragiadakis05].

On the other hand, during the last ten years a significant amount of papers have been published showing that by employing dielectric relaxation spectroscopy (DRS) [Kremer02] the interfacial polymer is not completely immobile for a variety of polymers [Fragiadakis05, Lacabanne11, Fullbrant13, Purohit14, Gong14, Holt14, Leng15, Lin15]. Moreover, it has been shown that the interfacial polymer demonstrates retarded dynamics, as compared to the bulk (α relaxation), and cooperativity, this being expressed by the recording of an additional relaxation process (α_{int}) (Fig. 1.3). With filler fraction in NCs increasing, the intensity (dielectric strength, $\Delta\varepsilon$ [Kremer02]) of the additional relaxation has been found to increase. In correlation with the above observation, the evaluation of interfacial polymer fraction has been attempted by carefully comparing the dielectric strength of α_{int} with the overall segmental response [Fragiadakis07, Fullbrant13]. In this approximation, we study here the particle–polymer bond strength, arising from the different type of particles, and the surface properties (roughness) of the initial particles as important parameters that affect the range of particles-polymer interaction [Klonos10A].

1.3. Computer simulations in polymer NCs

Computer simulations in combination with Theory [Binder12, Scheutjens79, Yan13, Ganesan14, Allegra08, Koski13, Vogiatzis13, Pfaller13, Hanakata14, Theodorou14, Harmandaris15] on polymer NCs have been proven useful tools for understanding the relationships between interactions, morphology, interface characteristics, and the phase behavior of polymers in NCs. To that aim, methodologies have been proposed for studying realistic polymer NCs at experimentally relevant length scales, taking into consideration several parameters, such as: the polymer chain length (grafted, in bulk etc.), the density of polymer grafting [Vogiatzis13], the type of attraction between particles [Karatrantos13, Karatrantos15], the size of primary particles [Kutvonen12], the density of crosslinks [Chao13, Kim15], and the polymer–filler interaction strength [Goswami09, Liu11, Hanakata14]. In the perspective of materials engineering and applications, simulations were found able to predict the final material properties (mainly mechanical and thermal stability) [Allegra08, Goswami09, Alaghemandi11, Yang12, Kutvonen12, Coto13, Ferdous13, Chao13, Pahlavanpour13]. The effects imposed on material properties by the various parameters, for example by geometrical and surface characteristics of the fillers [Chao13, Coto13], filler distribution in the polymer matrix [Ferdous13, Kalathi14], structure of the polymer matrix [Kutvonen12], and strength of polymer–particle [Goswami09, Liu11, Eslami13] and particle–particle [Karatrantos15, Karatrantos13] interactions, have been found to be related with each other [Chao13].

In general, in polymer NCs enhanced mechanical properties are observed as compared to the neat polymer matrix. This improvement has been suggested to depend mainly on the good filler dispersion in a polymer matrix in combination with the particles size [Chao13], while this improvement may decrease with polymer crosslink density [Kim15]. It is shown that the existence of polymer–polymer and/or polymer–particles crosslinks in NCs has a predominant role on mechanical reinforcement, over other parameters, such as the shape, size and concentration of nanoparticles in the same NC system [Kutvonen12]. For fixed dimensions of the nanoparticles the polymer–particle interaction strength and the temperature of the NC system have been found to be primarily responsible for the quality of filler dispersion [Goswami09, Liu11]. Finally, Kalathi *et al.* [Kalathi14, Kalathi12] showed that the nanoparticles distribution in polymer NCs may change as a result of changes in the average NC viscosity, the latter depending on polymer entanglement mesh size in relation to particles size.

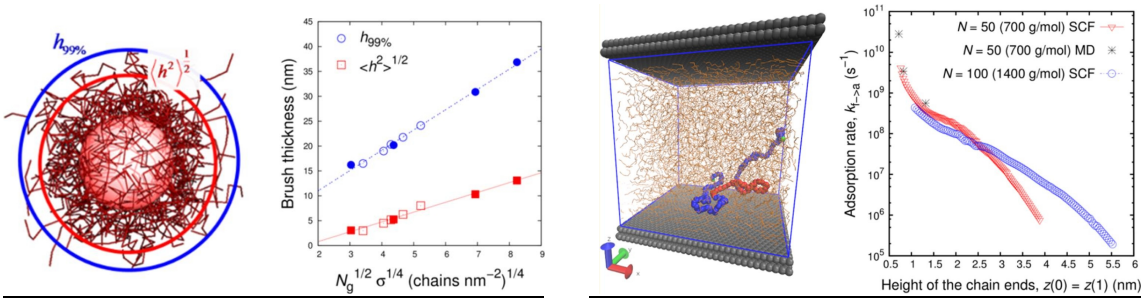

Fig. 1.4. (Left) schematic representation of polymer layers grafted to nanoparticles in silica–polystyrene NCs and results by computer simulations for the formed 'brush' thickness (either $\langle h^2 \rangle^{1/2}$ or $h_{99\%}$) plotted versus the square root of the degree of polymerization of grafted chains, $N_g^{1/2}$, times the fourth root of the grafting density, $\sigma^{1/4}$, taken from [Vogiatzis13]. (Right) computer simulation schematic and results for the desorption kinetics of polyethylene (PE) melts on graphite, taken from [Theodorou14].

Grafting of proper ligand (monomer, polymer) on the surfaces of nanoparticles can result to more uniform dispersion of the fillers in a polymer matrix, as compared to that in NC prepared with traditional mixing techniques [Binder12, Chao13]. Dodd *et al.* [Dodd12] suggested that the grafted layer thickness increases with polydispersity of the polymeric ligand, while Ginzburg [Ginzburg13] showed that for low filler loadings (3–5 %) grafting indeed results in fine filler dispersion and was able to predict new morphologies (of particles) for larger filler loadings. In polymer NCs of the *core–shell* type, Balmer *et al.* [Balmer11] demonstrated an agreement of results by Monte–Carlo simulations and those by structural (SEM), physicochemical (dynamic light scattering, thermogravimetry, BET surface area analysis), and, in addition, concluded that small angle X–ray scattering is ideally suited for the structural characterization of polymer NCs.

From the polymer mobility point of view, results by simulations are discussed in terms of glass transition temperature, T_g, [Qiao11, Starr13] and fragility, m, [Starr13] as well as in terms of segmental dynamics [Karatasos14, Harmandaris14, Vogiatzis14]. The effects imposed by the presence of nano–inclusions in a polymer matrix on T_g and m, are both positive and negative [Qiao11, Starr13], this effect originating mainly from changes on filler dispersion (clustering at high filler loadings) and the subsequent loss of interfacial (potential for interactions) surfaces. Results in graphene / hyper–branched polyesters [Karatasos14] revealed an additional (to bulk) glass–like transition at a considerably higher temperature (namely, a higher T_g) as compared to that of pristine polymer, which accompanied the slowing down in both the local and the global polymer dynamics in the same NCs. Rissanou

et al. [Harmandaris14] showed that polymer relaxation times decrease significantly (namely, acceleration of the overall segmental polymer dynamics) beyond the first adsorption layer of polymer (of three types, polyethylene, polystyrene, poly(methyl methacrylate)) on graphene nanosheets and, moreover, showed that the range of relaxation times of the adsorbed segments is broader, than that in bulk, the extent of these effects depending on the type of the polymer.

Computer simulations in polymers adsorbed on solid surfaces [Johnston13R, Mansfield89, Borodin03, Doxastakis14] have predicted increased density of the interfacial polymer, accompanied by slower dynamics, as compared to the bulk. The prolonged relaxation time of polymer in the surface region originates from the strong segment-surface attraction [Mansfiel89]. However, Borodin *et al.* [Borodin03] had previously demonstrated that slower dynamics of poly(ethylene oxide) (PEO) at the interface with TiO_2 is better determined by the surface structure and electrostatic PEO-TiO_2 interactions, rather than the increased interfacial polymer density. Results by Monte–Carlo techniques suggest that in the interfacial layer (1–2 nm [Termonia09], or even, up to 20 nm [Vogiatzis13] in thickness) polymer segments can be oriented tangentially (parallel) to the solid surface. Additionally, in some cases of polymer adsorption on the solid surfaces of nanoparticles there seems to be an accumulation of chain ends at interfaces accompanied by a decrease in the average interfacial polymer density, however, the density of different type of segments (free/grafted) depending on the distance from the solid surface [Vogiatzis13, Kritikos13] (Fig. 1.4). Adoption of various conformations by polymer chains (tails, loops, trains [Scheutjens79]) at the interfaces with solid surfaces was found also of importance for predicting interfacial polymer properties [Mansfield89, Harmandaris05, Bitsanis93, Daoulas05, Johnston13]. Theodorou and coworkers [Mansfield89, Theodorou14] showed that polymer chains close to an attractive solid surface are pronouncedly flattened, or else more parallel to the surface, as compared to those away from the surface, this result coming in agreement with respective experimental studies [Kumar99N, Rotella11] (Fig. 1.5). Bitsanis and Brinke [Bitsanis93] and Harmandaris and coworkers [Harmandaris05, Daoulas05, Johnston13] pointed to the polymer chain length as a critical parameter for adoption of different conformations of polymers adsorbed on solid surfaces and of polymer confined between solid surfaces, respectively. In addition, numerical Self Consistent Field (nSCF) method was employed [Kritikos13] to study and describe, computationally, the bound polydimethylsiloxane (PDMS) layer around spherical nanoparticles, such as silica, (a system similar to those under investigation in this thesis). The respective results showed that for PDMS chains grafted on the surfaces of silica ~50 nm in

diameter, the polymer conformations in the interfacial layer can be categorized in loops and tails [Kritikos13]. The volume fraction of loops is highest close to the interface and reduces (by almost 50 %) about 2–3 nm away from the interface, the opposite being true for the tails.

1.4. Polymers adsorbed on solid surfaces – Modeling

Throughout this study, especially in the chapters that present results obtained with *core–shell* NCs, we conclude that interfacial polymer can be studied in-depth better in *core–shell* NCs comparing with conventional NCs. This is mainly due to the preparation procedure of *core–shell* NCs. The preparation consists of a '*layer by layer*' polymer adsorption (Fig. 1.1b) onto the solid surfaces of the nanoparticles/aggregates [Bershtein09, Galaburda14]. Depending, thus, on the polymer content in NCs, the percentage of the interfacial polymer fraction can be varied significantly [Holt13, Holt14] and, most importantly, it can vary at our will. Therefore, interfacial polymer can be the majority, as compared to other polymer fractions/phases (bulk, crystalline etc.) in the same system. For these reasons, the study of the polymer–filler interactions and their effects on polymer dynamics in *core–shell* NCs, resembles that of polymers adsorbed onto solid surfaces, already studied as model systems for the last decades [Scheutjens79, Mansfield89, Guiselin91, Kumar99N, Starr01 Ackora09, Liu10 Harton10, Napolitano12, Koga12, Rotella11, Kalathi14, Koga14, Yin15].

Fig. 1.5. Schematic for the detected two different kinetic regimes during the adsorption of polystyrene on aluminum surface by thermal annealing at temperatures above T_g, taken from [Rotella11].

With respect to effects imposed on polymer structure and mobility the most widely studied parameter is glass transition. However, the more than one decade long discussion on effects imposed on glass transition temperature, T_g, in thin polymer films is controversial [DeMaggio97, Forrest01, Forrest02, O'Connell05, Fakhraai08, Napolitano08, Tress10, Paeng11, Tress13, Chai14, Hanakata14, Ediger14, Kremer14, Yin15], leaving still a not consistent picture. In the following, we will report selected results and proposed models from the literature, which will be related later within the interpretation of experimental findings in this thesis.

More than two decades ago Guiselin and coworkers [Guiselin91] have proven the existence of depletion layers and different modes of polystyrene (PS) adsorption on solid surfaces, employing neutron reflectivity methods and chemical annealing procedures. More recently, Wübbenhorst and coworkers have detected two different kinetic regimes (anisotropic orientations) [Rotella11] during the adsorption of polymers on aluminum surface (Fig. 1.5). Kumar and coworkers [Ackora09, Kalathi14] have demonstrated the dependence of the self–assembly characteristics of polymer–grafted nanoparticles on the adsorbed polymer chain length, while Harton *et al.* [Harton10] studied the adsorption of poly(2–vinylpyridine) (PVP) in both silica particles and flat surfaces (thin film, <100nm), with equivalent chemical procedure, and showed that although T_g (of bulk) is almost unchanged, yet, the polymer fragility was slightly reduced and the interfacial polymer fraction was found significantly smaller around the nanoparticles. Such studies attempt to shed more light on the still open debate about the changes in the bulk properties imposed by the presence of interfacial polymer. The obtained results, regarding the various changes on T_g (both increasing and decreasing) [Jancar10] and the dynamics of interfacial polymer fraction, have been interpreted by invoking various concepts, such as the *interfacial free volume* [Napolitano12] or/and the existence of the so called *dead polymer layer* [Napolitano10], the flattering of chain coils at the interfaces [Starr01] and the inter–balance between bimodal conformations (e.g. loop and tails) adopted by the interfacial polymer chains (Fig. 1.6) [Koga12 and Refs. 1–2 therein], and [Kritikos13, Koga14]. We should report that, in this thesis the latter model [Koga12] will be one of the main tools employed for interpreting our overall results related to interfacial polymer dynamics.

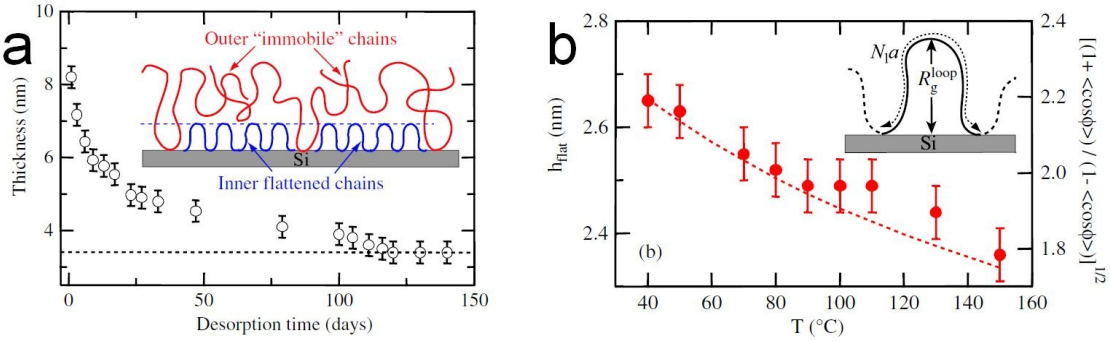

Fig. 1.6. (a) Desorption kinetics of the equilibrium adsorbed polystyrene layer on Si substrate during the chemical annealing (i.e. toluene leaching), the inset shows the schematic view of the two different chain conformations. (b) shows the temperature dependence of height of flattened chains (loops), h_{flat}, while the inset shows the schematic conformation of the flattened chains. Figures were taken from [Koga12].

Finally, differences between the density of interfacial polymer and that of polymer in bulk have been reported. For instance, polystyrene (PS) adsorbed on flat Si substrate has demonstrated higher density in the inner region of the interfacial layer than that in bulk, while the outer interfacial region is characterized by density equal to that in bulk [Koga12]. Computer simulations on PS grafted on spherical nanoparticles demonstrate that the density of grafted chains in the interfacial layer of the inner 2−3 nm is about double than that of polymer chains in bulk [Voyatzis13] (more detailed results in the previous section).

1.5. Confinement effects

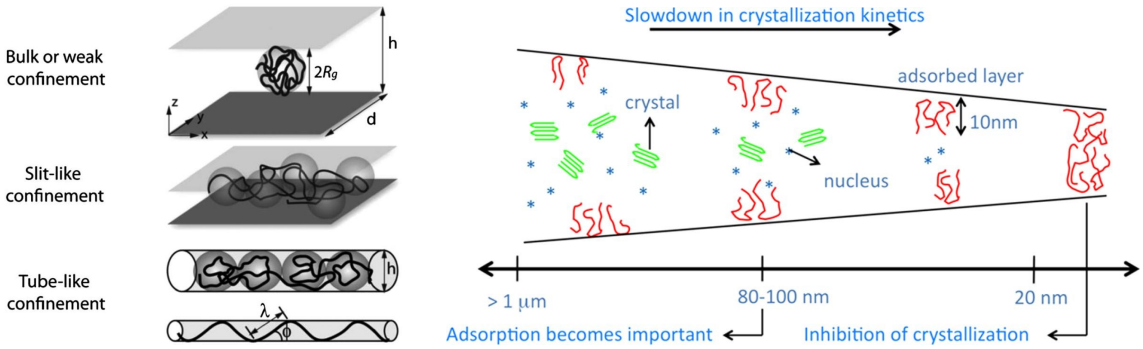

Fig.1.7. (Left) Schematics comparing polymer conformations in bulk solution, *slit-like* confinement, and *tube-like* confinement for given polymer radius of gyration R_g and confinement dimensions *h* and *d*, taken from [Mai12]. (Right) schematic for describing the slowing down of crystallization of poly(ethylene terephthalate) (PET) with gradually increasing of spatial confinement, taken from [Vanroy13].

Polymers constrained to spatial dimensions (confined) less than about 100 nm (Fig. 1.7, left) typically exhibit a shift of glass transition to lower temperatures and an acceleration of segmental dynamics as compared to the bulk. This effect is often discussed in terms of less intermolecular constraints and greater unoccupied volume [Mansfield89, Floudas97, Fukao00, Schönhals03, He07, Tress10, Krutyeva13, Frielinghaus13, Floudas13, Kremer14, Theodorou14, Yin15], as compared to constraints at larger dimensions. The extent of confinement depends, mainly, on the characteristics of the confining surface and the chemical properties of the polymer [Kremer14], on the type of the confining medium (solid inorganic or polymeric [Colmenero14, Colmenero10]), and the space dimensionality of the latter (1D [Napolitano11], 2D [Schönhals03, Frielinghaus13, Chrissopoulou13, Floudas14], and 3D [Yabu14]). Polymers in the form of thin polymer films, with thickness from 1 to 100 nm, are

also thought to be under spatial 1D confinement and for the last two decades they are studied as model systems [Forrest01, O'Connell05, Tress10, Chai14, Ediger14, Yin15] in the frame of this topic. In the case of thin polymer films effects by confinement on polymer mobility arise simply from the very small thickness, in general.

Wübbenhorst and coworkers [Napolitano12] performed experiments on polystyrene (PS) in the form of thin film at different thermal annealing conditions and showed that the observed shift in T_g is proportional to the degree of adsorption and, therefore, to the interfacial polymer volume. In addition, they studied [Vanroy13] the interplay between the thickness of the irreversibly adsorbed polymer and the range of spatial confinement (from μm to a few tens of nm), by monitoring the ability of poly(ethylene terephthalate) to crystallize being adsorbed on aluminum surfaces and, simultaneously, confined between the same surfaces (Fig. 1.7, right). Computer simulations by Lang *et al.* [Lang14] predicted that the T_g for a polymer adsorbed on a solid substrate demonstrates a linear additive dependence from the interfacial adhesion energy. Regarding polymer NCs, Srivastava and Basu [Srivastava07] were the first to report experimental observations, for PMMA filled with dispersed gold nanoparticles, of a crossover in the sign of T_g deviation for confined polymers by the variation of nanoparticle-polymer interface width and, simultaneously, keeping interparticle spacing fixed. Chandran *et al.* [Chandran14] observed in polymer-particles blend based films a systematic variation in the dispersion of nanoparticles with confinement for various compositions and matrix-polymer chain dimensions, while for fixed composition they observed a reduction of T_g with decreasing blend-film thickness. Li *et al.* [Li14, Li15] revealed the existence of two glass transition steps in poly(methyl methacrylate) (PMMA) confined in cylindrical pores after slow cooling (annealing), while a single T_g was observed after fast cooling (quenching or, in other words, vitrification). Two glass transition steps, one related to the bulk and the other to the confined part of the polymer, have been also recorded with different polymers [Merino13, Saiter13 and references therein]. Barroso *et al.* [Barroso13] studied poly(ethylene oxide) confined within graphite oxide (GO) nanosheets and recorded a faster relaxation, as compared to that in bulk, that is nearly independent of the polymer chain length.

Significant results have been reported for systems based on polydimethylsiloxane (PDMS) under confinement [Kirst93, Schönhals03, Colmenero10, Krutyeva13 and references therein], which is the polymer of interest in this thesis. Schönhals and coworkers [Schönhals03] showed that the dynamics of PDMS confined in the mesopores glasses becomes faster with lower activation energy on increasing of pore diameter. Colmenero and coworkers [Colmenero10, Krutyeva13] recorded similar effects for PDMS confined in

cavities of different dimensionality (1-3D) [Colmenero10] and they studied, further, the interplay between interfacial and confined PDMS in the same cylindrical pores by manipulating the hydrophilicity of the walls inside the pores. More recently, we recorded in silica-gel / PDMS core / shell type NCs the existence of two glass transition steps by DSC, one referring to the bulk (high T_g) and the second (lower T_g) referring to PDMS confined in the cylindrical like pores of silica-gel. Similarly to DSC, two respective segmental relaxation mechanisms were recorded by dielectric relaxation spectroscopy (DRS), accompanied by an additional process which monitors the interfacial polymer dynamics [Klonos15A]. In this frame, we study here effects imposed on bulk, interfacial and confined dynamics, all coexisting in the same NC systems, by crystallization annealing experiments and by properly modifying the solid surfaces of oxides before polymer adsorption, this modification resulting in manipulation of both the external surfaces and the diameters of pores (chapter 10). Respective results [Schönhals03, Krutyeva13], including results in this thesis, provide further support that confinement also in the case of polymer NCs arises mainly from size effects, similarly to polymer confined in solid porous means and in the form of thin films [Kremer14]. A general observation concerning PDMS, arising from the various respective studies [Schönhals03, Krutyeva13, Colmenero14 and references therein] suggests that, in general, 2D confinement may severely affect the dynamics of PDMS in the scale between 2 and 30 nm. This point will be further studied later in chapter 10.

In addition to the above, almost standard effects of confinement, peculiar effects have been also reported. For example, Schwartz *et al.* [Schwartz04] employed DRS to study confinement effects on oligomeric poly(propylene glycol) liquids confined in a 2D layer-structured clay. They showed that in the clay the normal mode relaxation becomes drastically slower with stronger intensity than the α relaxation (i.e. the dynamic glass transition), in contrast to the bulk samples where the opposite behavior is observed. Additionally, α relaxation is unaffected by the 2D confinement, suggesting that the underlying phenomena responsible for the glass transition are the same as in bulk. In addition, Saiter *et al.* [Saiter13] obtained strong reduction in cooperativity and the temperature dependence of the characteristic relaxation frequency of poly(propylene-co-ethylene) confined in the galleries of montmorillonite (intercalated nanocomposite), while in some cases the expected changes in glass transition due to confinement were not observed.

1.6. Polydimethylsilixane (PDMS) / metal oxide NCs

PDMS/metal oxide based NCs, such as the systems of interest of this thesis, have attracted a lot of attention for the last years due to their chemically mild processing, good mechanical and thermochemical (non toxic) properties and, therefore, they are used in many applications [Zou08, Takakashi06, Nodera06]. PDMS molecules can form a helix structure (Fig. 1.8) due to the corresponding rotations around the Si–O bonds [Gunko07]. Therefore, only a portion of lead segments can interact with the solid surface during the adsorption of PDMS onto silica, e.g., by the formation of the hydrogen bonds ≡SiO–H · O(Si(CH$_3$)$_2$–)$_2$ (Fig. 1.9) [Richardson77, Gunko07, Bokobza10].

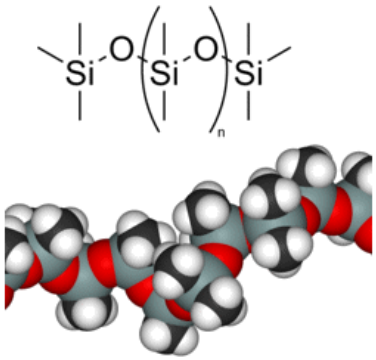

Fig. 1.8. Schematic of a polydimethylsiloxane (PDMS) chain.

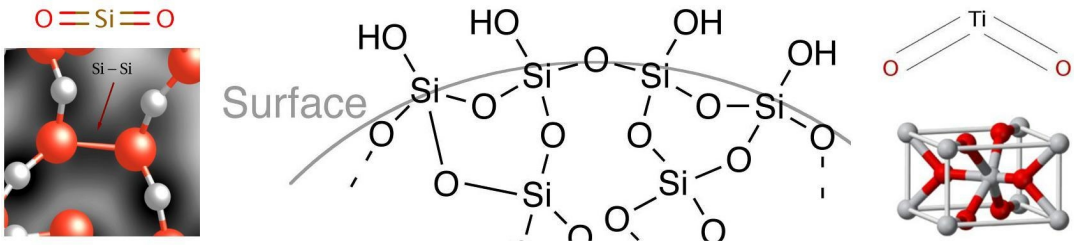

Fig. 1.9. Schematic view of silica (left, middle) and titania (right).

Measurements on NCs where silica particles are in situ generated by sol–gel techniques, in the presence of PDMS, revealed the existence of a fraction of polymers at the silica interface that is characterized by reduced mobility [Fragiadakis07]. Concerning the *core–shell* NCs, we will show that the structure of the adsorption complexes of the PDMS molecules depends on the conditions of the adsorption and the subsequent chemical/thermal treatment [Klonos15A, Klonos15C]. For instance, in concentrated solutions of PDMS in hexane, the fraction of unfolded molecules increases resulting in an increase in the density of

contact points between the PDMS molecules and the surface –OH (silanol) groups [Gunko07, Gunko14]. The adsorption of PDMS on various types of silica particles is proposed to be promoted by the external surface morphology of silica secondary particles with textural porosity [Galaburda14], mainly in fumed silica particles, and the intra– and inter–globule mesopores existed in various silica particles [Sulim09, Gunko07], engaging as free silanols as possible. The population of free silanols was found to depend on the surface water molecules [Gunko14], always existed in the surface of silica particles affecting, thus, the adsorption mechanism of PDMS chains and also the kinetics of the adsorbed chains [Gee04, Gunko07, Gunko14]. Finally, penetration of PDMS within nanopores and mesopores existed in the silica particles (aggregates) results in strong modification of their structure and dynamics [Gunko07, Gunko14, Klonos15A].

1.7. Present study – Motivation

Over the last ten years, Pissis and coworkers have studied interfacial effects in *conventional* polymer NCs, in particular, rubber/silica, focusing on polymer glass transition and segmental dynamics in the interfacial layer, studied by calorimetry and dielectric techniques [Fragiadakis05, Fragiadakis07, Klonos10A, Fragiadakis11, Klonos12]. In the frame of this thesis, we extended this work to *core–shell* (namely, metal oxides (core) / PDMS (shell)) type systems, in the form of powders, where polymer is adsorbed (although not grafted) onto silica and titania nanoparticles particles [Klonos15A, Klonos15B, Klonos15C]. We study interfacial dynamics of PDMS in NCs by recording directly the dielectric relaxation mechanism of the polymer in the interfacial layer, namely α_{int} relaxation. Comparing to other polymers [Fragiadakis11, Fullbrant13, Holt14], α_{int} in PDMS can be easily distinguished and analyzed, this being achievable, mainly, due to the high flexibility of PDMS chains and the significantly low interference of conductivity in the frequency/temperature region of segmental dynamics (related to glass transition) [Kremer02].

Next to fundamental interest, the issues related to interfacial polymer are also of practical significance in relation to a better understanding of structure–property relationships and, most probably, to prediction of properties of new materials for various technological and biomedical applications. In recent papers in the literature, results in polymer NCs (mainly calorimetric and dielectric) have been evaluated in terms of the fraction and dynamics of interfacial polymer and the thickness of the interfacial layer [Fragiadakis05, Wurm10, Fullbrant13, Holt14, Gong14]. It has been suggested that the latter depends on the size

[Gong14] and curvature [Harton10] of the nanoparticles, while here we examine as to whether the strength of polymer particle interaction bond is another relevant parameter [Klonos10A].

In the present thesis, we introduce the *nanometric roughness*, in terms of specific surface area, as a relevant parameter which takes into account aggregation and porosity of the nanoparticles. We study interfacial dynamics in: (a) *conventional* NCs of PDMS network reinforced with *in situ* generated silica and titania particles and (b) NCs of the *core–shell* type, based on linear PDMS (of two molecular weights) physically adsorbed on silica and titania of a wide range of specific surface area. Next to the surface roughness of the particles, we demonstrate the significance of interfacial hydration level for interfacial dynamics, in particular, and for polymer adsorption, in general, as the interaction between the metal oxides and PDMS or water molecules is, practically, of the same type, i.e. hydrogen bonding [Bokobza10, Gunko14]. In combination with the interesting effects imposed by the molecular weight of the polymer (chain length) [Kim12], we conclude that interfacial interactions and polymer dynamics at the interfaces, at least for PDMS, are dominated by the concentration of polymer–particles contact points and the structure and flexibility of the polymer [Klonos15A, Klonos15B, Klonos15C].

For this study we employ scanning electron microscopy (SEM) for the morphology, differential scanning calorimetry (DSC) for evaluating the interfacial polymer fraction from glass transition [Wurm10], and two dielectric relaxation spectroscopy techniques (DRS, TSDC) for the evaluation of interfacial polymer dynamics and fraction from the various contributions (namely, bulk, bulk–like and interfacial) to segmental dynamics in the NCs [Fragiadakis07]. For the calorimetric and dielectric techniques, we also employ different thermal treatments (e.g. annealing of crystallization), which have been proved quite revealing in recent studies in adsorbed polymers [Rotella11, Klonos15A, Klonos15C], and different hydration treatments.

1.8. Thesis outline

The thesis is divided into 11 chapters, as follows.

The present Chapter 1 introduces the concept of interfacial polymer fraction and its characteristics, in relation to changes in material properties in polymer NCs. Recent models for the description of the structure and dynamics of interfacial polymer are also presented. Next, we describe some physical/structural properties of PDMS in NCs based on metal oxide nanoparticles. Finally, we present briefly the motivation for this thesis and the employed experimental techniques.

In Chapter 2 we present briefly the materials under investigation and the respective methods of preparation.

Chapter 3 deals with the employed experimental techniques, i.e. scanning electron microscopy (SEM), differential scanning calorimetry (DSC), thermally stimulated depolarization currents (TSDC), dielectric relaxation spectroscopy (DRS), and equilibrium water sorption / desorption isotherms (ESI / EDI). In addition, we describe the respective methods of analysis, in terms of widely adopted models and mathematical equations, employed for the evaluation of the various effects. Finally, we give information on the experimental apparatus employed.

In Chapter 4 we present effects of polymer–filler interactions on molecular mobility in *conventional* NCs, based on PDMS networks filled with *in situ* generated silica (SiO_2) and titania (TiO_2) nanoparticles generated via sol–gel technique. Next to the size of initial particles, the parameters under investigation for interfacial interactions are the type and fraction of the filler [Klonos10A, Klonos11, Klonos12].

Chapter 5 deals with the effects of surface modification (by nanozirconia) and thermal annealing on interfacial polymer dynamics in *core–shell* NCs, based on high specific surface area fumed silica and physically adsorbed PDMS. The results are critically compared with results obtained, previously in Chapter 4, with *conventional* PDMS based NCs. Surface modification, results in lower specific surface area (mainly textural, i.e. more smooth surfaces) for neat oxides, and subsequently to suppressed polymer adsorption. Thermal annealing imposes suppression on interfacial polymer fraction and dynamics. Changes in the interfacial polymer dynamics and the overall dielectric response are explained in terms of changes in the concentration of polymer–particles contact points, as well as employing models that involve bimodal polymer chain conformations at the adsorbing surface (Fig. 1.6) [Klonos15C].

Chapter 6 deals with the effects of surface modification by nanozirconia on interfacial polymer dynamics in *core–shell* NCs, based on low specific surface area fumed silica and physically adsorbed PDMS. Contrary to Chapter 5, surface modification here results in surfaces of higher surface roughness for neat oxides, and subsequently to enhanced polymer adsorption [Klonos15B].

Motivated by the last two chapters, Chapter 7 deals with the dependence of the characteristics of the interfacial polymer fraction on surface roughness. We study interfacial polymer fraction, dynamics and cooperativity in PDMS adsorbed at a constant amount onto aggregates of fumed metal oxide particles (both silica and titania) of a wide range of nanometric surface roughness, for the initial oxide aggregates (no interference of surface modifications here) [Klonos15D].

Chapter 8 deals with the effects of water content in the NCs on interfacial dynamics. It is shown that dehydration of the samples results in suppression of polymer dynamics at the interfaces, similarly to effects imposed by smoothening of the same surfaces and, also, by thermal annealing.

In Chapter 9 we show effects imposed by polymer molecular weight on interfacial interactions in NCs of the *core–shell* type, based on titania and physically adsorbed linear PDMS of short and longer chains. It seems that for the shorter PDMS chains the polymer adsorption is stronger and interfacial dynamics slower, as compared to longer PDMS chains. This could be due to larger concentration of free chain ends for the shorter chains, resulting in engagement of more accessible contact points at the surfaces of titania.

Chapter 10 deals with the interplay between interfacial and confined PDMS dynamics, both present in the cylindrical–like pores of silica–gel. We follow the sensitivity of both dynamics on changes of spatial confinement, whereas only interfacial dynamics is affected by thermal annealing [Klonos15A].

Chapter 11 presents the general conclusions of the thesis.

Finally, the thesis is completed with the respective Literature.

2. Materials

1.1. Conventional NCs

The series of *conventional* polymer NCs under investigation consists of PDMS networks filled with several contents of silica (~6 to 36 wt%) and titania (~5 to 20 wt%) nanoparticles (Fig. 2.1). The materials were prepared by Professor Liliane Bokobza in the Laboratoire PPMD, E.S.P.C.I. (Paris, France). The unfilled network was prepared from hydroxyl–terminated PDMS (Gelest, *MW*=18000) by end–linking reactions using tetraethoxysilane (TEOS) as cross–linking agent. The cross–linked PDMS was swollen for a given time in titanium (IV) n–butoxide (TBO). Then the sample was hydrolyzed during 48 h and vacuum–dried at 80 ^{o}C for several days to constant weight. The difference between the final and initial weights represents the amount of filler [Bokobza10]. Films of ~1 mm in thickness were the finally produced samples.

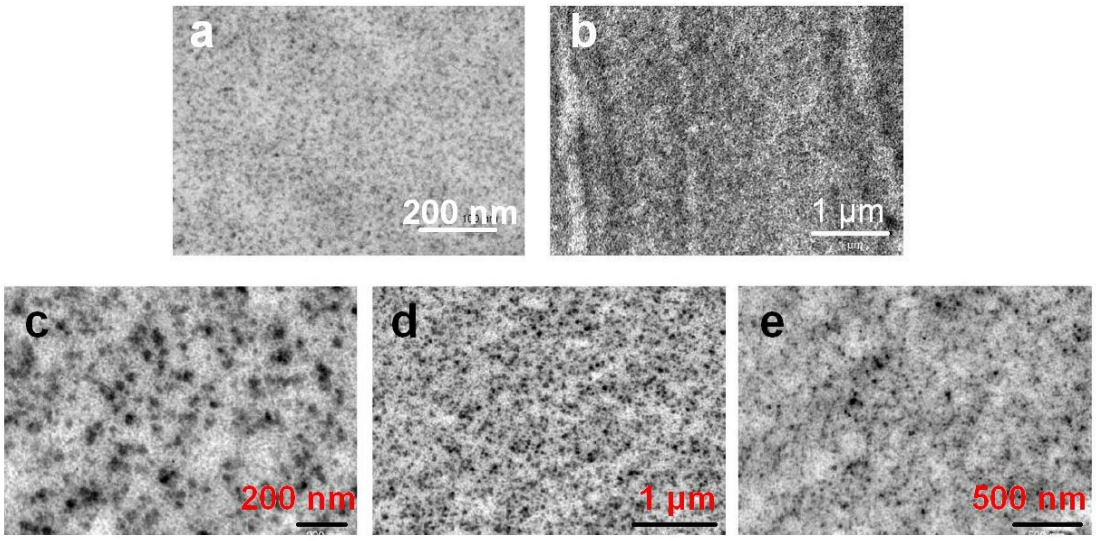

Fig. 2.1. TEM images of PDMS NCs filled with *in situ* generated nanoparticles: (a) 9 wt% SiO_2, (b) 22 wt% SiO_2, (c) 11 wt% TiO_2, (d) 11 wt% TiO_2, and (e) 20 wt% TiO_2. The images were taken from [Bokobza10].

The materials were partly characterized [Bokobza10] employing transmission electron microscopy (TEM), small–angle neutron scattering (SANS), stress–strain and equilibrium swelling measurements, by the group and other collaborators of Professor Liliane Bokobza. Transmission electron microscopy (TEM) measurements (Fig. 2.1) on the same systems show that titania nanoparticles are approximately spherical in shape with diameters between 20 and 40 nm and are well dispersed into the polymer matrix [Bokobza10]. Results by other techniques listed above will be briefly reported in Chapter 4, along with our results.

1.2. Core–shell NCs

Most of the discussion in this thesis concerns materials of the *core–shell* type, based on linear PDMS (*MW* ~2000 and ~8000, Kremniypolymer, Zaporozhye, Ukraine) adsorbed (via hydrogen bonding) on aggregates of fumed metal oxide particles of a wide range of specific surface area, S_{BET}. Most of the initial oxides were prepared in the pilot plant of the Institute of Surface Chemistry, National Academy of Sciences of Ukraine (Kiev, Ukraine) by the research group of Professor Vladimir M. Gun'ko. Some initial oxides are commercial and were bought from the companies Degussa and Merck.

The metal oxides used are titania (~70 nm in diameter for primary particles, ~800 nm in size for aggregates, S_{BET} ~ 25 m^2/g) and various silicas (8–85 nm in diameter for primary particles, 300–600 nm in size for aggregates, S_{BET} ~ 55–342 m^2/g). Figure. 2.2 shows SEM images for initial fumed silica and titania nanoparticles in the form of aggregates.

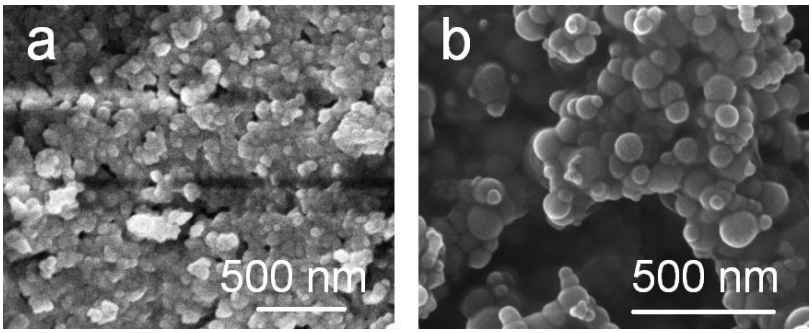

Fig. 2.2. SEM images of initial fumed (a) silica of S_{BET} ~340 m^2/g and (b) titania of S_{BET} ~25 m^2/g

PDMS was adsorbed onto the oxides at different contents (from 5 to 80 wt% PDMS), by adding different amounts of the same hexane–PDMS solution (1% PDMS) onto dried oxides. Figure 2.3. shows SEM images of the aggregates of nanooxides for gradually increasing PDMS loadings. One can easily observe the nanoparticles of ~10–70 nm in

diameter to form bunch–like aggregates varying between 250 nm and 1.5 μm in size (Figs. 2.3, 2.4).

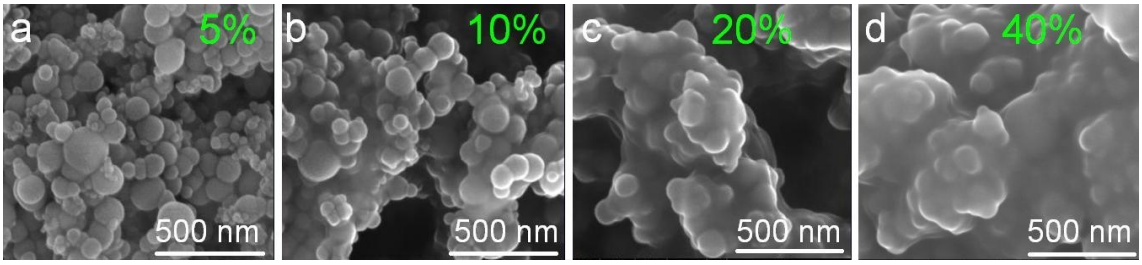

Fig. 2.3. SEM images of TiO_2/PDMS *core–shell* nanocomposites with PDMS (*MW* ~8000) at different polymer loadings (5 – 40 wt%)

Surface and porosity characteristics of some initial oxides have been studied previously employing isothermal Nitrogen adsorption–desorption techniques combined with Incremental Pores Size Distribution (IPSD) analysis [Sulim09]. The results suggest the formation of aggregates with initially non–porous particles that are characterized by textural porosity. Thus, S_{BET} values (25 – 342 m^2/g) describe well the nanometric roughness at the external surfaces. Polymer adsorption results in gradual decrease of textural porosity (smoothening of surfaces) (Figs. 2.3c,d). These changes can be followed for polymer loadings up to ~40 wt%, as at higher polymer loadings materials (Fig. 2.4) are in the liquid state rendering IPSD technique not applicable.

Additional information about the structural characteristics of these materials will be given in the respective chapters.

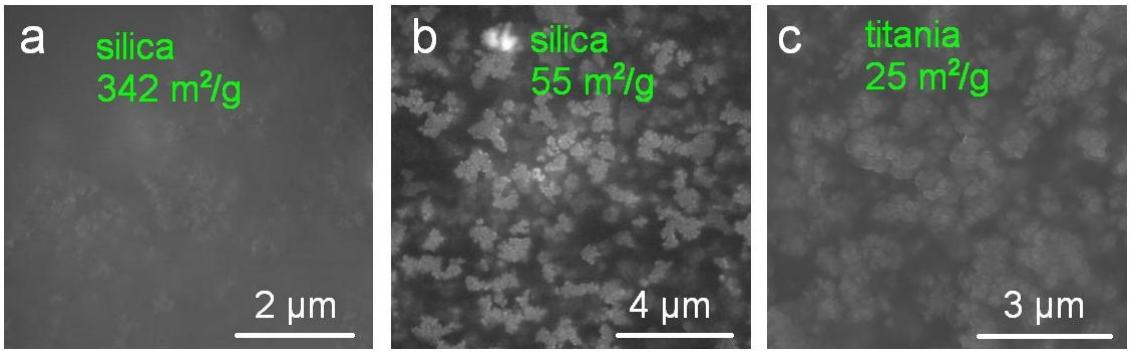

Fig. 2.4. SEM images of *core–shell* nanocomposites of fumed (a) silica 342 m^2/g, (b) silica 55 m^2/g , and (c) titania 25 m^2/g, filled with 80 wt% PDMS of *MW* ~8000 (liquid–like samples)

3. Experimental techniques

3.1. Scanning electron microscopy (SEM)

3.1.1. Experimental conditions

Morphology was examined by field emission Scanning Electron Microscopy employing a FEI Nova NanoSEM 230 apparatus at room temperature. For solid samples (powders, i.e. samples containing 40 wt% linear PDMS) the SEM chamber operated under high vacuum mode using a Through Lens Detector (TLD). Prior to the measurements the powders were compressed to form cylindrical pellets and then a golden thin layer was developed on their upper surfaces by sputtering. For liquid–like samples (namely samples containing 80 wt% linear PDMS), SEM chamber operated at room temperature under high vacuum mode using a Helix detector at a voltage of 30 kV.

3.1.2. SEM apparatus

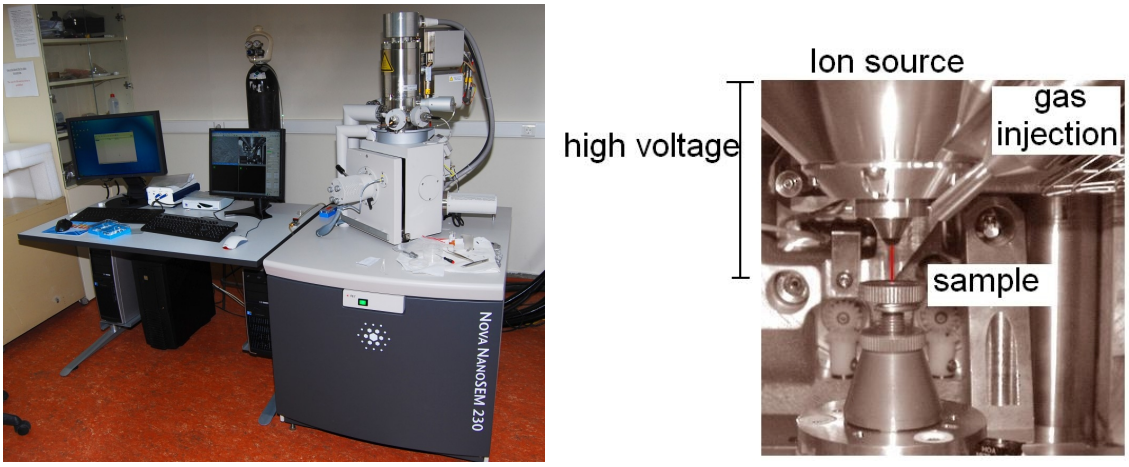

Fig. 3.1. The FEI Nova NanoSEM 230 SEM apparatus of the Department of Physics of the National Technical University of Athens (left) and measurement chamber (right).

3.2. Differential scanning calorimetry (DSC)

3.2.1. Experimental conditions

Thermal transitions [Sorai04] of the materials were investigated in helium atmosphere in the temperature range from –180 to 40 °C using a TA Q200 series DSC instrument, calibrated with Indium (for temperature and enthalpy) and Sapphires (for heat capacity). Samples of ~8 mg in mass were closed in standard Tzero aluminium pans (for powders) and Tzero hermetic aluminium pans (for liquids). Cooling and heating rates were fixed to 10 K/min for typical measurements (*Protocol A*). PDMS crystals melt at subzero temperatures, so a first heating scan for erasing thermal history was not necessary here. In order to enhance crystallization (during cooling), suppressed due to the presence of nanoparticles [Klonos10A, Klonos11, Klonos15A], measurements were carried out also after a 20 min isothermal stay (annealing) of the sample at a temperature between the onset and the peak (T_c) temperature of crystallization (*Protocol AC*). This annealing procedure resulted in maximum and stabilized degree of crystallinity, X_c. Finally, for initial PDMS we also performed fast cooling measurements (at ~90 K/min on average over the temperature region of crystallization, i.e. *quenching*) in order to evaluate the change in heat capacity at glass transition of the fully amorphous neat polymer during subsequent heating at 10 K/min.

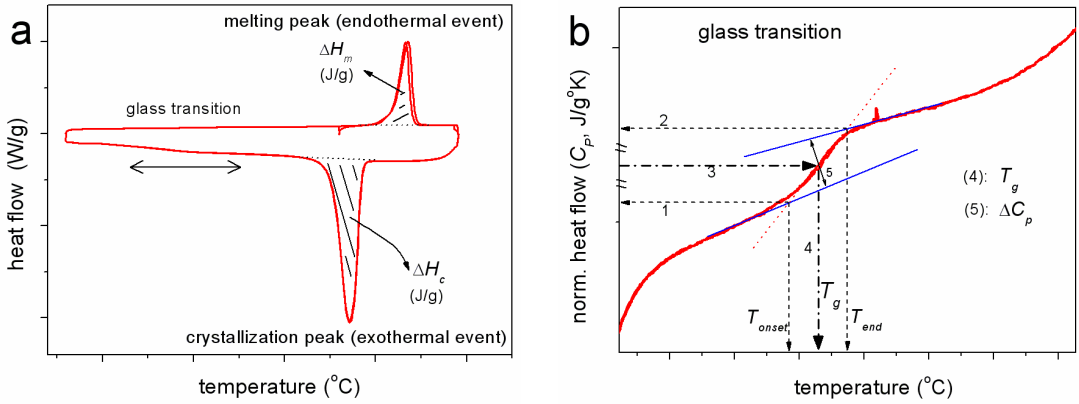

Fig. 3.2. (a) Typical DSC thermograms of a semicrystalline polymer during cooling and heating and (b) details in the glass transition region during heating. The arrows in (b) describe the estimation of T_g and ΔC_p.

3.2.2. Analysis of the results

Using the measured enthalpy of crystallization, $\Delta H_{c,DSC}$, and normalizing to the same polymer content, X_{PDMS}, according to Eq. (3.1)

$$\Delta H_{c,n} = \Delta H_{c,DSC} / X_{PDMS} \tag{3.1}$$

we have calculated the degree of crystallinity X_c employing Eq. (3.2),

$$X_c = \Delta H_{c,n} / \Delta H_{100\%} \tag{3.2}$$

in which $\Delta H_{100\%}$ is the enthalpy of fusion of fully crystallized PDMS, taken as 37.43 J/g [Aranguren98].

As far as glass transition is concerned, the characteristic temperature T_g was determined as the midpoint of the heat capacity step during the transition. As in previous works [Fragiadakis07, Klonos12], changes of ΔC_p between the neat polymer and nanocomposites based on the same polymer should be quantitavely compared, after the measured ΔC_p^{DSC} has been normalized to the same amorphous (not crystallized) polymer content, i.e. $X_{PDMS}(1-X_c)$. Therefore, we normalized our results according to Eq. (3.3)

$$\Delta C_{p,n} = \frac{\Delta C_p^{DSC}}{X_{PDMS}(1 - X_c)} \tag{3.3}$$

In many previous studies on various polymer nanocomposites, including polymer–silica nanocomposites, DSC results have often shown reduction of ΔC_p with filler fraction along with no significant variation of T_g . The results have been interpreted in terms of a Rigid Amorphous Fraction, *RAF* [Dobbertin96], being immobilized on the surface of the well–dispersed nano–inclusions thus making no contribution to the glass transition [Wurm10, Fragiadakis07, Klonos12, Papageorgiou14] and references therein. Furthermore, the deviation of ΔC_p of nanocomposites from that of the neat polymer proved a good measure of the degree of polymer–filler interaction [Dobbertin96, Wurm10]. On the other hand, the fraction of polymer which contributes to glass transition makes the Mobile Amorphous Fraction, *MAF* [Dobbertin96]. Thus, a '2–phase model' (*MAF* + *RAF*) has been previously employed for nanocomposites based on amorphous polymers [Wurm10], while an additional Crystalline Fraction, *CF* ($\sim X_c$), coexists in the '3–phase model' (i.e. *CF* + *MAF* + *RAF*) for semi–crystalline neat polymers [Dobbertin96]. For nanocomposites based on semicrystalline polymers the situation is more complex, as for X_c = 0, *RAF* represents the immobilized polymer at the particles–polymer interfaces (i.e. $RAF = RAF_{int}$), whereas for $X_c \neq 0$, *RAF* should also include the rigid amorphous polymer part immobilized within polymer crystals [Dobbertin96, Cebe04] (i.e. $RAF = RAF_{int} + RAF_{cryst}$). It has been suggested that RAF_{cryst} does not relax during glass transition [Dobbertin96, Purohit14] or that its relaxation may occur at temperatures close to melting, T_m, i.e. significantly higher than T_g of the bulk [Cebe04].

In the present study we categorize and evaluate the different polymer phases with respect to the type of their contribution to glass transition. Thus, we first estimated the amount of polymer which contributes to amorphous mobility, *MAF*, according to Eq. (3.4),

$$MAF = \frac{\Delta C_{p,n}}{\Delta C_{p,amorphous}^{PDMS}}\left(1 - X_c\right) \tag{3.4}$$

where $\Delta C_{p,amorphous}^{PDMS}$ is the $\Delta C_{p,n}$ of fully amorphous unaffected linear PDMS, found equal to 0.33 J/gK via fast cooling measurements. According to the widely used ATHAS Database [Wunderlich03] and Ref. 2 therein, ΔC_p of amorphous PDMS (in general over the various types) is equal to 0.37 J/gK, quite similar to our result. Bearing in mind that molecular dynamics of a polymer is related to its physical properties (e.g. chain–end groups, crosslinking density etc.) [Gedde95], we will use our experimental value (0.33 J/gK) for further calculations related to glass transition.

According to our calculations (next chapters), the sum of mobile amorphous and crystallized polymer fractions (*MAF* + *CF*) is lower than 1 in the nanocomposites, suggesting that, in the frame of the '3–phase model', one part of the response is missing from the calculated fractions. This deviation is thought to represent *RAF*, which can be easily calculated by Eq. (3.5).

$$RAF = 1 - CF - MAF = 1 - X_c - MAF \tag{3.5}$$

We should remind that all fractions refer to whole polymer mass according to the above equations employed for DSC. According to Schick and coworkers [Wurm10, Purohit14] in nanocomposites based on semicrystalline polymers, the RAF_{cryst} to X_c and RAF_{cryst} to RAF_{int} ratios may not be constant in DSC. Additionally, we have demonstrated that the interfacial polymer fraction can be temperature dependent according to DRS [Klonos15A]. Therefore, we will not attempt to calculate separately these fractions and we will consider results by Eqs. (3.4, 3.5) as simplified approximations for *MAF* and *RAF* at temperatures close to T_g.

3.2.3. DSC apparatus

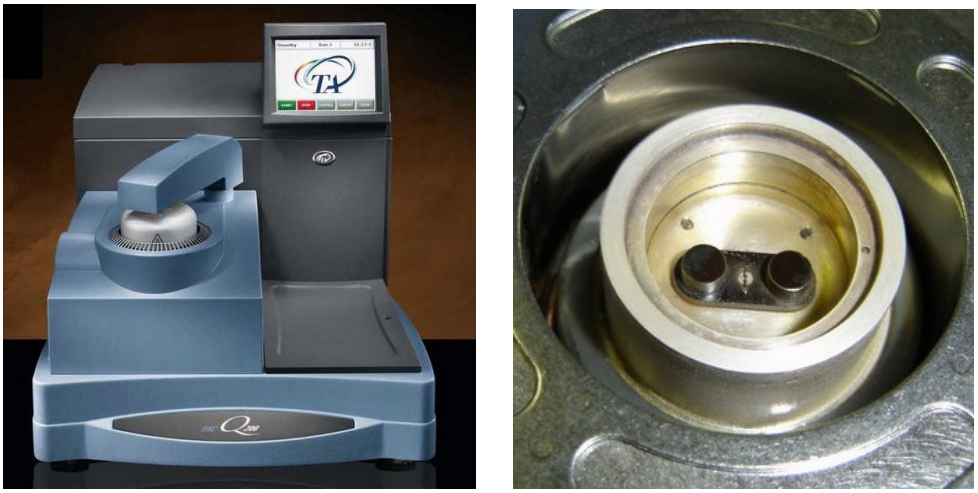

Fig. 3.3. Image of a TA Q200 DSC instrument (left) and detail in the measurement sample cell (right).

3.3. Thermally stimulated depolarization currents (TSDC)

3.3.1. Experimental conditions

Thermally stimulated depolarization currents (TSDC) is a special dielectric technique in the temperature domain, characterized by high sensitivity and high resolving power, the latter arising from its low equivalent frequency (10^{-4}–10^{-2} Hz) [Brauenlich79]. By this technique, the sample (12–20 mm in diameter and 0.05 – 1 mm in thickness) (powders were compressed to form pellets (under a pressure of 5 tons the thickness of the pellet created is about ~1 mm), while ~50 μm thin silica spacers of were used for liquids, to keep distance between the brass electrodes constant and ensure good electrical contacts) was inserted between the finely polished brass plates of a capacitor, placed in a Novocontrol TSDC sample cell and polarized by an electrostatic field E_p (~100 V/mm) at polarization temperature $T_p = 20$ °C for time $t_p = 5$ min for standard measurements and $T_p \approx T_c$ for time $t_p = 20$ min (similar to *Protocol AC*, as described above for DSC). With the field still applied, the sample was cooled down to –150 °C (cooling rate 10 K/min, under nitrogen flow), sufficiently low to prevent depolarization by thermal energy, then short–circuited and reheated up to 60 °C at a constant heating rate $b = 3$ K/min. Temperature control was achieved by means of a Novocontrol Quatro cryosystem. A discharge current was generated during heating and measured as a function of temperature with a sensitive programmable Keithley 617 electrometer.

3.3.2. TSDC apparatus

Fig. 3.4. Novocontrol TSDC apparatus in combination with quatro cryosystem and liquid nitrogen cooling system (left) and Novocontrol TSDC sample holder (right).

3.4. Dielectric relaxation spectroscopy (DRS)

3.4.1. Experimental conditions

Dielectric relaxation spectroscopy (DRS) [Kremer02] measurements were performed on samples same as those used for TSDC measurements, i.e. of ~1 mm in thickness for powders (compressed pellets) and ~50 μm in thickness for liquids. Samples were equilibrated under ambient conditions before measurements. Each sample was inserted between finely polished brass plates of a capacitor and an alternate voltage was applied in a Novocontrol sample cell (BDS1200 type). The complex dielectric permittivity, $\varepsilon^*=\varepsilon'-i\varepsilon''$, was recorded isothermally (in nitrogen atmosphere) as a function of frequency in the range from 10^{-1} to 10^6 Hz at temperatures from –150 to 60 ^oC, on heating in steps of 2.5, 5 and 10 K (depending on the process under investigation) using a Novocontrol Alpha analyzer. The temperature was controlled to better than 0.5 K with a Novocontrol Quatro cryosystem. Again, this measurement protocol will be referred to as *Protocol A*. In order to investigate effects of crystallinity on the segmental dynamics, measurements were carried out also following the *Protocol AC,* i.e. after a 20 min isothermal stay (annealing) of the sample at a temperature between the onset and the peak of crystallization, as it was defined from DSC measurements. The sample was cooled down to –150 ^oC and the isothermal steps started. This annealing procedure leaded to a maximum degree of crystallinity, X_c, and, thus, no further changes of crystallinity during the subsequent measurements were observed. DRS measurements were carried out on selected samples isochronally at 125 Hz during heating in the temperature range between –150 and 60 ^oC, at a rate of 2 K/min, in order to directly compare DSC and DRS responses in the temperature domain. Finally, DRS measurements were performed on selected samples during isothermal crystallization at temperatures in the region of crystallization, depending on the relaxation process under investigation. Continuous frequency isothermal scans taken every ~10 min provided an almost online view of changes in the dielectric response related to segmental dynamics during the evolution of the crystallization process [Wurm03, Lund08, Ezquerra04, Klonos15TA].

3.4.2. Analysis of experimental results

DRS results were analyzed by fitting model functions [Havriliak67] to the experimental data employing a proper software [FragiadakisSW], in order to evaluate the time scale (temperature dependence of the frequency maxima of dielectric loss), the dielectric strength

and the shape parameters of the recorded relaxations [Kremer02]. To that aim we employed the asymmetric Havriliak–Negami (HN) equation [Havriliak67].

$$\varepsilon^*(f) = \varepsilon_\infty + \frac{\Delta\varepsilon}{\left(1+\left(if/f_0\right)^{\alpha_{HN}}\right)^{\beta_{HN}}} \tag{3.6}$$

A sum of up to five HN terms of the type (3.6), one for each of the relaxations recorded (namely β, S, α, α_c, and α_{int}, details later in text), was critically fitted to the experimental data at each temperature and the fitting parameters were determined. The number of terms needed was different for different compositions and temperatures, depending on the number of relaxations present and the extent of their overlapping. Examples of fitting are shown in Fig. 3.5. In Eq. (3.6), $\Delta\varepsilon$ is the dielectric strength, which represents well the population of mobile molecular groups, and f_0 is a characteristic frequency related to the frequency of maximum dielectric loss (ε''), that can be considered representative for the degree of molecular mobility. ε_∞ describes the value of the real part of dielectric permittivity, ε', for $f >> f_0$. α_{HN} and β_{HN} are the shape parameters of the relaxation. We recall that the deviation of β_{HN} from 1 describes the asymmetry of the relaxation, whereas the deviation of α_{HN} from 1 the broadening of the relaxation. Thus, the symmetric Debye relaxation with a single relaxation time is characterized by $\alpha_{HN} = 1$, $\beta_{HN} = 1$ [Kremer02].

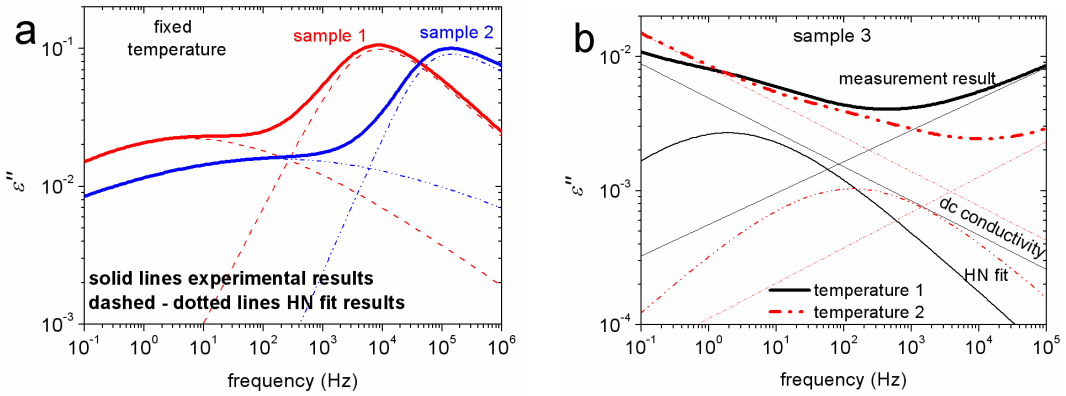

Fig. 3.5. Examples of analysis of isothermal DRS spectra of the imaginary part of dielectric permittivity, ε′′, in terms of individual *Havriliak-Negami* Eq. (3.6) and *dc conductivity* components.

Our study focuses mainly on segmental dynamics. The temperature dependence of segmental dynamics is typically described by Vogel–Tammann–Fulcher–Hesse (VTFH) equation [VTFH],

$$f = f_0 \exp\left(-\frac{DT_0}{T - T_0}\right) \tag{3.7}$$

where f_0 is a frequency constant, D is the strength parameter, and T_0 is the Vogel temperature. After fitting Eq. (3.7) to our experimental data and fixing the f_0 parameter to the phonon value 10^{13} Hz [Kremer02, Richert98], we obtained values for T_0 and D. D is related to the steepness or fragility index m according to the following equation [Boehmer93]

$$m = 16 + 590 / D \tag{3.8}$$

Finally, our results provide clear evidence about the origin of the various segmental relaxations (details in the next chapters). Thus, we calculate here the various fractions of polymer by evaluating the respective dielectric responses (i.e. $\Delta\varepsilon$). To that aim we employ a model analogue to the one used previously for DSC (i.e. Eqs. (3.4, 3.5)) and we calculate the mobile bulk, *MAF*, and the interfacial, RAF_{int}, polymer fractions according to the following equations

$$MAF = \frac{\Delta\varepsilon_{a+ac}}{\Delta\varepsilon_a + \Delta\varepsilon_{ac} + \Delta\varepsilon_{a\,\mathrm{int}}}\left(1 - X_c\right) \tag{3.9}$$

$$RAF_{\mathrm{int}} = \frac{\Delta\varepsilon_{a\,\mathrm{int}}}{\Delta\varepsilon_a + \Delta\varepsilon_{ac} + \Delta\varepsilon_{a\,\mathrm{int}}}\left(1 - X_c\right) \tag{3.10}$$

where $\Delta\varepsilon$ is the dielectric strength [Kremer02] of each relaxation and X_c is the degree of crystallinity for each sample (obtained from DSC). Bearing in mind that the dielectric strength changes with temperature, we employed DRS results at the same temperature –95 ^{o}C for *MAF* and RAF_{int}.

From the methodological point of view, Eqs. (3.9, 3.10) involve the total dielectric response of the segmental relaxations for each sample. Thus, we may assume that any systematic errors in the calculations and the comparison between different samples, arising from possible differences in polarizability of PDMS chains in the different fractions [Capponi12], are reduced by this calculation method. The suitability of Eqs. (3.9, 3.10) for calculating the different polymer fractions has been confirmed in NCs based on silica and various polymers [Fragiadakis11, Fullbrant13, Holt14, Klonos15B].

Coming back to molecular dynamics, except for segmental polymer dynamics (related to glass transition), in this thesis we will show results related to local polymer mobility (β relaxation [Klonos15C]) and, mainly, to local mobility related to the surface hydroxyls on the surface of nanoparticles (namely, the *S* relaxation in the following [Fontanella09,

Klonos15C]). The temperature dependence of local (not cooperative) dynamics is typically described by the Arrhenius equation [Arrhenius1889, Donth01],

$$f(T) = f_{0,Arrh} \exp\left(-\frac{E_{act}}{kT}\right) \tag{3.11}$$

where $f_{0,Arrh}$ is a frequency constant and E_{act} is the activation energy of the relaxation.

3.4.3. DRS apparatus

Fig. 3.6. Novocontrol DRS apparatus in combination with quatro cryosystem and liquid nitrogen cooling system (left) and Novocontrol DRS sample holder (right).

3.5. Equilibrium water sorption / desorption isotherms (ESI / EDI)

3.5.1. Experimental conditions

Hydration properties of selected samples (initial components and NCs) were studied employing ESI / EDI method [Stathopoulos10, Pissis13]. The isothermal sorption / desortpion curves were determined at room temperature by exposing the samples to water vapor atmospheres in sealed jars [Stathopoulos10]. The water activities, or else, relative humidities, *rh*, were achieved with appropriate binary saturated aqueous solutions [Greenspan77]. The samples were equilibrated for ~7 days to water activities of 0.02 (phosphor pentoxide, P_2O_5), 0.09, 0.19, 0.33, 0.43, 0.53, 0.64, 0.75, 0.85 and 0.95. The attainment of equilibrium was determined via recording of sample weight (m_{sample}). A Mettler Toledo balance with 10^{-5} g sensitivity was employed for these measurements. The weights of samples after equilibration over P_2O_5 were considered as weights in dry state ($m_{dry,sample}$). Once the equilibrium was attained, the hydration ($h_{dry,basis}$) was calculated on dry basis through the equation:

$$h = \frac{m_{water}}{m_{dry,sample}} = \frac{m_{hydrated,sample} - m_{dry,sample}}{m_{dry,sample}} \tag{3.12}$$

3.5.2. Analysis of experimental results

An example of ESI measurement is shown in Fig. 3.7 for a hydrophilic material, such as silica. The isothermal curves belong to type II of the Brunauer classification [Brunauer38]. A Type II isotherm describes the absorption on macroporous absorbents with strong absorbate–absorbent interactions. The relatively weak increase at low relative humidity, *rh*, values is describes the hydration of first layer, i.e. bound water molecules attached directly to the hydration sites of the hydrophilic surface. The strong increase in the water uptake for higher *rh* (> 0.6) is associated with the formation of water clusters [Brunauer40, Kyritsis95, Stathopoulos10, Pissis13].

The ESI curves were quantified according to Guggenheim-Anderson-de Boer (GAB) expression [Timmermann89],

$$h = h_m \frac{c \cdot f \cdot rh}{(1 - f \cdot rh)[1 + (c-1) f \cdot rh]} \tag{3.13}$$

where h_m is the weight fraction measured on a dry basis of water molecules directly attached to hydration sites (bound water, first sorption layer), c is a parameter related to the energy difference between the water molecules attached to hydration sites (bound water) and that adsorbed in second and higher sorption layers (semi-bound water), and f is a parameter that

measures the energy difference between the semi-bound water molecules and molecules of pure liquid water (free water).

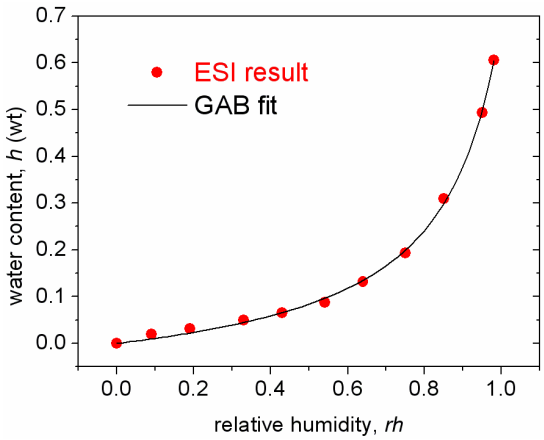

Fig. 3.7. Representative ESI curve for a hydrophilic sample (silica) at room temperature. The added line is the fitting results of GAB equation (details in text) to the experimental data.

4. Effects of filler type and fraction on interfacial interactions in conventional NCs of poly(dimethylsiloxane) (PDMS)

4.1. Introduction

In this chapter we study polymer–filler interactions and their effects on molecular mobility in PDMS networks filled with *in situ* generated silicon (SiO_2) and titanium (TiO_2) oxide nanoparticles generated via sol–gel technique [Bokobza10]. To that aim, we employ differential scanning calorimetry (DSC), and the two dielectric techniques described in chapter 3, thermally stimulated depolarization currents (TSDC) and dielectric relaxation spectroscopy (DRS), covering together a broad frequency range of 10^{-4} to 10^{6} Hz. Morphological characterization of the materials in the laboratory where they have been synthesized showed a good dispersion of nanoparticles, 5 and 20–40 nm in diameter for silica and titania nanocomposites, respectively, and revealed fine details of this dispersion [Bokobza10]. The mechanical properties were significantly improved in a different way for the two oxides, and that was correlated with the different strength of polymer–filler interaction and details of the nanoparticle dispersion [Bokobza10]. The results to be reported in this chapter show significant effects of the nanoparticles on segmental dynamics associated with the glass transition, originating from the severe restriction of crystallization ability and the strong reduction of molecular mobility in an interfacial layer of a few nm in thickness around the nanoparticles. The extent of these effects depends on the type of the filler (stronger for titania than for silica) and the quality of particle dispersion. The effects are quantified and the results may provide a basis for understanding and modeling the improvement of mechanical properties at the molecular level.

From the methodological point of view, the results of the present study illustrate the power of the two dielectric techniques used in combination with DSC for the investigation of effects of nanofiller on thermal transitions and molecular dynamics in the nanocomposites under investigation [Fragiadakis07, Fragiadakis11, Fullbrant13, Holt14]. In that respect the dielectric techniques, implemented not only for polymeric systems [Vralstad09, Syunyaev07], compete with and complement other methods employed, such as dynamic mechanical analysis measurements [Fragiadakis07, Tsagaropoulos95], changes in viscoelasticity [Robertson08] and DSC glass transition step [Fragiadakis05, Sargsyan07, Wurm10], electron spin resonance [Miwa04] and fluorescence/multilayer methods [Rittigstein06].

4.2. Materials

PDMS networks filled with several contents of silica (~6 to 36 wt%) and titania (~5 to 18 wt%) amorphous nanoparticles and, for comparison, unfilled PDMS network were studied in the present work. The unfilled polymer network was prepared from hydroxyl–terminated PDMS (Gelest, M_w=18000) by end–linking reactions using tetraethoxysilane (TEOS) as cross–linking agent. For composites preparation the unfilled extracted polymer network was swollen in TEOS for silica or in titanium (IV) n–butoxide (TBO) for titania, which were the precursors of the particles generation in the sol–gel process. Then the samples were hydrolyzed during 48 h and vacuum–dried at 80 ^{o}C for several days to constant weight. The amount of filler is represented by the difference between the final and initial weights. Films of ~1 mm in thickness were the finally produced samples [Bokobza10].

According to the statistical equation $\langle r^2\rangle = C_\infty / nl^2$ [Gedde95], by knowing the average number and length of the main–chain bond length, n and l respectively, the characteristic ratio C_∞ and the fact that the crosslinking occurred only on the endgroups of the PDMS chains, the end–to–end distance between crosslinks $\langle r^2\rangle^{1/2}$ was calculated around 11.2 nm. Transmission electron microscopy (TEM from [Bokobza10], Fig. 4.1), small–angle neutron scattering (SANS), stress–strain and equilibrium swelling measurements were carried out on the same materials in the laboratory where they have been synthesized [Bokobza10]. Results showed that silica nanoparticles are well dispersed in the polymer matrix with small domains around ~5 nm (Fig. 4.1 taken from [Bokobza10]) in diameter and rather diffuse surfaces. At higher than 10 wt% contents an interpenetrated polymer–silica structure is obtained. On the other hand, titania particles seem to be approximately spherical in shape with diameters between 20 and 40 nm (Fig. 4.1) and better defined (smooth) interfaces with PDMS than in the case of

silica. Even at the lowest titania content the particles are almost connected in a branched network structure. Distribution is better in case of silica giving a higher polymer–filler interfacial area but weaker bonds with PDMS, comparing with the strong PDMS–titania interactions. Mechanical measurements showed higher reinforcement of PDMS in case of silica. Tense transitions from linear (elastic) to sigmoidal (plastic) stress–strain behavior for ~18 wt% SiO_2 and ~8 wt% TiO_2 were observed, due to the forming of the inorganic networks at these compositions [Bokobza10]. The interactions of PDMS chain segments with the nanoparticles occur via hydroxyl groups (–OH) on the surfaces of the nanoparticles, which are proved by solid–state ^{29}Si–NMR, Infra Red (IR) and near–IR spectroscopy (results not shown here) as showed in previous work for PDMS/silica nanocomposites [Dewimille05].

It is useful to note that the measurements described above were performed at room temperature, where this polymer, semicrystalline at lower temperatures, is fully amorphous. So any effects in mechanical and swelling properties are affiliated only to filler–polymer and filler–filler interactions [Bokobza10].

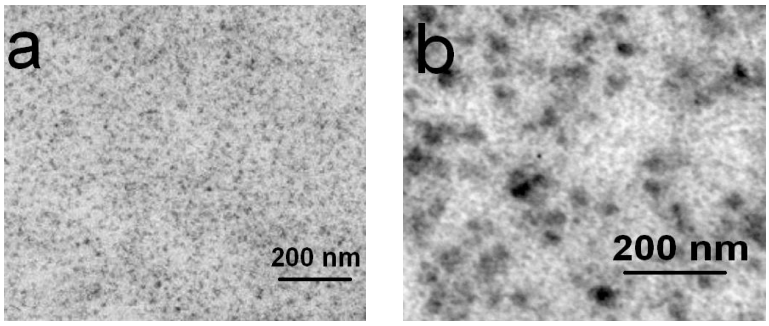

Fig. 4.1. TEM images for (a) PDMS + 9 wt% silica and (b) PDMS + 11 wt% titania, taken from [Bokobza10].

4.3. Results and discussion

4.3.1. DSC measurements

DSC measurements for PDMS/silica and PDMS/titania nanocomposites and for comparison unfilled PDMS are presented in Fig. 4.2. Heating scans are shown in these thermograms, comparing the changes in the thermal transitions of the polymer in the temperature range from –170 to 40 ^{o}C with the successive increasing of filler content. All the respective recorded and calculated values of interest are shown in Table 4.1.

The heating scans in Fig. 4.2a,b, for PDMS/silica and PDMS/titania, respectively, followed the cooling scans (not shown here) in the same temperature range and rate (10 K/min). In these cooling scans a single exothermic peak was observed around –103 to –78 ^{o}C,

representing the crystallization event [Sperling06, Aranguren98], and an endothermic step in the baseline around –130 to –125 °C, representing the glass transition of PDMS. In previous studies on linear and crosslinked PDMS systems [Fragiadakis07, Aranguren98, Clarson85, Soutzidou98, Carlberg04] the glass transition temperature has been observed between –130 and –115 °C and the crystallization temperature between –100 and –76 °C.

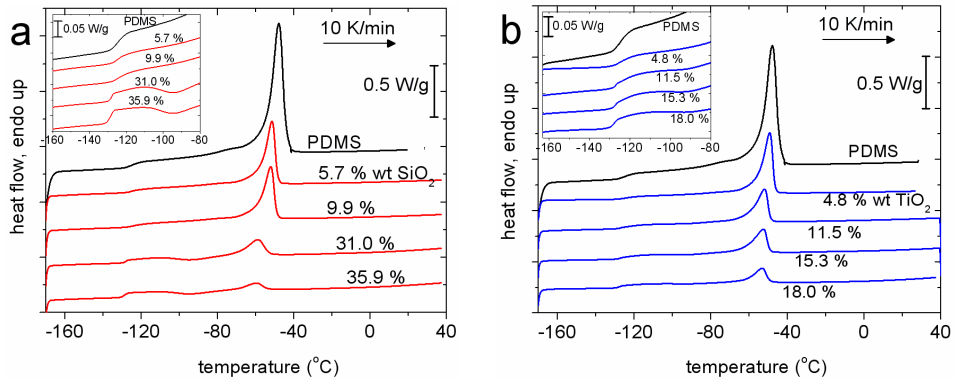

Fig. 4.2. Comparative DSC thermograms for unfilled PDMS, (a) PDMS/silica and (b) PDMS/titania nanocomposites during heating. Glass transition steps and melting peaks are observed for all samples. The insets show details in the glass transition region.

During heating the glass transition is recorded for all samples and the characteristic temperature T_g, determined as the midpoint of the heat capacity step at glass transition, was obtained between –129 and –123 °C. As temperature increases, in the case of nanocomposites with high filler contents, 31 wt% silica and higher and 18 wt% titania and higher, an exothermic event is observed close to T_c region, representing cold crystallization [Sorai04]. This is a result of uncompleted crystallization during cooling. For lower filler contents and pure PDMS this phenomenon is absent, indicating that at this cooling rate (10 K/min) crystallization is completed. Combining our observations on the crystallization–melting changes of PDMS, we gain strong indications that the addition of the fillers restricts the creation of crystallization nuclei [Aranguren98], so crystallization in these materials takes place not close to the nanoparticles.

In Fig. 4.2, at higher temperatures, complex endothermic melting peaks are observed between –60 and –48 °C. Complex and double melting peaks have been observed before in PDMS systems [Aranguren98, Clarson85]. The secondary weaker melting peak precedes the main one by 15–20 K. Two possible explanations about its origins [Aranguren98] are as follows: (a) during heating small metastable crystals [Sundararajan02] melt, then get recrystallized and melt again into the main event or (b) the two melting peaks correspond to

different types of crystallites. DSC measurements of crystallization annealing *protocol AC* (not shown here) provide support for explanation (a).

Using the respective enthalpies $\Delta H_{c/m,n}$ as recorded through DSC and also normalized to the same polymer content X_{PDMS} for each sample (Eq. (3.1)), the degree of crystallinity X_c was calculated according to Eq. (3.2).

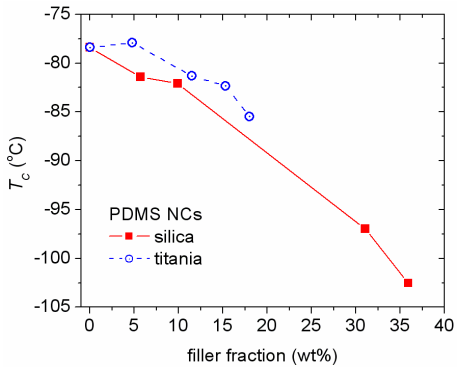

Fig. 4.3. Depression of PDMS crystallization temperature with the addition of silica and titania nanoparticles.

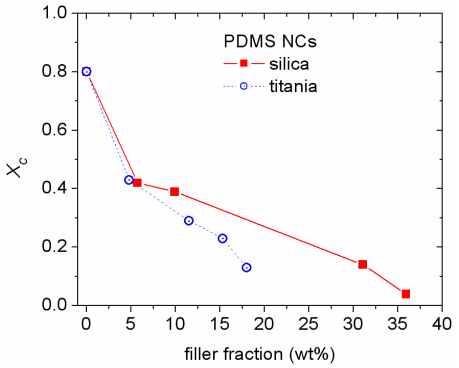

Fig. 4.4. Degree of crystallinity for PDMS and different compositions of PDMS/silica and PDMS/titania nanocomposites.

The results (Table 4.1) show that the crystallization temperature (Fig. 4.3) and the degree of crystallinity (Fig. 4.4) decrease systematically with the increasing of filler content. In particular, we see in Fig. 4.3 that the depression of T_c with the addition of silica is significant even at the lowest content, from –78 °C for neat PDMS to –103 °C for the highest loading, almost linearly. On the other hand, in the case of titania, significant changes on T_c start at about 10 wt% of filler content, but then follow a similar (parallel) trend as in silica. In Fig. 4.4 one can observe that by adding about 5 wt% of nanoparticles, silica or titania, the crystallinity degree of PDMS drops from 0.80 to 0.43 wt. For further filler addition it is clear

that the suppression of X_c is by far stronger in the case of titania. Thus, by comparing with each other the two types of nanocomposites in Fig. 4.3 and Fig. 4.4, we conclude that titania is more effective than silica in suppressing X_c and less effective in reducing T_c, possibly due to stronger interactions of PDMS with titania as compared to that of silica. Taking a glance on the melting temperature values (Table 4.1) one can observe that the addition of filler depresses also T_m, e.g. by 12 K at the maximum loading. The reduction of the values is again similar for PDMS/silica and PDMS/titania composites, indicating similar size and quality of crystals.

Table 4.1

Crystallization, melting and glass transition temperatures T_c, T_m and T_g respectively, normalized respective enthalpies $\Delta H_{c/m,norm}$ and degree of crystallinity X_c, normalized heat capacity step of glass transition $\Delta C_{p,n}$, calculated rigid amorphous fraction, *RAF*, and estimated thickness of immobilized polymer layer on the nanoparticles, d_{int}, for PDMS, PDMS/silica and PDMS/titania nanocomposites

Sample	X_{filler} (wt%)	X_{filler} (vol%)	T_c (°C)	$\Delta H_{c,norm}$ (J/g_{pdms}) (±1)	X_c (±5 %)	T_m (°C)	$\Delta H_{m,norm}$ (J/g_{pdms}) (±1)	T_g (°C) (±0.5)	$\Delta C_{p,n}$ (J/gK) (±0.01)	*RAF* (±10%)	d_{int} (nm) (±25%)
PDMS	0	0	–78	30	0.80	–48	31	–124	0.16	0.11	–
+TiO_2	4.8	1.9	–78	16	0.43	–49	15	–124	0.20	0.26	38
	11.5	4.7	–81	11	0.29	–52	11	–125	0.18	0.36	24
	15.3	6.4	–82	9	0.23	–52	9	–126	0.17	0.42	20
	18.0	7.7	–85	5	0.13	–53	5	–127	0.16	0.49	19
+SiO_2	5.7	3.3	–81	16	0.42	–52	16	–124	0.22	0.24	5
	9.9	6.0	–82	15	0.39	–52	14	–123	0.19	0.30	4
	31.0	22.3	–97	5	0.14	–59	8	–128	0.17	0.46	3
	35.9	26.0	–103	1	0.04	–60	4	–129	0.14	0.59	2

These results suggest that the interactions between the particles and PDMS (hydrogen bonding between the oxygens on the polymer backbone and the hydroxyls on the nanoparticle surfaces) strongly suppress the creation of crystallization nuclei and the growth and quality of the PDMS spherulites [Sundararajan02] in the nanocomposites. The depression of crystallization and melting enthalpies have very similar trends and show that the changes become stronger as the filler content gets higher than about 10 wt% for silica and about 8 wt% for titania, as compared to lower contents. Such behavior could be explained in terms of

the formation of an inorganic network throughout the polymer volume at these and higher filler contents, respectively, for the two types of filler. Such an inorganic network could be the main reason for the restriction of growing of crystals, due to the reduction of regions of free polymer mobility. The above results and suggestions for their explanation come in agreement with the results of TEM and stress–strain measurements on the same compositions [Bokobza10]. Formation of an inorganic silica network was observed also in poly(hydroxyethyl acrylate)/silica nanocomposites, where, similar to here, silica particles were generated by sol–gel process [Rodriguez08].

In the insets to Fig. 4.2 we can observe changes in the glass transition step with composition. For both cases of filler, T_g decreases by 1 to 4 K with the addition of filler, this decrease being stronger in the case of titania for comparable filler fractions (Table 4.1). A possible explanation for this behavior is the reduction of the degree of crystallinity with increasing filler content of the nanocomposites [Matejka00]. Another quantity of interest in Fig. 4.2 is the width of the glass transition, the difference between the onset and the completion temperature, T_{end}–T_{onset}, which is ~5 K for PDMS, gets broadened to 8–9 K for low filler addition and gradually narrows to almost 2 K at the higher filler contents. Changes are similar for silica and titania. At the same time, we record changes in the shape of the glass transition thermogram. In particular, the glass transition shape seems to be double structured in the case of nanocomposites with 31 wt% silica and 11.5 wt% titania and higher. As filler content increases the secondary contribution at the high–temperature side gets more clear, while at the same time the height of the first contribution (low–temperature side) is increased, in terms of heat capacity change ΔC_p. This secondary contribution seems to be related to the strong restriction of amorphous polymer between PDMS spherulites (highly reduced mobility) [Klonos12, Klonos15A]. Similar observations have been made before in polymer nanocomposites, either in the form of changes in the shape of the response [Fragiadakis05] or through significant changes of the heat capacity step at the glass transition [Wurm10, Kripotou10, Raftopoulos10, Klonos15B]. This point will be further discussed later in this section and also in combination with TSDC and DRS results.

Having firm evaluation of the crystallization (specifically the fraction of crystallized polymer), we can calculate from the data for the glass transition, in particular from the heat capacity step, the amount of rigid amorphous fraction, *RAF*, i.e. the amount of amorphous polymer which makes no contribution to the glass transition [Wurm10, Bershtein02]. In terms of heat capacity change $\Delta C_{p,n}$ as recorded from DSC and normalized with amorphous polymer fraction (Table 4.1) according to Eq. (3.3), we calculated *RAF* using Eq. (3.5)

Despite any uncertainty in the ΔC_p values, *RAF* was found to increase from 0 to ~0.60 wt with filler loading, this increase being slightly stronger for PDMS/titania samples in Fig. 4.5. We should report that in case *RAF* refers to the mass of amorphous polymer [i.e. in case the factor $(1–X_c)$ is missing from Eq. (3.5)], *RAF* was found to be almost constant between 0.73 and 0.83 (i.e. 73 and 83% of the non–crystallized polymer) in the nanocomposites for both silica and titania (not shown). These results suggest that the amount of amorphous polymer which participates to the glass transition is also constant in the nanocomposites. It has been reported for semicrystalline polymer nanocomposites that the presence of a certain constant amount of rigid amorphous phase (*RAF*) [Dobbertin96] around the individual lamellar crystals along with nanofillers which interact with the polymer lead to such results [Wurm10, Purohit14, Papageorgiou14].

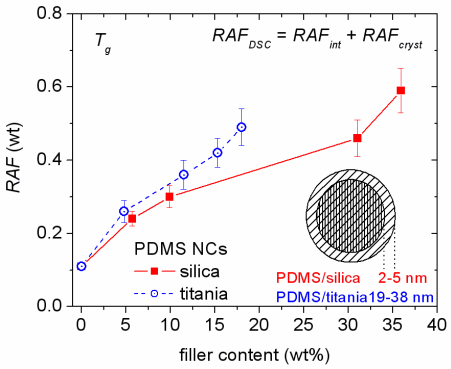

Fig. 4.5. Fraction of the rigid amorphous polymer, *RAF*, for PDMS/silica and PDMS/titania nanocomposites, as calculated from Eq. (3.5). The inset shows the simplified model used to calculate the thickness of the interfacial layer.

Following previous work [Fragiadakis07], by applying a simplified model (inset of Fig. 4.5), which is mathematically described in the following equation [Pelster99]

$$d_{\text{int}} = [(v_{\text{int}} / v_{filler})^{1/3} - 1] r_{filler} \tag{4.1}$$

where v_{int} and v_{filler} are the volume fractions of the rigid amorphous (immobilized) polymer and fillers in the nanocomposites, respectively, while r_{filler} is the radius of the nanoparticles, d_{int} was calculated to be about 2–5 nm for PDMS/silica and about 20–40 nm for PDMS/titania (Table 4.1). The volume fraction calculations (vol%, Table 4.1) were made transforming weight fractions (wt%) and using standard values for the densities of silica, titania and PDMS (2.65, 4.23 and 1.62 g/cm^3, respectively [Klonos10]). The decrease of d_{int} with increasing filler content in Table 4.1 reflects simply overlapping of the interfacial layers of individual

nanoparticles, which has not been taken into account in the simplified form of Eq. (4.1). However, we recall that RAF includes both RAF_{int} and RAF_{cryst} fractions in Eq. (3.5), thus d_{int} should be lower for samples of $X_c \neq 0$. The high difference between PDMS/silica and PDMS/titania d_{int} values is consistent with the results of characterization measurements (described above in section 4.2) [Bokobza10] about the interaction strength of titania particles with PDMS, which is higher in comparison with silica. With respect to absolute values for d_{int}, such values come in agreement with previous work [Fragiadakis07, Harton10, Fullbrant13, Gong14], as far as silica is concerned. High values of d_{int} have been also reported before in poly(methyl acrylate) (PMA) / clay [Miwa06] and in Poly(2-vinylpyridine) / silica nanocomposites [Holt14]. Results on poly(methyl methacrylate) (PMMA) / silica nanocomposites [Priestley07] have shown that the length of polymer–filler interfacial effects are by tens of nanometers higher than the cooperativity length ξ of segmental motions [Richert98, Gong14]. Similar observations have been made for thin polystyrene films, where the size of cooperatively rearranging region is much smaller than the distance over which interfacial effects propagate [Ellison03, Gong14]. We will come back to this point later in relation to DRS measurements.

4.3.2. TSDC measurements

The TSDC thermograms are presented in Fig. 4.6 for PDMS/silica and in Fig. 4.7 for PDMS/titania samples. In order to have better comparative evaluations, the depolarization current was normalized with the applied electric field, so that results for different samples can be compared to each other not only with respect to the temperature position of a peak (time scale of the corresponding relaxation) but also with respect to the magnitude of a peak (dielectric strength of the corresponding relaxation). In the temperature range from –140 to –100 ^{o}C, i.e. in the range of the calorimetric glass transition (Fig. 4.2 and Table 4.1), complex spectra consisting of three peaks are well discerned, for both types of nanocomposites. We know that the equivalent frequencies of TSDC and DSC measurements [Brauenlich79] are in a similar range, so we suggest at this stage and will provide additional evidence for that later that the three peaks (relaxations), called α, α_c and α_{int} in the order of increasing temperature, are dielectrically related with cooperative PDMS chain motions in the glass transition region.

It is interesting to discuss the systematic manner in which these three peaks contribute to the overall complex segmental dynamics in the nanocomposites (Fig. 4.6b and Fig. 4.7b). Being completely absent in unfilled PDMS, the magnitude of α_{int} relaxation (between –120 and –95 ^{o}C) increases with filler content. The α_c relaxation (at about –123 ^{o}C) is faster and

stronger than α_{int} and its position is not affected directly by the nanoparticles. The strength of this relaxation decreases with decreasing degree of crystallinity X_c (Table 4.1). Simultaneously with the filler addition and depression of α_c the upcoming of α relaxation is observed at –130 to –128 ^{o}C. This statement will be confirmed later in DRS isothermal crystallization measurements.

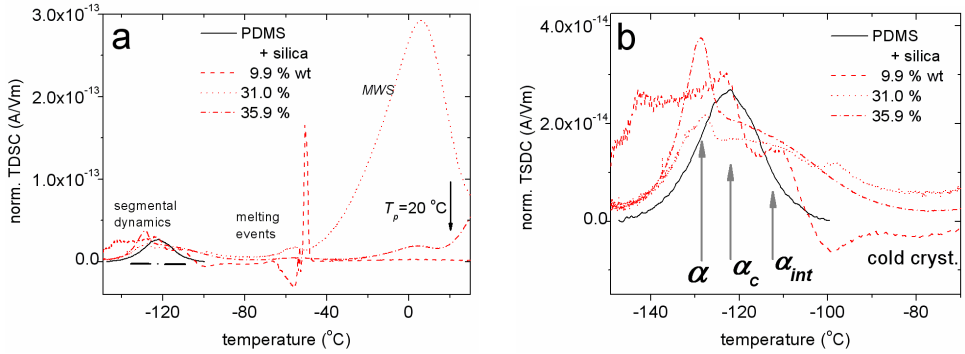

Fig. 4.6. Comparative TSDC thermograms for unfilled PDMS and PDMS/silica nanocomposites (a) overall behavior and (b) in the region of the glass transition

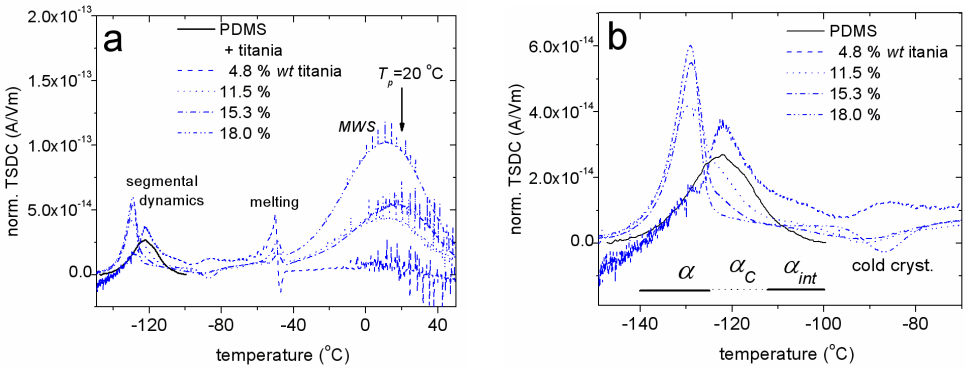

Fig. 4.7. Comparative TSDC thermograms for unfilled PDMS and PDMS/titania nanocomposites (a) overall behavior and (b) in the region of the glass transition. The reduction of the degree of crystallinity with filler content depresses the height of α_c relaxation and at the same time α, α_{int} and MWS relaxations arise.

The α_{int} extends in a broader temperature region than α and α_c, which enhances our suggestions related to the observed changes in the shape of the glass transition in the DSC thermograms (insets to Fig. 4.2). Also, it seems that the broadened glass transition of unfilled PDMS recorded through DSC corresponds directly to α_c relaxation, while the sharp shaped glass transition, recorded for the highest silica and titania contents corresponds directly to α relaxation. At this point, the three relaxations can be clearly defined as: glass transition of free

(bulk) polymer chains (α relaxation), reduced cooperative mobility of amorphous polymer confined between crystal regions (α_c relaxation) [Raftopoulos10, Lorthioir04, Napolitano07, Yu09] and relaxation of the polymeric chains which are semibound on the nanoparticle surfaces (α_{int} relaxation) [Fragiadakis07]. Please note that α_c shows a similar strength for PDMS, PDMS/silica and PDMS/titania, while α relaxation is stronger in the case of titania and α_{int} is stronger for silica. We can assume on the basis of the DSC results (very similar values of T_m for the two types of filler, Table 4.1) that the size and quality of the PDMS crystals are similar for both types of filler, giving similar position and dielectric strength to α_c relaxation. On the other hand, α and α_{int} carry together the relaxation strength of the segmental dynamics of the amorphous polymer and, in this sense, it is reasonable that either of them increases at the expenses of the other. We will come back to this point in a more quantitative way later on the basis of DRS results.

The events recorded in the temperature range between –100 and –80 ^{o}C seem to be related to cold crystallization. The reason for recording cold crystallization by TSDC is the low heating rate in this technique (3 K/min). Crystallization kinetics has been recorded before through anomalous behavior in dielectric measurements in poly(ethylene oxide) (PEO) and poly(3–hydroxybutyrate) (PHB) [Napolitano06].

The signal recorded between –65 to –40 ^{o}C corresponds to the melting of PDMS crystals. Electrical charges trapped inside or between crystals during cooling in the polarization step get massively disengaged while passing through the T_m region during heating and give rise to the response measured. In agreement with this interpretation, the observed strength of the signal (respective current range in Fig. 4.7a for this melting process) increases with X_c.

The strong peak which follows at higher temperatures is due to the interfacial Maxwell–Wagner–Sillars (MWS) relaxation. MWS arises from the trapping and the subsequent release of charges at the interfaces between polymer and filler [Fragiadakis07, Hedvig77]. In the case of PDMS + 35.9 wt% a huge internal electric field opposite to the external applied field [Page06] was created during polarization. For that reason the main relaxation occurred as a negative (inverted) peak. So in Fig. 4.6 we present a respective measurement, in which the polarization temperature was –60 ^{o}C, so that MWS polarization was not activated. The strength of the interfacial MWS relaxation increases with filler content, almost linearly. In the case of PDMS/titania (Fig. 4.7a) small electric discharges are observed over the MWS curve. This is an indication of the highly branched particle structure

or the too close distance between particles in general and comes in agreement with TEM results on the same materials [Bokobza10].

By employing special techniques like Thermal Sampling [Fragiadakis07], we gained supplementary evidence for the statements made above, in particular the assignment of the three relaxations in the glass transition region and evaluations about the activation energy and changes between α and α_c behavior with temperature.

4.3.3. DRS measurements

DRS results will be comparatively presented here in the form of frequency (Fig. 4.8, isothermal plots) or temperature dependence of the imaginary part of dielectric permittivity (dielectric loss) ε'' (Fig. 4.9, isochronal plots). We focus here on segmental dynamics, i.e. on the dielectric relaxations α, α_c and α_{int} corresponding to the TSDC response in the temperature range from –140 to –100 °C in Figs. 4.6 and 4.7.

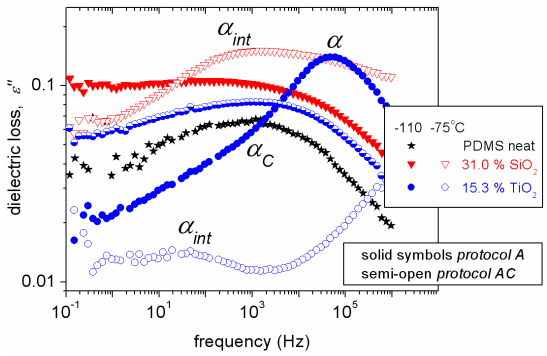

Fig. 4.8. Isothermal DRS plots of dielectric loss ε'' vs frequency for PDMS, PDMS + 31.0 wt% silica and PDMS + 15.3 wt% titania nanocomposites, at –110 °C (solid symbols) and –75 °C (open symbols)

Recorded at –110 °C, one can observe in Fig. 4.8 α_c and α relaxations of PDMS, PDMS + 31.0 wt% silica and PDMS + 15.3 wt% titania at around 1 and 50 kHz, respectively. Based on the values of the degree of crystallinity, as calculated from DSC measurements (Table 4.1), along with the strength and frequency range of the α_c relaxation for the two types of filler in PDMS, the identification of the two relaxations is similar to that in the TSDC results, compare section 4.3.2. With the open symbols in Fig. 4.8 we follow the data of the isothermal measurements for the two nanocomposites at –75 °C. Significant changes are recorded here for α_{int} relaxation, which is by far stronger and faster (by 2 orders of magnitude in frequency) in case of PDMS/silica, as compared to PDMS/titania, again in agreement with TSDC. In the case of PDMS + 15.3 wt% titania at –110 °C, it is clear that the recorded

relaxation is complex, as a superposition of α_c (~1 kHz) and α (~50 kHz) relaxations. The results described up to this point were obtained by measurements carried out under the thermal *protocol A* (almost amorphous polymer). Included in Fig. 4.8 are also data (semi–open circles) of measurements of the PDMS/titania sample under the *protocol AC* (annealed at crystallization temperature, semi–crystalline polymer). For the polymer allowed to get crystallized, the segmental dynamics is mainly expressed as the broadened, weaker and slower α_c relaxation, which is reasonable on the basis of the DSC results.

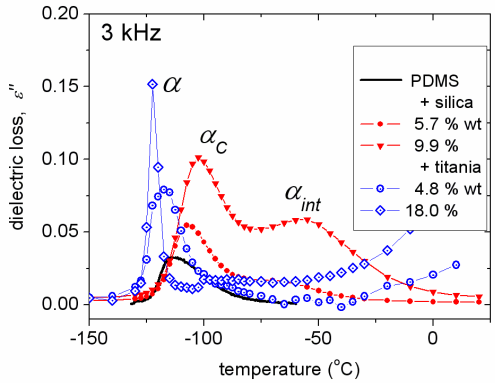

Fig. 4.9. Comparative isochronal plots of the imaginary part of dielectric permittivity ε'', replotted from DRS measurements at 3 kHz for PDMS/silica (solid symbols) and PDMS/titania nanocomposites (open symbols)

Data recorded isothermally were replotted in Fig. 4.9 as isochronal $\varepsilon''(T)$ plots to facilitate direct comparison with the TSDC thermograms of Fig. 4.6 and Fig. 4.7. A higher frequency of 3 kHz was selected for the plots to suppress effects of conductivity [Kremer02]. In general, α relaxation is stronger in the case of titania, and α_c and α_{int} are stronger in the case of silica. The strength of α_c and α_{int} shows significant variation with composition in PDMS/silica, but not in the case of PDMS/titania, while in both cases the temperature position of α_c and α_{int} does not change significantly with composition. The results agree well with those of TSDC, while the slight shift to higher temperatures in Fig. 4.9, as compared to Figs. 4.6 and 4.7, arises from the higher frequency of presentation [Fragiadakis07].

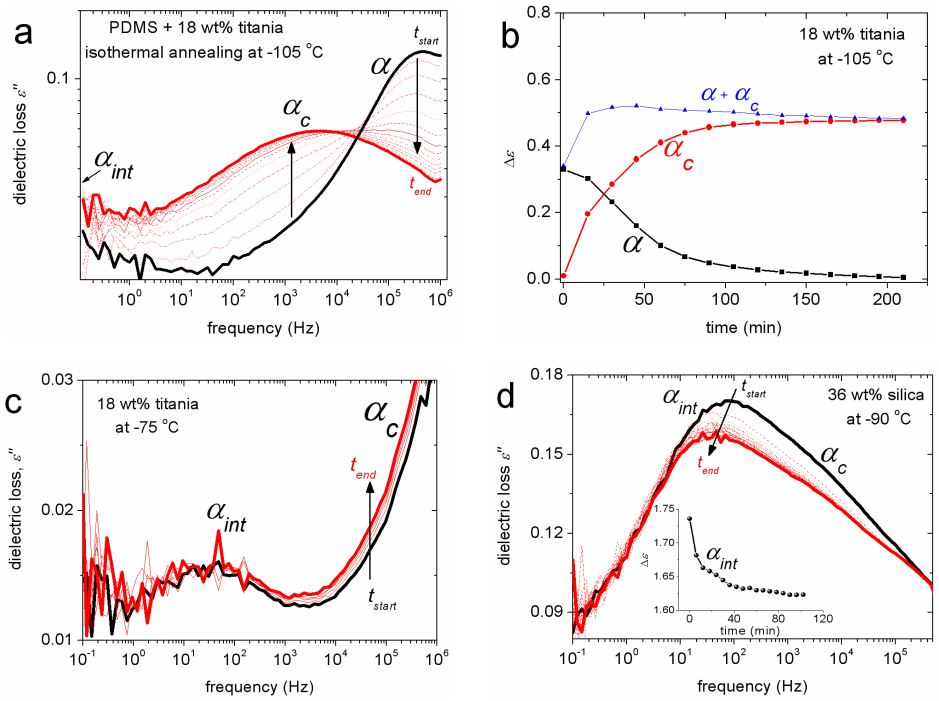

Fig. 4.10. Dielectric loss ε'' vs frequency for (a-c) PDMS + 18 wt% titania and (d) PDMS + 36 wt% silica nanocomposites, as recorded during isothermal crystallization at selected temperatures. Segmental dynamics expression changes with time from α to α_c behavior in (a,b), while annealing suppresses α_{int} only for nanocomposites of high silica loading in (d).

The isothermal $\varepsilon''(f)$ plots in Fig. 4.10a present spectra recorded every 15 min continuously for 3 hours, to follow effects of crystallization at –105 °C for PDMS + 18 wt% titania. The temperature of –105 °C was selected on the basis of the DSC results in the crystallization region to enable following isothermal crystallization over a few hours. In the beginning we record segmental dynamics expressed exclusively as α relaxation. As time passes, the degree of crystallinity increases along with α_c relaxation. As α_c increases in magnitude, α is depressed and the spectra become complex, consisting clearly of two contributions. Finally, after 3 hours α relaxation is vanished and α_c dominates the response of the sample. Fig. 4.10b shows the respective time evolution of $\Delta\varepsilon$ for both relaxations. The weak increase of the ε'' response at the lower frequencies represents the incoming of α_{int} relaxation into the measurement window. It would be interesting if we were able to record in a broader frequency range of Fig. 4.10a, at the same time, α_{int} relaxation in the spectra, expecting to verify that no significant changes would be observed during this isothermal experiment. However, the latter is somehow verified with the respective isothermal measurement at –75 °C in Fig. 4.10c. The result is similar for α_{int} in all PDMS/titania samples and the samples of low silica content (not shown). Interestingly, for the samples of 31 and 36

wt% silica (Fig. 4.10d) α_{int} is getting gradually weaker as the '*crystallization annealing*' proceeds (please follow the $\Delta\varepsilon(T)$ in the inset to Fig. 4.10d). Simultaneously with the weakening of α_{int} the respective dielectric loss peak has been immigrating towards lower frequencies (reduction of f_{max}). These last results suggest that for the high silica loaded samples the annealing of crystallization results, most probably, to lower amount of interfacial polymer and slowing of the respective dynamics at interfaces. This effect will be further investigated in the next chapter.

Coming back to results by isothermal measurements, by plotting the frequency of maximum of ε'' against reciprocal temperature for the three segmental relaxations, the Arrhenius plot (activation diagram) of Fig. 4.11 was constructed. The time scale of all relaxations for the various samples and thermal protocols can be discussed well using such plots. A main observation in Fig. 4.11 is that α and α_c have very similar frequency–temperature traces. The behavior is typical for segmental dynamics, ruled by the Vogel–Tammann–Fulcher–Hesse (VTFH) behavior (Eq. (3.7)) [VTFH] and is practically not affected by the addition of nanoparticles. On the other hand, α_{int} tends to be strongly separated from α and α_c, and its time scale is practically described by a straight line (Arrhenius behavior, Eq. (3.11) [Arrhenius1889, Donth01]) characterized by lower activation energy (~0.52 and ~0.50 eV for silica and titania, respectively), as compared to α and α_c. The result is very similar to that observed for a different PDMS network filled with silica nanoparticles [Fragiadakis07].

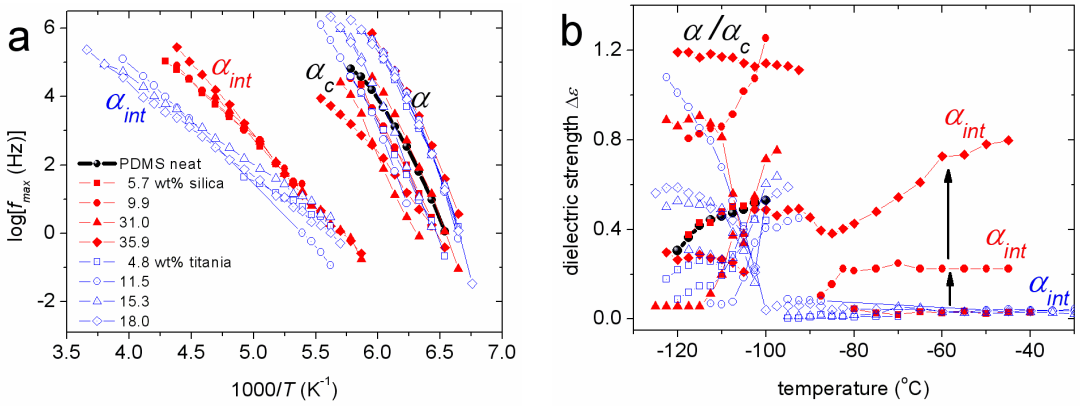

Fig. 4.11. (a) Arrhenius plot and (b) temperature dependence of dielectric strength of the segmental and interfacial dynamics for PDMS PDMS/silica and PDMS/titania nanocomposites.

In the Arrhenius plot (Fig. 4.11) the α_{int} relaxation traces look linear (Arrhenius behavior), but judging from the respective TSDC temperature range we conclude that the best

fitting to the data is given by the VTFH equation, Eq. (3.7) [Richert98]. After fixing the f_0 parameter to the phonon value 10^{13} Hz [Kremer02, Richert98], by fitting Eq. (3.7) to our experimental data we obtained values for the D parameter. D is related to the steepness or fragility index m according to Eq. (3.8) [Boehmer93]. The average fragility index values were calculated (Eq. (3.8)) to be 110, 97, 44 and 21 respectively for α, α_c, α_{int} (of PDMS/silica) and α_{int} (of PDMS/titania) relaxations. The uncertainty for these fragility values is about 5. Lorthior *et al.* have calculated similar values for α and α_c [Lorthioir04]. The VTFH behavior is indicative of cooperative relaxation mechanisms, so this is another strong indication that α_{int} relaxation in these nanocomposites is indeed affiliated to segmental polymer chain motions (glass transition). The reduced fragility values of α_{int}, in comparison with α and α_c relaxations, is explained by means of reduced cooperativity of segmental motions [Adam65]. Thus, our results suggest that the cooperativity length, ξ, [Sappelt93] is larger in the PDMS/silica than in the PDMS/titania nanocomposites.

Another point of interest is the temperature dependence of $\Delta\varepsilon$ for α_{int} relaxation. We follow in Fig. 4.11b that for the strong α_{int} relaxations samples with 31 and 36 wt% silica $\Delta\varepsilon$ increases with temperature, suggesting, possibly, increasing of the concentration of the polymer at the interfacial layer [Koga12, Klonos15A]. Simultaneously with the weakening of α_{int} relaxation with lower silica loading and in all cases of PDMS/titania, $\Delta\varepsilon$ tends to decrease with temperature (Fig. 4.11b). This last behavior resembles that of conventional nanocomposites of crosslinked PDMS [Fragiadakis05] and natural rubber [Fragiadakis11], suggesting that the concentration of polymer chains with modified (retarded) mobility in the interfacial layer reduces with temperature, drifted by the increasing of the mobile amorphous polymer (both in concentration and dynamics).

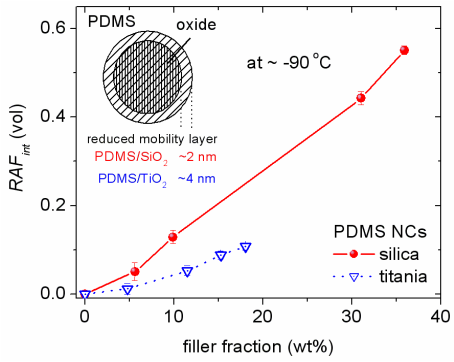

Fig. 4.12. The fraction of PDMS with reduced mobility, RAF_{int}, vs silica and titania content obtained from Eq. (3.10) at ~ –90 °C. The inset shows the simplified model used to calculate the thickness of the interfacial layer.

Having now clear evidence about the origins of the relaxations described above and in combination with DSC and DRS results, we can calculate the reduced mobility polymer fraction RAF_{int} (the fraction of polymer in the interfacial layer, Fig. 4.12) by Eq. (3.10). The results show that in the case of PDMS/silica the interfacial polymer fraction increases from 0.05 to 0.55 at the highest filler content (Fig. 4.12), while at the same time the degree of crystallinity drops from 0.42 to almost 0 (Table 4.1). In the case of PDMS/titania RAF_{int} is significantly lower and increases from 0 to 0.14 at the highest loading (Fig. 4.12), while X_c drops from 0.43 to 0.13 (Table 4.1). Following the same procedure as with the respective DSC results, by exploiting the information from the TEM measurements on the morphology and the dimensions of the nanoparticles [Bokobza10], it is possible to make an estimation of the thickness of the interfacial layer d_{int}, now more clearly from the DRS results. By applying Eq. (4.1), d_{int} was calculated to be ~2 nm for PDMS/silica and ~4 nm for PDMS/titania nanocomposites (Fig. 4.12). Combining our conclusions for the changes in segmental dynamics with the RAF_{int} trends (Fig. 4.12), we get additional support for the large total interactive surface area of the smaller silica particles (calculated geometrically ~453 m^2/g) and the respective smaller total interactive surface area of the larger titania particles (~47 m^2/g).

Results about the estimation of the interfacial influence (d_{int}) of silica on the PDMS chain mobility agree with the respective DSC values (d_{int}). However the results are different in the case of titania nanocomposites, in the sense that the restriction is higher in DSC and lower in DRS, the absolute values being also different for the two techniques (larger in the case of DSC). We should keep in mind that in DRS measurements RAF_{int} was estimated through the direct and additive contribution of the nanoparticles to the segmental dynamics (α_{int} relaxation), whereas in DSC measurements RAF was estimated more indirectly through the missing of the corresponding contribution to the heat capacity jump at the glass transition (reduction of ΔC_p step). Moreover, the DRS measurements provide, through the variation of both independent variables, frequency and temperature, the possibility to follow the evolution of the isothermal $\varepsilon''(f)$ spectra (and, thus, the evolution of RAF_{int}) with temperature [Fragiadakis05]). On the other hand, we observe in Figs. 4.7 and 4.9 that as X_c increases the whole dielectric response in the glass transition region gets lower. It is not clear at this stage to which extent the reduction of the fraction of the amorphous polymer and the constraints imposed by the polymer crystallites (i.e. the amount and influence of the rigid amorphous phase [Dobbertin96]), on the one hand, and a direct effect of the nanoparticles through the reduction of molecular mobility in the interfacial layer, on the other hand, are responsible for

that [Huo92]. Further DRS experiments in future work would help to quantitatively further follow this point. Please note also that by using Eq. (3.10) to calculate RAF_{int} it is implicitly assumed that the dielectric permittivity of PDMS is the same in the interfacial layer and the bulk amorphous and crystalline fractions. It is interesting to note in this connection that DSC, DRS and TSDC measurements in (amorphous) polyurethane/clay [Kripotou10] and poly(L–lactic acid)/grapheme oxide [Papageorgiou14] nanocomposites show, in agreement to each other, that a fraction of polymer is immobilized, making no contribution to the measured response by neither of the three techniques, and that this fraction is larger by DRS than by DSC.

4.4. Conclusions

The effects of nanoparticles on glass transition and molecular dynamics were studied in two series of PDMS/silica and PDMS/titania nanocomposites by employing calorimerty and dielectric techniques. Extended measurements using different thermal treatments showed that the good dispersion and strong interactions of the nanoparticles with PDMS restrict crystallization and segmental mobility of the polymer. In addition to calorimetry, the dielectric DRS and TSDC techniques provided significant information on the overall mobility, mostly on the segmental dynamics of the polymer (dynamic glass transition), which was found to consist of three discrete and well defined relaxations. These relaxations arise from the bulk (unaffected) polymer (α relaxation), the mobility of polymer chains restricted between condensed crystalline regions (α_c relaxation) and the segmental dynamics in an interfacial polymer layer around (or, in general, close to) the nanoparticles (α_{int} relaxation).

Compared with PDMS/silica in this work and in a previous work with a slightly different PDMS [Fragiadakis07], the effects were stronger in the series of PDMS/titania nanocomposites. These are characterized by stronger polymer–filler interactions, reflected in a shift of α_{int} to lower frequencies / higher temperatures and a larger thickness of the interfacial layer. A first explanation is that this can be attributed to (i) stronger hydrogen bonds [Bokobza10] and/or (ii) the larger size [Gong14] of nanoparticles in the case of titania, as compared to silica. In the next chapter we will provide evidence that the surface roughness of the particles is, also, at the origin of the differences in the overall response in the nanocomposites and the exceptional behaviors of samples of the high silica loading.

At temperatures lower than the melting point of the crystalline PDMS phase, the neat polymer (zero filler content) is presented in two phases: as crystallized (immobilized) and

amorphous in close proximity to the crystals (RAF_{cryst}). As filler content increases, some amount of PDMS becomes bound (reduced mobility) on the surfaces of the particles due to hydrogen bonding and the other two phases described above get restricted, while amorphous islands of PDMS (bulk / free mobility) start growing between the crystals and the nanoparticles (four phases). At the higher loadings the crystallization is practically absent along with the lamellar/*RAF* and the polymer is mainly composed of bulk and bound on the nanoparticles (two phases). For both types of filler the amount of PDMS which shows amorphous properties, participating in the glass transition, seems to be constant at ~12 wt% of the amorphous polymer. This molecular view, which emerges from the experimental results, indicates some kind of self–organization of the systems under investigation, where the polymer is composed of different phases and the composition changes in a continuous way under the external influences of the addition of nanoparticles and the variation of the temperature.

It should be noted, from the methodological point of view, that, although the three techniques employed agree with each other in the overall picture of reduction of molecular mobility in the nanocomposites, there are distinct differences between the quantitative results obtained by DSC, on the one hand, and by the two dielectric techniques, on the other hand.

Thermal sampling TSDC measurements in future work may provide more quantitative information on a possible distribution of relaxation times and glass transition temperatures in the interfacial layer [Fragiadakis07, Ellison03]. Finally, DSC measurements with temperature modulation (TMDSC) may provide further information on polymer mobility near the polymer crystals and the nanoparticles [Wurm10, Xu04].

5. Effects of surface modification and thermal annealing on interfacial polymer fraction and dynamics of PDMS in core–shell NCs based on high specific surface area silica

5.1. Introduction

In this chapter we study the dynamics and evaluate the fractions of interfacial polymer (polymer in the interfacial layer in close proximity to a solid surface) and of bulk and bulk–like polymer, all coexisting in the same silica/PDMS systems. Materials under investigation consist of linear polydimethylsiloxane (PDMS) adsorbed in amorphous fumed silica (SiO_2) aggregates, in systems of the *core–shell* type [Sulim09]. The adsorption is thought mainly physical (hydrogen bonding) [Gunko14]. In our recent publication on PDMS adsorbed on the same initial (unmodified) silica [Klonos15A], results have indicated that during the first stages of polymer adsorption (low polymer loading) PDMS adsorbed on the external surfaces of silica aggregates (high roughness) was ruled by slower dynamics (interfacial), as compared to the bulk. Bulk–like mobility of the polymer was observed only in samples of high PDMS loading, demonstrating however slower dynamics as compared to the bulk, affiliated to spatial constraints in the voids of silica aggregates [Klonos15A]. In order to study in more depth the above effects, we manipulate here the surface characteristics of the initial silica by generating crystalline zirconia nanoparticles on the initial silica particles (smoothened surfaces), before adsorption of the polymer [Sulim09]. The investigation involves differential scanning calorimetry (DSC) for thermal transitions and broadband dielectric relaxation spectroscopy (DRS) for polymer dynamics. In addition to severe restriction of polymer crystallization, the results reveal significant effects of the silica particles on the segmental dynamics (related to glass transition), originating mainly from the strong reduction of molecular mobility at the interfaces. Surface effects were further studied by employing different thermal treatments

(annealing of crystallization), which had been proved quite revealing in our recent studies on similar PDMS based nanocomposites [Klonos10A, Klonos15A].

5.2. Materials and code names

Preparation and morphological characterization of initial oxides have been previously described (section 2.2 and [Sulim09]), therefore we repeat here briefly the preparation procedure. Fumed silica A–380 (pilot plant of the Institute of Surface Chemistry, Kalush, Ukraine) was used as initial substrate for the development of zirconia nanoparticles at various amounts by reiteration of the respective reaction cycle from 1 to 4 (resulted in ~6 and ~16 wt% zirconia, respectively [Sulim09]). Linear polydimethylsiloxane (Kremniypolymer, Zaporozhye, Ukraine, *MW* ~7960, degree of polymerization 105, viscosity ~1000 cPS) was adsorbed onto dry silica at the amounts of 40 and 80 wt% from a hexane solution of PDMS (1 wt% PDMS). The suspensions were mechanically stirred and finally dried to remove solvents. Samples at PDMS content of 40 wt% are in the form of powder similar to initial A–380 powder, while at higher PDMS contents of 80 wt% and 100 wt%, the samples are liquid–like and liquid, respectively. In the finally produced materials silica (primary particle size ~8 nm) was found to form aggregates, varying in size between 100 and 500 nm as observed previously by SEM (section 2.2 and [Klonos15A]). Materials prepared and studied here and the specific surface modification by zirconia are interesting also in the perspective of biomedical applications, on the basis of biocompatibility of the components and control of hydrophilicity of initial silica [Morks08, Stamatopoulou14].

Seven polymer nanocomposite compositions were prepared and studied in this chapter, i..e. the initial PDMS, silica/PDMS with 40 and 80 wt% PDMS, and silica/zirconia/PDMS containing silica modified with 1 and 4 cycles of zirconia, again with 40 and 80 wt% PDMS. Throughout the text and in the figures and tables of this chapter, representative code names that describe the samples are used. For instance (i) *A380P80* corresponds to the sample in which PDMS at 80 wt% is adsorbed onto initial unmodified A–380, (ii) *A380Z1P40* corresponds to the sample in which PDMS at 40 wt% is adsorbed onto A–380 that previously suffered 1 cycle of zirconia reaction, and (iii) *A380Z4P80* corresponds to the sample in which PDMS at 80 wt% is adsorbed onto A–380 that previously suffered 4 cycles of zirconia reaction.

5.3. Results

5.3.1. Characteristics of materials under investigation

Results concerning the modification of silica A–380, before the polymer adsorption have been published [Sulim09] and they will be only briefly summarized here. A–380 consists of tightly packed spherical nanoparticles (~8 nm in diameter) forming aggregates of 100–500 nm [Klonos15A]. The initiator of the zirconia synthesis ($Zi(acac)_3$) reacts with the free silanol (≡Si–OH) groups of silica (both in the inner and external surfaces) forming ≡Si– $Zi(acac)_3$ groups, upon which the zirconia nanoparticles were subsequently generated. According to FTIR coverage of free silanols was not complete. It has been reported that zirconia suppresses, in general, the concentration of free hydroxyl groups in the modified A–380 particles [Gunko13B].

Table 5.1

Textural and porosity characteristics of unmodified A–380 and modified A–380/ZrO_2 oxides as taken from previous study [Sulim09]. Z1 and Z4 correspond to 1 and 4 reaction cycles of zirconia grafting, respectively. Zirconia content according to XRD, C_{ZrO2}, specific surface area as recorded by Nitrogen adsorption–desorption isotherms, S_{BET}, average volume of pores, V_p, of mesopores (details in text), V_{meso}, and of macropores, V_{macro}.

Oxide	C_{ZrO2} (wt.%)	S_{BET} (m^2/g)	V_p (cm^3/g)	V_{meso} (cm^3/g)	V_{macro} (cm^3/g)
A380 unmodified	0	342	1.160	0.311	0.849
A380Z1	5.9	262	1.996	0.142	1.854
A380Z4	15.5	237	1.186	0.390	0.796

According to XRD measurements [Sulim09], the 13–32 nm in diameter zirconia was found to be in the crystalline state, while its content was found equal to 5.9 wt% and 15.5 wt%, for 1 and 4 cycles of zirconia reaction, respectively (Table 5.1). The specific surface area, S_{BET}, of initial A–380, representative for the silica–polymer interaction area, was measured employing nitrogen adsorption–desorption isotherms [Gunko13B] to 342 m^2/g. S_{BET} decreased to 262 m^2/g and, further, to 237 m^2/g after the 1st and 4th zirconia reaction cycle, respectively (Table 5.1) [Sulim09]. Mesopores (2 nm < diameter < 50 nm) and macropores (diameter ≥ 50 nm) at the surfaces and voids of aggregates contribute mainly to the relatively high S_{BET} values. High S_{BET} for nanosilicas with mainly textural porosity (e.g. fumed silicas A–240, A–300, A–380 [Gunko13B, Stamatopoulou14, Klonos10B]) has been previously shown to describe well high degree of accessibility for both the gas molecules and the PDMS

chains [Klonos15A, Galaburda14, Sulym14]. The decrease of S_{BET} after modification with zirconia was suggested to originate from the development of zirconia nanoparticles mainly onto the external silica surfaces, reducing this way their roughness.

5.3.2. Differential scanning calorimetry (DSC)

5.3.2.1. Protocol A

Figure 5.1 presents comparative DSC thermograms in the glass transition region for silica/PDMS core–shell based nanocomposites and for neat PDMS, for measurements under *protocol A* (section 3.2) (Fig. 5.1a,b) and for neat PDMS previously quenched (Fig. 5.1c). The crystallization of neat PDMS occurs during cooling at –76 °C and X_c ~0.65 wt (Table 5.2). Crystallization is almost absent during cooling for A380P40 and A380Z1P40, whereas X_c increases to ~0.13 for A380Z4P40 (Table 5.2). X_c increases significantly at the higher polymer loading (80 wt%, Table 5.2).

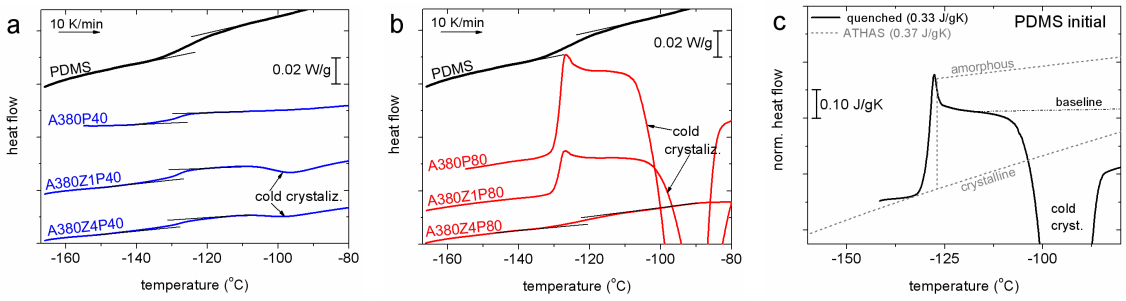

Fig. 5.1. Comparative DSC thermograms in the glass transition region of samples of (a) 40 wt% and (b) 80 wt% PDMS adsorbed onto unmodified and modified A–380, and for comparison for neat PDMS, for measurements of *Protocol A*. The curves are normalized to sample mass. The added lines represent the baselines of the thermograms before and after glass transition. (c) shows DSC thermogram in the glass transition of initial amorphous PDMS during heating at 10 K/min of a sample previously cooled at ~90 K/min (quenched, solid line). DSC heat flow is normalized to heating rate and, thus, is presented in specific heat capacity, C_p, units. Results for C_p of PDMS against temperature taken from ATHAS databank [Wunderlich03] and Ref. 2 therein are comparatively shown in (c) (dashed lines).

Table 5.2

Quantities of interest from DSC measurements of *Protocols A and AC*: crystallization temperature, T_c, glass transition temperature, T_g, normalized heat capacity step of glass transition, $\Delta C_{p,n}$, temperature maxima of melting, $T_{m1,2}$, normalized melting enthalpy $\Delta H_{m,n}$, degree of crystallinity, X_c, rigid and mobile amorphous polymer fractions, *RAF* and *MAF*, respectively. Note: X_c, *RAF* and *MAF* refer to whole polymer mass (i.e. X_c + *RAF* + *MAF* = 1).

protocol	*sample*	T_c (°C) (±0.5)	T_g (°C) (±0.5)	$\Delta C_{p,n}$ (J/g K) (±0.02)	T_{m1} (°C) (±0.2)	T_{m2} (°C) (±0.2)	$\Delta H_{m,n}$ (J/g) (±1)	X_c (wt) (±5%)	*RAF* (wt) (±10%)	*MAF* (wt) (±10%)
Protocol A	A380P40	–	–129	0.07	–48	–	0	0.00	0.79	0.21
	A380Z1P40	–103	–133	0.09	–50	–	3	0.01	0.72	0.27
	A380Z4P40	–95	–135	0.09	–50	–	8	0.13	0.63	0.24
	A380P80	–98	–129	0.28	–48	–39	22	0.08	0.14	0.78
	A380Z1P80	–97	–129	0.22	–49	–40	19	0.05	0.32	0.63
	A380Z4P80	–90	–128	0.07	–49	–40	19	0.45	0.43	0.12
	PDMS	–76	–127	0.22	–47	–40	24	0.65	0.12	0.23
Protocol AC	A380P40	–	–129	0.09	–	–	0	0.00	0.73	0.27
	A380Z1P40	–	–129	0.03	–50	–	5	0.12	0.80	0.08
	A380Z4P40	–	–127	0.04	–51	–	9	0.23	0.67	0.10
	A380P80	–	–122	0.15	–47	–39	23	0.61	0.21	0.18
	A380Z1P80	–	–121	0.02	–50	–40	19	0.52	0.45	0.03
	A380Z4P80	–	–122	0.02	–51	–40	19	0.51	0.46	0.03
	PDMS	–	–126	0.15	–46	–40	25	0.67	0.18	0.15

During the heating in measurements of *Protocol A*, in Fig. 5.1, all samples demonstrated single glass transition steps in the region between –140 °C and –115 °C, with T_g values between –135 °C (A380Z4P40) and –127 °C (neat PDMS) (Table 5.2). The value for neat PDMS is in agreement with previous studies of PDMS [Aranguren98, Klonos10A, Lund08, Galaburda14]. Interestingly, T_g of the core–shell systems is by 2 K lower than that of neat PDMS and it is further reduced on addition of nanozirconia by 1–8 K. $\Delta C_{p,n}$ for nanocomposites of 40 wt% PDMS is smaller than for neat PDMS. A slight increase is observed in nanocomposites with zirconia modification. On the other hand, for A380P80 $\Delta C_{p,n}$ value is larger as compared to neat PDMS.

As temperature increases above T_g during heating, an exothermic event was observed in the case of A380Z1P40, A380Z4P40 and all nanocomposites of 80 wt% PDMS loading

(Fig. 5.1), representing cold crystallization, a phenomenon which follows uncompleted crystallization during cooling [Gedde95, Zhuravlev14].

At higher temperatures, complex endothermic melting peaks are observed between –48 and –39 °C (T_{m1}, T_{m2} in Table 5.2). In consistency with cooling thermograms, melting is absent for A380P40 and quite weak for A380Z1P40 and A380Z4P40. Strong double melting peaks are observed for all nanocomposites of 80 wt% PDMS. As discussed in previous work [Aranguren98, Klonos12] events of recrystallization and melting contribute in the temperature region of melting. For that reason, in measurements of *Protocol A* the degree of crystallinity was not calculated from the melting enthalpy. Nevertheless, the melting enthalpy normalized to the same polymer fraction, $\Delta H_{m,n}$, is lower in the nanocomposites than in neat PDMS (Table 5.2).

5.3.2.2. Protocol AC

Figure 5.2 shows DSC thermograms in the glass transition region during heating after a 20 min annealing of crystallization (*Protocol AC*, details in section 3.2). We should note that the annealing temperature was different for different samples, aiming at maximum degree of crystallinity. Obviously, this affects the evolution of crystallization and the structure of polymer crystals [Zhuravlev14]. In the case of annealed samples X_c was estimated employing the normalized melting enthalpy, $\Delta H_{m,n}$, in Eq. (3.1). Results were analyzed and evaluated and the respective values of interest are shown in Table 5.2.

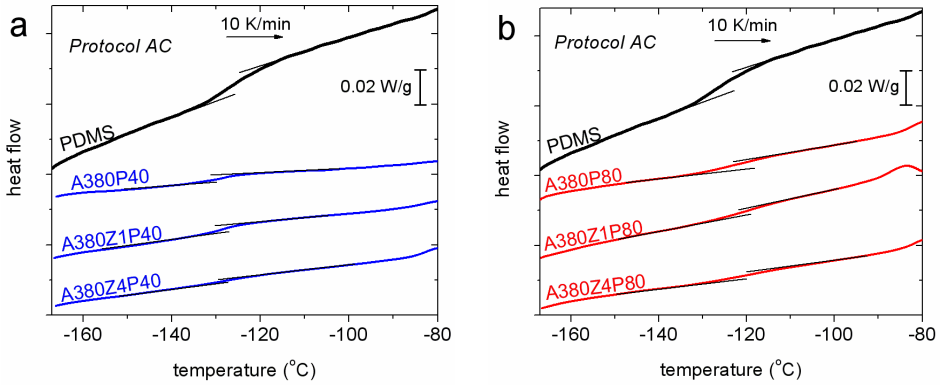

Fig. 5.2. Comparative DSC thermograms in the glass transition region of (a) 40 wt% PDMS and (b) 80 wt% PDMS adsorbed in unmodified and modified A–380, and for comparison of neat PDMS. Results are shown for measurements of *Protocol AC* (i.e. annealed samples) during heating. The curves are normalized to sample mass.

Crystallization was again absent for A380P40, while T_g remained the same as in *Protocol A*. Interestingly, $\Delta C_{p,n}$ was slightly increased from 0.07 to 0.09 J/gK (Table 5.2). With the exception of A380P40, crystallization annealing resulted in increased degree of crystallinity for all samples, significantly higher for samples of 80 wt% PDMS. T_g increased slightly on annealing for 40 wt% PDMS samples, still remaining lower than that of neat PDMS (Fig. 5.2a, Table 5.2). On the other hand, T_g for nanocomposites of 80 wt% PDMS increased strongly to values higher than in neat PDMS (Fig. 5.2b, Table 5.2).

Summarizing the findings from DSC, the interaction between A–380 and the polymer in the core–shell systems suppresses highly the crystallization ability of PDMS, which is in general extremely weak for the 40 wt% PDMS content, while glass transition is enhanced (T_g decreases, $\Delta C_{p,n}$ increases). Annealing procedure increases either $\Delta C_{p,n}$ or X_c (Table 5.2). In the case of high polymer content, zirconia modification suppresses glass transition (T_g increases, $\Delta C_{p,n}$ decreases) and enhances simultaneously crystallization. Similar effects are caused by thermal annealing.

5.3.2.3. Evaluation of polymer fractions according to calorimetric response

We categorize and evaluate the different polymer phases with respect to the type of their contribution to glass transition. Thus, we first estimated the amount of polymer which contributes to amorphous mobility, *MAF*, according to Eq. (3.4). According to our calculations (Table 5.2), the sum of mobile amorphous and crystallized polymer fractions ($MAF + X_c$) is lower than 1 in the nanocomposites, suggesting that, in the frame of the '3–phase model', one part of the response is missing from the calculated fractions (details in section 3.2). This deviation is thought to represent *RAF*, which can be easily calculated by Eq. (3.5). The calculated fractions of various polymer phases are included in Table 5.2, for measurements under both protocols. We should remind that all fractions refer to whole polymer mass according to the employed equations.

The sum of X_c and *MAF* is higher for 80 wt% PDMS, while, as expected, *RAF* is higher for samples of 40 wt% PDMS. In addition, from a first glance in Table 5.2, the above fractions change systematically with zirconia modification (X_c + *MAF* increases and *RAF* decreases), while, changes of *RAF* for low polymer adsorption (no significant interference of crystallinity) seem to follow the respective changes of S_{BET} (Table 5.1). These effects will be discussed later in comparison with respective DRS results.

5.3.3. Dielectric relaxation spectroscopy (DRS)

5.3.3.1. Raw data and analysis

DRS results will be comparatively presented here in the form of frequency dependence of the real, ε', (Fig. 5.3) and imaginary part of dielectric permittivity, ε'' (Fig. 5.4, isothermal plots). The main focus is on segmental dynamics, i.e. on the dielectric relaxations corresponding to the DSC response in the region of glass transition in Figs. 5.1,5.2 (namely α, α_c and α_{int}).

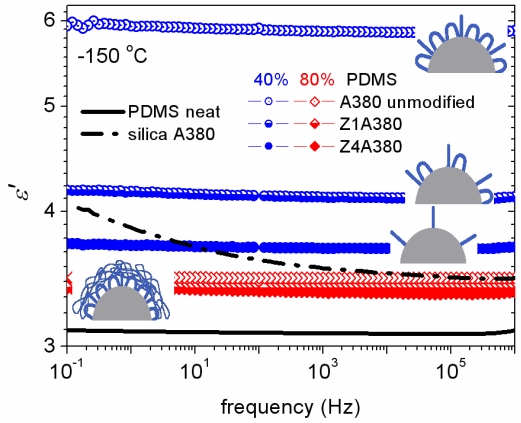

Fig. 5.3. Comparative DRS spectra of the real part of dielectric permittivity, ε', against frequency at –150 °C, for samples loaded with (○) 40 wt% and (◊) 80 wt% PDMS. Results for initial silica A–380 (dash–dotted line) and neat PDMS (solid line) were added for comparison with the nanocomposites. The inset schemes show simplified models for the conformations of interfacial polymer chains adsorbed on the surface of silica.

The dielectric response was found significantly higher for the samples containing 40 wt% PDMS as compared to 80 wt% PDMS (Figs. 5.3,5.4). This difference is confirmed also by the results for the AC conductivity, σ_{AC}, (not shown). This can be explained in terms of polymer chain conformations on the surfaces of the nanoparticles with higher polarizability (orientation, insets to Fig. 5.3), as interfacial polymer is the majority at low PDMS loading (40 wt%) and dominates the dielectric response [Klonos15A]. In the case of high PDMS loading (80 wt%) the additional polymer chains connect to the additional contact points and, most probably, form additional polymer layer(s). This implies significant obstacles to the orientation of interfacial chain segments, resulting in reduction of dielectric response (ε' in Fig. 5.3).

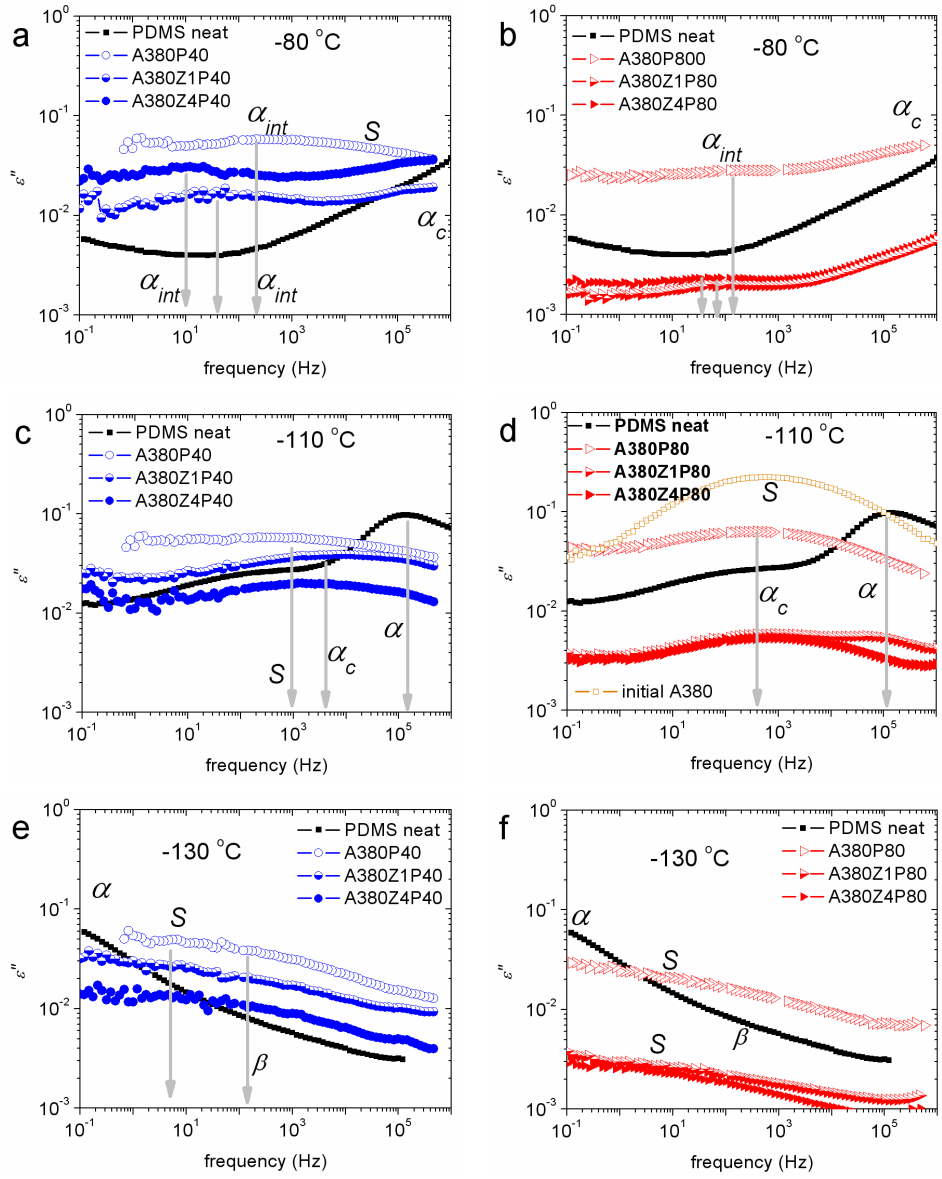

Fig. 5.4. Isothermal DRS plots of the imaginary part of dielectric permittivity, ε'', vs frequency for PDMS and the composites with (a,c,e) 40 and (b,d,f) 80 wt% adsorbed PDMS, at –80, –110 and –130 °C. Results are shown for measurements of thermal *Protocol A*. Indicated are the dielectric relaxations related to segmental and local dynamics. Results for initial A–380 (*S* relaxation) at –110 °C have been included in (d).

After analysis of the complex DRS spectra (details in Section 3.4), the plots of Figs. 5.5,5.6 were constructed, by plotting f_{max} and $\Delta\varepsilon$ of the three segmental and the two local (β and *S*) relaxations against reciprocal temperature. Included in the Arrhenius plots of Figs. 5.5a,5.6a are results by DSC and TSDC (raw data not presented here), namely glass transition temperatures and peak temperatures, respectively, at the equivalent frequencies of the techniques, 20 mHz and 1.6 mHz, respectively [Fragiadakis07]. Selected DRS results will be shown here also in the form of temperature dependence of ε'' (Fig. 5.7, isochronal plots).

5.3.3.2. Interfacial relaxation

α_{int} relaxation in Figs. 5.4a,b, located, in the broad range from 10 to $2 \cdot 10^2$ Hz at –80 °C, represents the dynamics of semi–bound polymer chains in the interfacial layer, with strongly reduced mobility due to interactions with the surface hydroxyls of A–380 [Klonos15A, Klonos10A]. The temperature dependence of segmental dynamics is typically described by Vogel–Tammann–Fulcher–Hesse (VTFH) equation, Eq. (3.7) [Richert98]. After fitting Eq. (3.7) to our experimental data and fixing the f_0 parameter to the phonon value 10^{13} Hz [Kremer02, Richert98], we obtained values for T_0 and D. D is related to the steepness or fragility index m [Boehmer93] according to Eq. (3.8). The fragility (cooperativity) index values for all segmental relaxations (α_{int}, α_c and α) were calculated and are listed in Table 5.3.

From a first glance at the Arrhenius plots (Figs. 5.5a,5.6a), the time scale of α_{int} relaxations seems to tend to more linear–like behavior (Arrhenius (Eq. 3.11), constant activation energy) as compared to α and α_c, especially as zirconia grafting increases. Additionally, α_{int} becomes slower, while its strength (Figs. 5.5b and 5.6b) and cooperativity (m in Table 5.3) are reduced with zirconia modification (addition of ~6 and ~16 wt% zirconia, Table 5.1). The strength of α_{int} is smaller for composites with 80 wt% PDMS (Fig. 5.6b), as compared to 40 wt% PDMS (Fig. 5.5b). The respective changes with zirconia modification are more pronounced for the samples of the low polymer loading.

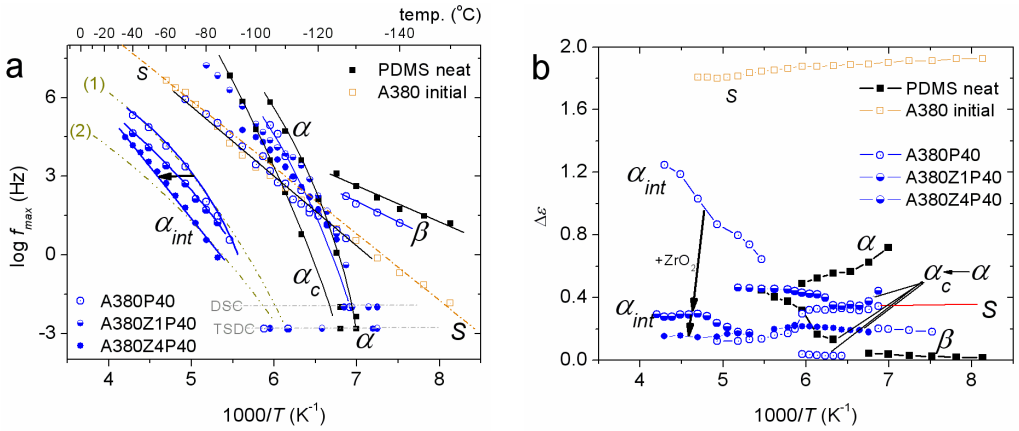

Fig. 5.5. (a) Arrhenius plots and (b) dielectric strength vs reciprocal temperature of the local (β, S) and segmental bulk (α), constrained in voids or/and between polymer crystals (α_c) and interfacial (α_{int}) dynamics for initial A–380, neat PDMS, A380P40, A380Z1P40 and A380Z4P40 recorded in isothermal DRS measurements under thermal *Protocol A*. Respective DSC and TSDC data have been added in (a). The lines in (a) are fittings of the Arrhenius and the VTFH equations (details in text). The arrows mark changes in α_{int} relaxation imposed by zirconia modification of grafting on the initial A–380 particles. Lines (1) and (2) in (a) correspond to the interfacial relaxation in conventional PDMS/silica and PDMS/titania nanocomposites, respectively [Klonos10A].

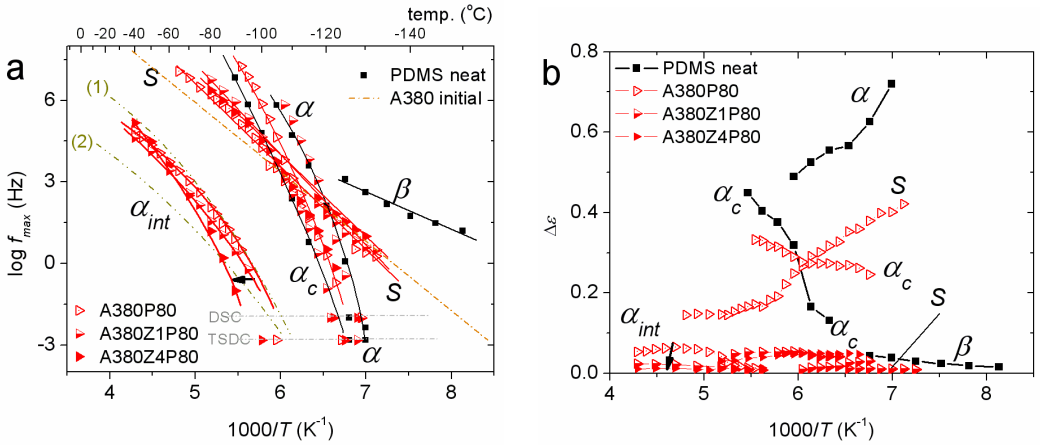

Fig. 5.6. (a) Arrhenius plots and (b) dielectric strength vs reciprocal temperature, of the local (β, *S*) and segmental bulk (α), constrained in voids or/and between polymer crystals (α_c) and interfacial (α_{int}) dynamics for initial A–380, neat PDMS, A380P80, A380Z1P80 and A380Z4P80 recorded in isothermal DRS measurements under thermal *Protocol A*. Respective DSC and TSDC data have been added in (a). The lines in (a) are fittings of the Arrhenius and the VTFH equations (details in text). The arrows mark the changes in α_{int} relaxation imposed by zirconia modification on the initial A–380 particles. Lines (1) and (2) in (a) correspond to the interfacial relaxation in conventional PDMS/silica and PDMS/titania nanocomposites, respectively [Klonos10A].

Table 5.3

Shape parameters of the fitted HN equation (Section 3.4, Eq. (3.6)) a_{HN} and β_{HN} (on average over temperature), fragility index, *m*, for the recorded dielectric segmental relaxations, and interfacial polymer fraction at –95 °C, RAF_{int} (Eq. (3.10)). (*) corresponds to relaxations that do not obey VTFH equation.

process	α (*Protocol A*)			α_c (*Protocol A*)			α_{int} (*Protocol A*)				α_{int} (*Protocol AC*)			
parameter	a_{HN}	β_{HN}	*m*	a_{HN}	β_{HN}	*m*	a_{HN}	β_{HN}	*m*	RAF_{int} (vol)	a_{HN}	β_{HN}	*m*	RAF_{int} (vol)
sample														
A380P40	–	–	–	–	–	–	0.26	1	43	0.86	0.24	1	*	0.55
A380Z1P40	–	–	105	0.23	1	92	0.30	1	34	0.34	0.28	1	31	0.22
A380Z4P40	–	–	–	0.21	1	*	0.26	1	32	0.23	0.25	1	31	0.16
A380P80	–	–	–	0.44	1	102	0.45	1	52	0.05	0.30	1	38	0.02
A380Z1P80	0.41	0.9	122	0.24	1	87	0.30	1	36	0.27	0.30	1	35	0.14
A380Z4P80	–	–	–	0.33	1	67	0.37	1	32	0.13	0.35	1	33	0.10
PDMS	0.43	0.9	106	0.30	1	96	–	–	–	0.00	–	–	–	0.00

5.3.3.3. Bulk–like relaxations

α relaxation in Fig. 5.4c,d at around 10^5 Hz at –110 °C is associated with the glass transition of the amorphous unaffected (bulk) polymer fraction [Klonos10A, Klonos12, Lund08], observed only in neat PDMS and A380Z1P80. This relaxation corresponds to the lower temperature sharp–shaped glass transition step in DSC (Figs. 5.1b,c). Next to α, at around (10^3 Hz, –110 °C), α_c relaxation originates from polymer chains restricted either between condensed crystal regions [Klonos10A, Lund08] (i.e. case of neat and 80 wt% PDMS, Fig. 5.4d) or in the voids between nanoparticles in their aggregates (i.e. case of core–shell nanocomposites at low polymer loading, Fig. 5.4c) [Klonos15A, Floudas13]. The dynamics of each of these relaxations is almost identical in the nanocomposites and in neat PDMS in Figs. 5.5a and 5.6a.

Additional support about the origin of α_c and α relaxations is provided by isochronal measurements. Data recorded isothermally were comparatively replotted in Fig. 5.7 as isochronal $\varepsilon''(T)$ plots to facilitate direct comparison with the DSC thermograms of Figs. 5.1,5.2. The frequency of 121 Hz was selected as representative for this comparison. Despite the fact that these diagrams are not real isochronal measurements but replottings of isothermals, the results are not far from reality, as confirmed by comparison with real isochronal DRS measurements at 125 Hz for pure PDMS (Fig. 5.7a) and A380P80 (Fig. 5.7b). The results are consistent with those of DSC regarding T_g, the shifts of α and α_c relaxations to higher temperatures in Fig. 5.7, as compared to Figs. 5.1 and 5.2, arising from the higher frequency of presentation [Fragiadakis07].

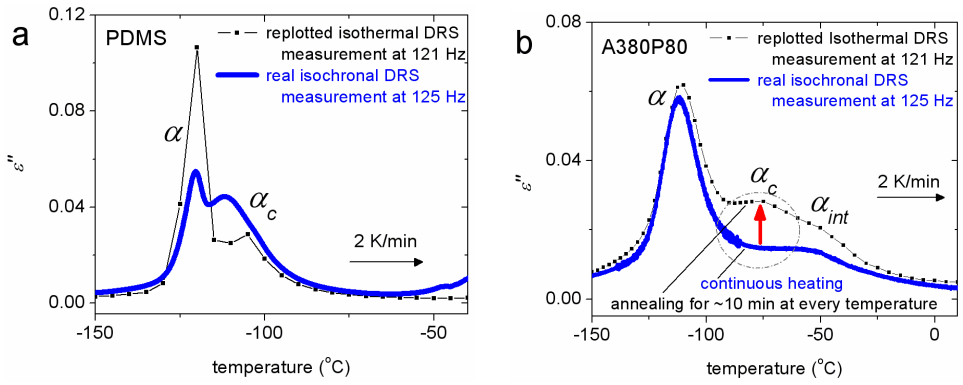

Fig. 5.7. Comparative isochronal plots of the imaginary part of dielectric permittivity, ε'', replotted from DRS isothermal measurements at 121 Hz (black pointed curves) and directly measured at 125 Hz (red solid curves), for (a) neat PDMS and (b) A380P80. Indicated are the recorded relaxations.

A further comment refers to the different recordings of α_c relaxation Fig. 5.7b. In the case of A380P80, we recall from the DSC data (Table 5.2) that the presence of silica in A380P80 suppresses strongly the degree of crystallinity, X_c (0.08), and T_c (–98 ^{o}C). Thus, we expect that α_c relaxation should be absent in a continuous heating measurement at 2 K/min. This is true in fact in the real isochronal measurements of Fig. 5.7b. In the case of the isochronal replottings, the ~10 min isothermal annealing of the sample at each temperature of measurement, including the T_c region, necessary for stabilizing the temperature and for scanning the frequency range of measurements, leaded to the arising of α_c relaxation. Thus, the sample is more amorphous in the real isochronal measurements in Fig. 5.7 as compared to the isochronal replottings of the DRS measurements. The situation is different for neat PDMS in Fig. 5.7a, due to the higher crystallization temperature of the neat polymer (–76 ^{o}C in Table 5.2) and the already high degree of crystallization (~0.65 in Table 5.2).

Effects of nanozirconia and filler content on the bulk–like relaxations (mainly on their strength in Figs. 5.5b,5.6b, and cooperativity, m, in Table 5.3) are indirect and mainly expressed via the changes induced on the degree of crystallinity (Table 5.2), in agreement to previous studies of PDMS [Klonos10A, Klonos12, Lund08].

5.3.3.4. Local relaxation of –OH groups on silica surface

S relaxation [Fontanella09] located at around (10^3 Hz, –110 ^{o}C) in Fig. 5.4d, is related with motions of the silanol surface groups of silica (Si–OH) with attached water molecules [Fragiadakis07, Kirst93, Klonos13]. We observe in Fig. 5.4d that the *S* relaxation dominates the response for initial silica A–380 (with ambient hydration of about 10 wt%). After careful analysis of the results, *S* shows exactly the same time scale with the *S* relaxation measured in A380P40 and all nanocomposites of 80 wt% PDMS loading. As expected, $\Delta\varepsilon$ of *S* is lower in the nanocomposites than in neat A–380 (Figs. 5.5a,5.6a). In our previous studies on similar core–shell systems of PDMS and silica, it has been demonstrated that *S* relaxation becomes weaker as the degree of polymer adsorption (surface coverage of the particles) increases [Klonos15A, Galaburda14, Sulym14].

5.3.3.5. Secondary (local) polymer relaxation

A faster but relatively weak relaxation is located at around 100 Hz at –130 ^{o}C in Fig. 5.4e. The relaxation named here 'β', has not been reported in previous work in PDMS, focusing however on segmental dynamics [Fragiadakis07, Kirst93, Schönhals03, Lund08]. Analysis of the results shows that β (α_{HN}~0.23, β_{HN}=1.0): (i) obeys Arrhenius equation (Eq. (3.11), i.e.

linear trace in Fig. 5.5a, activation energy ~0.26 eV), (ii) is weaker by one order of ε'' magnitude as compared to segmental relaxations in Fig. 5.5b, and (iii) slightly increases in dielectric strength with temperature (Figs. 5.5b). According to Ngai [Ngai98] these characteristics suggest that β is a local (secondary) relaxation of the polymer. In consistency with that, β relaxation shows quite similar behavior in the nanocomposites (whenever recorded, depending on the availability and the quality of low temperature measurement) as in the case of initial PDMS. The limited information available at present (only a few points in Figs. 5.5,5.6) precludes any further discussion on the molecular origin of the relaxation at this stage.

5.3.3.6. Evaluation of polymer phases according to dielectric response

The results reported above provide clear evidence about the origin of the various segmental relaxations. Thus, we may calculate the various fractions of polymer by evaluating the respective dielectric responses (i.e. $\Delta\varepsilon$). To that aim we employ a model analogue to the one used previously for DSC (i.e. Eqs. (3.4, 3.5), section 3.2) and we calculate the mobile bulk, *MAF*, and the interfacial, RAF_{int}, polymer fractions according to Eqs. (3.9) and (3.10), respectively. We recall that the dielectric strength changes with temperature in Figs. 5.5b, 5.6b, thus, we employed DRS results at the same temperature –95 ^{o}C for *MAF* and RAF_{int}. Results of RAF_{int} are shown in Table 5.3. They show that RAF_{int} reduces with surface modification from 0.86 to 0.23 wt for samples of 40 wt% PDMS. As expected, RAF_{int} is weaker for higher polymer loading (80 wt%) and changes with surface modification are not systematic. The results will be discussed later comparatively with those obtained by DSC (Table 5.2).

5.3.3.7. Effects of thermal (crystallization) treatment

We turn now attention to the effects of crystallization annealing on α_{int} relaxation. To that aim, in Fig. 5.8 we compare results of measurements under standard treatment (*Protocol A*) and annealing of crystallization before the DRS measurements (*Protocol AC*) for samples of low polymer loading. Similar results were obtained also for samples at high polymer loading (not shown). In addition, we show and evaluate in Fig. 5.9 online measurements during isothermal annealing.

It becomes clear that annealing of crystallization leads in general to slower α_{int} relaxation (Fig. 5.8a), with lower dielectric strength (Fig. 5.8b), suppressed fragility (*m*) and RAF_{int} (Table 5.3) for both polymer loadings. The effects imposed by annealing on α_{int}

become gradually weaker with increasing of surface modification. Paralell to changes imposed on α_{int} by annealing, α_c relaxation tends also to become slower (Fig. 5.8a), whereas its strength increases (Fig. 5.8b).

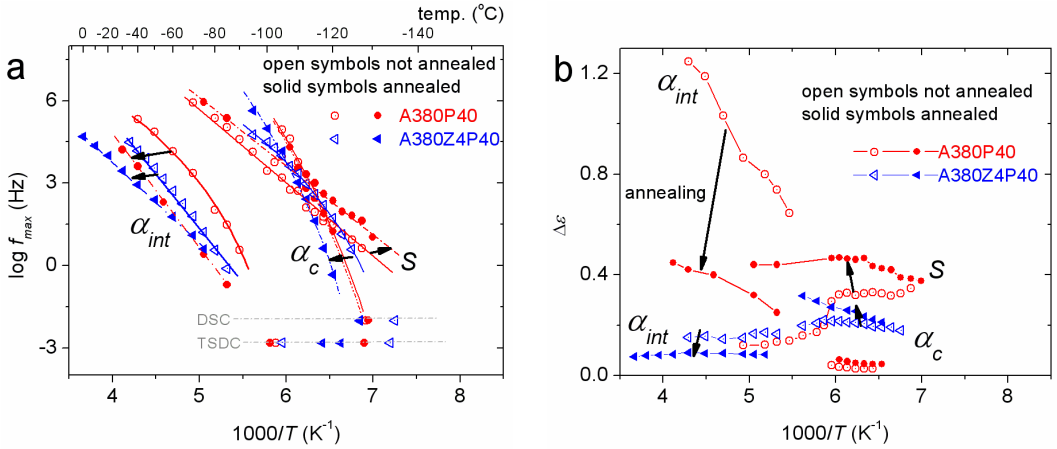

Fig. 5.8. Comparative (a) Arrhenius plots and (b) dielectric strength vs reciprocal temperature of the local (*S*), segmental bulk–like (α_c), and interfacial polymer dynamics (α_{int}) for A380P40 (cycles) and A380Z4P40 (triangles) composites, recorded in isothermal DRS measurements under thermal *Protocols A* (open symbols) and *AC* (solid symbols). Respective DSC and TSDC data have been added in (a). The lines in (a) are fittings of the Arrhenius and the VTFH equations. The arrows mark changes induced by annealing.

In Fig. 5.9 we demonstrate an online time–monitoring of the effects imposed by isothermal annealing on segmental dynamics in neat PDMS at –114 °C (Fig. 5.9a) and in A380P80 at –85 °C (Fig. 5.9b). The response of the initially highly crystallized neat PDMS (X_c ~0.65 wt at the beginning and ~0.75 wt at the end) was expressed via both α and α_c relaxations in Fig. 5.9a, while during isothermal annealing α_c becomes stronger and α weaker. The recordings are similar to those in previous studies of PDMS [Lund08, Klonos10A]. Analysis showed that the total dielectric strength ($\Delta\varepsilon_{\alpha+\alpha c}$) decreased with annealing time (inset to Fig. 5.9a). Moreover, $\Delta\varepsilon_{\alpha+\alpha c}$ was decreased by a factor of about 2 at the end of annealing, while the degree of crystallinity increased by only ~15 wt%. This would suggest that the growth and interference of a rigid amorphous fraction in close proximity to crystals, RAF_{cryst}, [Dobbertin96, Xu04, Ezquerra04] is significant also in the nanocomposites, especially in the case of high PDMS loading. In the case of A380P80, X_c was increased from 0.08 to 0.61 during the annealing at –85 °C (Table 5.2) and at the same time α_c remained almost unchanged (weakly suppressed) in Fig. 5.9b. Interestingly, α_{int} relaxation became weaker during annealing (inset to Fig. 5.9b) and shifted to lower frequencies, in agreement also to the results in Fig. 5.8. Results are similar to those in conventional nanocomposites of crosslinked

PDMS filled high amounts of silica (shown previously in Fig. 4.10 of chapter 4). Taken together the results for neat PDMS and A380P80 in Fig. 5.9 provide additional evidence that α_{int} does not represent the relaxation of RAF_{cryst}, but is directly related to RAF_{int}.

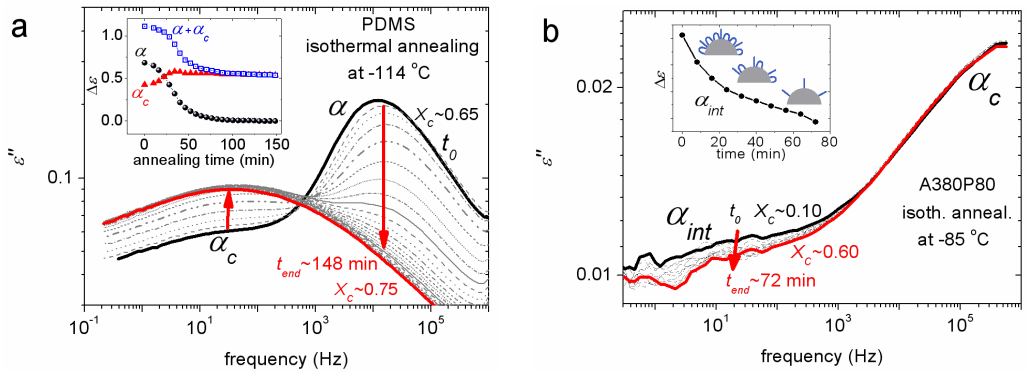

Fig. 5.9. Time evolution of the dielectric relaxation mechanisms associated to segmental dynamics during the isothermal crystallization annealing, for (a) neat PDMS at –114 °C and (b) A380P80 at –85 °C. Indicated in (a) and (b) are the estimated degree of crystallinity values, X_c, according to DSC, at the beginning, t_0, and at the end, t_{end}, of the annealing procedure. The insets show the respective time evolution of $\Delta\varepsilon$ for the relaxations under investigation.

5.4. Discussion

5.4.1. Polymer crystallization

Independently of surface modification and thermal treatment, the presence of A–380 results in reduction of crystallization temperature, T_c, and degree of crystallinity, X_c, as compared to neat PDMS (Table 5.2). These results suggest that the particles / aggregates do not act as crystallization nuclei [Gedde95]. Crystallization during cooling is absent in the cases of composites with 40 wt% PDMS, due to the strong polymer–filler interaction (hydrogen bonding) which gives birth to significant amount of interfacial polymer fraction [Fragiadakis07] close to the nanoparticles according to both DSC and DRS. Interfacial polymer affects negatively the ability of bulk polymer to form crystals, due to suppression of chain mobility / diffusion [Klonos10A] and/or of the available (free) volume in the nanocomposites [Koga12, Vanroy13]. It has been pointed out that the crystallization process can be the driving force for rearrangement of nanoparticles distribution in a polymer matrix [Khan09]. This is compatible with our findings for the 80 wt% PDMS samples, as the polymer matrix consists of linear polymer of low viscocity (~1000 cPS) and high crystallization ability (X_c ~ 0.5 – 0.8 wt [Aranguren98, Klonos10A]) and the distribution of

the quite large A–380 aggregates (~300 nm, section 2.2) could change during the growing of the even larger PDMS spherulites (~10^2 μm in size [Sundararajan02]).

5.4.2. Glass transition

Glass transition of the bulk was recorded extremely weak for samples of low polymer loading (40 wt% PDMS). T_g was lower in all cases of nanocomposites, dominated by: (a) spatial confinement effects [Krutyeva13, Schönhals03] in case of lower PDMS loading and (b) suppressed X_c in case of higher PDMS loading. For samples of high PDMS loading (80 wt%), T_g increases due to higher X_c in Table 5.2, since physical and spatial constraints imposed by the spherulites [Sundararajan02] hinder the diffusion of polymer chains [Gedde95, Lund08, Floudas13]. Annealing of crystallization of the composite samples results in further suppression of bulk dynamics, increasing X_c and T_g (Table 5.2).

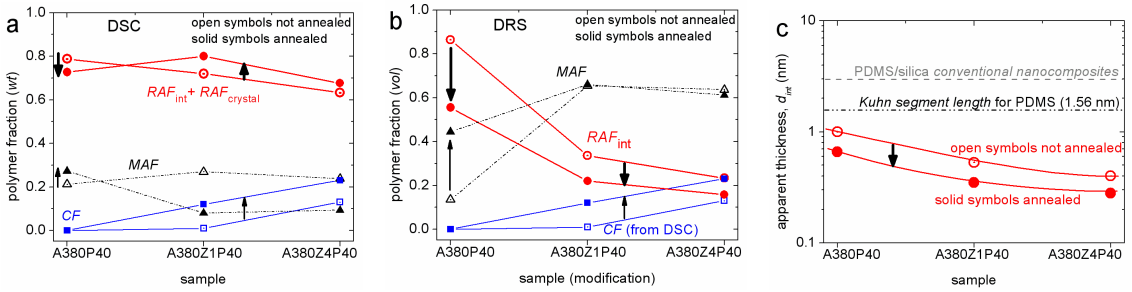

Fig. 5.10. Effects of surface modifications and thermal annealing (open / solid symbols) on (a,b) the various polymer fractions, i.e. rigid amorphous (*RAF*), mobile amorphous (*MAF*) and crystalline polymer (*CF*), and on (c) the apparent thickness of the interfacial layer, d_{int} (Eq. 5.1), for samples of 40 wt% adsorbed PDMS. Results are shown comparatively as estimated from (a) DSC and (b,c) DRS measurements (details in text). The arrows mark changes imposed by thermal annealing.

Independently of the changes in T_g, the presence of a rigid amorphous polymer fraction (immobile according to DSC [Wurm10]), most probably located at the interfaces with A–380, is manifested by the suppression of $\Delta C_{p,n}$ in the nanocomposites (Table 5.2). According to commonly employed equations (Eqs. (3.4, 3.5)), this fraction (*RAF*) was estimated around 0.8 wt of the whole polymer mass in A380P40 (Table 5.2). *RAF* decreases with surface modification down to ~0.6 wt (Fig. 5.10a). As expected, this decrease of interfacial polymer results in an increase of bulk–like polymer (i.e. *CF* + *MAF*, Fig. 5.10a). *RAF* calculations in samples of $X_c \neq 0$ on the basis of DSC include also the rigid amorphous polymer around crystals (RAF_{cryst}) [Dobbertin96], with the effect that the results of thermal annealing on *RAF* are controversial in Fig. 5.10a. Thermal annealing imposes an interplay

between $CF + MAF + RAF_{cryst}$, on the one hand, and RAF_{int}, on the other hand. The situation becomes more clear in DRS results which follow (Fig. 5.10b, next section).

5.4.3. Bulk–like dynamics (α and α_c relaxations)

Exploiting the high resolving power of DRS technique, the dielectrically active polymer phases (i.e. bulk–like and interfacial) could be evaluated in the nanocomposites (Fig. 5.10b).

Bulk–unaffected mobility of PDMS is monitored by α relaxation, characterized by an almost universal time scale in the Arrhenius diagram (Fig. 5.5a), as compared to different types of PDMS [Kirst93, Klonos10A]. The relaxation is present in A380Z1P40 and neat PDMS. α is the only asymmetric in shape ($\beta_{HN}<1$) relaxation recorded in the present work (Table 5.3), while its strength, $\Delta\varepsilon$, decreases with temperature (Fig. 5.5b), as expected for bulk–unconstrained segmental dynamics [Kremer02, Donth01].

Quite standard is also the time scale of α_c relaxation (Figs. 5.5a and 5.6a), which describes the retarded dynamics of polymer chains restricted inside A–380 voids or/and due to the PDMS crystals [Klonos10A, Klonos15A], and is recorded in all samples. $\Delta\varepsilon$ of α_c increases with temperature (Figs. 5.5b,5.6b), as the constraints imposed by the crystals are gradually loosened [Gedde95, Lund98]. In the case of measurements after crystallization annealing, α_c and S relaxations, whenever recorded, are enhanced (Fig. 5.8) at the expenses of bulk and interfacial polymer (α and α_{int}, respectively), without significant changes in fragility and shape parameters.

Any effects of zirconia modification on the evolution of α and α_c relaxations are again indirect, depending on the changes in X_c.

5.4.4. Interfacial dynamics (α_{int} relaxation)

We suggest that α_{int} monitors directly the dynamics of semi–bound polymer chains in the interfacial layer (RAF_{int}) [Fragiadakis07, Klonos10A, Fragiadakis11, Klonos15A]. Its dielectric strength in Figs. 5.5b, 5.6b is higher for unmodified A–380, for both amounts of adsorbed PDMS. The relaxation tends to become slower, weaker and less fragile (cooperative) with zirconia modification (Figs. 5.5,5.6, Table 5.3). The changes recorded by DRS follow very nicely the respective changes in specific surface area, S_{BET}, in Table 5.1. From the methodological point of view, these results may suggest that the adsorption of gas molecules (Nitrogen in our case) on surfaces of nanometric roughness is representative also for polymer chains adsorption [Klonos15A].

Another point of interest is the temperature dependence of $\Delta\varepsilon$ for α_{int} relaxation. We follow in Figs. 5.5b,5.6b that for the strong α_{int} relaxations of A380P40 and A380P80 (i.e. unmodified samples) $\Delta\varepsilon$ increases with temperature. Simultaneously with the weakening of α_{int} relaxation with zirconia modification, $\Delta\varepsilon$ tends to decrease with temperature (Figs. 5.5b,5.6b). This behavior resembles that of conventional nanocomposites of crosslinked PDMS (chapter 4, Fig. 4.11) and natural rubber [Fragiadakis11] filled with *in situ* generated silica particles (~5 nm in diameter), where $\Delta\varepsilon$ of α_{int} relaxation was lower than that of α and decreased with increasing temperature.

5.4.5. Interpretation in terms of models

In a recent study concerning interfacial phenomena in the same unmodified *core–shell* systems we have proposed that the characteristics of α_{int} relaxation are determined by PDMS chain conformations and polarizability at interfaces [Klonos15A]. More specifically, according to recent studies on adsorbed polymers [Koga12, Rotella11, Kritikos13] there may exist two populations of chain segments at interfaces which can be considered responsible for the molecular mobility recorded in DRS as the interfacial α_{int} process, i.e. (a) extended tails with bulk–like density but reduced mobility and cooperativity (Scheme 5.1a), and (b) flattened chain segments which form the inner quite dense region due to multiple contact points with the silica surface (loops, Scheme 5.1a). We assume that in our *core–shell* nanocomposites, the relatively high S_{BET} values of A–380 particles are responsible for the successful adsorption of PDMS chains with a high ratio of loops/tails (Scheme 5.1a), due to the high number of potential particle–polymer contact points.

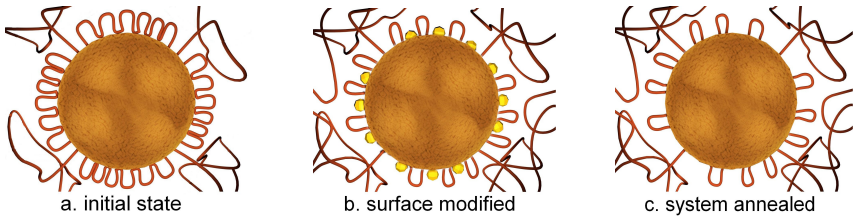

Scheme 5.1. Proposed 2–D schematic simplified models for describing interfacial polymer dynamics for (a) unmodified A–380 particles, (b) surface modified A–380 and (c) thermally annealed systems.

Additionally, for samples of respectively high/low interfacial polymer fraction (RAF_{int}) we may interpret the respective increase/decrease of $\Delta\varepsilon$ of α_{int} relaxation with temperature (Figs. 5.5b,5.6b) as follows. According to the models described above, the loop–like conformed chains are weakly attached (Fig. 1.3a) [Koga12, Rotella11] on the surfaces

and their concentration can increase as temperature increases, without change in interfacial polymer density, e.g. by simultaneous decrease of loops' maximum distance (height) from the adsorbing surface (Fig. 1.3b) [Koga12], similarly to polymers adsorbed onto solid surfaces during chemical [Guiselin91] and thermal [Rotella11] annealing. On the other hand, in the case of higher tail/loop ratio (Schemes 5.1b,c, i.e. case of lower RAF_{int} and, respectively, lower $\Delta\varepsilon$ of α_{int}) the mobility of the tails (bulk–like density) can gradually increase, drifted by the increasing of bulk–like polymer mobility. Thus, the degree of '*immobilization*' and '*orientation*' of the tails at the interfaces is suppressed, leading to lowering of $\Delta\varepsilon$ for α_{int} with temperature (thinner interfacial layer [Fragiadakis07, Fragiadakis11]).

Finally, we recall that in PDMS filled with *in situ* generated and finely dispersed silica (~5 nm) and titania (~30 nm) nanoparticles, the thickness of the interfacial layer, d_{int}, was ~2 nm for silica and ~4 nm for titania [Fragiadakis07, Klonos10A]. Similar values can be compatible with our results and the above models about polymer chain conformations (Scheme 5.1) of the bound polymer layer(s), taking into consideration that the length of *Kuhn segment* for a PDMS in melt is ~1.56 nm [Gilra11]. However, the geometrical models employed previously for the estimation of interfacial layer thickness [Fragiadakis07, Klonos10A, Gong14] cannot not be employed here, due to the high degree of initial particles aggregation [Klonos15A], the not well defined shape of aggregates (SEM images in [Klonos15A]), and the significant intraparticle porosity [Sulim09]. Nevertheless, we may calculate the '*apparent*' interfacial layer thickness in our core–shell nanocomposites from the fraction of interfacial polymer, estimated above, and the specific surface area of the oxide sample before polymer adsorption, S_{BET}, determined by nitrogen adsorption–desorption measurements (Table 5.1). Assuming (i) constant density of PDMS in the interfacial layer and in bulk, equal to that of neat PDMS (ρ_{PDMS}=1.62 g/m^3 [Klonos10A]) and (ii) accessibility of the whole oxide surface area corresponding to S_{BET} to PDMS, we estimate the *apparent interfacial layer thickness*, d_{int}, by Eq. (5.1).

$$d_{\text{int}} = \frac{volume_{\text{int}erfacial,PDMS}}{surface_{\text{int}erfacial}} = \frac{mass_{sample} \cdot X_{PDMS} \cdot RAF_{\text{int}} / \rho_{PDMS}}{mass_{sample} \cdot (1 - X_{PDMS}) \cdot S_{BET}} \qquad (5.1)$$

Please note that because of assumption (ii) the calculated values represent a lower bound of the interfacial layer thickness. The results of d_{int} calculation are shown in Fig. 5.10c comparatively for modified (0.40 – 0.53 nm) / unmodified (1.00 nm) and annealed (0.28 – 0.66 nm) / not annealed (0.40 – 1.00 nm) samples. Thus, d_{int} decreases on surface modification by zirconia and on annealing. Absolute values of d_{int} in our core–shell nanocomposites (0.28 – 1.00 nm) are smaller than values obtained in conventional

PDMS/silica nanocomposites (~2 nm) (chapter 4 and [Fragiadakis07]) and also smaller than the *Kuhn segment length* for PDMS (~1.56 nm, Fig. 5.10c, [Gilra11]). Please compare [Gong14] with respect to the discussion of d_{int} in relation to *Kuhn segment length*. The relatively low absolute values can be probably understood in terms of assumption (ii) above. Results could be rationalized in future work by recording changes in density of the interfacial polymer, which has been found higher than that in bulk in previous work on polystyrene (PS) [Koga12,Vogiatzis11].

5.4.5.1. Effects of surface modification

The suppression of textural pore volume, V_p in Table 5.1, and of RAF_{int} (Fig. 5.10) with surface modification and, at the same time, of interfacial dynamics (Figs. 5.5 and 5.6) and cooperativity (Table 5.3) suggest strongly that, according to the model described above, the loops/tails ratio on A–380 is lower for modified samples (Scheme 5.1b). This assumption can be rationalized in terms of decreasing of the number of polymer–silica contact points due to the smoothening of interfacial areas [Sulim09], in general. Additionally, this decrease in contact–points concentration implies an increase of the cooperativity length ξ and, thus, in the frame of Adam–Gibbs theory [Adam65, Hodge97], slower and less cooperative segmental dynamics, in agreement with results for α_{int} in the present work. Similar effects were previously reported on the interfacial PDMS fraction in conventional nanocomposites, which was suppressed at the smoothed surfaces of titania (relatively low surface area, ~47 m^2/g), as compared to the rather diffused surfaces of silica (relatively high surface area, ~453 m^2/g) (details in Chapter 4).

5.4.5.2. Effects of thermal (crystallization) annealing

In the nanocomposites of both modified and unmodified A–380 which have suffered thermal annealing (a) α_{int} relaxation has immigrated towards higher temperatures / lower frequencies (Fig. 5.8a) and (b) $\Delta\varepsilon$ of α_{int} has been suppressed (Figs. 5.8b,5.9b). The changes are less pronounced for the samples of modified A–380, where α_{int} was already weaker and slower as compared to the unmodified A–380. Thus, the effects imposed by annealing seem to be in the same direction with those of surface modification, as far as interfacial dynamics and fraction is concerned. The changes can be interpreted, again, in terms of reorganization of chain distribution in the interfacial layer. More specifically, some of the chains could be detached during annealing, resulting in the restriction of concentration and mobility of the loops (Scheme 5.1c), which are probably more loosely attached onto the surfaces as compared to

the tails [Koga12, Rotella11]. Additional support to this explanation is given by (a) DSC in Table 5.2 (Fig. 5.10a) for A380P40, for which we follow increasing of $\Delta C_{p,n}$ (*MAF*) after annealing, without simultaneous increase in X_c (*CF*), and (b) DRS in Fig. 5.8 where we observed an increase of *S* relaxation, assigned to increase of the concentration of free (not engaged by the polymer) surface hydroxyls. Other models proposed for explaining the effects of annealing in these and similar systems involve the diffusion of free volume holes at the interfaces between polymer and nanoparticles [Colmenero13SM] or redistribution of interfacial free polymer volume [Napolitano12], and, also, possible changes in interfacial polymer density [Vogiatzis11].

5.5. Conclusions

Effects of surface modification and subsequent thermal treatment on the molecular dynamics in silica/PDMS nanocomposites of *core–shell* type were studied in this chapter. The strong hydrogen bonding developed between the surface hydroxyls of silica and the oxygens of the backbone of PDMS resulted to successive adsorption of the polymer, in particular to the formation of an interfacial polymer layer on the surfaces of the particles in the silica aggregates. The amount of interfacial polymer was estimated by both calorimetric and dielectric methods to employ quite high fraction of the whole polymer (up to 90 % at the low polymer loading of 40 wt% PDMS). This amount decreased for high polymer loadings, as expected. The interaction between particles and polymer was suppressed after the grafting of zirconia particles onto the surfaces of silica, by suppression of the surface available for polymer–filler interaction. The changes were reflected both in the thermal transitions (e.g. enhanced crystallization and glass transition) and the evolution of segmental dynamics, as recorded through specific dielectric relaxations.

DRS was found able to record the segmental dynamics of PDMS in the polymer–particle interfacial layer (α_{int} relaxation). Surface modification and thermal annealing were found to impose similar effects on interfacial dynamics, both resulting in a reduction of the number of polymer–particle contact points on the surfaces of silica. As a result, interfacial polymer fraction, dynamics and cooperativity were suppressed. Furthermore, changes in specific characteristics of the interfacial relaxation could be interpreted in terms of bimodal conformations (tail– and loop–like) of the adsorbed PDMS chains at interfaces, the concentration of which seems to decrease, especially that of loops, with the reduction of the number of contact points accessible to polymer on the modified surfaces. By employing a combination of DSC and DRS results we were able to monitor the additional lowering of

interfacial polymer density after thermal annealing (related also with enhanced crystallization) of the samples. This result suggests that the loop–like interfacial polymer conformations are more weakly attached than tail–like chains [Koga12]. In addition, the results obtained in the present work enabled to reconsider previous results on conventional PDMS/silica and PDMS/titania nanocomposites (chapter 4), now from a different perspective. Thus, we concluded that the reported shift of interfacial dynamics to lower frequencies/higher temperatures in the titania as compared to the silica nanocomposites may not originate exclusively from the higher strength of PDMS–titania hydrogen bonding (type of particle) [Klonos10A] or from the size of oxide particles [Gong14], but determined also by the concentration of contact points on the surfaces of aggregates / nanoparticles available for polymer adsorption, the latter being quantitatively well described by the surface roughness (S_{BET}) of the aggregates / particles.

The results presented and discussed in this chapter indicate that *core–shell* nanocomposites provide an alternative system for the investigation of molecular dynamics of polymer adsorbed onto a solid surface. With respect to dynamics, conformations and density of polymer in the interfacial layer, new challenging questions arose from the present study and will be further followed, partly in the next two chapters, by experiments on PDMS adsorbed at various amounts on fumed silica and silica–like (e.g. titania, zirconia) particles of a broad range of specific surface area (surface roughness).

6. Effects of surface modification on interfacial dynamics in *core–shell* NCs based on low specific surface area fumed silica and PDMS

6.1. Introduction

The present chapter focuses on the effects of surface and structure properties of silica nanoparticles (in the form of aggregates) on the characteristics of interfacial polymer in NCs of the *core–shell* type (although polymer in not grafted on silica), based on low specific surface area (~58 m^2/g) fumed silica (~15–100 nm in size for primary particles) and physically adsorbed linear PDMS. Before polymer adsorption, the initial silica particle surfaces were partly modified by the chemical development of amorphous zirconia nanoparticles (similar process of modification as for high surface area silica, A–380, in the previous Chapter). The porosity properties of initial and modified silica and silica/PDMS NCs were investigated using low temperature nitrogen adsorption/desorption and Incremental Pore Size Distribution (IPSD) analysis. The morphology was examined employing scanning electron microscopy (SEM), while phase transitions of PDMS in the NCs were studied using differential scanning calorimetry (DSC). Finally, PDMS segmental dynamics (dynamic glass transition) at interfaces and in bulk was studied using dielectric relaxation spectroscopy (DRS). Results are critically discussed and compared with similar results obtained with other *conventional* (Chapter 4) and *core–shell* (Chapter 5) PDMS–based NCs.

6.2. Materials and code names

Commercial fumed pyrogenic silica OX–50 (Degussa, ~15–100 nm in diameter, amorphous) was used as substrate, neat and modified with zirconia. Zirconium acetylacetonate (Aldrich,

>98% $Zr(acac)_4$) was used as a reactant to develop zirconia onto silica. The reactions and procedures of preparation have been previously discussed in detail [Sulim09]. Variation in the amount of grafted zirconia was provided by reiteration of all the reaction cycles from 1 to 4. The amorphous nature and content of zirconia (2.6 wt% and 8.4 wt% ZrO_2 for the 1st and 4th reaction cycles, respectively) were determined employing X–ray diffraction [Sulim09]. Specific surface area, $S_{BET,}$ for initial and modified oxides and NCs was measured using low temperature desorption of nitrogen, and values are given in Table 6.1. Polydimethylsiloxane (PDMS, Kremniypolymer, Zaporozhye, Ukraine, molecular weight $MW \approx 7960$, degree of polymerization d_p~105) was adsorbed onto dried oxide samples in the amounts of 40 and 80 wt%. Different amounts of a hexane solution of PDMS at a constant concentration (1 wt% PDMS) were added to fixed amount of dry silica–zirconia powder, up to the wanted polymer content. The suspension was mechanically stirred and finally dried at room temperature for 15–17 h and, subsequently, at 120 °C for 1.5 h. Low PDMS content (40 wt%) samples are powders similar to initial OX–50 powder, while at higher PDMS contents of 80 wt% and 100 wt% samples are liquid–like and liquid, respectively.

Seven polymer nanocomposite compositions were prepared and studied in the present work, the initial PDMS, silica/PDMS with 40 and 80 wt% PDMS and silica/zirconia/PDMS, containing modified silica with 1 and 4 cycles of zirconia, again with 40 and 80 wt% PDMS. The two degrees of zirconia modification enable to follow effects of zirconia fraction on porosity and interfacial characteristics. Based on previous work on similar systems (Chapter 5), two PDMS loadings have been selected, 40 wt% where interfacial effects dominate the behavior, and 80 wt% where bulk behavior dominates, similarly to conventional NCs. Throughout the text and in the figures and tables in this chapter, representative code names that describe the samples are used. For instance (i) *OX50Z1P80* corresponds to the sample in which PDMS at 80 wt% is adsorbed onto OX–50 that had previously suffered 1 cycle of zirconia reaction (2.6 wt% ZrO_2), (ii) *OX50Z4P40* corresponds to the sample in which PDMS at 40 wt% is adsorbed onto OX–50 that had previously suffered 4 cycles of zirconia reaction (8.4 wt% ZrO_2), and (iii) *OX50P80* corresponds to the sample in which PDMS at 80 wt% is adsorbed onto OX–50 that has not suffered any zirconia reaction (unmodified).

6.3. Results and discussion

6.3.1. Surface characterization (IPSD)

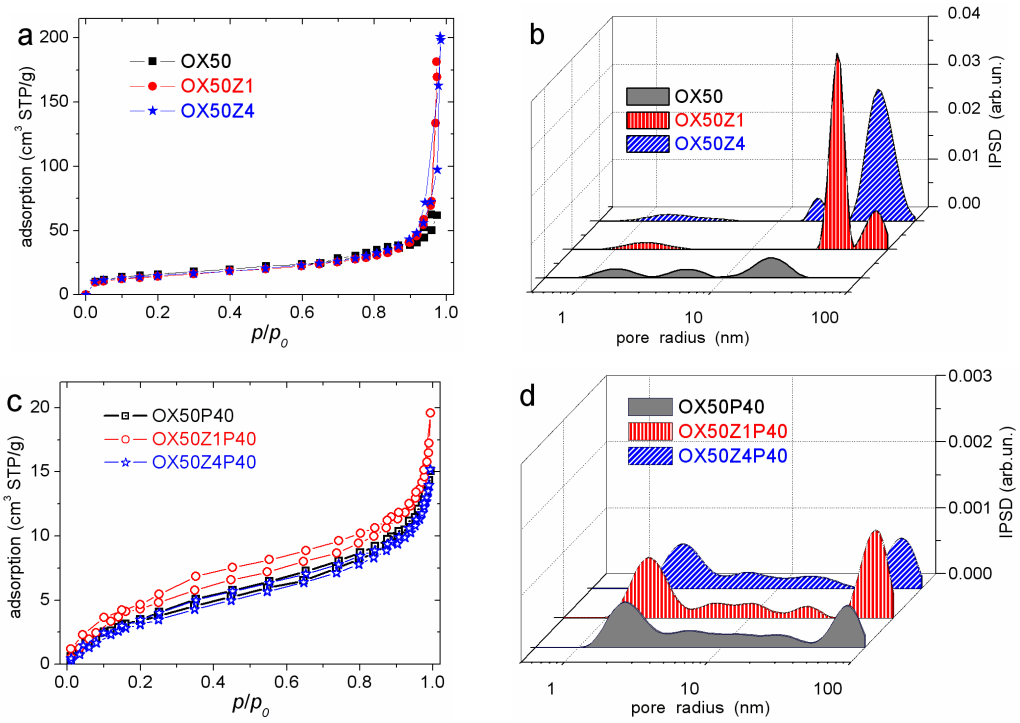

Fig. 6.1. Nitrogen adsorption–desorption isotherms (a,c) and incremental pore size distributions (b,d) of oxides before (a,b) and after adsorption of PDMS (c,d).

Nitrogen adsorption–desorption isotherms for neat oxides (OX–50, OX50Z1, OX50Z4) (Fig. 6.1, Table 6.1) and after adsorption of PDMS at 40 wt% (OX50P40, OX50Z1P40, OX50Z4P40) demonstrate sigmoidal–shaped behavior with narrow hysteresis loops of the H3 type (Fig. 6.1a,c) [Gregg82, Kruk01]. This behavior indicates the formation of aggregates with initially non–porous particles that are characterized by textural porosity. With respect to IUPAC classification of pores, the nitrogen adsorption–desorption isotherms correspond to type II [Gregg82]. The distributions of voids between particles in aggregates (Fig. 6.1b) show that the textural characteristics of OX–50 change after modification. Although the values of the specific surface area S_{BET} (58, 51 and 52 m^2/g for OX50, OX50Z1 and OX50Z4, respectively, Table 6.1) do not show significant changes with nanozirconia modification, the gas adsorption modes changed (Table 6.1), suggesting certain differences in meso– and macroporosity. Furthermore, the shape of the adsorption–desorption isotherms of the NCs (Fig. 6.1c) and the analysis of the results (Appendix A.6.1) suggest that nitrogen effectively fills mesopores in aggregates of initial OX–50 and mainly macropores of modified OX–50. We observe in Table 6.1 and Fig. 6.1b that the volume of mesopores (1 nm < R < 25 nm) of initial OX–50 (0.081 cm^3/g) decreases by a factor of 2–4 after zirconia modification. Macroporosity (25 nm < R < 100 nm), on the

contrary, increases by ~20 times for modified samples (OX50Z1 and OX50Z4). In general, the average pore radii (<R_V>, <R_S> in Table 6.1) are by 3–4 times larger in OX50Z1 and OX50Z4, as compared to unmodified OX–50.

Table 6.1

Textural characteristics of initial oxides and oxide/PDMS composites: Specific surface area in total, S_{BET}, of micropores, S_{micro}, mesopores, S_{meso}, macropores, S_{macro}, and respective specific pore volume, V_p, V_{micro}, V_{meso}, V_{macro}. R_V and R_S represent the average pore radii determined from the differential PSD with respect to pore volume and specific surface area, respectively.

Oxide	C_{ZrO2} (wt%)	S_{BET} (m^2/g)	S_{nano} (m^2/g)	S_{meso} (m^2/g)	S_{macro} (m^2/g)	V_p (cm^3/g)	V_{nano} (cm^3/g)	V_{meso} (cm^3/g)	V_{macro} (cm^3/g)	<R_V> (nm)	<R_S> (nm)
OX50	0	58	5	52	1	0.096	0.002	0.081	0.013	13.3	4.3
OX50P40	0	18	0	17	1	0.023	0.0	0.016	0.007	23.5	4.3
OX50Z1	2.6	51	5	31	15	0.280	0.002	0.019	0.259	45.4	14.1
OX50Z1P40	2.6	23	0	22	1	0.029	0.0	0.017	0.012	31.8	4.2
OX50Z4	8.4	52	7	33	12	0.311	0.003	0.046	0.262	48.7	14.1
OX50Z4P40	8.4	18	0	17	1	0.022	0.0	0.015	0.007	26.8	4.5

The textural characteristics of the oxides were modified on adsorption of PDMS (Table 6.1 and Fig. 6.1d). The value of S_{BET} decreases by 69 %, 55 % and 65 % (in comparison to the initial oxides) for OX50P40, OX50Z1P40 and OX50Z4P40, respectively, after PDMS adsorption in the amount of 40 wt% (Table 6.1). Polymer adsorption leads to suppression of pore volume (V_p) as well as of V_{meso} and V_{macro}. The decrease is systematically stronger for OX50Z4P40 as compared to OX50Z1P40. After addition of PDMS, the average pore radii (Table 6.1, <R_V> and <R_S>) decrease sharply. The adsorbed macromolecules can merge both the oxide nanoparticles and their aggregates into more compact structures, leading to decrease in the volume of voids between particles. This is a general effect in polymer/nanooxide composites [Gunko13B].

6.3.2. Morphology (SEM)

Figure 6.2 shows SEM images of the aggregates of OX–50 dispersed in OX50P80. One can clearly observe in Fig. 6.2a bunch–like structures varying between 250 nm and 1.5 μm in size. At higher magnification for the same sample in Fig. 6.2b the initial particles of OX–50 (~15–100 nm in diameter) structuring the larger aggregates can be recognized. Similar images were obtained for the zirconia modified nanocomposite samples. Micrographs of the developed zirconia nanoparticles onto the surfaces of silica have been shown in a previous study on initial oxides [Sulim09].

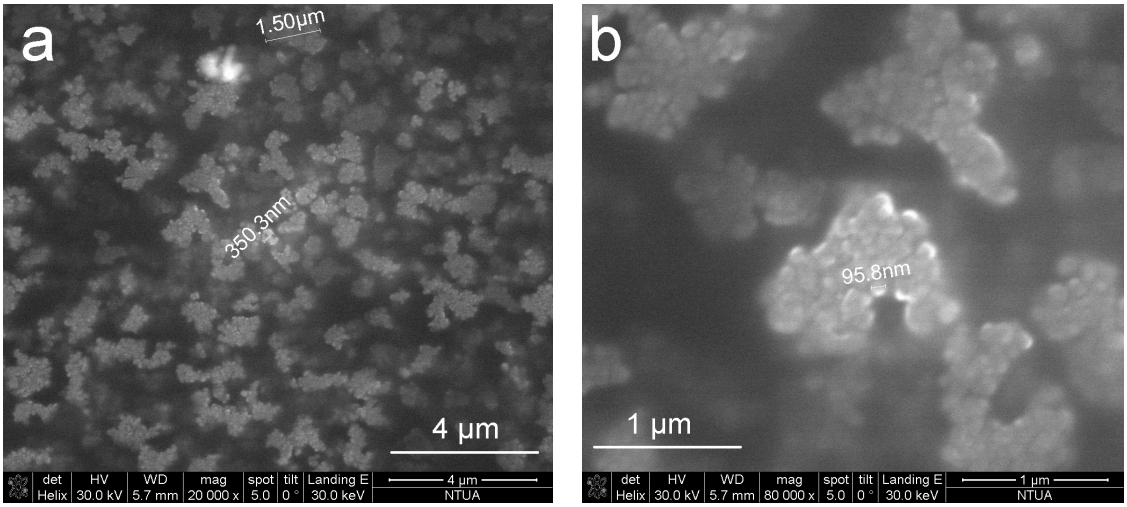

Fig. 6.2. SEM micrographs of OX50P80 composite.

6.3.3. Thermal transitions (DSC)

6.3.3.1. Polymer crystallization

During cooling of OX–50/PDMS core–shell based NCs in DSC at 10 K/min from 20 ^{o}C to –170 ^{o}C single crystallization peaks were observed between –95 and –76 ^{o}C for all samples (Table 6.2, Fig. 6.3a,b). During the subsequent heating in Fig. 6.3c,d the endothermic step of glass transition (–129 to –123 ^{o}C, Table 6.2) and cold crystallization exothermic peaks (–110 to –90 ^{o}C) are observed for neat PDMS and NCs with 80 wt% PDMS. Finally, complex endothermic peaks during melting of PDMS were recorded for all samples between –55 and –35 ^{o}C (Table 6.2, Fig. 6.3c,d). The measured and calculated quantities of interest are shown in Table 6.2.

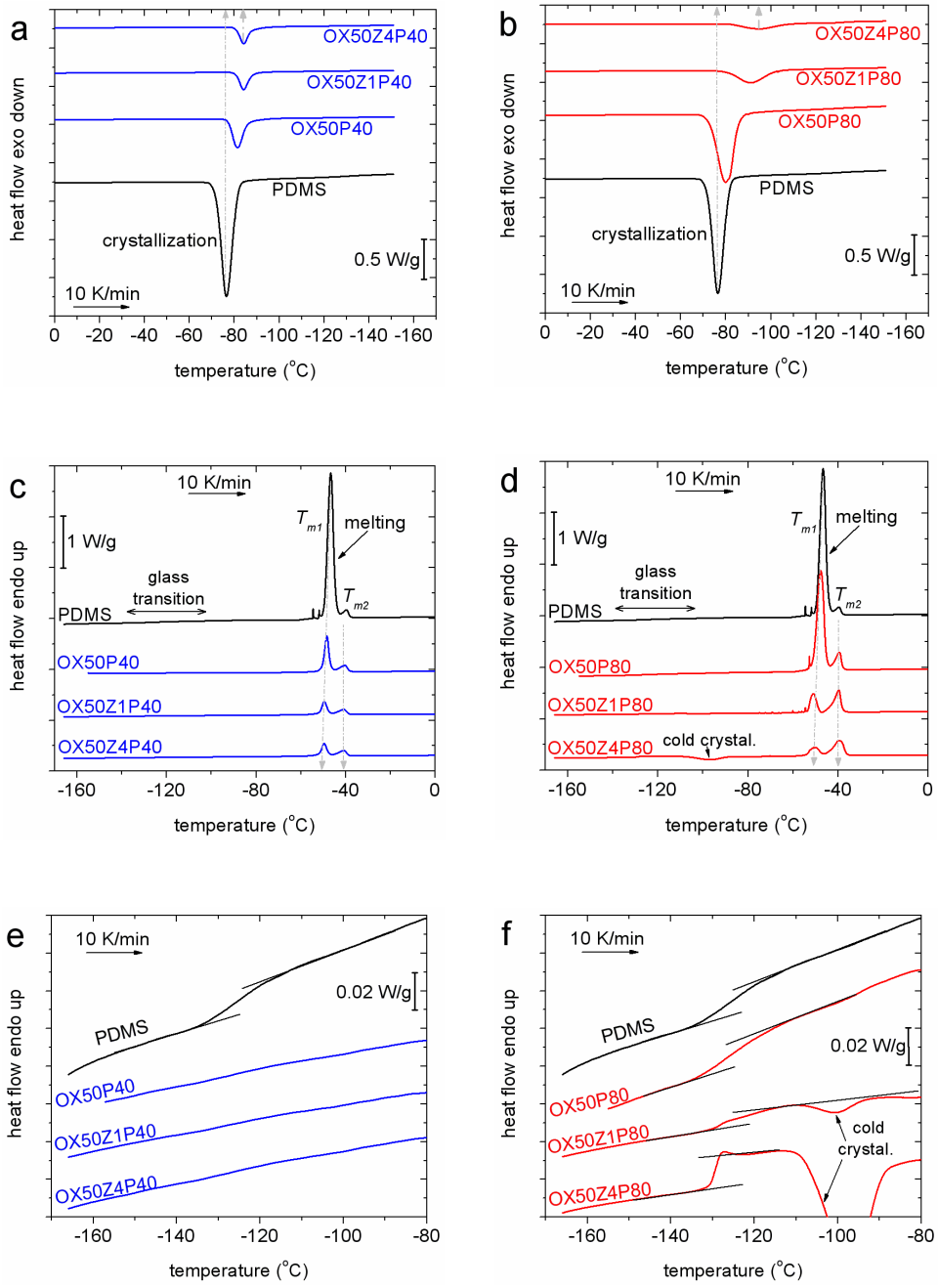

Fig. 6.3. Comparative DSC thermograms of OX–50/PDMS, OX–50/Z1/PDMS, OX–50/Z4/PDMS and neat PDMS during (a,b) cooling and (c,d) subsequent heating at 10 °C/min. Details in the glass transition region during heating are shown in (e,f). (a,c,e) Correspond to samples with 40 wt% PDMS, while (b,d,f) correspond to samples with 80 wt% PDMS. Indicated are the main thermal events, i.e. crystallization, glass transition, cold crystallization and melting. The lines in (e,f) represent the baselines of the thermograms before and after glass transition.

Table 6.2

Quantities of interest from DSC measurements: crystallization temperature, T_c, degree of crystallinity, X_c, glass transition temperature, T_g, normalized heat capacity step at glass transition, $\Delta C_{p,n}$, interfacial and amorphous polymer fraction (at T_g), RAF_{DSC} and MAF_{DSC}, respectively, temperature maxima of melting peaks, $T_{m1,2}$.

sample	T_c (°C) (±0.2)	X_c (wt) (±5 %)	T_g (°C) (±0.5)	$\Delta C_{p,n}$ (J/gK) (±0.02)	RAF_{DSC} (wt) (±10%)	MAF_{DSC} (wt) (±10%)	T_{m1} (°C) (±0.2)	T_{m2} (°C) (±0.2)
OX50P40	–81	0.53	–	0.00	0.47	0.00	–48	–40
OX50Z1P40	–84	0.46	–	0.00	0.54	0.00	–48	–41
OX50Z4P40	–84	0.46	–	0.00	0.54	0.00	–48	–41
OX50P80	–80	0.57	–126	0.15	0.23	0.20	–48	–40
OX50Z1P80	–92	0.46	–123	0.03	0.49	0.05	–51	–40
OX50Z4P80	–95	0.23	–129	0.04	0.68	0.09	–50	–39
PDMS	–76	0.65	–127	0.22	0.12	0.23	–47	–40

Neat PDMS crystallizes at –76 °C and X_c is 0.65 wt (Table 6.2). Both crystallization temperature, T_c, and degree of crystallinity, X_c, are suppressed in all OX–50/PDMS samples. Suppression gets stronger with zirconia modification for both polymer loadings (Table 6.2). Crystallization during cooling at 10 K/min is very weak for OX50Z1P80 and OX50Z4P80 (Table 6.2), thus PDMS in these samples crystallizes partially during heating (cold crystallization [Gedde95], Fig. 6.3f). The results suggest that silica particles do not act as crystallization nuclei [Gedde95]). Results similar to those presented here have been obtained in previous work on silica/PDMS NCs [Aranguren98, Klonos11, Sulym14], as well as on polymers confined between solid surfaces [Vanroy13].

At higher temperatures, complex endothermic melting peaks are observed between –51 and –39 °C (T_{m1}, T_{m2} in Table 6.2). The temperature difference between these two peaks varies between 7 and 11 K (Table 6.2). T_{m1} is lower in the case of NCs as compared to neat PDMS, suggesting lower density (worse lamellae packing [Gedde95, Dobbertin96, Aranguren98]) of PDMS spherulites in OX–50/PDMS core–shell NCs. Complex and double melting peaks have been observed before in PDMS systems [Aranguren98, Klonos10A], probably related also with events of recrystallization and subsequent melting of metastable crystals [Aranguren98, Klonos12, Gedde95]. Thus, X_c was not estimated from the melting enthalpy in the present work.

6.3.3.2. Polymer glass transition

Coming now to glass transition (Fig. 6.3e,f), the corresponding exothermic step was recorded during heating for the high polymer content samples (i.e. 80 wt%) and initial PDMS (Fig. 6.3f). The glass transition step is absent (or extremely weak) for samples of 40 wt% PDMS (Fig. 6.3e). The characteristic temperature T_g, determined as the midpoint of the heat capacity step at glass transition, is –127 °C in neat PDMS and varies in the NCs between –123 (OX50Z1P80) and –129 °C (OX50Z4P80) (Table 6.2). T_g and the change in heat capacity, $\Delta C_{p,n}$, are ruled by spatial and physical constraints imposed by, both, the presence of oxide nanoparticles (strong interfacial interactions) and condensed polymer crystal regions [Klonos10A, Klonos15A]. Thus, T_g should increase in the NCs, as compared to neat PDMS, due to PDMS–silica interactions and decrease due to lowering of crystallinity X_c (Table 6.2). The results in Table 6.2, in particular the decrease of T_g in OX50Z4P80, suggest that changes in crystallinity dominate over the effects of PDMS–silica interactions.

In addition to T_g, the temperature range of glass transition, T_{onset}–T_{end}, is worth discussing. In previous works [Klonos12, Klonos10A] we have demonstrated the close dependence of T_{onset}–T_{end} on the degree of crystallinity X_c of PDMS. Looking now at Fig. 6.3f, we suggest that the smooth shaped glass transition steps (large T_{onset}–T_{end}) for initial PDMS and OX50P80 with higher T_g values correspond to highly crystallized polymer. The sharp shaped glass transition (small T_{onset}–T_{end}) of OX50Z4P80 with lower T_g, on the other hand, corresponds to a sample of highly suppressed degree of crystallinity (Table 6.2). It is interesting to focus on the dual–structured glass transition for OX50Z1P80 (Fig. 6.3f), which demonstrates the presence of both behaviors in the same sample (one dominated by the unaffected amorphous part of the polymer and the second by the amorphous polymer constrained between spherulites [Klonos10A, Yu09, Papageorgiou14]). This result will be confirmed later by DRS.

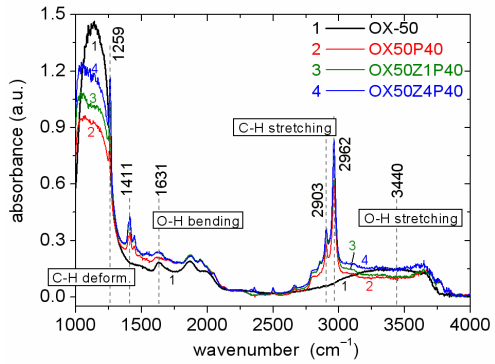

Fig. 6.4. FTIR spectra of initial OX–50, OX50P40, OX50Z1P40 and OX50Z4P40.

We recall at this point that the physical adsorption of PDMS onto silica is accompanied by the formation of hydrogen bonds between surface hydroxyls and the O atoms of the PDMS backbone [Gunko13, Bokobza10]. The intensity of FTIR spectra (Fig. 6.4) in the region of O–H vibrations decreases with polymer adsorption (details in Appendix A.6.2), the decrease being stronger in the NCs of modified oxides. The decrease suggests that a significant amount of free surface hydroxyls [Gunko13] are disturbed by PDMS chains. The disturbance is stronger for the zirconia modified oxides, suggesting that the number of contact points between silica and polymer chains increases with zirconia. Further support for that will be provided in the following DSC and DRS results.

The above discussion suggests that the particles–polymer interactions should be responsible for the formation of a rigid amorphous polymer fraction [Wurm10] in the interfacial layer, similarly to previous works in PDMS [Fragiadakis07, Klonos10A, Klonos15A]. We proceed now with calculation of the various polymer fractions using Eqs. (3.4,3.5) (Section 3.2).

The calculated values are listed in Table 6.2. RAF_{DSC} varies between 0.47 and 0.54 wt for the samples of low polymer loading and between 0.23 and 0.68 wt for the samples of high polymer loading. For neat PDMS, the respective value is 0.12 wt and it corresponds to $RAF_{cryst,DSC}$, while CF is 0.65 wt. Considering that X_c is in general lower for the NCs with modified oxides for both polymer loadings while, at the same time, RAF_{DSC} is higher (changes are systematic for 80 wt% PDMS), we conclude that the increase on RAF_{DSC} originates from an increase of $RAF_{int,DSC}$.

In agreement with the values of V_p in Table 6.1, the increase of $RAF_{int,DSC}$ reflects the increasing of accessible volume for polymer chains in the macro–pores. According to DSC results (and DRS later) the calculated V_p distributions (Table 6.1) seem to describe better the adsorption of PDMS chains in the voids of OX–50 aggregates, rather than S_{BET}. Finally, by comparing the DSC results for the different surface modification of OX–50, we can follow in Table 6.2 that with increase of zirconia content (from 0 to 2.6, and to 8.4 wt%, Table 6.1) polymer adsorption is enhanced (RAF_{DSC} increases) at the expenses of bulk mobility and crystallization (the sum $MAF + X_c$ decreases in Table 6.2).

6.3.4. Segmental dynamics (DRS)

DRS results are comparatively presented in the form of frequency dependence of the imaginary part of dielectric permittivity (dielectric loss), ε'' (Fig. 6.5, isothermal plots) for two selected temperatures. We focus again on segmental dynamics, i.e. on the dielectric

relaxations α, α_c and α_{int} [Klonos10A, Klonos15A] corresponding to the calorimetric glass transition in Figs. 6.3e,f. The origin of these relaxations (see below) has been described in our previous works on PDMS systems [Fragiadakis07, Klonos10A, Klonos15A].

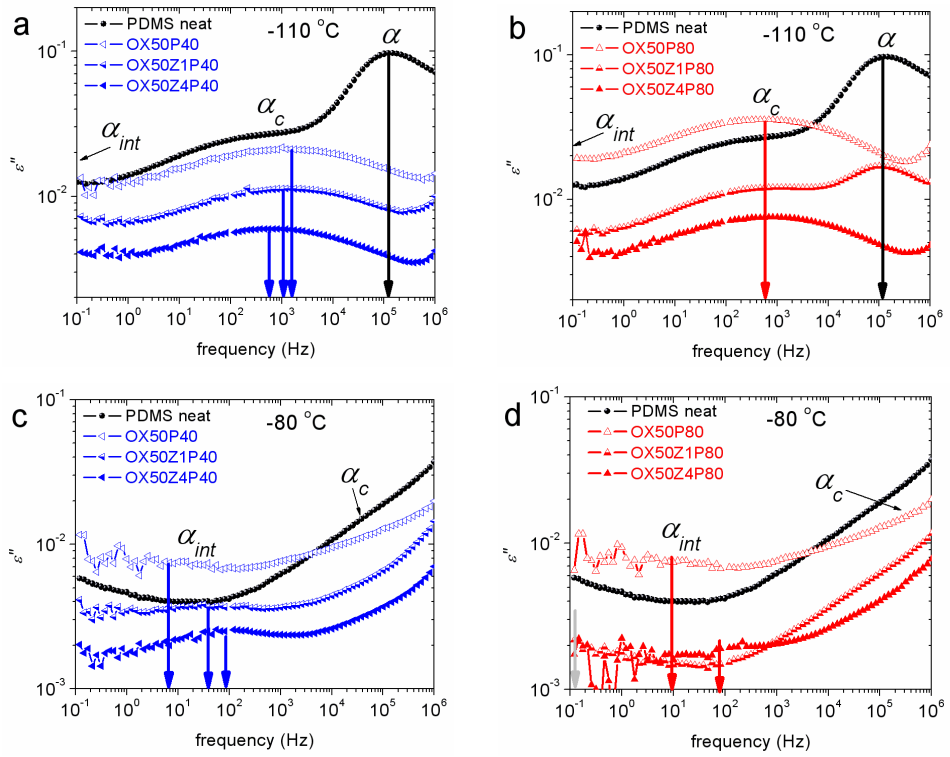

Fig. 6.5. Isothermal DRS plots of the imaginary part of dielectric permittivity (dielectric loss), ε'', vs frequency for PDMS and for composites with (a,c) 40 wt% adsorbed PDMS and (b,d) 80 wt% PDMS, at –110 °C (a,b) and –80 °C (c,d). The arrows mark the frequency of ε'' maximum for each relaxation.

6.3.4.1. Raw data and analysis

In Figs. 6.5a,b α relaxation at around 10^5 Hz at –110 °C is associated with the glass transition of the bulk amorphous unaffected polymer fraction [Klonos10A, Klonos12, Klonos15A]. This relaxation corresponds to the lower temperature sharp–shaped glass transition step in DSC for the amorphous part of the polymer (Fig. 6.3f). Next to α, at around 10^3 Hz at –110 °C in Figs. 6.5a,b, α_c relaxation originates from polymer chains restricted either between condensed crystal regions [Klonos10A, Yu09, Papageorgiou14] (which is the case of neat and 80 wt% PDMS, Fig. 6.5b) or in the voids between nanoparticles in their aggregates (which is the case of core–shell NCs at low polymer loading, Fig. 6.5a) [Klonos15A]. Finally, α_{int} relaxation in the broad range from $5{\cdot}10^0$ to 10^2 Hz at –80 °C (Figs. 6.5c,d) represents the dynamics of semi–bound polymer chains in the interfacial layer, with strongly reduced mobility due to interactions with the surface hydroxyls of OX–50 [Fragiadakis07, Klonos10A, Klonos15A].

DRS results were analyzed in terms of Havriliak-Negami equation (Eq. (3.6), details in Section 3.4) and values of the fitting parameters for the shape of the relaxations (mean values over the temperature range of measurements) are listed in Table 6.3. By plotting the frequency of maximum of ε'' from Eq. (3.6) against reciprocal temperature for the three segmental relaxations, the Arrhenius plot of Fig. 6.6a was constructed. Included in the Arrhenius plots of Fig. 6.6a are the respective peak temperatures at the equivalent frequencies of DSC and TSDC [Klonos15A] (i.e. 20 mHz and 1.6 mHz, respectively [Fragiadakis07]). TSDC (Thermally Stimulated Depolarization Currents, Section 3.3) is a special dielectric technique in the temperature domain which was employed here to determine peak temperatures at the equivalent frequency of the technique. The Vogel–Tammann–Fulcher–Hesse (*VTFH*) equation (Eq. (3.7), [VTFH]), characteristic of cooperative processes [Richert98] has been fitted to the data of Fig. 6.6a (lines) and the fragility index m was determined (Table 6.3). We recall that m is a measure of cooperativity (deviation from linear behavior) [Klonos15A, Richert98]. VTFH could not be fitted to the data for α_{int} in OX50P40 and OX50P80, which are described by the Arrhenius equation (Eq. (3.11) [Arrhenius1889], straight lines in Fig. 6.6a). Finally, we present in Fig. 6.6b the reciprocal temperature dependence of $\Delta\varepsilon$ from Eq. (3.6) for the relaxations of all measured samples.

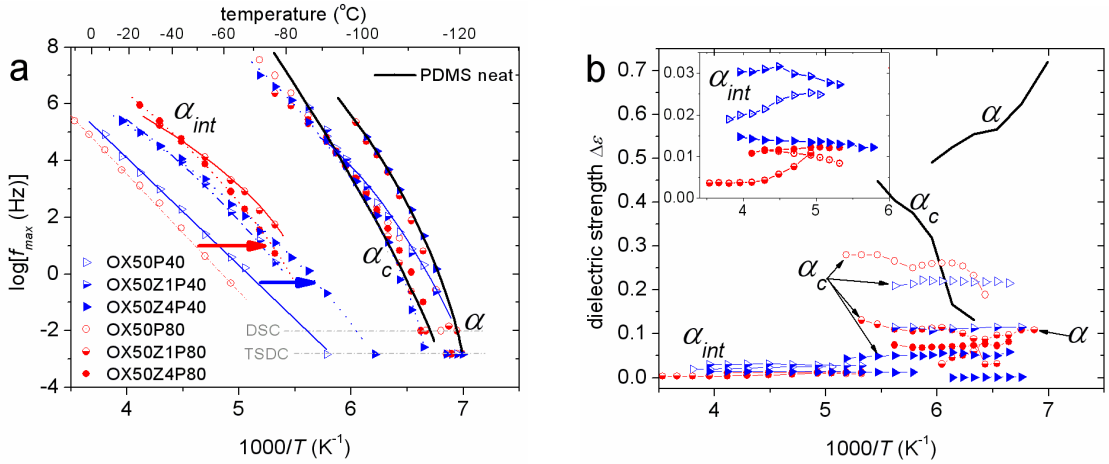

Fig. 6.6. (a) Arrhenius plots and (b) dielectric strength vs reciprocal temperature of the segmental relaxations: bulk polymer (α), restricted in voids and crystal regions (α_c) and interfacial polymer (α_{int}) for OX–50/Zr/PDMS composites and neat PDMS. The blue triangles correspond to 40 wt% adsorbed PDMS, while the red cycles correspond to 80 wt% adsorbed PDMS. Included in (a) are the respective DSC and TSDC points. The lines in (a) are fittings of the VTFH and Arrhenius equations Eqs. (3.7,3.11) to the data for the recorded relaxations. The inset in (b) shows in more detail the region of α_{int} relaxation. The arrows in (a) mark changes on α_{int} between unmodified and modified of OX–50.

Table 6.3

Values of interest from DRS results: Shape parameters, α_{HN} and β_{HN}, and fragility index, m, for the recorded dielectric relaxations, interfacial polymer fraction, $RAF_{int,DRS}$, and mobile amorphous fraction, MAF_{DRS}, at ~ –95 ^{o}C. (*) corresponds to relaxations which do not obey VTFH equation.

Process parameter / *sample*	α			α_c			α_{int}			$RAF_{int,DRS}$ (vt)	MAF_{DRS} (vt)
	α_{HN}	β_{HN}	m	α_{HN}	β_{HN}	m	α_{HN}	β_{HN}	m		
OX50P40	–	–	–	0.23	1.0	72	0.47	1.0	*	0.05	0.42
OX50Z1P40	–	–	–	0.25	1.0	80	0.30	1.0	30	0.10	0.44
OX50Z4P40	–	–	–	0.29	1.0	96	0.40	1.0	35	0.10	0.44
OX50P80	–	–	–	0.31	1.0	88	0.49	1.0	*	0.01	0.42
OX50Z1P80	0.60	0.8	115	0.30	1.0	87	0.30	1.0	34	0.04	0.50
OX50Z4P80	–	–	–	0.27	1.0	82	0.30	1.0	49	0.11	0.67
PDMS	0.35	0.9	106	0.30	1.0	96	–	–	–	0.00	0.25

6.3.4.2. Bulk dynamics (α and α_c relaxations)

We discuss separately bulk dynamics (α and α_c relaxations) in this section and interfacial dynamics (α_{int}) in the next section. The dual character of α_c relaxation (characterized by shape parameters α_{HN}~0.25, β_{HN}=1, mean values over the temperature range of the relaxation), concerning the type of spatial restriction of PDMS chains (between PDMS crystals [Klonos10A, Yu09] and in voids of OX–50 aggregates), is better revealed by dividing the discussion into low (40 wt%) and higher polymer contents (80–100 wt%). For the low PDMS content, α_c originates from the reduced segmental mobility of PDMS chains inside the voids in the layers above the interfacial layer. In Fig. 6.5a and Figs. 6.6a,b we follow that in theses samples time–scale and strength of α_c are suppressed with zirconia. This result is consistent with the simultaneous increase of the interfacial layer in the voids of OX–50 (Table 6.2), which increases the constraints imposed on polymer bulk–like mobility. Recalling DSC results, it is worth to point out the absence of glass transition for the 40 wt% PDMS NCs (Fig. 6.3e). On the other hand, owing to the higher resolving power of DRS, both the interfacial (α_{int} in Fig. 6.5c) and the bulk–like segmental dynamics (α_c in Fig. 6.5a) are recorded by DRS in these NCs.

For the high polymer loading α_c relaxation seems to dominate the segmental response of PDMS in Fig. 6.5b. In addition, the frequency–temperature position of α_c in Fig. 6.6a is almost identical for these samples, contrary to α_c for low polymer loading which slows down with nanozirconia modification. We recall that the DSC results for 80 wt% PDMS samples

and neat PDMS (Fig. 6.3) show crystallization events (either at cooling or at heating, at 10 K/min). Considering that during DRS measurements the samples stay at each temperature of measurements for about 10 minutes (isothermals), this procedure of measurements could be considered as a type of multi–temperature crystallization annealing, which leads to increased degree of crystallinity, most probably higher than in DSC measurements. That is the reason for the same pattern of α_c relaxation in neat PDMS and the composites of 80 wt% PDMS (Fig. 6.5b), despite different degrees of crystallinity by DSC (Table 6.2). Please note also that α_c and α were simultaneously recorded at –110 ^{o}C (Fig. 6.5b) for OX50Z1P80, similarly to the dual structured glass transition recorded by DSC (Fig. 6.3f).

Bulk unaffected PDMS mobility is recorded via α relaxation only for two samples (Fig. 6.5b), namely the initial PDMS (α_{HN}~0.35, β_{HN}=0.9) and OX50Z1P80 (α_{HN}~0.60, β_{HN}=0.8) (Table 6.3). The absence of unaffected polymer mobility (bulk) in the majority of the NCs reveals the high degree of constraints imposed on polymer mobility in these highly complex systems.

6.3.4.3. Interfacial dynamics (α_{int} relaxation)

The relaxation process of PDMS in the interfacial layer (α_{int}, characterized by mean values of the shape parameters over the temperature range of the relaxation α_{HN}~0.30 – 0.49, β_{HN}=1) on the surfaces of OX–50 (inner walls in the voids and external walls of the aggregates) is the slowest of the three segmental relaxations. We should remind, at this point, that the assignment of this process to PDMS in the interfacial layer is supported by the following observations are: (i) α_{int} is absent in neat PDMS, (ii) its time–scale trace extrapolated to the respective DSC equivalent frequency (~10^{-2} Hz [Fragiadakis07]) approaches the region of T_g, and (iii) its $f_{max}(T)$ dependence is, in general, of the VTFH type [Klonos10A, Klonos15A] revealing its cooperative character. Similar results have been obtained recently by employing DRS in NCs of various polymers [Fragiadakis11, Fullbrant13, Holt14].

For both polymer loadings in Fig. 6.6a α_{int} is slower for unmodified OX–50 than for zirconia modified samples. As surface modification increases (zirconia content increases from 0 to 2.6, and 8.4 wt%, Table 6.1) α_{int} immigrates towards higher frequencies / lower temperatures and its cooperativity increases (increased m, Table 6.3), suggesting gradual enhancing of polymer dynamics at the OX–50/PDMS interface. At the same time, $\Delta\varepsilon$ for α_{int} in Fig. 6.6b exhibits higher values for the lower PDMS loading NCs, whereas changes with degree of modification are non–systematic. The same is true for the real part of dielectric permittivity, ε', (Fig. 6.7) and AC conductivity, σ_{AC} (not shown), which are, however, higher

than additivity values [Kramarenko05]. These results can be rationalized in terms of increased orientational polarization in the interfacial layer (inset schemes to Fig. 6.7), at the lower PDMS content (to be further discussed below), in agreement with results reported recently for similar systems [Klonos15A].

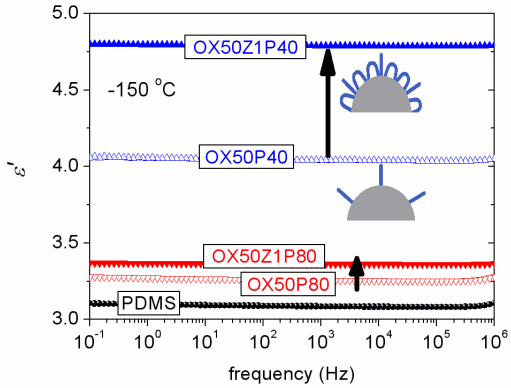

Fig. 6.7. Selected results of the real part of dielectric permittivity, ε', against frequency at –150 °C. The inset schemes show simplified models for the conformations of interfacial polymer chains adsorbed on the surface of unmodified and modified silica. The arrows mark changes imposed by zirconia modification in the nanocomposites.

The fraction of polymer in the interfacial layer (the reduced mobility polymer fraction) $RAF_{int,DRS}$ was calculated employing Eq. (3.10) (Section 3.4). Bearing in mind that the dielectric strength changes with temperature, we employed DRS results at a temperature (–95 °C) where all relaxations were simultaneously recorded. Similar to RAF_{DSC} (Table 6.2), $RAF_{int,DRS}$ calculated by DRS increases systematically with surface modification of OX–50. We recall that, in addition to $RAF_{int,DRS}$ increase (Fig. 6.8a), the dynamics at the interface is also accelerated (Fig. 6.6a). We suggest that the increase of the concentration contact points at the interfaces accessible to PDMS is at the origin of both these results (inset to Fig. 6.8a).

The insets to Fig. 6.8a show the simplified model employed for the interpretation of our results. According to this model and previous experimental findings obtained with silica/PDMS core–shell systems with high surface area fumed silica (previous Chapter), it is suggested that adsorption of PDMS proceeds via two chain conformations, which can be considered responsible for the molecular mobility recorded by DRS as interfacial α_{int} relaxation process: (a) extended tails forming the outer region, with bulk–like density but reduced mobility and (b) flattened chain segments which form the inner quite dense region due to multiple contact points (loops) with the silica surface [Koga12]. It has been also suggested that for low polymer contents the tails are mobile enough to cooperate with each

other, but being sparsely distributed on the surfaces of the nanoparticles their cooperativity length (ξ) [Richert98] is relatively large. The extended (orientated) tails imply high polarizability and, this way, increase ε', ε'' and $\Delta\varepsilon$, in agreement with experimental results obtained with PDMS adsorbed on high surface area silica (Chapter 5 and [Klonos15A]). Similar results have been obtained here for the 40 wt% PDMS systems. In addition, surface modification of OX–50 by zirconia in the present work leads to increased number of contact points and, therefore, more dense interfacial layer. This implies reduction of the cooperativity length ξ and, thus, in the frame of Adam–Gibbs theory [Adam65, Hodge97], faster and more cooperative segmental dynamics, in agreement with results for α_{int} in the present work (Fig. 6.6a, Table 6.3). The additional polymer chains that connect to the additional contact points (in agreement to FTIR, discussion in section 6.3.3.2) can form both extra tails and loops. This implies serious obstacles to the orientation of the tails, resulting in reduction of dielectric response ($\Delta\varepsilon$ and ε', *in* Fig. 6.6b and Fig. 6.7, respectively).

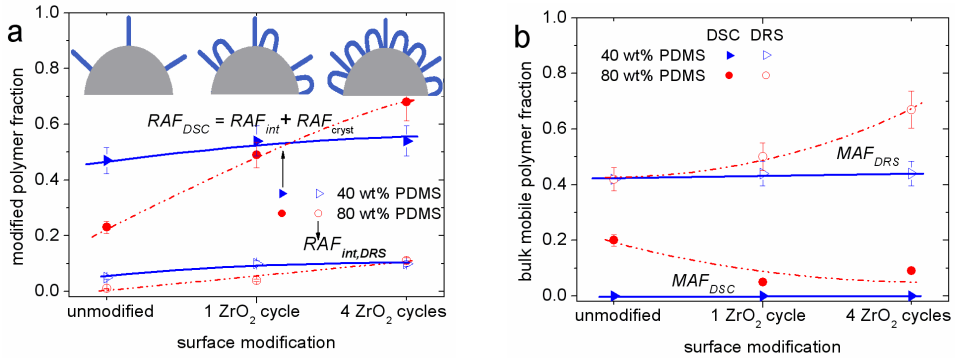

Fig. 6.8. Estimated (a) modified polymer fractions (RAF_{DSC}, $RAF_{int,DRS}$), and (b) bulk mobile amorphous polymer fraction, *MAF*, against the amount of surface modification of initial OX–50 particles with nanozirconia, for systems loaded with 40 wt% PDMS (blue triangles) and 80 wt% PDMS (red cycles). Results for RAF_{DSC} are shown comparatively at T_g (solid symbols) and for $RAF_{int,DRS}$ at –95 °C (empty symbols) (details in text). The lines are used as guides to the eyes. The insets to (a) show simplified models for the conformations of polymer chains during the first stages of adsorption on the surface of silica at 40 wt% PDMS loading for the different surface modifications of OX–50.

So far the discussion was limited to the 40 wt% PDMS NCs. $RAF_{int,DRS}$ for samples of 80 wt% adsorbed PDMS are again in close qualitative agreement with DSC (Fig. 6.8a). Also, interfacial dynamics accelerates systematically with zirconia in Fig. 6.6a. In addition, *MAF* follows opposite trends with zirconia modification for DSC and DRS in Fig. 6.8b for the high PDMS loading, while *MAF* for the low polymer loading is almost constant for both DSC and DRS. These results reflect, on the one hand, the suppression of interfacial polarizability at

high polymer loading (ε' in Fig. 6.7) and, on the other hand, the significance of the degree of crystallinity in the determination of MAF ($MAF = 1 - X_c - RAF$). Kumar and coworkers pointed to the primary role of crystallization in semicrystalline PNCs, affecting also filler distribution and aggregation [Khan09].

Increased orientational polarizability in the interfacial layer as compared to bulk is also at the origin of differences in the absolute values of $RAF_{int,DRS}$ and RAF_{DSC} and in their dependence on surface modification in Fig. 6.8a. It is interesting to note in this connection the significantly lower dielectric response of the NCs of the present study, as compared to similar NCs based on high surface area silica in a previous study [Klonos15A]. Please note also that the two procedures of determining RAF_{int}, based on different experimental methods, are different in principle [Eslami13]. So, as mentioned previously, $RAF_{int,DRS}$ was determined through the contribution of interfacial polymer fraction to total polarization (Eq. (3.10)), while RAF_{DSC} (Eq. (3.5)) through the missing of the corresponding contribution to the heat capacity jump at the glass transition.

In Fig. 6.9 we compare time scale of interfacial dynamics in the present and in previous works in (a) conventional PDMS/silica and PDMS/titania NCs (Chapter 4), i.e. spherical nanoparticles *in situ* generated and dispersed in a matrix of crosslinked PDMS [Fragiadakis07, Klonos10A], and (b) in core–shell systems based on high specific surface area silica and linear PDMS [Klonos15A].

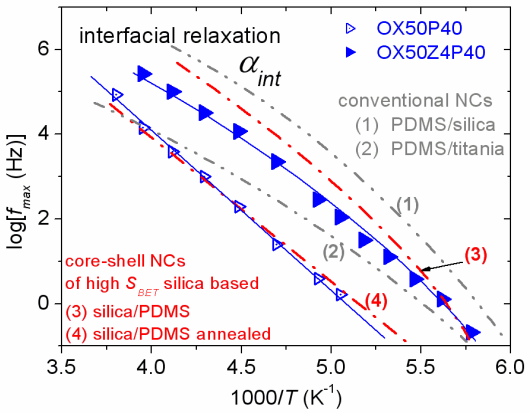

Fig. 6.9. Comparative Arrhenius plots of interfacial dynamics (α_{int}) in core–shell and conventional oxide/PDMS nanocomposites. Open and solid triangles correspond to OX50P40 and OX50Z4P40 core–shell systems, respectively (present work). Lines (1) and (2) correspond to the interfacial relaxation in conventional (sol–gel) PDMS/silica and PDMS/titania nanocomposites, respectively [Klonos10A]. Line (3) corresponds to core–shell system based on fumed silica of high surface area (A380, S_{BET}~342 m^2/g) on which 40 wt% of PDMS has been adsorbed [Klonos15A]. Line (4) corresponds to the interfacial relaxation of the same system after thermal (crystallization) annealing [Klonos15A].

The traces of the recorded α_{int} in the present study (Fig. 6.9) are, in general, similar to those of *conventional* (Chapter 4 [Klonos10A]) and core–shell based (Chapter 5 [Klonos15A]) silica/PDMS from previous work. Differences for different types of filler, i.e. slower for conventional titania/PDMS than for silica/PDMS, grey dash–dotted lines (2) and (1), respectively, in Fig. 6.9 and [Klonos10A], have been previously ascribed to stronger hydrogen bonding between PDMS and the –OH of titania [Bokobza10] as compared to silica [Klonos10A, Klonos11]. Evidence against this interpretation was provided in the previous Chapter, by the study of PDMS adsorbed on fumed silica and silica gel (with high S_{BET} for both) [Klonos15A], where the traces of α_{int} in the Arrhenius plot at 40 wt% and 80 wt% polymer loadings were found to coincide with those of titania/PDMS and silica/PDMS [Klonos10A], respectively. Moreover, thermal annealing of the systems at the temperature of PDMS crystallization was found to suppress significantly both dynamics and strength of α_{int} relaxation, especially in the case where PDMS crystallization was absent (i.e. for NCs with 40 wt% PDMS, red dotted lines (3) and (4) in Fig. 6.9).

Combining all the above observations we suggest that the strength of polymer–particle hydrogen bond is not the main factor dominating interfacial dynamics. Similar to results in high specific surface area silica in previous chapter, we gain here additional support that interfacial dynamics is mainly ruled by: (a) the number and accessibility of contact points (surface properties of the particles) and (b) structure and flexibility of polymer chain (polymer topology at the interfaces). Additionally, our results could be, again, explained by employing models proposed previously involving different conformations of polymers adsorbed onto a solid surface [Koga12, Rotella11, Kritikos13].

6.4. Conclusions

Structure, porosity and interfacial characteristics of low specific surface area (S_{BET}~58 m^2/g) fumed silica nanoparticles (~15–100 nm in average diameter), partly modified via nanozirconia grafting, along with polymer organization during polymer adsorption and preparation of core–shell based nanocomposites (NCs), were in the center of interest for this study. To that aim adsorption–desorption nitrogen isotherms, morphology (SEM), thermal (DSC) and dielectric (DRS) techniques were employed. From the fundamental point of view, this work provides additional evidence that the *core–shell* type NCs present an alternative model system for the investigation of interfacial dynamics: by controlling polymer content,

the recorded DSC and DRS responses may be dominated by the interfacial polymer layer, being the majority among other polymer fractions.

Amorphous silica nanoparticles were found to aggregate with each other in the 10^2 nm scale, forming interparticle voids of the meso (1 nm < R_{void} < 25 nm) and macro (R_{void} > 25 nm) scale. Nanozirconia modification increased the macroporosity and simultaneously suppressed the mesoporosity in the aggregates. Results indicate that during the initial stages of polymer adsorption strong hydrogen bonding develops between the surface hydroxyls of silica and the oxygens on PDMS backbone, resulting in high coverage of both the inner and external surfaces of silica aggregates. Results by DSC and DRS, in agreement with each other, reveal higher degree of initial PDMS adsorption in the case of modified surfaces. This last result was obtained by monitoring the fraction and dynamics of polymer chains at the interface (α_{int} process), and interpreted in terms of increased density of contact points of silica (accessible hydroxyl groups) with PDMS chains. The increase of concentration of polymer chains at the interface is accompanied by faster dynamics and increased cooperativity. According to a previously proposed model [Klonos15A], we suggest that during the initial adsorption of PDMS the chains are strongly attached (although sparsely distributed) and highly orientated (tails) over the surfaces, characterized by lower cooperativity. Nanozirconia modification increases the concentration of accessible to PDMS contact points and, thus, the number of tails. Further polymer adsorption proceeds via loop–like conformations, probably in more dense packing onto the surfaces, resulting in increase of the degree of cooperativity of polymer chains in the interfacial layer and in faster interfacial dynamics [Klonos15A]. Thus, number and accessibility of contact points (surface properties of the particles) and structure and flexibility of polymer chain (polymer topology at the interfaces) dominate interfacial interactions. Finally, it becomes clear that the characteristics of interfacial polymer and, most probably, polymer adsorption depend on the surface roughness of the hosting particles, the latter being described by S_{BET} in case of high textural porosity. Therefore, in the following Chapter we investigate the above dependence in NCs based on PDMS and metal oxide nanoparticles of a wide range of S_{BET}.

APPENDIX A.6

A.6.1. Incremental Pore Size Distribution (IPSD) and analysis

To analyze the textural characteristics of nanooxides, low–temperature (77.4 K) nitrogen adsorption–desorption isotherms were recorded using a Sorptometer KELVIN 1042

(COSTECH Instruments) adsorption analyzer. Samples were previously out–gassed at 473 K for several hours. The specific surface area (S_{BET}) was calculated according to the standard BET method [Brunauer38].

The total pore volume V_p was evaluated from the nitrogen adsorption at $p/p_0 \approx 0.99$, where p and p_0 denote the equilibrium and saturation pressure of nitrogen at 77.4 K, respectively. The nitrogen desorption data were used to compute the pore size distributions (PSDs, differential $f_V(R) \sim dV_p/dR$ and $f_S(R) \sim dS/dR$) using a self–consistent regularization (SCR) procedure under non–negativity condition ($f_V(R) \geq 0$ at any pore radius R) at a fixed regularization parameter $\alpha = 0.01$ with a complex pore model with cylindrical (C) pores and voids (V) between spherical nonporous nanoparticles packed in random aggregates (void–cylindrical pore model was used for silica (CV/SCR model) or silica and zirconia (VCV/SCR model)). The differential PSDs with respect to pore volume $f_V(R) \sim dV/dR$, $\int f_V(R)dR \sim V_p$ were re–calculated to incremental PSD (IPSD) at $\Phi_V(R_i) = (f_V(R_{i+1}) + f_V(R_i))(R_{i+1} - R_i)/2$ at $\sum\Phi_V(R_i) = V_p$). The differential $f_S(R)$ functions were used to estimate the deviation of the pore shape from the model as follows

$$\Delta w = \left(S_{BET} / \int_{R_{min}}^{R_{max}} f_S(R)dR \right) - 1 \quad (1)$$

where R_{max} and R_{min} are the maximal and minimal pore radii, respectively. The $f_V(R)$ and $f_S(R)$ functions were also used to calculate contributions of nanopores (V_{nano} and S_{nano} at 0.35 nm < R < 1 nm), mesopores (V_{meso} and S_{meso} at 1 nm < R < 25 nm), and macropores (V_{macro} and S_{macro} at 25 nm < R < 100 nm). The average values of the pore radii were determined with respect to both pore volume and specific surface area, respectively, as the corresponding moments of the distribution functions

$$< R_V >= \int_{R_{min}}^{R_{max}} R f_V(R)dR \Big/ \int_{R_{min}}^{R_{max}} f_V(R)dR \quad (2)$$

$$< R_S >= \int_{R_{min}}^{R_{max}} R f_S(R)dR \Big/ \int_{R_{min}}^{R_{max}} f_S(R)dR \quad (3)$$

A.6.2. Fourier transform infrared spectroscopy (FTIR)

FTIR spectra of powdered samples (grinded with KBr at the mass ratio 1:9) over the 400 – 4000 cm^{-1} range were recorded employing a ThermoNicolet FTIR spectrometer in diffuse reflectance mode.

7. Dependence of interfacial polymer fraction and dynamics on roughness of hosting surfaces

7.1. Introduction

The existence of an *interfacial polymer fraction* in polymer nanocomposites (PNCs) [Wurm10, Ackora09, Boucher10], characterized by a modified structure [Eslami13, Voyatzis 13, Harmandaris14, Voyatzis14], slower dynamics [Fragiadakis05, Klonos10A, Fragiadakis11, Fullbrant13, Holt14, Klonos15A] and increased thermal stability [Galaburda14, Sulym14], as compared to the bulk, has been found to affect significantly or even dominate the properties of PNCs [Schmidt10]. In chapter 4 we suggested that the stronger polymer–particle hydrogen bonding is at the origin of the increased interfacial layer thickness in polydimethylsiloxane (PDMS) / titania as compared to PDMS / silica conventional PNCs [Klonos10A]. Kumar and coworkers suggested that the interfacial layer thickness may decrease with curvature of the adsorbing surface [Harton10] and increase with size of nanoparticles [Gong14]. In chapters 5–6 we demonstrated systematic changes on interfacial PDMS fraction and dynamics on the surface and porosity characteristics (roughness) of fumed silicas. The latter are reflected in the specific surface area, S_{BET} [Fullbrant14, Klonos15A, Klonos15B], especially in case of silicas with mainly textural meso– and macro– porosity (i.e. surface pores of >2 nm diameter).

An interesting question, so far not considered in the respective literature, refers to the dependence of the characteristics of the interfacial polymer fraction on surface roughness. Therefore, we present in this chapter results by differential scanning calorimetry (DSC) and dielectric relaxation spectroscopy (DRS) in systems based on linear PDMS (40 wt%) adsorbed (via hydrogen bonding) on aggregates of fumed metal oxide particles of a wide range of nanometric surface roughness (S_{BET}, 25–342 m^2/g). Results are discussed in terms of

dynamics in the interfacial layer and evaluation of the interfacial polymer fraction and apparent thickness/density of the interfacial layer. The interfacial polymer fraction (Rigid Amorphous Fraction, *RAF*) was evaluated in DSC by the deviation (missing part) of the heat capacity step of the nanocomposites (NCs) at glass transition, ΔC_p, from that of the neat polymer [Wurm10]. In DRS, on the contrary, the segmental dynamics of the polymer at the interfaces was recorded (α_{int} relaxation) [Klonos10A, Klonos15B] and *RAF* was evaluated by comparing its dielectric strength ($\Delta\varepsilon$) with that of the total segmental response (interfacial and bulk). The methodology for that has been described in Chapter 3 and already used in chapters 4–6.

7.2. Materials

The metal oxides used [Sulim09] are titania (~70 nm in diameter for primary particles, ~800 nm in size for aggregates, S_{BET} ~ 25 m^2/g, details of preparation later in chapter 9) and various silicas (8–85 nm in diameter for primary particles, 300–600 nm in size for aggregates, S_{BET} ~ 55–342 m^2/g, details of preparation in chapters 5 and 6). PDMS (Kremniypolymer, Zaporozhye, Ukraine, linear, *MW* ~ 7960, degree of polymerization ~105 monomers/chain, –CH_3 terminated) was physically adsorbed onto dried oxides at the constant amount of 40 wt%. This specific fraction of PDMS loading was selected as results in our previous studies on similar systems [Klonos15A, Klonos15B, Galaburda14, Sulym14] have indicated that the accessible area (accessible contact points) of metal oxides can be fully covered already at 40 wt% PDMS in all cases of S_{BET}. Thus, keeping most of the parameters constant (type and fraction of polymer, preparation process, type of porosity (namely textural) of initial oxides) we will attempt to directly record the effects of changes in surface roughness on interfacial interactions and polymer dynamics in the interfacial layer.

7.3. Results and discussion

7.3.1. Differential scanning calorimetry (DSC)

Figure 7.1 presents comparative DSC thermograms in the glass transition region for PDMS and NCs. The glass transition temperatures, T_g, determined as the midpoint of the heat capacity step, ΔC_p, (Table 7.1) increases in the NCs by 1–5 K, comparing to neat amorphous PDMS (–129 °C). The heat capacity step, normalized to the same amorphous PDMS mass, $\Delta C_{p,n}$ (Eq. (3.3) in section 3.2.), decreases in the NCs, due to the growth of the interfacial Rigid Amorphous Fraction, RAF_{int} [Wurm10]. Because of the semi–crystalline nature of

PDMS, an additional Rigid Amorphous Fraction exists in close proximity to polymer crystals, RAF_{cryst} [Dobbertin96]. RAF_{int} and RAF_{cryst} do not contribute to ΔC_p, forming together *RAF*. Furthermore, we employ Eq. (3.5) according to a '*3–phase model*' (section 3.2) and calculate *RAF* (Table 7.1). In Fig. 7.1b we follow that *RAF* increases with S_{BET} almost linearly, varying between 0.35 wt (titania, S_{BET} ~25 m^2/g) and 0.79 wt (silica of S_{BET} ~342 m^2/g).

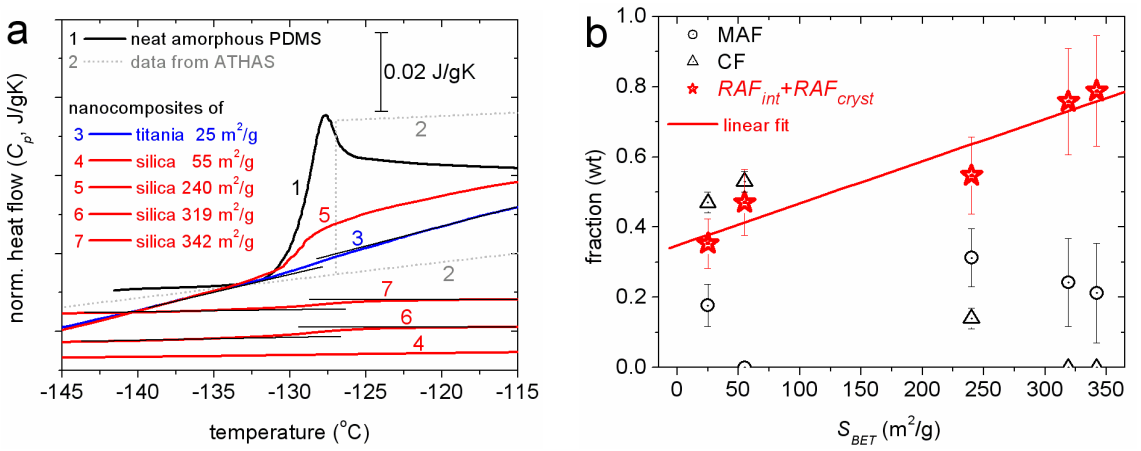

Fig. 7.1. (a) Comparative DSC thermograms for samples of 40 wt% PDMS adsorbed on silica and titania particles and for pure amorphous PDMS, in the glass transition region. Heat capacity curves for PDMS from the ATHAS databank ([Wunderlich95, Wunderlich03]) are also shown. The curves are normalized to sample mass. (b) fractions of rigid amorphous polymer (*RAF*), mobile amorphous polymer (*MAF*) and crystalline polymer (*CF*) against specific surface area, S_{BET}, of the hosting particles.

Table 7.1

Quantities of interest from DSC measurements: glass transition temperature, T_g, normalized heat capacity step at glass transition, $\Delta C_{p,n}$, rigid and mobile amorphous polymer fractions (at T_g), *RAF* and *MAF,* respectively, and crystalline polymer fraction, *CF*.

S_{BET} (m^2/g)	T_g (°C)	$\Delta C_{p,n}$ (J/gK)	*RAF* (wt)	*MAF* (wt)	*CF* (wt)
25	–128	0.11	0.35	0.18	0.47
55	–	0.00	0.47	0.00	0.53
240	–129	0.12	0.55	0.31	0.14
319	–129	0.08	0.76	0.24	0.00
342	–129	0.07	0.79	0.21	0.00

7.3.2. Dielectric relaxation spectroscopy (DRS)

DRS results recorded isothermally (section 3.4) have been replotted in Fig. 7.2 as isochronal imaginary part of dielectric permittivity $\varepsilon''(T)$ plots to facilitate direct comparison with the DSC thermograms of Fig. 7.1a. A relative to DSC high frequency of 3.1 kHz was selected to suppress effects of conductivity [Kremer02]. Additionally, DRS results were analyzed by fitting the Havriliak–Negami (HN) equation (Eq. (3.6), details in section 3.4) to the experimental data in order to evaluate the time scale (temperature dependence of the frequency maxima) (Fig. 7.3a) and the dielectric strength, $\Delta\varepsilon$, (Fig. 7.3b) of the various relaxations [Kremer02]. One HN term for each of the relaxations (namely S_{OH}, α, α_c, and α_{int}) was critically fitted to the experimental data at each temperature and the fitting parameters were determined.

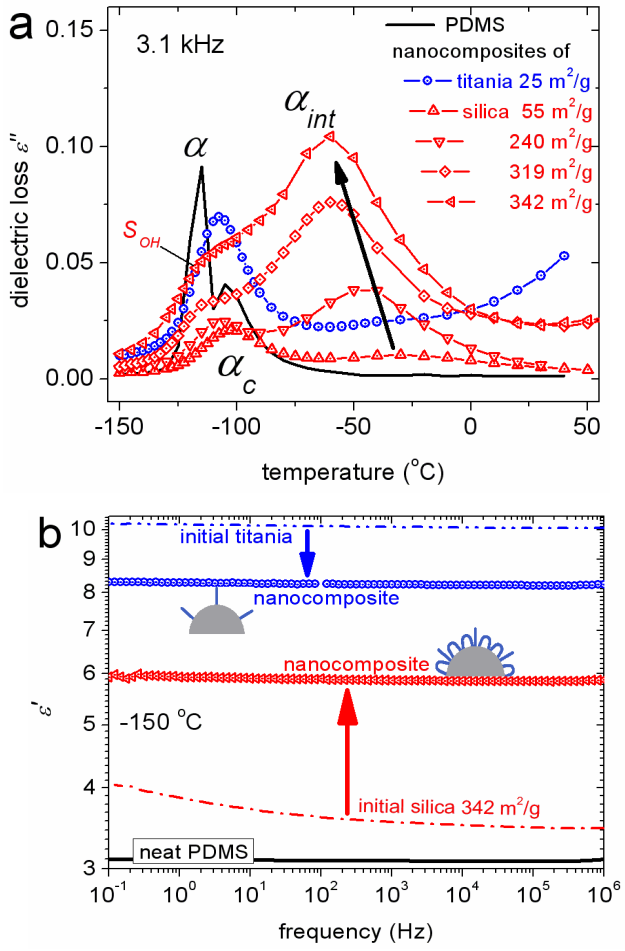

Fig. 7.2. (a) Comparative isochronal plots of the imaginary part of dielectric permittivity (dielectric loss), ε'', at 3.1 kHz for 40 wt% PDMS adsorbed in silica and titania and for pure PDMS. (b) shows selected results for the

real part of dielectric permittivity, ε', at –150 °C against frequency for the initial components (titania, silica and PDMS) and the respective nanocomposites.

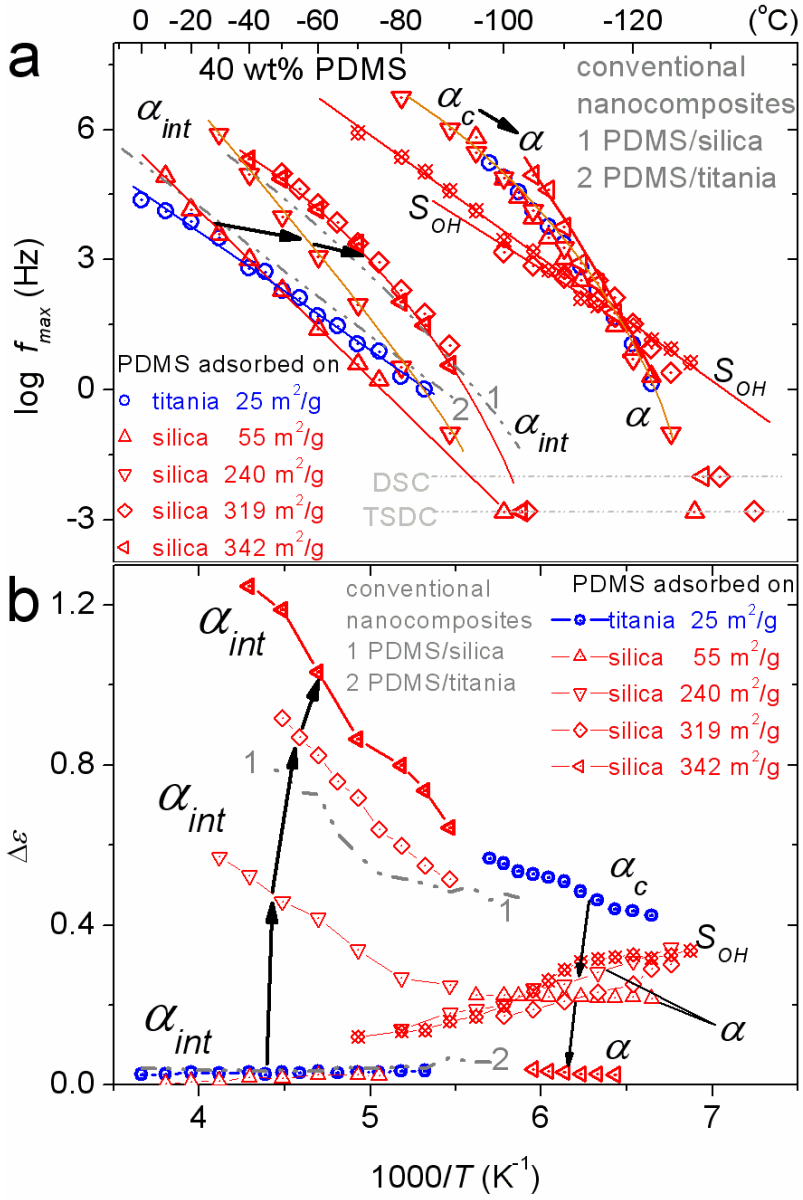

Fig. 7.3. (a) Arrhenius plots and (b) dielectric strength vs reciprocal temperature for the segmental relaxations of bulk (α_{bulk}) and interfacial polymer (α_{int}) and for the local relaxation of the –OH groups on the surface of the particles (S_{OH}). The lines in (a) are fittings of the VTFH and Arrhenius equations (Eqs. (3.7,3.11) in section 3.4). The lines (1),(2) in both (a) and (b) correspond to the interfacial relaxation in conventional (1) PDMS/silica and (2) PDMS/titania nanocomposites (chapter 4, Fig. 4.11). Included in (a) are DSC and TSDC data. The arrows mark changes imposed by the increasing of S_{BET}.

The bulk segmental relaxation consists of two contributions in Fig. 7.2a, arising from extended amorphous regions (α) and from polymer chains restricted between condensed crystalline regions (α_c), respectively, more clearly discerned for neat PDMS. In the NCs one of the two contributions dominates depending on the degree of crystallinity. α_c becomes gradually weaker with the increasing of S_{BET} and α dominates (Fig. 7.3). The S_{OH} relaxation, related to local motion of free hydroxyls on the surface of the oxide particles (Si–OH, Ti–OH) [Fontanella09], dominates the response of initial nanooxides (not shown) [Klonos15A] and is present here in the NCs of high specific surface area (Fig. 7.3). Please compare S_{OH} relaxation here with S relaxation in chapter 5 (Fig. 5.8) in relation to changes imposed by thermal (crystallization) annealing.

The most interesting results come from the slower α_{int} process (Figs. 7.2a,7.3a), which monitors the segmental dynamics in the interfacial polymer layer [Fragiadakis07, Klonos10A, Klonos15A]. With S_{BET} increasing, α_{int} becomes faster (Fig. 7.3a), stronger (Fig. 7.3b), and more cooperative (higher fragility index m in Fig. 7.4, details of calculation in section 3.4, Eq. (3.8), Table 7.2).

Table 7.2

Quantities of interest from DRS measurements: interfacial polymer fraction and fragility index, RAF_{int} and m, respectively, apparent interfacial polymer layer thickness and density, d_{int} and ρ_{int}, respectively, and estimated really accessible surface areas, $S_{d,int}$ and $S_{\rho,int}$ (Eqs. (7.3),(7.4)).

S_{BET} (m^2/g)	RAF_{int} (vol)	m	d_{int} (nm)	ρ_{int} (g/cm^3)	$S_{d,int}$ (m^2/g)	$S_{\rho,int}$ (m^2/g)
25	0.04	5	0.64	0.234	10	4
55	0.05	10	0.37	0.137	13	5
240	0.50	30	0.86	0.321	132	48
319	0.76	48	0.98	0.367	200	72
342	0.94	52	1.10	0.424	241	90

By employing a model analogue to the one used previously for DSC we calculate the interfacial PDMS fraction in the NCs, RAF_{int}, according to Eq. (3.10) (Table 7.2). Results for RAF_{int} are shown in Fig. 7.4, for –95 °C ($\Delta\varepsilon$ changes with temperature, Fig. 7.3b). They reveal that, next to enhanced dynamics and cooperativity, RAF_{int} increases systematically with S_{BET}, in qualitative agreement with DSC, despite *in principle* different methods of measurement and calculation [Eslami13]. Interestingly, the dependence of RAF_{int} on S_{BET} is not linear in Fig. 7.4, as we would expect. Similarly to this result, non-linear dependence of RAF_{int} on

nanoparticle fraction, obtained also by DRS, has been previously reported for polymer nanocomposites (however not discussed) [Klonos10A, Fullbrant13, Holt14].

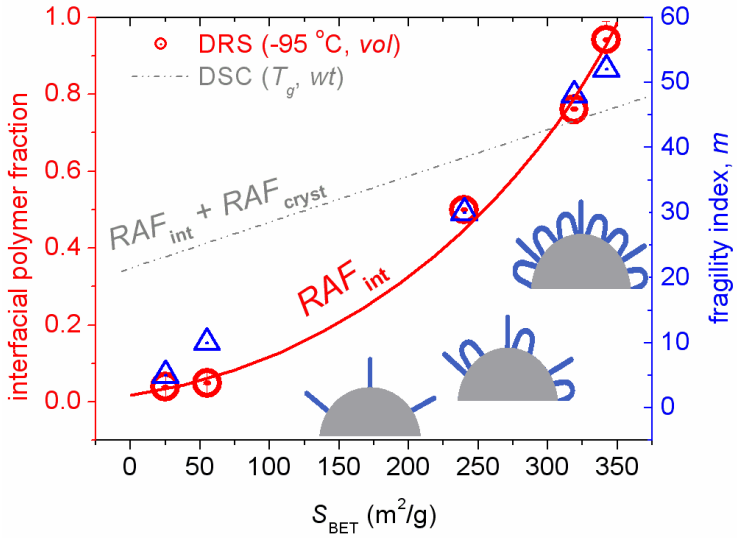

Fig. 7.4. (Left axis, cycles) interfacial polymer fraction (RAF_{int}) and (right axis, squares) fragility index, m, of the interfacial relaxation (α_{int}) against specific surface area, S_{BET}, obtained by DRS at –95 °C. *RAF* (interfacial and around crystals) at T_g obtained by DSC is also shown (dash–dotted line, values refer to the left axis).

In the previous 2 chapters we have discussed results on similar *core–shell* systems for the interfacial α_{int} process in terms of the formation of two types of segment conformations at interfaces, namely (a) extended tails with bulk–like density but reduced mobility, and (b) loop–like chain segments with multiple contact points with the silica surface resulting in increased density and cooperativity (schemes in Fig. 7.4) [Koga12, Klonos15A]. Obviously, both types of segments are characterized by increased orientation (order) and polarizability, as compared to segments in the bulk, which explains the increased dielectric response in the NCs beyond additivity (Fig. 7.2b). The loops / tails ratio increases with increasing S_{BET} as depicted in Fig. 7.4. This dependence is also at the origin of an explanation for the increase / decrease of $\Delta\varepsilon$ of α_{int} relaxation with temperature, for samples of respectively high / low interfacial polymer fraction in Fig. 7.3b. In addition, increase in nanometric surface roughness in the present work leads to increased number of contact points and, therefore, gradually denser interfacial layer. This implies reduction of the cooperativity length ξ, thus, in the frame of Adam–Gibbs theory [Adam65], faster and more cooperative segmental dynamics is expected [Hodge97], in agreement with results for α_{int} here (Figs. 7.3a,7.4).

7.3.3. Evaluation of interfacial polymer layer thickness / density

The thickness of the interfacial layer is often employed for the description of the extent of polymer–filler interactions [Gong14]. We employ here Eq. (7.1) for the estimation of interfacial layer thickness (same as in chapter 5, i.e. Eq. (5.1)). We recall that by using this equation we assume (i) constant density of PDMS in the interfacial layer and in bulk, equal to that of neat PDMS (ρ_{PDMS}=1.62 g/cm^3) [Klonos10A], and (ii) accessibility of the whole oxide surface area, S_{BET}, to PDMS. Please note that S_{BET} was determined from nitrogen adsorption–desorption measurements [Sulim09]. Thus, we estimate the *'apparent' interfacial layer thickness*, d_{int}, by the following equation.

$$d_{\text{int}} = \frac{volume_{\text{int}\,erfacial,PDMS}}{surface_{\text{int}\,erfacial}} = \frac{mass_{sample} \cdot X_{PDMS} \cdot RAF_{\text{int}} / \rho_{PDMS}}{mass_{sample} \cdot (1 - X_{PDMS}) \cdot S_{BET}} \tag{7.1}$$

The results show that d_{int} increases in general with S_{BET} varying between 0.37 and 1.10 nm (Table 7.2). The relatively low absolute values, smaller than values obtained in conventional PDMS/silica NCs (~2 nm) [Fragiadakis07, Klonos10A], also smaller than the *Kuhn segment length* for PDMS by a factor of 2 − 4, can be probably understood in terms of assumption (ii) above (apparent values). Kumar and coworkers discussed d_{int} values in relation to *Kuhn segment length*, which should be at the upper limit of d_{int} [Gong14]. Combining this last statement with the changes in interfacial polymer chain conformations (insets to Fig. 7.4), which explain our overall findings by DRS, we proceed with the calculation of the 'apparent' interfacial polymer density. Under the above assumption (ii) and supposing now that d_{int} is constant and equal to *Kuhn segment length* (~1.56 nm for PDMS [Gilra11]) for all PNCs, we estimate the '*apparent interfacial layer density*', ρ_{int}, by the following equation

$$\rho_{\text{int}} = \frac{mass_{\text{int}\,erfacial,PDMS}}{volume_{\text{int}\,erfacial,PDMS}} = \frac{mass_{sample} \cdot X_{PDMS} \cdot RAF_{\text{int}\,erfaces}}{mass_{sample} \cdot (1 - X_{PDMS}) \cdot S \cdot 1.56(nm)} \tag{7.2}$$

The absolute values of ρ_{int} increase with S_{BET}, varying between 0.137 and 0.424 g/cm^3 (Table 7.2). ρ_{int} is smaller than bulk density (1.62 g/cm^3) by a factor of 4 − 12. The deviation of d_{int} and ρ_{int} from the *Kuhn segment length* and bulk density of PDMS, respectively, may be useful for rationalizing results by Eqs. (7.1,7.2) in the frame of assumption (ii). Thus, we attempt to estimate the really accessible surface area ($S_{d\text{int}}$, $S_{\rho\text{int}}$) of the particles according to the following equations

$$S_{d\,\text{int}} = S_{BET} \frac{d_{\text{int}}}{Kuhn,length} = S_{BET} \frac{d_{\text{int}}}{1.56(nm)} \tag{7.3}$$

$$S_{\rho\,\mathrm{int}} = S_{BET}\frac{\rho_{\mathrm{int}}}{\rho_{PDMS}} = S_{BET}\frac{\rho_{\mathrm{int}}}{1.62(nm)} \tag{7.4}$$

Results are shown in Fig. 7.5 and suggest that the really accessible (to PDMS) surface area should vary between 10 and 241 m^2/g (squares in Fig. 7.5) or between 4 and 90 m^2/g (triangles in Fig. 7.5) with the measured S_{BET}, based on Eq. (7.3) or (7.4), respectively.

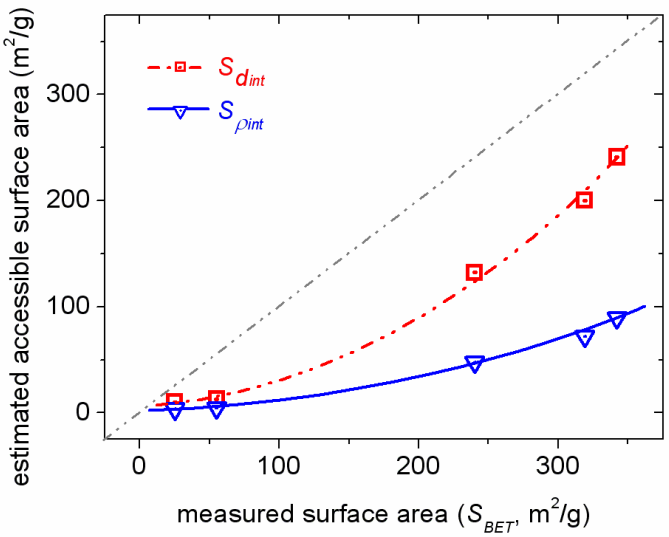

Fig. 7.5. Estimated accessible surface area of the hosting particles, $S_{d,\mathrm{int}}$ and $S_{\rho,\mathrm{int}}$ (details in text), against the measured specific surface area S_{BET} (determined by nitrogen adsorption–desorption). The lines are used to guide the eyes.

At this point we cannot conclude as to whether interfacial polymer density is lower or higher comparing to density in bulk, since respective results in the literature are not clear. Polystyrene (PS) adsorbed on flat Si substrate has demonstrated higher density than that in bulk in the inner region of the interfacial layer, while the outer interfacial region is characterized by density equal to that in bulk [Koga12]. Computer simulations in PS grafted on spherical nanoparticles demonstrate that the density of grafted chains in the interfacial layer of the inner 2−3 nm is about double than that of polymer chains in bulk [Voyatzis13]. On the other hand, results by Small Angle X−ray Scattering (SAXS) in poly(2–vinylpyridine) (P2VP) absorbed on silica nanoparticles (Ref. [Holt14] and personal communication) indicate lower density of interfacial polymer as compared to that in bulk. Similar studies in future work on NCs based on various levels of surface roughness is expected to provide further insight into polymer structure and dynamics. Finally, work is in progress for understanding the non linear dependence of RAF_{int} and m on S_{BET}.

7.4. Conclusions

DRS in combination with DSC revealed that the increase of specific surface area, S_{BET}, of silica–like oxide particles results in increase of polymer–particle contact points, reflected in increased interfacial polymer fraction and, furthermore, enhanced mobility and cooperativity. In an attempt to explain the changes in the overall dielectric response (ε'', ε', $\Delta\varepsilon$), the characteristics of interfacial relaxation were interpreted in terms of bimodal conformations (tail– and loop–like) of PDMS at the oxide surface. The increase of interfacial polymer density / thickness (apparent values) with S_{BET}, surprising at first glance, is probably related to the reported increase of mean pore size (roughness) with S_{BET} [Sulim09], resulting in increased accessibility of the oxide surface to PDMS, a point worth to be followed in future work.

8. Effects of hydration on interfacial polymer dynamics

8.1. Introduction

Effects of hydration (moisture) on the properties of polymer nanocomposites (PNCs) are often discussed [Plueddeman82, Feldman01, Schönhals02, Karul09, Pissis13, Wang15], along with the general study of PNCs based on both hydrophobic and hydrophilic substances (such as in this thesis, where PDMS is hydrophobic and metal oxides are hydrophilic). On the basis of these effects and the respective employed experimental methods, similarities between artificial and natural polymers (e.g. proteins) have been reported [Cebe14A, Cebe14B, Khodadadi15]. Jhon and Andrade have suggested [Jhon73] that, regarding structure and molecular mobility, adsorbed water molecules can be classified to (a) *bound*, (b) *semi–bound*, and (c) *free* water [Pissis13, Stathopoulos10, Pandis11]. Bound water consists of molecules interacting directly with the hydrophilic surface, via strong bonding (e.g. hydrogen bonding) with the primary hydration sites of the surface. Water molecules with weaker interaction, or else interacting at second level, form the semi–bound water. Finally, free (unbound) water is formed by molecules not interacting with the hydrophilic sites of the surface and, also, with bound water. It has been suggested [Plueddeman82, Yang14] that a part of bound (*interfacial*) water cannot be removed from the hydrophilic surfaces, at least by conventional drying techniques (for example, by heating at 80 ^{o}C in vacuum). In addition, the presence of interfacial water cannot be avoided in PNCs even if the composites are prepared under perfectly dried conditions [Plueddeman82, Gunko13B].

The structure and mobility of water molecules in PNCs depend on their state (liquid, ice) [Wu10, Wolf12, Panagopoulou12], on the strength of interaction with the hydrophilic surface (surface properties of nanoparticles) [Stirnemann11], and on the scale of spatial confinement (e.g. in the pores of metal oxide aggregates) [Gunko13B]. Except of the surface properties and distribution of the nanoparticles, the transport of water molecules in a PNC

depends also on the degree of agglomeration [Gedde11] and the size [Tigger11] of nanoparticles. The combination of these last two characteristics resembles the accessible surface area of the nanoparticles, which is thought to be well described by specific surface area, S_{BET} [Gunko13B, Klonos15A, Klonos15B]. In computer simulations, the presence of interfacial (bound) water in PNCs has been considered of high significance for polymer adhesion [Wang15, Wang14], the latter has been found to increase with hydration. Polymer adhesion on a solid surface in the presence of interfacial water is preserved well [Kochumalayil13, Wang15], resulting, among others, in retarded thermal degradation of the polymer [Galaburda14, Sulym14]. Regarding the state of polymer in PNCs, Karul *et al.* [Karul09] demonstrated differences in accumulation of moisture on a hydrophilic solid surface coated with thin polymer layer between rubber (low accumulation) and glassy polymers (higher accumulation). Gee *et al.* [Gee04] showed that dehydration of PDMS/silica NCs results in a decrease of polymer–silica contact distance [Gunko13B, Schönhals15], accompanied with decreased mobility of interfacial polymer, so that an overall stiffening of the polymer matrix is observed. By employing dielectric spectroscopy techniques, the main technique of investigation in this chapter, the molecular dynamics of interfacial water has been studied via recording of a specific dielectric relaxation mechanism in PNCs (i.e. the local relaxation of the –OH groups on the surface of the particles with one water molecule attached) [Fontanella09, Kirst93, Klonos13, Galaburda14, Klonos15A], while the presence of semibound and free water has been recorded indirectly via changes in local and segmental polymer dynamics in aqueous polymer mixtures [Shinyashiki07, Shinyashiki07B, Stathopoulos10]. Interfacial water has been also proposed to be at the origin of changes in the interfacial Maxwell–Wagner–Sillars (*MWS*) relaxation [Mijovic06, Pissis08, Siengchin08] and also of changes in the dc conductivity [Feldman01, Schönhals02, Nikaj10, Pissis13, Yang14, Schönhals15].

In this chapter, we discuss effects imposed by hydration–dehydration of PNCs on molecular dynamics in systems based on silica / titania and adsorbed PDMS. Except for the type of nanooxides, we also study specific surface area, S_{BET}, as a relative parameter, by studying PNCs based on silicas of different S_{BET}. We present changes in the dynamics and fraction of the polymer in the interfacial layer. Hydration/dehydration of the samples and evaluation of water content in the NCs is achieved by employing equilibrium water sorption–desorption isotherms (ESI, EDI), while molecular dynamics is followed by dielectric relaxation spectroscopy (DRS). Similarly to previous chapters, the effects of water content on

interfacial dynamics are finally discussed in terms of additive contribution of interfacial water to the concentration of polymer–particle contact points [Klonos15A, Klonos15B].

8.2. Experimental

In this chapter we show results obtained by the ESI method (section 3.5) and by DRS (section 3.4) for initial silica and titania oxides and respective PNCs of the same oxides and adsorbed PDMS. The metal oxides used are two types of silica (~10 nm in diameter for primary particles, ~300 nm in size for aggregates, S_{BET} ~ 242 and 342 m^2/g, details of preparation in chapter 5) and titania (~70 nm in diameter for primary particles, ~800 nm in size for aggregates, S_{BET} ~25 m^2/g, details of preparation later in chapter 9). PDMS (Kremniypolymer, Zaporozhye, Ukraine, linear, *MW* ~7960, degree of polymerization ~105 monomers/chain, –CH_3 terminated, code name PDMS–1000) was physically adsorbed onto dried oxides at the amounts of 40 and 80 wt%.

8.3. Results and discussion

8.3.1. Equilibrium water sorption isotherms (ESI)

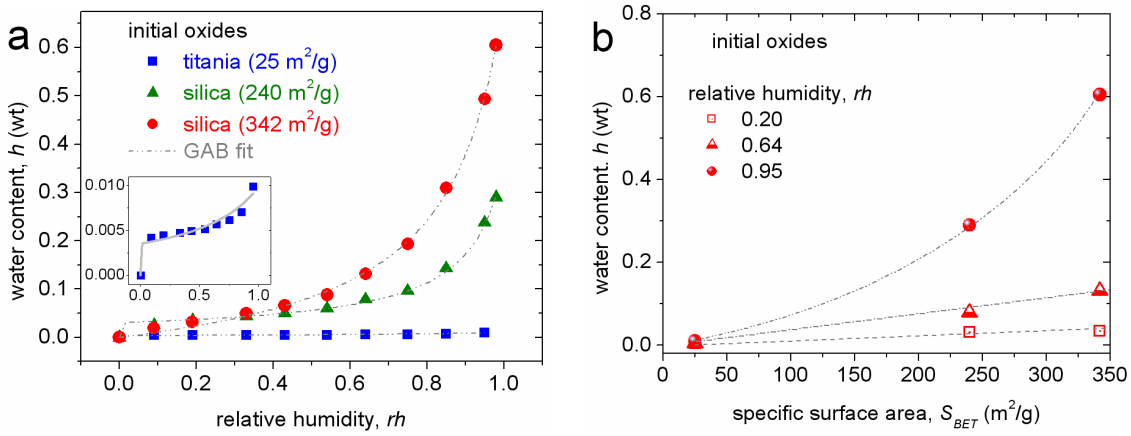

Fig. 8.1. (a) Comparative ESI measurements of the initial nanooxides: titania (S_{BET} ~25 m^2/g) and silica (S_{BET} ~240 and 342 m^2/g). The inset shows in more detail the ESI result for initial titania. The lines are fittings of GAB equation (Eq. (3.13)) to the experimental data. (b) water content vs specific surface area of the nanooxides at selected *rh* levels. The lines were added as guides to the eyes.

Figure 8.1a presents results of ESI measurements for neat silica and titania nanooxides. The water sorption isotherms of Fig. 8.1a are of class I in the Brunauer classification [Brunauer38] for initial nanooxides, judging from the strong increase in *h* at very low *rh*. Water sorption isotherms of Type I are characterized by their approach to a

limiting value of adsorption and usually describe adsorption onto microporous adsorbents. This behavior, especially in the case of titania Fig. 9.1a, is consistent with previous results of initial silica in the form of network prepared by Sol-Gel technique [Pandis11]. In addition, it has been shown [Pandis11] that the data for initial oxides, such as silica, can be analyzed according to so called *Langmuir* equation [Kumar05]. Coming back to the obtained data, a steep increase of water content is observed at *rh* values above ~0.6, reflecting the completion of the first hydration layer (bound water) and the existence of semi–bound and free water molecules around the primary hydration sites [Pissis13]. The hydrophilicity of silica for both S_{BET} is remarkably higher as compared to that of titania. The water uptake, *h*, (Eq. (3.12)) increases systematically with increasing of S_{BET} as shown in Fig. 8.1b. The $h(S_{BET})$ dependence is almost linear for *rh* up to 0.64, while for higher *rh* increase in *h* becomes stronger with S_{BET}. It is worthy to report that the hydration / dehydration processes by ESI/EDI methods were non reversible for initial fillers (formation of a gel on the specific surface of the samples during hydration), while the opposite was found true in the case of silica nanoparticles prepared by sol–gel technique [Pandis11, Stathopoulos10].

Hydration of the respective PNCs (not shown) is significantly weaker. We report that ambient *h* of nanocomposites based on 40 and 80 wt% PDMS is ~0.002 wt, while *h* increases to ~0.003 wt for *rh*=0.95, these values being representative for all types of nanooxides. These results reveal the strong coverage of the hydrophilic sites of the nanooxides by the PDMS chains (hydrophobic polymer). However, due to the low absolute values of *h* differences in polymer filler interactions between the various fillers cannot be reliably evaluated via changes in hydration of the PNCs. On the contrary, DRS has been proved quite more revealing in such evaluation [Klonos10A, Klonos15B], in particular by demonstrating a systematic increase in interfacial (bound) polymer fraction with increasing of S_{BET} (chapter 7). Therefore, we proceed with the presentation of results by DRS that show the effects of hydration–dehydration on the fraction and dynamics of PDMS at the nanooxide–polymer interface.

8.3.2. Dielectric relaxation spectroscopy (DRS)

Figure 8.2 presents the frequency dependence of the imaginary part of dielectric permittivity, $\varepsilon''(f)$, at different temperatures for initial PDMS for samples previously equilibrated in the ambience (i.e. ~0.40 *rh*) and in environment of high relative humidity (0.85 *rh*). We follow in Fig. 8.2a,b the segmental relaxations related to glass transition at –115 ^{o}C, namely, α and α_c, affiliated to bulk amorphous polymer and to amorphous polymer spatially confined between condensed crystal regions, respectively (details in chapter 4). It seems in Fig. 8.1a that α is

more pronounced, as compared to α_c, in the case of ambient hydration of the sample, while α_c dominates the response for the sample previously equilibrated at 0.85 *rh*. At this point we should report that the mass of the neat PDMS samples was the same for both cases of *rh*, suggesting unchanged level of hydration (within experimental error of the measurements). Thus, we suggest that any changes in segmental dynamics arise, most probably, from changes in the degree of crystallinity, X_c. Crystallization of polymer-based systems is expected to increase with hydration [Bolhuis75, Miyazaki02]. In agreement to that, Gee *at al.* [Gee04] reported a slight decrease in the polymer melting enthalpy (by ~6 %) upon desiccation of silica/PDMS systems. However, with temperature increasing at –105 °C, i.e. within the temperature range of cold crystallization of PDMS (please compare with Fig. 5.1), X_c increases for both samples and, as a result, the intensity of α decreases and, subsequently, α_c becomes stronger in Fig. 8.2b.

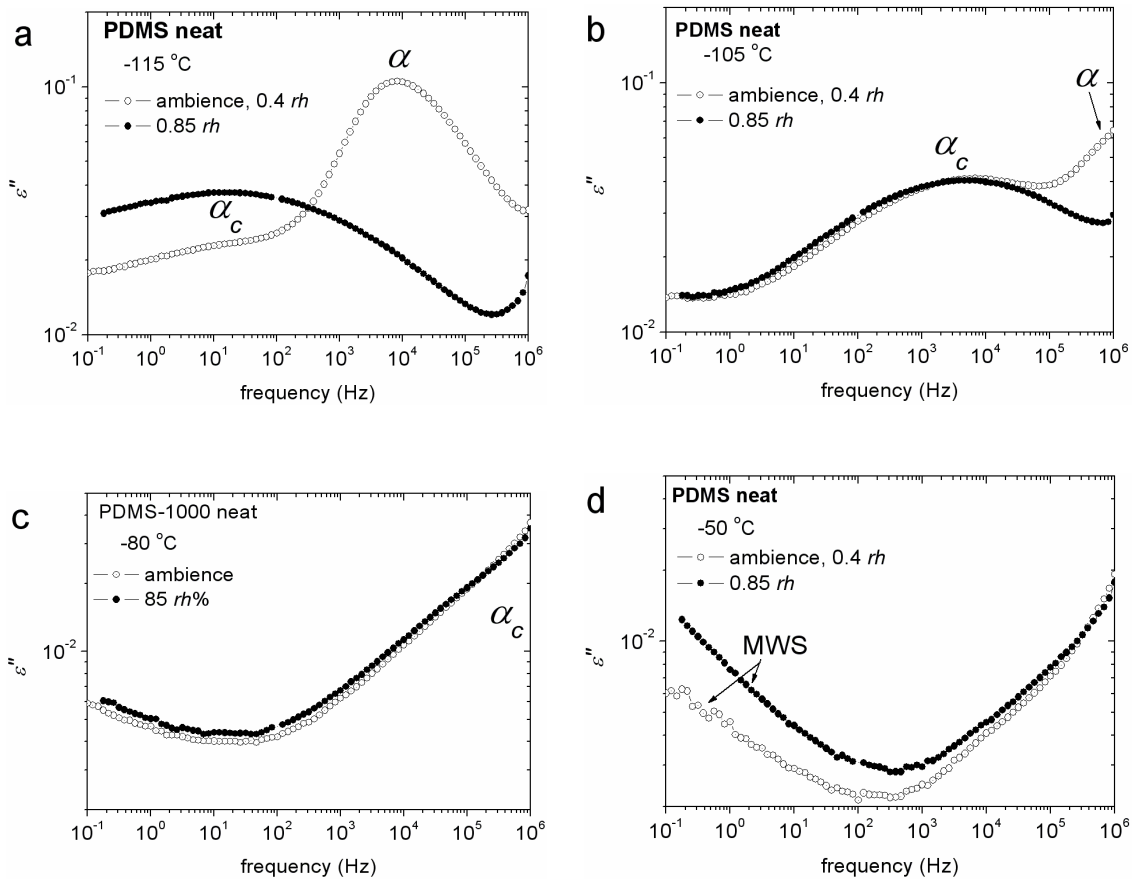

Fig. 8.2. Comparative isothermal DRS plots of dielectric loss, ε'', at (a) –115 °C, (b) –105 °C, (c) –80 °C, and (d) –50 °C, versus frequency for neat PDMS previously equilibrated in the ambience (open symbols) and in 0.85 *rh* (solid symbols). The arrows indicate the recorded relaxations.

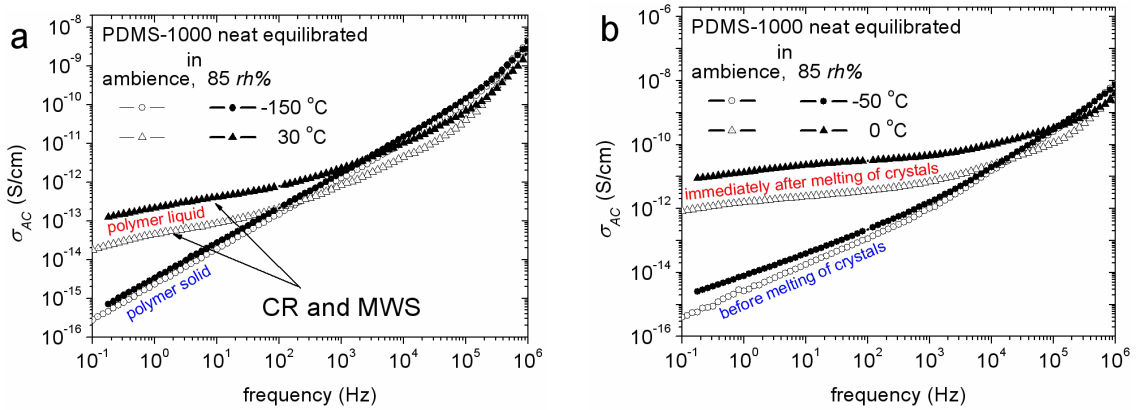

Fig. 8.3. Comparative isothermal DRS plots of AC conductivity, σ_{AC}, versus frequency for neat PDMS previously equilibrated in the ambience (open symbols) and in 0.85 *rh* (solid symbols) at (a) –150 and 30 °C for comparing between fully immobile and fully mobile polymer chains and at (b) –50 and 0 °C for comparing before and immediately after melting of polymer crystals.

For higher temperatures (–80 and –50 °C in Figs. 8.2c,d, respectively) the low frequency side of the ε'' spectra is dominated by effects related to electrical charges trapped at interfaces (*MWS* relaxation) and dc conductivity (conductivity relaxation, *CR*), these phenomena being more pronounced for samples equilibrated at the higher *rh*. *MWS* relaxation is related to crystallized/amorphous PDMS interface (possibly, the case in Fig. 8.2d, $X_c \neq 0$) and also with the interface between the polymer and the brass electrodes. In Fig. 8.3 interfacial electrode polarization along with dc conductivity dominate AC conductivity, $\sigma_{AC}(f)$, for the low frequencies at 30 °C where $X_c=0$ (melting point of PDMS is ~ –40 °C).

Summarizing all the above observations, we conclude that the hydration level of neat PDMS equilibrated at high *rh* is similar to that at ambient *rh*. Segmental dynamics of PDMS equilibrated at low and high *rh* is practically unchanged, while conductivity-related phenomena are more pronounced for high *rh*, as compared to those recorded for lower *rh*.

We may focus now on the effects of hydration in PNCs. Figure 8.4 shows DRS spectra of $\varepsilon''(f)$ for the sample A380P80, i.e. 80 wt% PDMS adsorbed on silica of high S_{BET} ~342 m^2/g (A–380). The sample had been previously equilibrated at 0.02, 0.40 and 0.85 *rh*, this procedure resulting in *h* (on dry basis) equal to 0, 0.2 and 0.3 wt%, respectively. DRS results were analyzed in terms of the Havriliak–Negami equation (Eq. (3.6), details in section 3.4). By plotting the frequency of maximum of ε'' from Eq. (3.6) against reciprocal temperature for the three segmental relaxations, the Arrhenius plots of Fig. 8.5a were constructed. The Vogel–Tammann–Fulcher–Hesse (*VTFH*) equation (Eq. (3.7)), characteristic of cooperative processes [Richert98] was fitted to the data of Fig. 8.5a (lines) and the fragility

index *m* was determined. We recall that *m* is a measure of cooperativity (deviation from linear behavior) [Klonos15A, Richert98]. *S* relaxation and in the case of dried nanocomposites α_{int} relaxation (details in the following) were described-fitted by the Arrhenius equation (Eq. (3.11), straight lines in Fig. 8.5a). Finally, we present in Fig. 8.5b the reciprocal temperature dependence of $\Delta\varepsilon$ from Eq. (3.6) for all recorded relaxations. Similar measurements and analysis were performed for nanocomposites based on titania (S_{BET} ~25 m^2/g) and the same PDMS. The respective results for titania/PDMS NCs are compared with those of silica/PDMS in terms of time scale and reciprocal temperature dependence of dielectric strength in Figs. 8.6a and b, respectively.

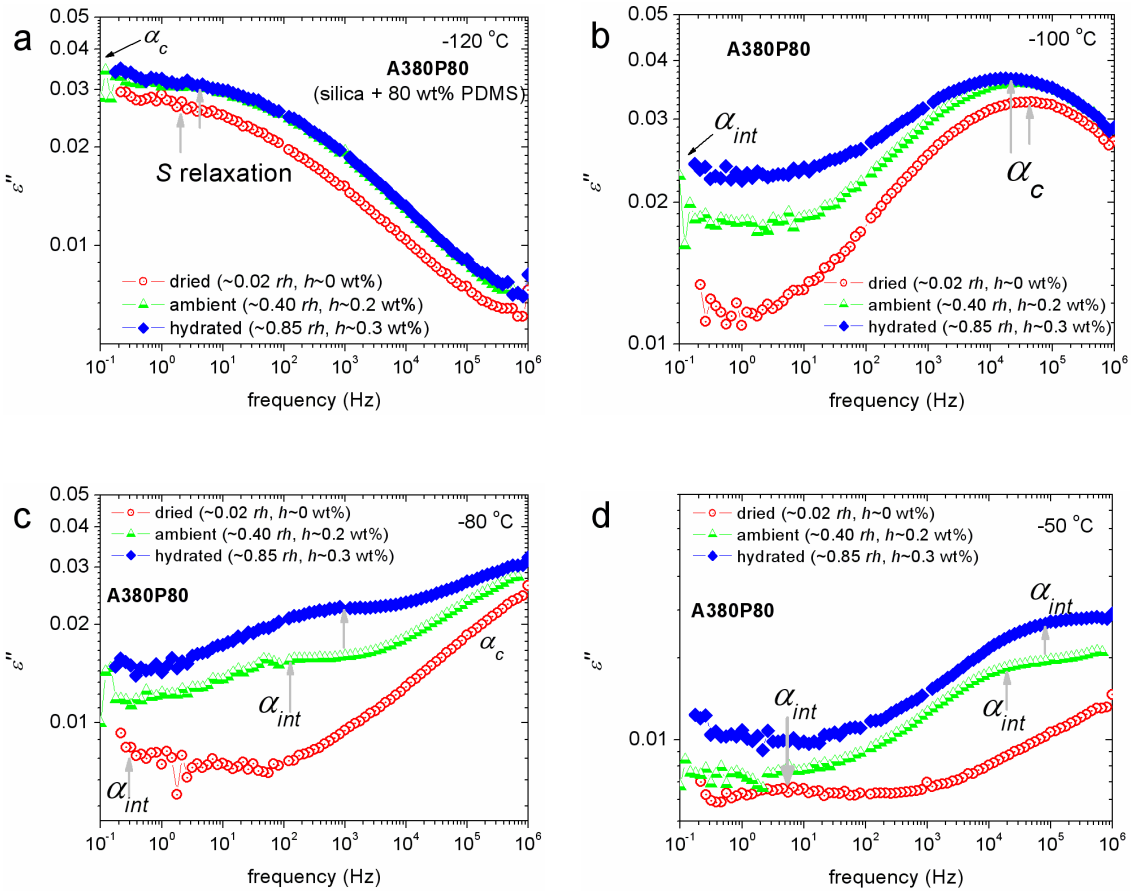

Fig. 8.4. Comparative isothermal DRS plots of dielectric loss, ε'', at (a) –120 °C, (b) –100 °C, (c) –80 °C, and (d) –50 °C, versus frequency for A380P80 (details in the text) at different hydration levels, indicated on the plots. Arrows mark the peak frequency, f_{max}, of the various relaxations.

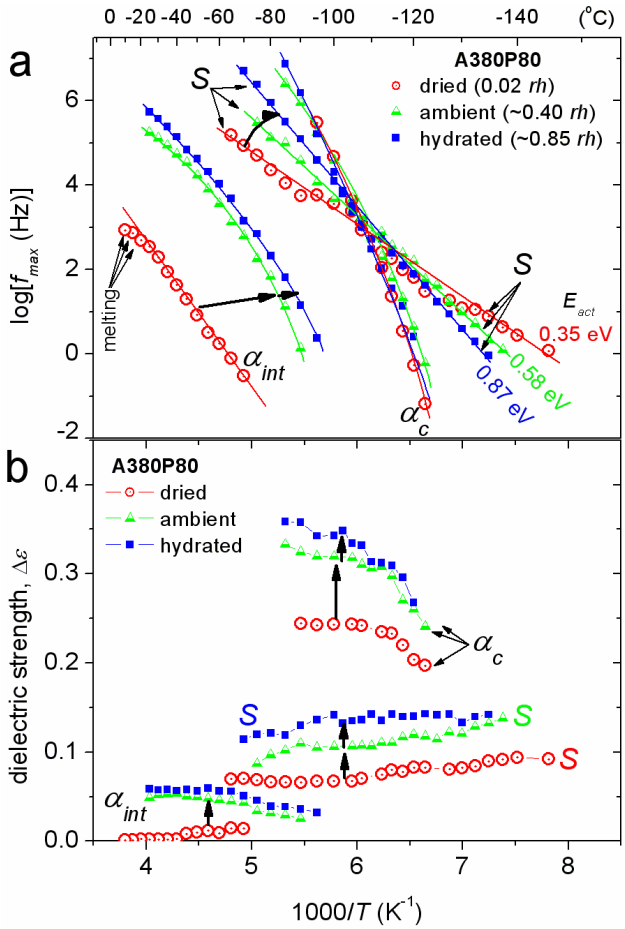

Fig. 8.5. Comparative (a) Arrhenius plots and (b) dielectric strength vs reciprocal temperature of the local (*S*), segmental bulk–like (α_c), and interfacial polymer dynamics (α_{int}) for A380P80, at different hydration levels. The lines in (a) are fittings of the VTFH and the Arrhenius equations. The arrows mark changes induced by hydration. Values for the activation energy, E_{act}, for *S* relaxation have been added in (a).

In general, the increase in hydration results in an increase of the overall dielectric response for the samples (Fig. 8.5b). Regarding molecular dynamics, we follow in Fig. 8.4a and Fig. 8.5 that increase in hydration results in an increase of the strength and the average activation energy, E_{act}, of *S* relaxation (related to the free surface hydroxyls at the surface of silica). These results would suggest an increase of the concentration of free hydroxyl groups with *h* increasing (although absolute values of *h* are quite low). Bulk–like dynamics in this nanocomposite is expressed via α_c relaxation, the time scale of which is practically unchanged with hydration in Fig. 8.5a, while its dielectric strength seems to increase (Fig. 8.5b), most probably drifted by the overall increase in dielectric response (increased conductivity).

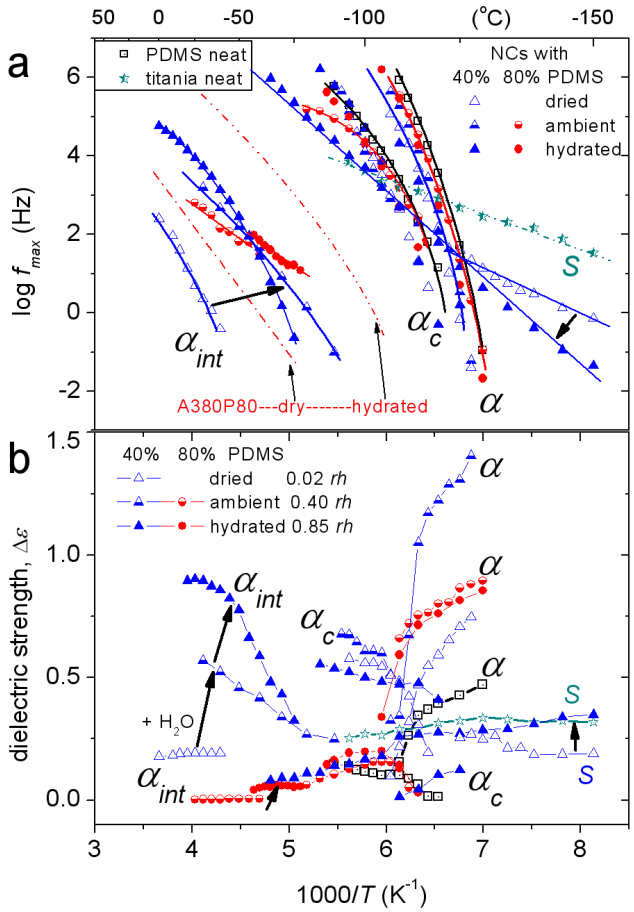

Fig. 8.6. Comparative (a) Arrhenius plots and (b) dielectric strength vs reciprocal temperature of the local (*S*), segmental bulk and bulk–like (α and α_c, respectively), and interfacial polymer dynamics (α_{int}) for NCs of titania and PDMS at 40 wt% (triangles) and 80 wt% (cycles), at different hydration levels. The stars (★) represent results for initial titania (*S* relaxation). The lines in (a) are fittings of the VTFH and the Arrhenius equations. Selected results for α_{int} of A380P80 (i.e. silica/PDMS) have been added in (a). The arrows mark changes induced by hydration.

The most interesting results, with respect to hydration of the NCs, are observed for α_{int} relaxation. We recall that α_{int} is suggested [Fragiadakis05, Fragiadakis07, Klonos10, Klonos15A] to monitor the retarded segmental dynamics of the fraction of PDMS in the silica/polymer interfacial layer. In Fig. 8.4d the difference in the $\varepsilon''(f)$ response between the dried and the hydrated samples is remarkable, as α_{int} is recorded by more than 3 orders of frequency magnitude slower and by 3–4 times weaker (Fig. 8.5b) for the dried samples as compared to the hydrated ones. In addition, the increase in water content imposes increase in the cooperativity (fragility *m*, Eqs. 3.7–8) of α_{int}. The results are qualitatively similar in the case of PDMS adsorbed on titania of significantly lower S_{BET} ~25 m^2/g (Fig. 8.6), although the changes imposed by hydration are weaker for 80 wt% PDMS and stronger for 40 wt%

PDMS. In all cases of titania/PDMS systems, α_{int} is recorded slower as compared to that in silica/PDMS for the same *rh*. It is interesting to report, from the methodological point of view, that changes imposed on α_{int} with hydration/dehydration were reversible, as obtained with respective experiments (not shown). The suppression of interfacial dynamics with dehydration here resembles the effect on α_{int}, observed previously, with crystallization annealing (chapter 5, Fig. 5.8) and, also, with the decrease in specific surface area of the hosting nanooxides (chapter 7, Fig. 7.3).

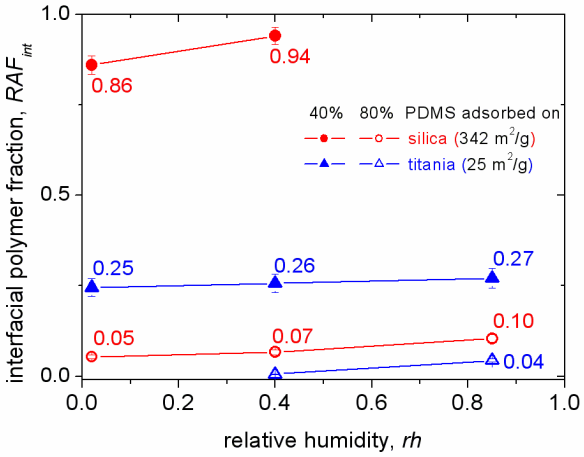

Fig. 8.7. Effects of hydration level on the interfacial polymer fraction (RAF_{int}) for samples of 40 wt% and 80 wt% PDMS (solid and open symbols, respectively) adsorbed on silica and titania (cycles and triangles, respectively). Absolute values for RAF_{int} were added beside the respective points.

Having clear evidence about the origin of the recorded relaxations, we now proceed with the calculation of interfacial polymer fraction, RAF_{int}, according to Eq. (3.10). We recall that the dielectric strength changes with temperature in Figs. 8.5b, 8.6b, thus, we employ DRS results at the same temperature –95 ^{o}C for RAF_{int}. Results of RAF_{int} are shown in Fig. 8.7. They reveal that RAF_{int} tends to increase with hydration (*rh*) for all NCs compositions. RAF_{int} is larger for lower polymer loading (40 wt%) in Fig. 8.7, as expected. In addition, RAF_{int} is larger for silica/PDMS as compared to titania/PDMS systems.

We showed previously that hydration/dehydration does not affect directly bulk–like dynamics of PDMS in both the neat PDMS samples and in NCs, we suggest that all recorded changes in segmental dynamics originate from changes on the surface of the hydrophilic oxides. Thus, following the same formalism as in the previous 3 chapters, we suggest that with hydration of NCs increasing the concentration of polymer/particle contacts also increases. This would imply increase in the fraction of interfacial polymer (Fig. 8.7) and

decrease in the cooperativity length ξ, thus, faster and more cooperative segmental dynamics [Adam65, Hodge97], in agreement with results for RAF_{int} (Fig. 8.7) and α_{int} here (Figs. 8.5a, 8.6a). Gee *et al.* [Gee04] studied PDMS/silica NCs by employing computer simulations for molecular dynamics in combination with experimental techniques for the structure and demonstrated that dehydration of NCs imposed a decrease of polymer–silica contact distance by 1.5 Å (i.e. equal to the approximate size of a chemisorbed silanol group) accompanied with decreased mobility of interfacial polymer. Therefore, combining our results with those obtained by Gee *et al.* we propose that the additional interfacial water molecules make additional contact points on the surface of the nanooxides for interaction with the polymer (Scheme 8.1), as the presence of interfacial water molecules induces, among other structural changes [Gunko13B, Gunko14B], an increase in the concentration of free surface hydroxyls. We report that the maximum distance between the –OH sites of the same water molecule is ~0.2 nm [Kim91], while the radius of gyration for PDMS varies between 0.2 – 4 nm [Melnichnko03, Luo11]. Thus, it is reasonable that a part of the additional free hydroxyls cannot be engaged by PDMS. The latter can be supported by the recorded upcoming of the dielectric strength of *S* relaxation with *h* in Figs. 8.5b, 8.6b. Also, the increase of RAF_{int} with hydration is consistent with respective predictions by computer simulations [Wang15], demonstrating that the adhesion of biopolymers on the surfaces of nano-clays increases with interfacial hydration of the same surfaces.

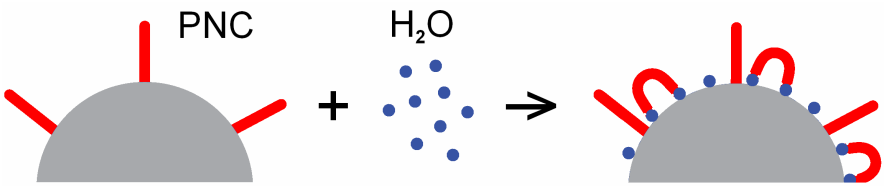

Scheme 8.1. Schematic simplified model for describing how interfacial water molecules (blue dots) may act as additional contact points between the hydrophilic surface of nanooxides and the polymer chain segments (red tails/loops).

It is, however, remarkable how such weak changes in hydration (0.1–0.2 wt%, Fig. 8.4) lead to tremendous changes in the dynamics of interfacial polymer. The high resolving power of DRS, especially for investigating effects related to interfacial phenomena (e.g. *MWS* relaxation) and water at the same interfaces has been previously demonstrated [Feldman01, Schönhals02, Schönhals15].

8.4. Conclusions

DRS in combination with ESI in polymer nanocomposites based on hydrophilic nanooxides (silica, titania) and adsorbed PDMS revealed that the increase of hydration of oxide particles results in increase of polymer–particle contact points, reflected in enhanced mobility/cooperativity and fraction of the interfacial polymer. Effects on interfacial polymer relaxation (α_{int}) by hydration were found qualitatively similar to effects imposed by thermal annealing and changes in the surface roughness of nanooxides (chapters 5 and 7, respectively). Results were found consistent with observations from the literature, in the sense of increased adhesion of the polymer onto the hydrophilic surface in the presence of moisture. From the methodological point of view, the very weak changes of the amount of the adsorbed water in the PNCs (0.2–0.3 wt%) were proved sufficient enough for DRS for recording changes in interfacial dynamics, more specifically, in both the segmental dynamics of interfacial polymer and the local dynamics of surface hydroxyls of nanooxides. These effects imposed by hydration/dehydration of the samples are worth to be followed in future work, in combination with DSC (also, in Temperature Modulation mode) and by employing different thermal protocols (e.g. temperature annealing).

9. Effects of polymer molecular weight on interfacial interactions in nanocomposites based on titania and physically adsorbed PDMS

9.1. Introduction

In the present chapter, the focus is on the surface characterization and interfacial interactions in systems of linear polydimethylsiloxane (PDMS), of short and long polymer chains and of various amounts, that is adsorbed physically on aggregates of titania (TiO_2) nanoparticles, characterized by respectively low nanometric roughness (i.e. low specific surface area, ~25 m^2/g). We study and discuss the effects of surface characteristics, morphology and polymer–filler interactions on the fraction and dynamics of the polymer in the interfacial titania/PDMS layer. We follow the effects of polymer chain length on polymer adsorption, by means of two types of linear PDMS with different molecular weights ($MW \sim$ 7960 and 1700). The structural and adsorption properties of initial TiO_2 and TiO_2/PDMS nanocomposites were investigated employing low temperature nitrogen adsorption/desorption technique, while morphology was examined employing scanning electron microscopy (SEM). The evaluation of interfacial polymer characteristics was achieved via the critical comparison between the bulk and interfacial (rigid) segmental polymer responses (related to glass transition) as recorded by two techniques, namely DSC and DRS, following in both widely adopted formalisms [Wurm10, Fragiadakis07].

9.2. Materials

Initial fumed titania (TiO_2) (pilot plant of Chuiko Institute of Surface Chemistry, Kalush, Ukraine) is characterized by low specific surface area (S_{BET} ~25 m^2/g, Table 9.1, Appendix A.9.1) and average nanoparticle diameter of ~58 nm. Nanoparticles are crystalline according to XRD (Appendix A.9.2). Commercial polydimethylsiloxane (PDMS) (Kremniypolimer, Zaporozhye, Ukraine, linear, $–CH_3$ terminated) of two molecular weights (code names: *PDMS–1000* and *PDMS–20* for PDMS with molecular weight *MW* ~7960, degree of polymerization d_p = 105, and *MW* ~ 1700, d_p = 22, respectively) was adsorbed onto titania in the amounts of 5, 10, 20, 40 and 80 wt% in dry samples. Before adsorption, the oxide samples were dried at 150 °C for 1.5 h. Different amounts of hexane solution of PDMS at a constant concentration (1 wt% PDMS) were added to fixed amounts of dry titania powder. The suspension was mechanically stirred and finally dried at room temperature for 24 h and then at 80 °C for 3 h. Samples at PDMS concentration from 0 to 40 wt% are in the form of powder, similar to the initial titania powder, while at higher PDMS concentrations of 80 wt% and 100 wt% the samples are liquid–like and liquid, respectively.

9.3. Results and discussion

9.3.1. Surface and porosity characterization

The nitrogen adsorption–desorption isotherms (not shown) for initial TiO_2 and both types of composites (TiO_2/PDMS–1000 and TiO_2/PDMS–20) demonstrate narrow hysteresis loops of the H3 type [Gregg82, Kruk01] in the p/p_0 range between 0.8 and 1.0. The isotherms are sigmoidal–shaped for all the samples and correspond to type II of the IUPAC classification of pores [Gregg82, Kruk01]. The distribution functions of voids between particles in aggregates (Fig. 9.1, details of analysis in Appendix A.9.1) show that the textural characteristics of the TiO_2/PDMS materials depend on the molecular weight of PDMS. The specific surface area, S_{BET}, of composites was reduced with increasing polymer adsorption (X_{PDMS}). The reduction of S_{BET} is stronger for PDMS–1000 at $X_{PDMS} \leq$ 20 wt%, while at X_{PDMS} = 40 wt% S_{BET} decreases by 69 % and 79 % (in comparison to the initial titania powder) after the adsorption of PDMS–1000 and PDMS–20, respectively (Table 9.1). As expected, the pore volume of TiO_2/PDMS composites decreases with increase of X_{PDMS} (Table 9.1). In addition, this decrease is systematically stronger for the polymer of a shorter chain (PDMS–20) with the exception of 5 wt% PDMS.

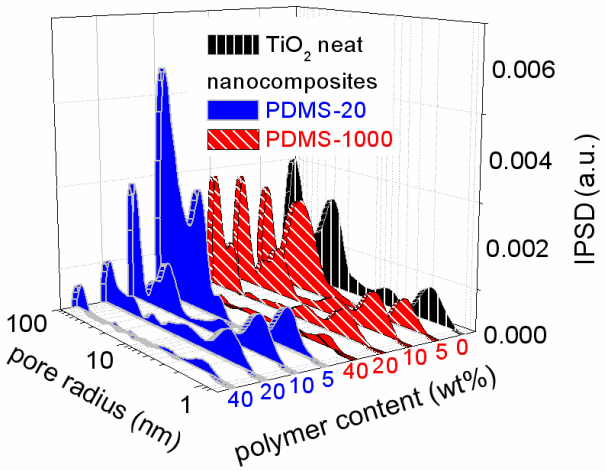

Fig. 9.1. Incremental pore size distributions for initial TiO_2 and TiO_2/PDMS composites, based on polymer of low and high molecular weight, PDMS–20 and PDMS–1000, respectively. Details of the analysis are given in Appendix A.9.1.

Table 9.1

Textural characteristics of initial TiO_2 and TiO_2/PDMS composites. Specific surface area in total, S_{BET}, of micropores, S_{micro}, mesopores, S_{meso}, macropores, S_{macro}, and respective specific pore volumes, V_p, V_{micro}, V_{meso}, V_{macro}. $<R_{p,V}>$ and $<R_{p,S}>$ represent the average radii of the pores with respect to the pore volume and specific surface area, respectively.

sample	S_{BET} (m^2/g)	S_{micro} (m^2/g)	S_{meso} (m^2/g)	S_{macro} (m^2/g)	V_{micro} (cm^3/g)	V_{meso} (cm^3/g)	V_{macro} (cm^3/g)	V_p (cm^3/g)	$R_{p,V}$ (nm)	$R_{p,S}$ (nm)
TiO_2 initial	25	1.3	21.1	2.4	0.001	0.04	0.044	0.081	37	9
TiO_2/(5 %)PDMS–1000	22	0.8	17.9	2.9	0.000	0.03	0.038	0.064	37	10
TiO_2/(10 %)PDMS–1000	23	0.3	20.8	1.4	0.000	0.03	0.028	0.053	37	6
TiO_2/(20 %)PDMS–1000	16	0.1	14.8	1.1	0.000	0.01	0.026	0.040	47	7
TiO_2/(40 %)PDMS–1000	8	0.1	7.4	0.2	0.000	0.01	0.003	0.009	21	4
TiO_2/(5 %)PDMS–20	23	0.2	18.3	4.3	0.000	0.03	0.080	0.110	47	13
TiO_2/(10 %)PDMS–20	24	0.2	22.4	1.5	0.000	0.02	0.026	0.049	37	6
TiO_2/(20 %)PDMS–20	18	0.2	17.5	0.6	0.000	0.02	0.013	0.031	29	5
TiO_2/(40 %)PDMS–20	5	0.0	5.1	0.1	0.000	0.00	0.003	0.007	37	4

The nitrogen adsorption–desorption isotherms of the composites and the analysis of the results (Appendix A.9.1) suggest the existence of mainly mesoporosity (V_{meso} and S_{meso} at 1 nm < *pore radius* < 25 nm) and secondly macroporosity (V_{macro} and S_{macro} at 25 nm < *pore radius* < 100 nm) of aggregates of nanoparticles or PDMS/nanoparticles and their agglomerates. The respective changes in S_{meso}, V_{meso}, S_{macro}, and V_{macro} are listed in Table 9.1. The polymer adsorption leads to suppression in the specific surface area, S_{BET}, and volume,

V_p, of the pores (voids between TiO_2 particles in their aggregates) (Table 9.1). The suppression in S_{BET} values is stronger in the case of TiO_2/PDMS–1000 in comparison with TiO_2/PDMS–20 (Table 9.1). In general, the addition of polymer can change the porosity characteristics because each long macromolecule may bind several oxide nanoparticles [Kim12, Bershtein09, Gunko13]. Thus, the aggregates become denser with increasing the amount of polymer and the volume of voids decreases. At X_{PDMS} = 40 wt% the porosity decreases sharply (Table 9.1) since PDMS fills the voids between particles.

9.3.2. Morphology

SEM images of initial titania (Fig. 9.2) show well–formed and spherical–like TiO_2 particles varying in size between 40 and 140 nm. Figures 9.3a–h demonstrate changes in the outer surfaces of samples due to the adsorption of PDMS. The gradual covering of titania with increasing polymer layer simultaneously with smoothening of the surfaces is observed due to *layer–by–layer polymer growth* on the surfaces of aggregated nanoparticles. Up to 10 wt% PDMS (Fig. 9.3a–d) the nanoparticles can be visually distinguished, suggesting that the average thickness of adsorbed polymer layers is less than 10 nm. Additionally, the voids between nanoparticles in aggregates are not fully filled with PDMS at low PDMS concentrations. Addition of more PDMS leads to thicker coverage of the surface resulting in no further distinguishable nanoparticles at 40 wt% PDMS (Fig. 9.3g–h) due to complete filling of the voids. The last observation supplements the results by the gas adsorption technique (section 9.3.1). The S_{BET} values of initial TiO_2, TiO_2/(5 wt%)PDMS and TiO_2/(10 wt%)PDMS (for both polymer types) are rather similar (Table 9.1) in contrast to the samples at 40 wt% PDMS. So, in the case of intra–aggregate porosity (i.e. voids between nanoparticles in aggregates) of a broad range, flexible PDMS can nearly completely fill these voids at X_{PDMS} = 40 wt% and higher. At lower amounts of the polymers, ≤ 20 wt%, the nanoparticulate structure remains and the system is in the powder state.

The smooth coverage of the titania surfaces at X_{PDMS} = 40 wt% (Fig. 9.3g–h) seems to be at higher extent for the shorter PDMS–20, than for the longer PDMS–1000. This is also in good agreement with the textural analysis results (Table 9.1), where the suppression of porosity was found stronger in TiO_2/PDMS–20 than in TiO_2/PDMS–1000. This result suggests that the interfacial polymer layer with shorter PDMS fills more strongly the contact zones between adjacent titania nanoparticles. This point will be further discussed later in relation to DSC and DRS results.

Figure 9.4 shows SEM images for TiO_2/(80wt%)PDMS–1000 representatively for samples at high polymer concentration. The titania aggregates of ~500 nm in average size are well distributed in the samples.

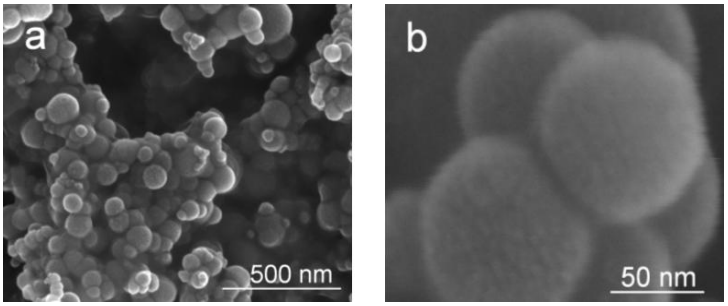

Fig. 9.2. SEM micrographs for initial titania aggregates.

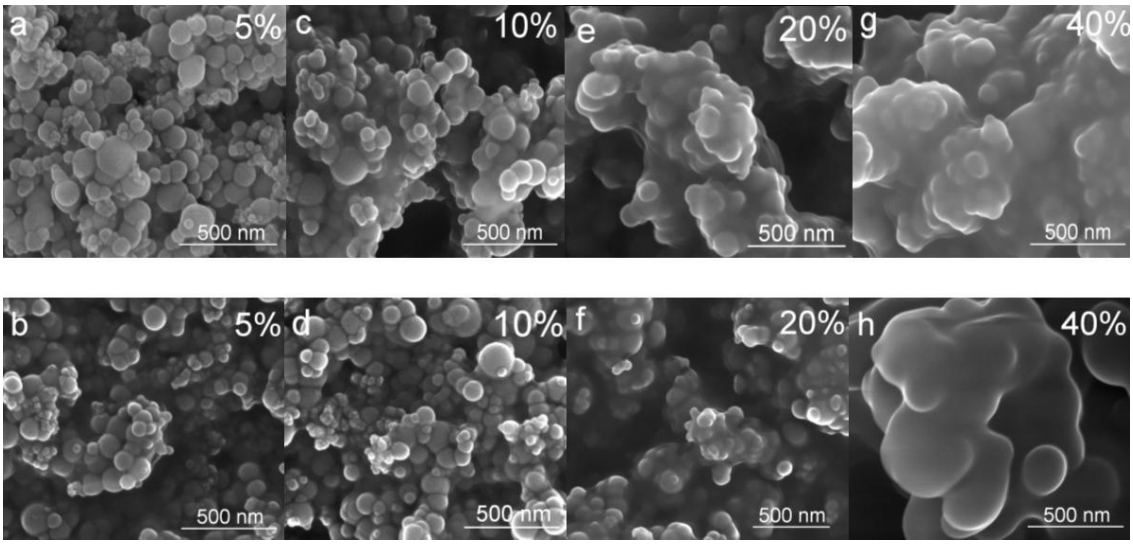

Fig. 9.3. SEM micrographs of TiO_2/PDMS composites (solid samples – powders) with PDMS–1000 (a, c, e, g) and PDMS–20 (b, d, f, h) at different X_{PDMS} (5 – 40 wt%)

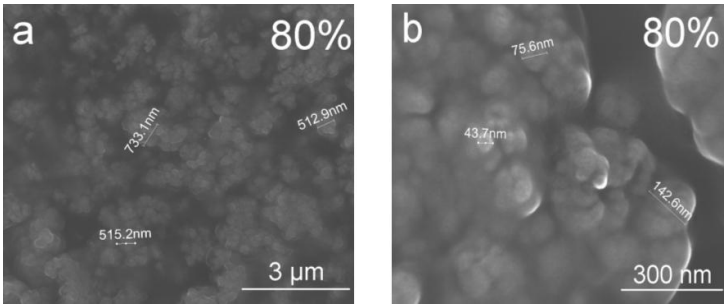

Fig. 9.4. SEM micrographs of TiO_2/(80 wt%)PDMS–1000 composite (liquid sample)

9.3.3. Thermal transitions

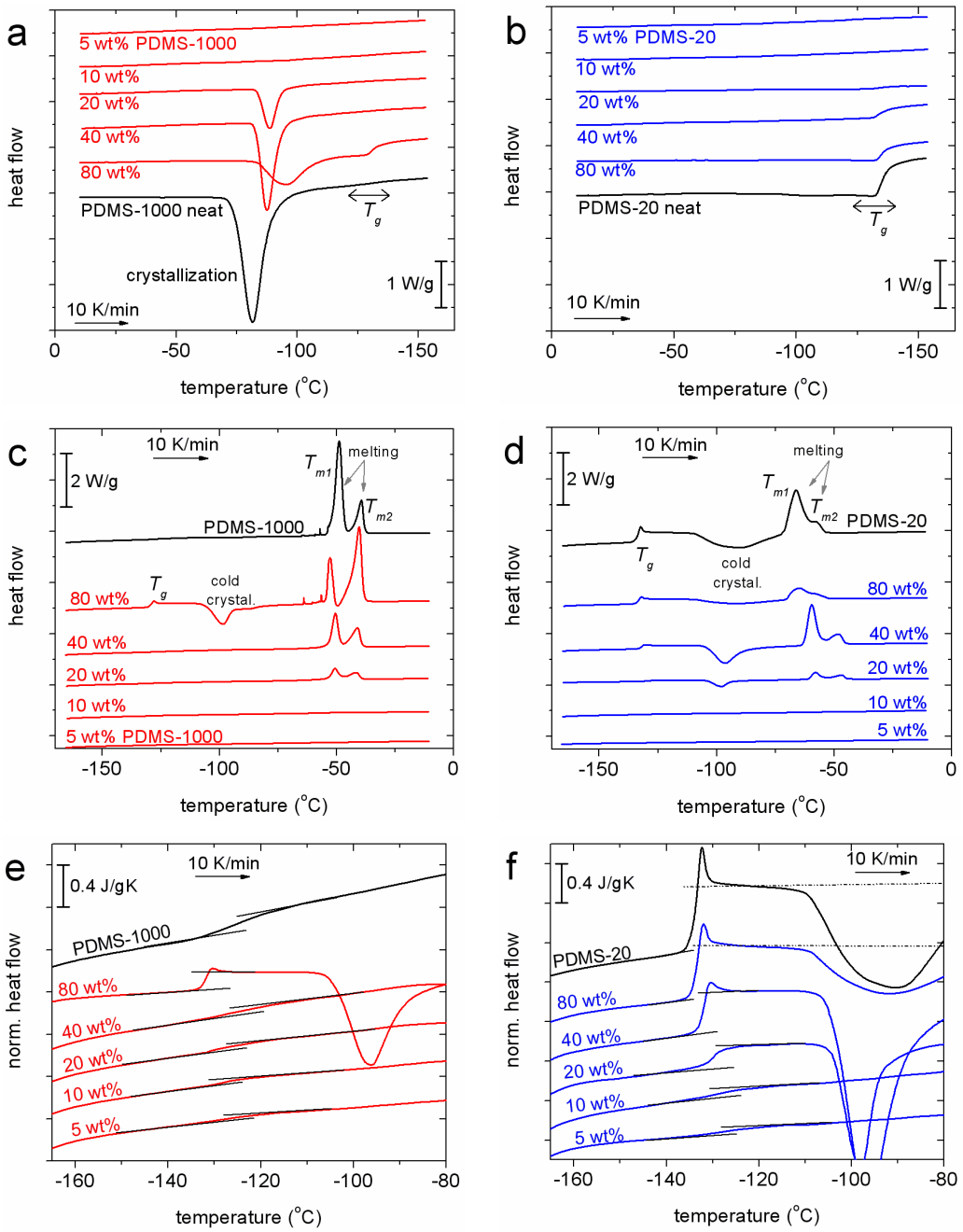

Fig. 9.5. Comparative DSC thermograms of PDMS–1000 (a,c,e) and PDMS–20 (b,d,f) adsorbed in TiO_2, and for comparison of pure PDMS, during (a,b) cooling and (c,d) subsequent heating. Indicated are the main thermal events of crystallization, melting and glass transition. Details in the glass transition region are given in (e) and (f) for the composites of PDMS–1000 and PDMS–20, respectively. The heat flow curves of (e,f) are normalized to the mass of the amorphous polymer and to heating rate (specific heat capacity, C_p). The lines represent the baselines of the thermograms before and after glass transition.

9.3.3.1. Polymer crystallization and melting

During cooling in DSC at 10 K/min crystallization for the different polymer loadings of TiO_2/PDMS–1000 and TiO_2/PDMS–20 occurs in the region between –110 and –85 °C (Figs. 9.5a,b, Table 9.2). The degree of crystallinity, X_c, was calculated from crystallization enthalpy according to Eq. (3.2). Crystallization of neat PDMS–1000 occurs at –82 °C and X_c is 0.65 wt (i.e. 0.65 by weight) (Table 9.2). The crystallization peak position, T_c, and degree of crystallinity, X_c, are both suppressed in TiO_2/PDMS–1000 systems. In the case of 10 wt% PDMS–1000 crystallization is extremely weak, while for 5 wt% PDMS–1000 it is completely absent. Similar results are obtained for melting, during heating, for the same samples. Crystallization during cooling, at 10 K/min, is completely absent in all TiO_2/PDMS–20 samples and neat PDMS–20 (Fig. 9.5b). Samples with polymer concentration from 20 to 100 wt% were crystallized partially during heating (cold crystallization [Gedde95] in Figs. 9.5c,d). The peak temperature for the recorded cold crystallization event is, in all cases, lower than the initial T_c of neat PDMS. The combination of the changes related to crystallization in the nanocomposites suggests strongly that TiO_2 particles do not act as crystallization nuclei and the crystallization event of PDMS is developed not close to the surface of the nanoparticles [Gedde95, Vanroy13]. The last observations are similar to those in systems of silica/PDMS (Chapters 4–6).

At higher temperatures, complex endothermic melting peaks are observed between –66 and –39 °C (T_{m1}, T_{m2} in Figs. 9.5c,d and Table 9.2). Both peak temperatures are lower in the case of nanocomposites as compared to neat PDMS, suggesting worse lamellae packing [Gedde95] of the PDMS spherulites in TiO_2/PDMS systems. Complex and double melting peaks are typical for PDMS systems [Aranguren98].

9.3.3.2. Glass transition and evaluation of rigid amorphous fraction (RAF)

Figures 9.5e,f show raw data of DSC measurements in the region of the glass transition for titania/PDMS nanocomposites and for comparison neat PDMS. We recorded this exothermic step during heating at 10 K/min for all the samples. The characteristic temperature T_g was obtained between –134 °C (neat PDMS–20) and –125 °C (TiO_2/(5 wt%)PDMS–20) (Table 9.2). Results of T_g in neat polymers here (–127 °C and –134 °C for PDMS–1000 and PDMS–20, respectively, Table 9.2) are quite similar with previous study of linear PDMS for a wige range of molecular weight [Hintermeyer08]. The temperature position (T_g) and temperature range ($T_{end} - T_{onset}$) of the glass transition are systematically ruled by the spatial constraints

imposed by (i) the presence of nanooxide particles (interfaces and voids) [Klonos15A, Klonos10B] and (ii) condensed polymer crystal regions [Klonos10A]. In both cases of constraints T_g increases. Case (i) is the one dominating the changes in glass transition for all TiO_2/PDMS–20 samples and samples with 5–10 wt% adsorbed PDMS–1000. Case (ii) is responsible for the respective changes for samples with 20–80 wt% adsorbed PDMS–1000 and for neat PDMS–1000. The increase of T_g in the presence of nanooxides is quite systematic, the effects being more clear in the series of TiO_2/PDMS–20 where crystallization during cooling is absent. Moreover, the increase in T_g is accompanied by a broadening of the glass transition temperature range $T_{end} - T_{onset}$, suggesting slowing down of dynamics and increasing in the population of '*relaxation times*' in glass transition, respectively. As expected, the physical and spatial constraints, imposed by the nanoparticles and/or spherulites, act as obstacles to polymer diffusion during glass transition [Gedde95].

Table 9.2

Values of interest from DSC measurements of initial TiO_2 and TiO_2/PDMS composites: glass transition temperatures, T_g, normalized heat capacity change at the glass transition, $\Delta C_{p,n}$, rigid amorphous polymer fraction, *RAF*, mobile amorphous polymer fraction, *MAF*, crystallization, cold crystallization, and melting temperatures, T_c, T_{cc}, and $T_{m1,2}$, respectively, and degree of crystallinity, X_c, for PDMS and TiO_2/PDMS systems.

sample	T_c (°C)	X_c (wt) (±5%)	T_g (°C) (±0.5)	$\Delta C_{p,n}$ (J/gK) (±0.02)	*RAF* (wt) (±10%)	*MAF* (wt) (±10%)	T_{cc} (°C)	T_{m1} (°C)	T_{m2} (°C)
TiO_2/(5 wt%)PDMS–1000	–	0.00	–126	0.05	0.85	0.15	–	–	–
TiO_2/(10 wt%)PDMS–1000	–99	0.03	–128	0.06	0.79	0.18	–	–49	–43
TiO_2/(20 wt%)PDMS–1000	–89	0.23	–128	0.08	0.58	0.19	–	–51	–41
TiO_2/(40 wt%)PDMS–1000	–88	0.47	–128	0.11	0.35	0.18	–74	–50	–41
TiO_2/(80 wt%)PDMS–1000	–96	0.57	–130	0.19	0.18	0.25	–98	–53	–40
PDMS–1000 neat	–82	0.65	–127	0.22	0.12	0.23	–93	–49	–39
TiO_2/(5 wt%)PDMS–20	–	0.00	–125	0.08	0.86	0.14	–	–	–
TiO_2/(10 wt%)PDMS–20	–	0.00	–128	0.10	0.82	0.18	–	–	–
TiO_2/(20 wt%)PDMS–20	–	0.00	–130	0.27	0.52	0.48	–98	–58	–46
TiO_2/(40 wt%)PDMS–20	–	0.00	–132	0.41	0.27	0.73	–96	–60	–49
TiO_2/(80 wt%)PDMS–20	–	0.00	–134	0.49	0.13	0.87	–92	–65	–58
PDMS–20 neat	–	0.00	–134	0.56	0.00	1.00	–91	–66	–58

We can now calculate from the data for the glass transition, in particular from the heat capacity step, $\Delta C_{p,DSC}$, the Rigid and Mobile Amorphous polymer Fractions, *RAF* and *MAF*, respectively, employing a '3–phase model' (*CF* + *MAF* + *RAF*) [Dobbertin96] and Eqs. (3.4, 3.5).

RAF varies between 0.85 and 0.18 wt for TiO_2/PDMS–1000 and, quite similarly, between 0.86 and 0.13 for TiO_2/PDMS–20 (Table 9.2). From the present data we cannot distinguish RAF_{int} and RAF_{cryst} for the nanocomposites, as the extent of effects of X_c simultaneously with polymer immobilization on the surfaces on *RAF* are not clear [Purohit14]. However, *RAF* in Table 9.2 for neat PDMS–1000 represents uniquely RAF_{cryst} (0.12 wt), while in case of all PDMS–20 based systems *RAF* represents RAF_{int} since X_c=0. Considering the increased X_c in samples based on PDMS–1000 and the above discussion about RAF_{int} and RAF_{cryst}, practically no changes of *RAF* at the interfaces are observed between 5 and 80 wt% adsorbed polymer, in both PDMS–1000 and PDMS–20 composites (Table 9.2). In agreement with S_{BET} results, this suggests high degree of immobilization of the polymer in the TiO_2 aggregates, in general. Moreover, up to about 40 wt% PDMS each grown polymer layer seems to depend on the surface roughness (S_{BET}, Table 9.1) of the previous layer (*shell*), this being indicative of the *core–shell* character of these nanocomposites. As polymer adsorption increases the fraction of *RAF* decreases at the benefit of bulk mobility (Table 9.2, *MAF*) and, for TiO_2/PDMS–1000, also crystallization (Table 9.2).

9.3.4. Molecular dynamics (DRS)

9.3.4.1. Raw data and analysis of the DRS spectra

Before we proceed with discussion on molecular mobility, we would like to briefly present some quantitative results for the real part of dielectric permittivity of the systems under investigation. Dielectric permittivity, ε', for initial PDMS of both types and initial TiO_2 was recorded equal to 3.1 and 10.2 (Fig. 9.6), respectively, at –150 °C and equal to 3.1 and 12.0, respectively, at 30 °C (not shown). The respective values for TiO_2/PDMS composites of various compositions are located between the values of the initial components. However, the changes with composition do not follow the predictions of Effective Medium Theories (EMT) [Pelster01], providing additional support for strong polymer–filler interactions and possibly increased polarization at the interfaces [Klonos15A].

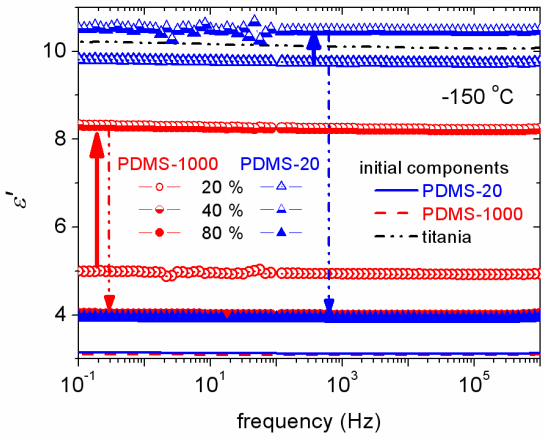

Fig. 9.6. Real part of dielectric permittivity, ε', against frequency at –150 °C for initial components (lines), for nanocomposites with 20 wt% (open symbols), 40 wt% (semi–solid symbols) and 80 wt% (solid symbols) adsorbed polymer. The arrows mark changes imposed by the gradual increase of the adsorbed polymer from 20 to 40 and to 80 wt%.

We will now focus on DRS recordings of segmental dynamics, related to glass transition. Results are representatively presented here in the form of frequency and temperature dependence of the imaginary part of dielectric permittivity (dielectric loss) ε'' (isothermal plots of Fig. 9.7 and isochronal plots of Fig. 9.8, respectively). Isochronal plots of Fig. 9.8 facilitate comparison with the DSC thermograms in the temperature range from –140 to –120 °C in Figs. 9.5e,f. A higher frequency of 3 kHz has been selected for the plots, aiming to suppress effects of conductivity [Kremer02].

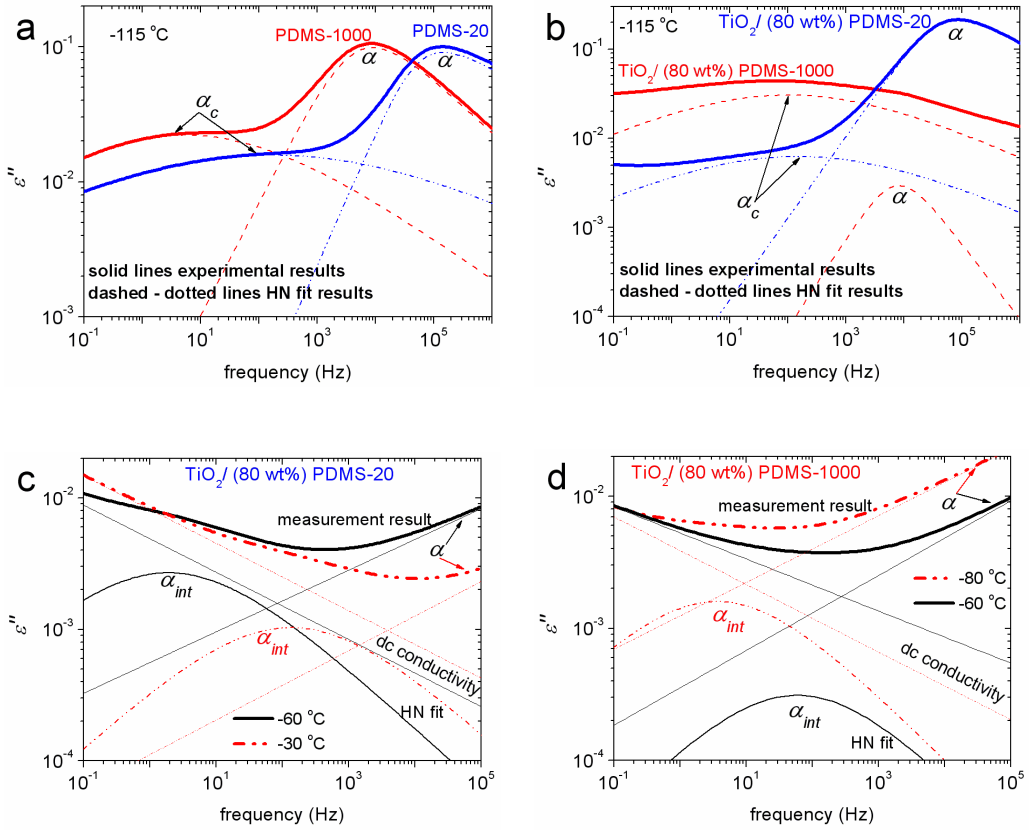

Fig. 9.7. Imaginary part of dielectric permittivity (dielectric loss), ε'', against frequency at selected temperatures, showing experimental results and the respective analysis results, in terms of individual Havriliak–Negami (Eq. (3.6)) components, for each of the segmental relaxations (α, α_c, α_{int}), and dc conductivity in (a) neat polymers and (b–d) nanocomposites with 80 wt% PDMS.

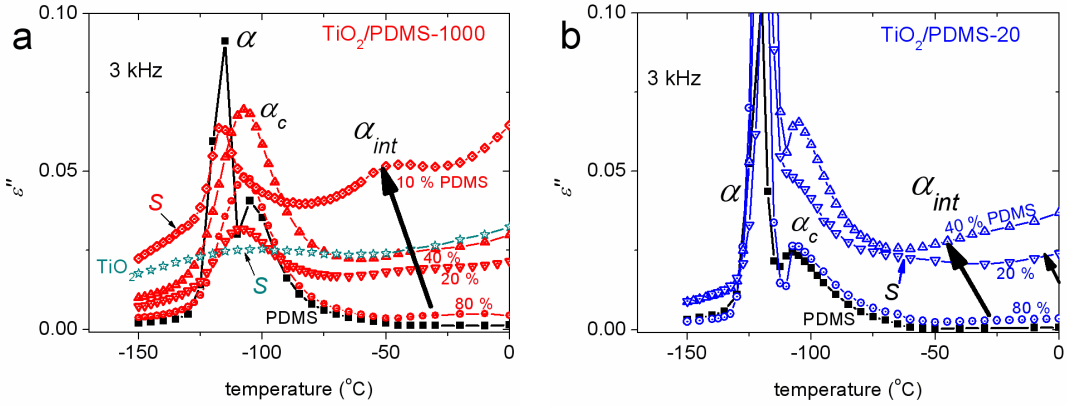

Fig. 9.8. Comparative isochronal plots of the imaginary part of dielectric permittivity, ε'', at 3 kHz, replotted from DRS isothermal measurements for (a) TiO_2/PDMS–1000 composites and (b) TiO_2/PDMS–20 composites, in the temperature region from –150 °C to 0 °C. Included, in both (a) and (b), are the respective plots of initial TiO_2 and neat PDMS. Indicated are the dielectric relaxation mechanisms related to segmental dynamics (i.e. α, α_c and α_{int}) and the relaxation of surface –OH (hydroxyls) groups of TiO_2 (i.e. *S*).

DRS results were analyzed by fitting the asymmetric Havriliak–Negami (HN) equation (Eq. (3.6)) [Havriliak67] to the experimental data [Kremer02] (examples of fitting are shown in Fig. 9.8). By plotting the frequency of maximum of ε'' against reciprocal temperature for the three segmental relaxations, the Arrhenius plot of Fig. 9.9a was constructed. In Fig. 9.9b we present the reciprocal temperature dependence of $\Delta\varepsilon$ for the relaxations of all compositions studied.

9.3.4.2. Bulk–like segmental dynamics (α and α_c relaxations)

α relaxation at around 10^4–10^5 Hz in Figs. 9.7a,b and at –120 °C in Fig. 9.8a,b is associated with the glass transition of the bulk amorphous polymer fraction [Klonos10A, Klonos12, Klonos15A]. α (characterized by mean values of the shape parameters over the temperature range of the relaxation α_{HN}~0.35, β_{HN}=0.9) is recorded for all cases of PDMS samples (composites and neat PDMS). According to the results on shape parameters, α could be satisfactorily fitted only with the asymmetric HN, uniquely among the recorded segmental relaxations, as expected for bulk (unaffected) dynamics [Ezquerra04]. Comparing the two types of PDMS chains, it is observed in Fig. 9.10 that for the shorter polymer chains (PDMS–20) the relaxation is faster (Fig. 9.9a) and stronger (Fig. 9.9b).

Next to α, at around 10^1–10^2 Hz in Figs. 9.7a,b and at –110 °C in Figs. 9.8a,b, α_c relaxation originates from polymer chains restricted either between condensed crystal regions [Klonos10A] (i.e. case of neat PDMS–1000) or in the voids between nanoparticles in their aggregates (i.e. case of nanocomposites) [Klonos15A]. This dual character of the α_c relaxation (characterized by mean values of the shape parameters over the temperature range of the relaxation α_{HN}~0.30, β_{HN}=1), concerning the type of spatial restriction of the PDMS chains, requires that the discussion should be divided into two parts, low (10–40 wt% PDMS) and higher polymer content samples (80–100 wt%). For low PDMS contents α_c originates from the reduced segmental mobility of PDMS chains inside the voids, i.e. above the interfacial polymer layer.

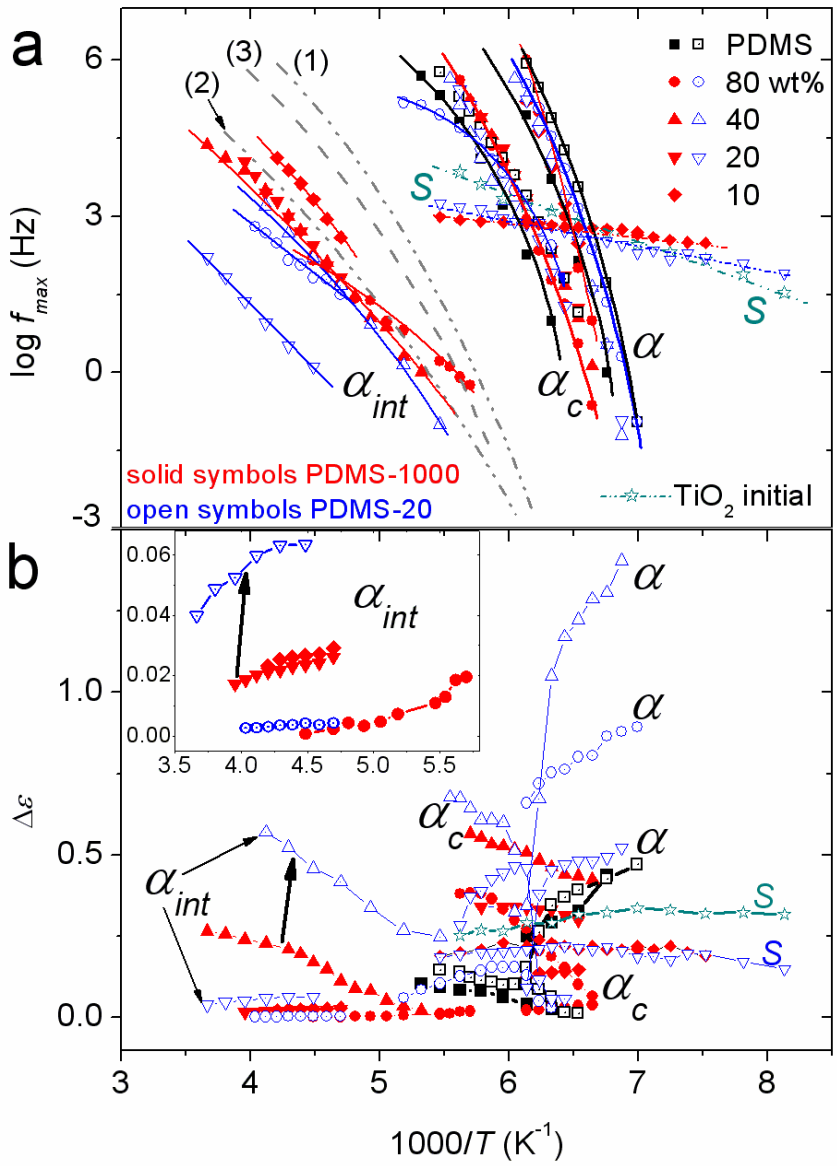

Fig. 9.9. (a) Arrhenius plots and (b) dielectric strength vs reciprocal temperature of the local relaxation (*S*) and segmental relaxations: bulk polymer (α), polymer restricted in voids and crystal regions (α_c) and interfacial polymer (α_{int}) dynamics for TiO_2/PDMS composites, neat PDMS and initial TiO_2. The red solid symbols correspond to TiO_2/PDMS–1000 systems, the blue open symbols correspond to TiO_2/PDMS–20 and the green open stars correspond to initial TiO_2. The lines that connect the experimental data for the recorded relaxations in (a) are fittings of the VTFH [VTFH] and Arrhenius [Arrhenius1889] equations. In (a), the dash–dotted lines correspond to the interfacial relaxation in conventional (1) PDMS/silica and (2) PDMS/titania nanocomposites (Chapter 4), while line (3) describes α_{int} in nanocomposites based on PDMS–1000 and silica of high specific surface area (Chapter 5). The inset in (b) shows in more detail the region of α_{int} relaxation. The arrows in (b) mark representative changes in α_{int} between PDMS–1000 and PDMS–20.

For the samples with 10–40 wt% PDMS we follow in Fig. 9.9a that the time scale of α_c is identical, while values of dielectric strength in Fig. 9.9b are rather similar to each other. For the higher polymer content samples, TiO_2/(80 wt%)PDMS and neat PDMS(–1000, –20), we recall that the DSC results in Table 9.2 show crystallization events (either at cooling or at heating, at 10 K/min). Considering now that during DRS measurements the samples stay at different temperatures (isothermals) for about 10 minutes at each temperature, this procedure of measurement could be thought of as a type of multi–temperature crystallization annealing, which, for sure, leads to increased degree of polymer crystallinity, most probably higher than in DSC at standard cooling–heating. This could be the explanation for recording α_c relaxation in both neat PDMS–1000 and PDMS–20 and composites of 80 wt% PDMS. For neat PDMS–20, α_c is faster (Fig. 9.9a) and weaker (Fig. 9.9b) than for PDMS–1000. This suggests that the constraints imposed by the PDMS–20 crystals are, possibly, more loose than those imposed by the crystals of PDMS–1000. This may be also related to lower density (worse quality) of PDMS–20 crystals, manifested by lower melting points in DSC (Table 9.2, $T_{m1,2}$), as compared to PDMS–1000. The respective trends (both in timescale and strength) of the relaxation in the samples of 80 wt% PDMS are quite similar for both types of PDMS, suggesting a balance in the interplay between effects arising from the extent of volume restriction (volume between crystals and volume of voids between nanoparticles) and from the average length of polymer chains.

One might expect that the mobility of polymer chains restricted in a volume in a scale of tens of nm could be, also, dominated by confinement effects [Kremer14], thus its dynamics (in our case α_c relaxation) could be faster than that in bulk. In previous studies of PDMS in well defined cylindrical pores (25–35 nm) of anodic aluminum oxide (AAO) [Krutyeva13], in mesopores (5–20 nm) glasses [Schönhals03], and in cylindrical intraparticle cavities (6–20 nm) of silica–gel (Chapter 10, [Klonos15A]) it has been shown that spatial confinement may severely affect the dynamics of polymers, at least for PDMS, in the scale between 1 and 30 nm, in 2–D confinement. Additionally, it has been demonstrated previously [Sundararajan02] that PDMS crystallizes in the form of spherulites of ~20 – 100 μm in diameter. In this case we may expect that the dimension of amorphous polymer between the crystals should be in the scale of 100 nm and higher. Similar is the scale of the dimension of the voids in TiO_2 aggregates in the present study ($R_{p,V}$ in Table 9.1). Consequently, in both cases of volume restriction of PDMS, the spatial dimensions are higher than the confinement scale. These points provide additional support for our interpretation of the α_c relaxation.

9.3.4.3. Local relaxation of –OH groups of titania surface (S relaxation)

S relaxation at ~–105 °C in Fig. 9.8 dominates the response of initial nanooxides. S is thought to represent the local dielectric relaxation mechanism of hydroxyl surface groups of titania (Ti–OH) with attached water molecules [Fontanella09]. *S* relaxation contributes also to the response of TiO_2/PDMS composites, more strongly at lower polymer contents (i.e. 10 wt% PDMS–1000 and 20 wt% PDMS–20 in Fig. 9.8). Results on dried samples and samples hydrated at gradually higher levels (shown partly in the previous Chapter) have clarified its origins. *S* relaxation has been previously recorded also in both neat silica samples [Fontanella09, Klonos15A] and in polymer nanocomposites [Fragiadakis07, Klonos15A, Sulym14, Galaburda14]. The *S* relaxation (characterized by shape parameters α_{HN}~0.40, β_{HN} = 1, mean values over the temperature range of recording) was recorded for the initial TiO_2, TiO_2/(10 wt%)PDMS–1000 and TiO_2/(20 wt%)PDMS–20 samples, slightly suppressed in the nanocomposites (both in time scale and relaxation strength, Figs. 9.9a and b, respectively). Bearing in mind that the *S* relaxation is related to interfacial free –OH groups on the surface of TiO_2 particles [Fontanella09], our findings indicate that the surface coverage of the nanoparticles by PDMS is lower at these low polymer loadings, as compared to higher PDMS loadings, in agreement to FTIR findings (Appendix A.9.3, please compare in Fig. A.9.3 the two FTIR peaks related to –OH groups between initial TiO_2 and the nanocomposites).

9.3.4.4. Interfacial polymer dynamics (α_{int} relaxation)

α_{int} relaxation in the broad range from –50 °C to –20 °C of Figs. 9.7,9.8 represents the dynamics of semi–bound polymer chains in the interfacial layer, with strongly reduced mobility due to hydrogen bonding with TiO_2 [Klonos11, Fragiadakis07, Holt14]. α_{int} is characterized by α_{HN}~0.41, β_{HN} = 1, mean values over the temperature range the relaxation is recorded. α_{int} is recorded in the high temperature–low frequency part of the Arrhenius Diagram (Fig. 9.9a). This means that, in consistency with the raw data in Figs. 9.7,9.8, α_{int} is the slowest among the three segmental relaxations recorded. The main reasons for proposing, now and previously (Chapters 4–6), that α_{int} represents segmental mobility (not local) in the interfacial layer are: (a) α_{int} is absent in neat PDMS, (b) its $f_{max}(T)$ dependence is, in general, of the VTFH type revealing its cooperative character, and (c) its trace of time scale extrapolated to the respective DSC equivalent frequency (~10^{-2} Hz) approaches the region of T_g. Point (c) gains additional support by the previously observed increased T_g values in DSC (section 9.3.3.2) and the simultaneous broadening of glass transition step in the nanocomposites (more clear for PDMS–20) in Fig. 9.5f. The results in Fig. 9.9a suggest

further that α_{int} is, in general, slower for the shorter PDMS chains, i.e. slower for the TiO_2/PDMS–20 samples as compared to the TiO_2/PDMS–1000 samples. As polymer adsorption decreases α_{int} immigrates towards lower frequencies–higher temperatures (i.e. its dynamics slows down) and cooperativity decreases (becomes more Arrhenius–like), except for the case of TiO_2/(10 wt%)PDMS–1000, where α_{int} is recorded faster than in any other sample. This exceptional behavior is related to the higher interfacial water content for this sample (main discussion in Chapter 8).

At the same time, by comparing samples of the same polymer amount between PDMS–20 and PDMS–1000, we observe that the strength of the respective α_{int} relaxation, $\Delta\varepsilon$ in Fig. 9.9b, is stronger in the case of shorter polymer chains. $\Delta\varepsilon$ seems to change with composition not in a systematic way. The same was found true previously for the changes of ε' with composition (Fig. 9.6). These results can be explained in terms of increased orientational polarization in the interfacial layer [Klonos10A, Klonos10B], which results in increased dielectric response of the samples with lower PDMS content (5 to 40 wt% PDMS), where the interfacial to bulk polymer ratio is higher, as compared to samples with higher PDMS content (80 wt%) (Scheme 9.1).

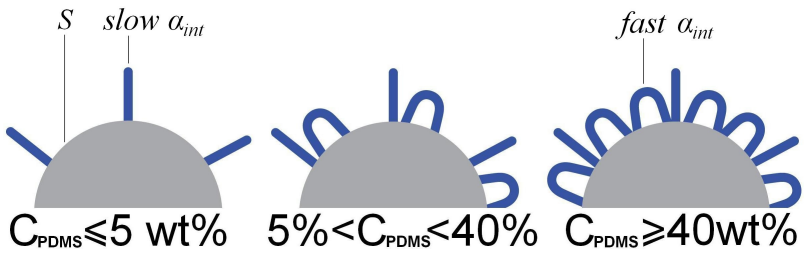

Scheme 9.1. Schematic view of the different polymer chain conformations for the gradually increasing PDMS concentration

Similar effects have been observed in previous work on fumed silica/PDMS–1000 core–shell systems in Chapters 5 and 6, suggesting that the adsorption of PDMS in the first layer(s) onto the surfaces of the oxide particles proceeds via two, at least, chain segment conformations at the interfaces, which can be considered responsible for the molecular mobility recorded by DRS as interfacial α_{int} relaxation process: (a) extended tails with bulk like density but reduced mobility and cooperativity and (b) flattened chain segments in the inner quite dense region due to multiple contact points with the silica surface (Scheme 9.1) [Koga12, Kritikos13]. It has been also suggested that for low polymer contents (up to 40 wt%) the tails can be mobile enough to cooperate with each other, but being distributed

sparsely on the surfaces of the nanoparticles their cooperativity length (ξ) [Donth01] is relatively large [Hodge97]. Both conformations are characterized by increased orientation (order), implying high polarizability and increased ε', ε'' and $\Delta\varepsilon$ values [Klonos15A, Klonos15B]. Results obtained in the present work with the titania–based materials at low PDMS contents, 10 – 40 wt%, are similar to those obtained with the silica–based materials (Chapter 5). On the other hand, for higher polymer adsorption (i.e. 80 wt% PDMS), the loops/tails ratio increases in population, resulting in higher degree of cooperativity (decreased ξ length) (Scheme 9.1c) [Hodge97]. In combination with cooperative motions of the tails, the additional polymer layers that cover and disturb the initial layer(s) imply serious obstacles to the orientation of the tails and, thus, the dielectric response (ε' in Fig. 9.6 and $\Delta\varepsilon$ in Fig. 9.9b) decreases. This interpretation of the results obtained with the silica–based materials fits, again, very well with the present results for samples with 80 wt% PDMS.

Concerning now the effects imposed by the different molecular weight of PDMS, we suggest that the shorter polymer chains of PDMS–20 are folded at a lower extent (increased concentration of free chain ends) than those of PDMS–1000, resulting in easier adopting of contact points and higher orientation (stretching) onto the surfaces of TiO_2 (Scheme 9.2). The opposite should be true for PDMS–1000, where the increased concentration of folds along each chain most probably hinders the orientated conformations (tails), and, promotes, this way, loop–like conformations in the interfacial layer (Scheme 9.2). Support to the above suggestions is given here in Fig. 9.9 in which we observe that α_{int} for titania/PDMS–1000 is faster with increased cooperativity (more VTFH–like) (Fig. 9.9a) and suppressed $\Delta\varepsilon$ (Fig. 9.9b), as compared to titania/PDMS–20.

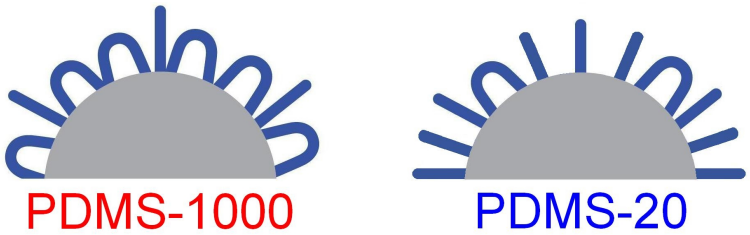

Scheme 9.2. Simplified model for the description of the different polymer chain conformations for the polymer nanocomposites based on (left) PDMS–1000 with long chains and (right) PDMS–20 with shorter chains.

9.3.4.5. Evaluation of the interfacial polymer fraction (RAF_{int})

We can now discuss the not systematic changes of $\Delta\varepsilon$ with composition in our samples in Fig. 9.9b. We calculate the reduced mobility polymer fraction RAF_{int} (the fraction of polymer in the interfacial layer) by Eq. (3.10). Results of RAF_{int} for all samples are shown in Fig. 9.10a, comparatively with results for RAF obtained with DSC.

RAF_{int} is larger for PDMS–20 and decreases systematically with polymer content. As discussed above, the increase of concentration of nanoparticles in the polymer composites results in increased polymer/particle interfacial area and, subsequently, higher interfacial polymer fraction. This result was reflected in the suppression of $\Delta C_{p,n}$ in DSC measurements (Table 9.2). In contrast to DSC, in the case of DRS measurements the polymer in the interfacial layer is thought mobile (represented by α_{int} process) and at the same time it seems to imply additional polarization, increasing both ε' and $\Delta\varepsilon$ in DRS. According to previous dielectric studies on polymer thin films adsorbed on solid substrates [Capponi12], one would suggest that this fact (increased polarizability in the interfacial layer) is inconsistent with the use of Eq. (3.10) for our calculations. Nevertheless, the calculations of RAF_{int} via the simple Eq. (3.10) revealed the higher effects of internal polarization due to the interfaces for low polymer loading between the two types of PDMS (Fig. 9.10a).

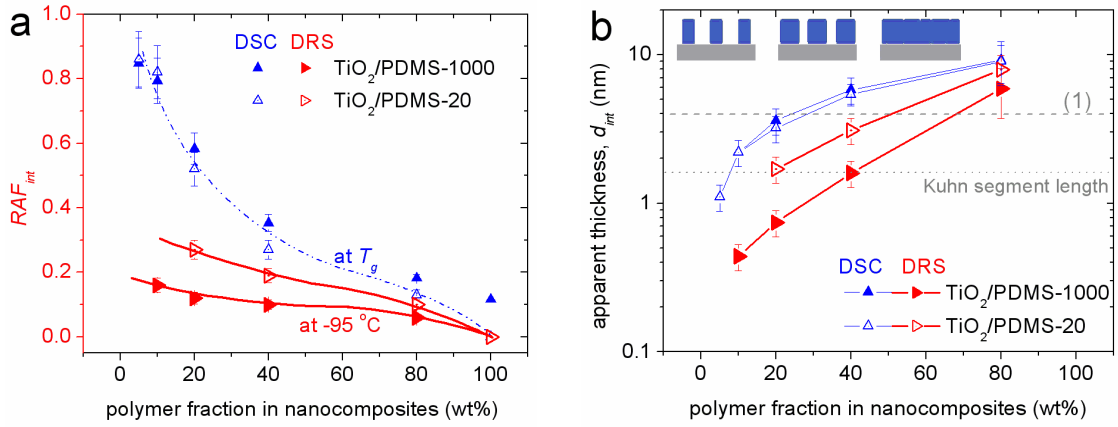

Fig. 9.10. (a) interfacial polymer fraction, RAF_{int}, calculated from the additive contribution of α_{int} relaxation to the total dielectric relaxation strength of segmental mobility, $\Delta\varepsilon$, at –95 °C, in DRS (black symbols, solid lines) and rigid amorphous polymer fractions, RAF, at T_g, from the suppression of ΔC_p in DSC measurements (red symbols, dash–dot lines). The lines are used as guides to the eyes. (b) interfacial layer thickness, d_{int}, as estimated from DRS and DSC results. Line (1) in (b) corresponds to d_{int} in conventional PDMS/titania nanocomposites (Chapter 4) [Klonos10A]. The inset schemes in (b) present our estimation for the gradual polymer adsorption at the surface of titania.

9.3.4.6. Evaluation in terms of thickness of the interfacial polymer layer (d_{int})

A term often used to describe the extent of polymer–particles interactions [Holt14, Harton10] is the *thickness of the interfacial polymer layer*. A quite useful tool for employing such calculation here is the knowledge of S_{BET} value for the initial titania aggregates (Table 9.1). Thus, assuming that (i) the whole oxide surface area (S_{BET}) is accessible to PDMS chains, and (ii) the density of PDMS in the interfacial layer and in bulk is constant and equal to that of neat PDMS, we estimate the '*apparent*' interfacial layer thickness, d_{int}, by the simple Eq. (5.1). The results show that d_{int} increases in general with the adsorbed polymer fraction in Fig. 9.10b varying between 0.4 and ~6 nm for titania/PDMS–1000 and between 1.5 and ~7 nm for titania/PDMS–20.

The absolute values of d_{int} seem relatively low for the lower polymer contents, but most probably results could be rationalized in the sense of not uniform coverage of titania surface at low polymer loadings (formation of separated islands of interfacial polymer, insets to Fig. 9.10b). The latter is supported by recording *S* relaxation for low polymer loadings, suggesting a significant amount of free Ti-OH groups on the surface of particles, i.e. not engaged by PDMS chains (scheme 9.1). Moreover, the above results are consistent with other findings for low polymer loading; on the one hand, with changes in aggregation observed in PSD (section 9.3.1) and SEM (section 9.3.2) and, on the other hand, by the recording of bulk mobility (namely, existence of glass transition in DSC and α relaxation in DRS) for the same nanocomposites compositions. Thus, in the frame of the above assumption (i) the used S_{BET} in Eq. (5.1) is higher than the really covered (by PDMS) surface of titania, at least for low PDMS adsorption. As expected with polymer adsorption increasing values demonstrate a saturation-like trend, showing a maximum at ~6 nm, this value being, within the experimental error, similar for both types of PDMS.

The case of high polymer loading (20 wt% titania) in core-shell nanocomposites here, resembles that of conventional nanocomposites, which are in general loaded with ≤50% nanoparticles, while nanocomposites of higher loadings have been more rarely studied [Sargsyan07, Wurm10, Holt13, Holt14]. In addition the relatively high d_{int} for 80 wt% PDMS can be understood in terms of increasing of void volume at polymer loadings ≥ 40 wt% (increasing of distance between particles / aggregates). Kumar and coworkers have pointed to the primary role of polymer kinetics on the filler distribution and aggregation of nanoparticles in a polymer matrix [Khan09, Kalathi14], while they have discussed [Gong14] the relation between d_{int} in polymer nanocomposites and the *Kuhn segment length* (~1.56 nm for PDMS [Gilra14]) of the respective polymer. The latter should be an upper limit for confined chain

segments at the interfaces [Gong14]. This was not found true here. In combination with the discussion above (changes in aggregation, selective polymer adsorption on the surface), it seems more likely that the evaluation of interfacial layer thickness has possibly different physical meaning between conventional and core-shell type nanocomposites. From the methodological point of view, we can observe in Figs. 9.10a,b that the results for RAF_{int} and d_{int} by the two techniques coincide better (quantitative agreement also) at higher polymer loadings. This has been observed also in previous work in polymer nanocomposites (Chapter 4 and [Galaburda14]).

Finally, we may compare our findings with those in previous work on PDMS/titania and PDMS/silica conventional nanocomposites (Chapter 4), i.e. spherical silica particles *in situ* generated and well dispersed in a matrix of crosslinked PDMS (MW ~18000). Significant similarities with respect to the interfacial dynamics were recorded in the present work. In Fig. 9.9a lines (1) and (2) were added, representing the dynamics of PDMS in the interfacial layer of silica and titania, respectively, in the conventional nanocomposites mentioned above. The traces of α_{int} for conventional and core–shell type titania/PDMS nanocomposites are quite similar. Interestingly, d_{int} was calculated ~2 nm for PDMS/silica, whereas d_{int} was found almost double for PDMS/titania (line 1 in Fig. 9.10b). The difference between the α_{int} traces and d_{int} between the two types of filler (α_{int} slower and d_{int} higher for titania) was thought to originate from the stronger hydrogen bonding between the –OH of titania with PDMS (Ti–OH more acidic than Si–OH [Bokobza10]). This suggestion was proved rather weak, as we recently showed that the traces of α_{int} in the Arrhenius plot at 40 wt% (almost identical to line 2 in Fig. 9.9a) and 80 wt% (line 3 in Fig. 9.9a) polymer loadings were found to coincide with the trace of lines (2) and (1), respectively, in Fig. 9.9a. Moreover, thermal annealing of the systems at the temperature of PDMS crystallization was found to slow down and weaken α_{int} relaxation, especially in the case where no PDMS crystallization is promoted (nanocomposites with 40 wt% PDMS). Thus, similarly to Chapters 5–7, we confirm also here that the differences in the strength of polymer–particle hydrogen bonding, arising from the type of metal–oxide particle, do not form the main factor that affects interfacial effects. In terms of models proposed for the description of conformations of polymers adsorbed onto a solid surface [Koga12, Klonos15A], the interfacial segmental polymer dynamics should be ruled more strongly by: (a) the concentration and accessibility of contact points (increasing with surface roughness of the particles in Chapter 7 and with interfacial water content in Chapter 8), and (b) the structure and flexibility of polymer chain (e.g. in Schemes 9.1,9.2).

9.4. Conclusions

Effects of structure / surface characteristics of titania nanooxides on the fraction and dynamics of physically adsorbed polydimethylsiloxane nanocomposites of the *core–shell* type were in the center of interest in this Chapter. Moreover, effects of polymer chain length on the development of PDMS onto the low specific surface area (S_{BET} ~25 m^2/g) of spherical titania (TiO_2) nanoparticles (~70 nm in average diameter) were studied employing nitrogen adsorption–desorption isotherms, morphology (SEM), thermal (DSC) and dielectric (DRS) techniques.

The TiO_2 nanoparticles were aggregated with each other in the 10^2 nm scale, forming intraparticle *meso*– and *macro*–pores (voids). Results indicate that during the first stages of *layer–by–layer* polymer adsorption strong hydrogen bonding has been developed between the surface hydroxyls of titania and the oxygens of the backbone of PDMS, resulting in high coverage of TiO_2 surfaces.. The adsorption on the initial interfacial layers leaded to gradual filling of the voids at the polymer content of 40 wt%. The reduction of specific surface area (S_{BET}), corresponding to the reduction of pore (void) volume with polymer content, was stronger in the case of PDMS with longer chains (i.e. PDMS–1000, ~105 monomers/chain) as compared to shorter polymer chains (i.e. PDMS–20, ~22 monomers/chain). However, employing the high resolving power of DRS we were able to reveal that the fraction of interfacial PDMS chains is higher and the respective dynamics (α_{int} process) is slower for the short polymer chains as compared to longer chains. This last result could be interpreted in terms of increased number of contact points of the short PDMS chains with the surface of titania. In terms of interfacial layer thickness, similar values (~6 nm in apparent values) were obtained for both short and long PDMS chains in nanocomposites.

From the methodological point of view, the isothermal gas adsorption–desorption method was proved able to describe, in a sufficiently good degree, changes in the textural porosity due to the adsorption of flexible macromolecules, such as those of PDMS. Comparing with previous works on conventional (Chapter 4) and core-shell (Chapters 5–7) nanocomposites based on PDMS, the characteristics of α_{int} relaxation (time scale, dielectric strength) were found to depend mainly on the surface characteristics of the hosting metal oxide particles (available surface for interaction), rather than on the type of particle (hydrogen bond strength). The present work provides additional support that nanocomposites based on polymer physically adsorbed (although not grafted) on nanoparticles can be considered of the

core–shell type and that they can provide, among others, an alternative system for the investigation of molecular dynamics of polymer adsorbed onto a solid surface.

APPENDIX A.9

A.9.1. Textural characterization of initial oxides and nanocomposites

The textural characteristics of TiO_2 and TiO_2/PDMS (5 – 40 wt% PDMS) systems were studied employing low temperature (77.4 K) nitrogen adsorption–desorption technique [Gunko14] using a Micromeritics ASAP 2405 N adsorption analyzer. Similar measurements for the liquid–like sample at 80 wt% PDMS were not possible. Before measurements the samples were outgassed by heating at 110 ^{o}C in a vacuum chamber. The specific surface area (S_{BET}) was calculated according to the standard BET method [Gregg82]. Additionally, the specific surface area was measured using low temperature desorption of argon. The total pore volume V_p was evaluated by converting the volume of adsorbed nitrogen at $p/p_0 = 0.98 – 0.99$ (p and p_0 denote the equilibrium pressure and the saturation pressure of nitrogen at 77.4 K, respectively) to the volume of liquid nitrogen per gram of the adsorbent.

The nitrogen desorption data were used to compute the pore size distributions (PSDs, differential $f_V \sim dV_p/dR$ and $f_S \sim dS/dR$) using a self–consistent regularisation (SCR) procedure under non–negativity condition ($f_V \geq 0$ at any pore radius R) at a fixed regularisation parameter $\alpha = 0.01$. A complex pore model was used for that with slit–shaped (S) and cylindrical (C) pores and voids (V) between spherical nonporous nanoparticles packed in random aggregates (SCV/SCR model) with model parameters for titania (anatase) and polymer (PDMS) [Gunko14]. The differential PSDs with respect to pore volume $f_V \sim dV/dR$, $\int f_V dR \sim V_p$ were re–calculated to incremental PSD (IPSD) at $\Phi_V(R_i) = (f_V(R_{i+1}) + f_V(R_i))(R_{i+1} - R_i)/2$ at $\sum\Phi_V(R_i) = V_p$). The f_V and f_S functions were also used to calculate contributions of nanopores (V_{nano} and S_{nano} at 0.35 nm < R < 1 nm), mesopores (V_{meso} and S_{meso} at 1 nm < R < 25 nm), and macropores (V_{macro} and S_{macro} at 25 nm < R < 100 nm). Thus, the average radius, R_p, with respect to the pore volume and specific surface area can be calculated from the differential PSD according to the equations

$$<R_{p,V}> = \int_{R_{min}}^{R_{max}} Rf_V(R)dR \Big/ \int_{R_{min}}^{R_{max}} f_V(R)dR \quad \text{and} \quad <R_{p,S}> = \int_{R_{min}}^{R_{max}} Rf_S(R)dR \Big/ \int_{R_{min}}^{R_{max}} f_S(R)dR\,,$$

respectively, where $R_{min} = 0.35$ nm and $R_{max} = 100$ nm.

A.9.2. X–ray analysis

X–ray diffraction (XRD) patterns were recorded in 2θ range between 10° and 60° employing a DRON–3M (Burevestnik, St.–Petersburg, Russia) diffractometer using CuK_α radiation (λ=0.15418 nm) in combination with a Ni filter. The average size of titania nanocrystallites was estimated according to the Scherrer equation [Gorelik70]. Titania crystalline structure was analyzed using the JCPDS Database [JCPDS01].

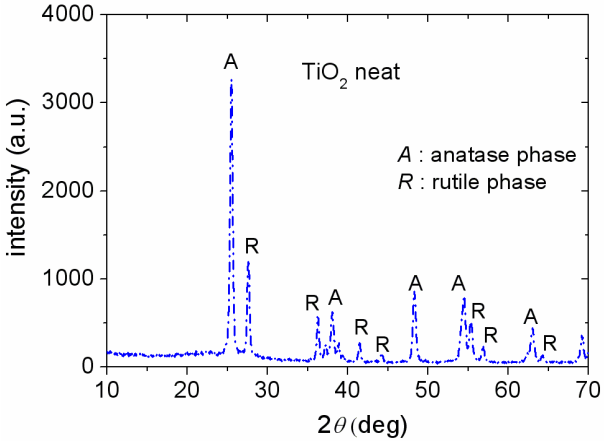

Fig. A.9.2. X–ray diffraction patterns for initial pyrogenic TiO_2. A – identifier of anatase phase, R – identifier of rutile phase.

A.9.3. Fourier transform infrared spectroscopy (FTIR)

FTIR spectra of powdered samples (grinded with KBr at the mass ratio 1:9) over the 400 – 4000 cm^{-1} range were recorded employing a ThermoNicolet FTIR spectrometer in diffuse reflectance mode.

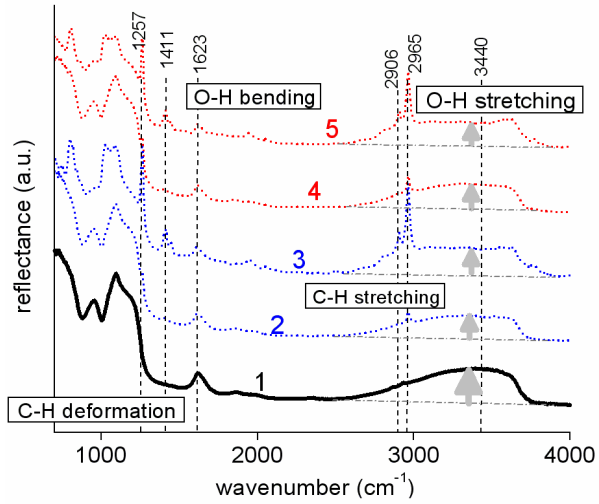

Fig. A.9.3. FTIR spectra of (1) neat TiO_2, (2, 3) TiO_2/PDMS–20 and (4, 5) TiO_2/PDMS–1000, at X_{PDMS} = 5 wt% (2, 4) and 40 wt% (3, 5).

10. Effects of surface modification and thermal annealing on interfacial and confined polymer dynamics of PDMS adsorbed at the interfaces and in the pores of silica–gel

10.1. Introduction

Polymers constrained to spatial dimensions less than about 100 nm typically exhibit a shift of glass transition to lower temperatures and an acceleration of segmental dynamics as compared to the bulk, often discussed in terms of less intermolecular constraints and greater unoccupied volume [Krutyeva13, Fukao00, Floudas97]. Confinement is a widely used term for the description of the above effects. The extent of confinement depends, among other factors, on the characteristics of the confining surface and the chemical properties of the polymer [Kremer14], on the type of the confining medium (solid inorganic or polymeric [Colmenero14, Colmenero10]), and the space dimensionality of the latter (1D [Napolitano11], 2D [Chrissopoulou13, Schönhals03], and 3D [Yabu14]).

A strong correlation between the behavior of polymers under confinement and the presence of the layers directly adsorbed onto supporting solid substrates has been widely suggested [Guiselin91, Napolitano14, Rotella11, Vanroy13, Capponi12]. To that aim, analytical models have been proposed describing the evolution of polymer adsorption [Napolitano14], in combination with chemical and thermal annealing procedures during adsorption [Guiselin91, Rotella11, Capponi12]. In addition, Schönhals *et al.* [Schönhals03] and more recently Colmenero and coworkers [Krutyeva13] studied the interplay between surface and confinement effects, by manipulating the surface interactions (from maximum to zero) of polymers inside cylindrical pores (2D). For polydimethylsiloxane (PDMS) [Schönhals03, Krutyeva13], the polymer of interest in the present work, the confining length

with an upper limit of 30 nm has been discussed in relation to the cooperativity length of the glass transition [Hodge97].

In this chapter we study the interplay between confined, interfacial, spatially constrained and bulk dynamics in the same polymer nanocomposite systems, through the study of linear PDMS physically adsorbed (by hydrogen bonding) on silica–gel particles of high intraparticle porosity. The specific system offers the possibility to study the interfacial dynamics of the adsorbed polymer simultaneously with the 2–D confined dynamics, both coexisting in the 6–20 nm in diameter cylindrical–like pores of silica–gel. In order to manipulate the surface and study in more depth the above effects, we modify here both the surface and porosity characteristics of the initial silica–gel by generating small amorphous zirconia nanoparticles on silica particles, before the adsorption of the polymer [Sulim09]. The investigation involves differential scanning calorimetry (DSC) for thermal transitions and dielectric relaxation spectroscopy (DRS) for segmental dynamics. Surface and confinement effects were also studied employing different thermal treatments (annealing of crystallization), which have been proved quite revealing in our previous study on similar nanocomposites (chapters 4,5 and [Klonos12, Klonos15A, Klonos15C]).

10.2. Materials

Commercial silica–gel Si–60 (Merck) was used as the substrate for the development of zirconia nanoparticles [Sulim09] at various amounts by reiteration of the zirconia reaction cycle from 1 to 4 (resulting in ~6 to 16 wt% ZrO_2, respectively, Table 10.1). Linear polydimethylsiloxane (PDMS, Kremniypolymer, Zaporozhye, Ukraine, molecular weight *MW* ~ 7960, degree of polymerization 105, $–CH_3$ terminated) was adsorbed at the amounts of 40 and 80 wt% from hexane solution of PDMS (1 wt% PDMS) onto dried silica–gel samples [Sulim09].

Seven polymer nanocomposite compositions were prepared and studied in the present chapter, the initial PDMS, silica/PDMS with 40 and 80 wt% PDMS and silica/zirconia/PDMS, containing modified silica with 1 and 4 cycles of zirconia, again with 40 and 80 wt% PDMS. Throughout the chapter, specific code names that describe the samples are used. For instance (i) *Si60Z1P40* corresponds to the sample in which PDMS at 40 wt% is adsorbed onto 60 wt% Si–60 that previously suffered 1 cycle of zirconia reaction (i.e. ~6 wt% ZrO_2), (ii) *Si60Z4P80* corresponds to the sample in which PDMS at 80 wt% is adsorbed onto 20 wt% Si–60 that previously suffered 4 cycles of zirconia reaction (16 wt% ZrO_2), and (iii)

Si60P80 corresponds to the sample in which PDMS at 80 wt% is adsorbed onto 20 wt% Si–60 that has not suffered any zirconia reaction.

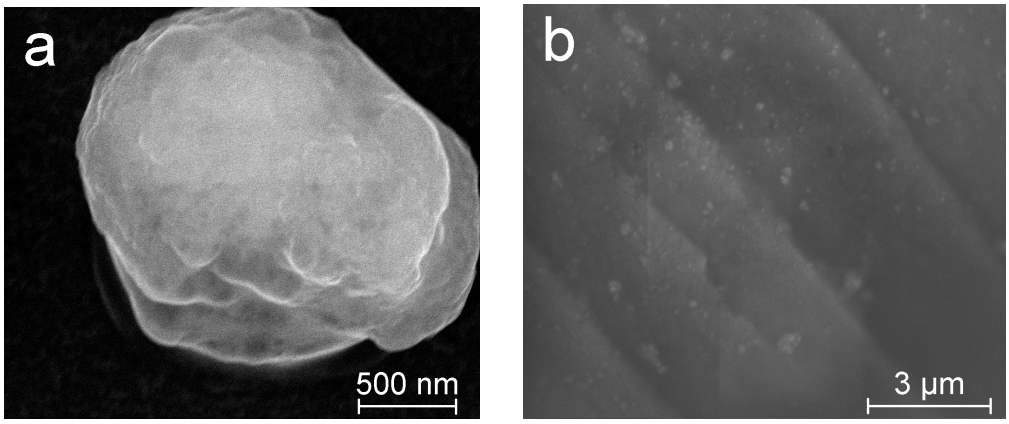

Fig. 10.1. SEM images of (a) a large Si−60 globule and (b) Si60P80 nanocomposite

10.3. Results

10.3.1. Structural characteristics of materials under investigation

We will now describe briefly the modification of silica–gel before polymer adsorption [Sulim09]. Silica–gel Si–60 consists of porous globules with rigidly binding and tightly packed large spherical particles (0.5–1.0 μm in diameter, SEM images in Fig. 10.1) [Klonos15A], with rather smooth surface, characterized by intra–particle cylindrical pores with diameters between 6 and 20 nm [Sulim09]. The initiator of zirconia synthesis ($Zi(acac)_3$) reacted with the free silanol (≡Si–OH) groups of silica–gel (both in the inner and external surfaces) forming ≡Si–$Zi(acac)_3$ groups, on which zirconia nanoparticles were subsequently generated. According to FTIR [Sulim09] the coverage of the free silanols was not complete. It should be noted that zirconia seems to suppress, in general, the concentration of free hydroxyl groups in the modified Si–60 particles. We should also report that according to a study of fumed silicas (aerosils) modified with zirconia via different techniques, contribution of nano–zirconia to the concentration of free –OH in the mixed oxides is a controversial issue [Kickelbick12].

Table 10.1

Surface and porosity characteristics of initial unmodified and modified Si–60 oxides. Z1 and Z4 correspond to 1 and 4 reaction cycles of zirconia grafting, respectively. Zirconia content, C_{ZrO2}, specific surface area as recorded by Nitrogen adsorption–desorption isotherms, S_{BET}, average pore volume, V_p, average volume of mesopores (2 nm < *pore diameter* < 50 nm), V_{meso}, and macropores (50 nm < *pore diameter*), V_{macro}, average pore diameter, $<2R_p>$.

Oxide	C_{ZrO2} (wt%)	S_{BET} (m^2/g)	V_p (cm^3/g)	V_{meso} (cm^3/g)	V_{macro} (cm^3/g)	$<2R_p>$ (nm)
Si60 unmodified	0	384	0.788	0.752	0.032	11.0
Si60Z1	5.6	388	0.770	0.685	0.084	10.4
Si60Z4	16.0	355	0.625	0.612	0.008	9.6

According to XRD measurements [Sulim09], zirconia of ~3–10 nm in diameter was found to be in the amorphous state, while its content, C_{ZrO2}, was found equal to ~6 wt% and 16 wt% for 1 and 4 cycles of grafting reaction, respectively. The specific surface area, S_{BET}, of initial Si–60, representative for polymer–silica interaction area, was measured employing nitrogen adsorption isotherms [Gunko05] to 384 m^2/g (Table 10.1) [Sulim09]. S_{BET} was slightly increased to 388 m^2/g after the 1st reaction cycle and, subsequently, reduced to 355 m^2/g after the 4th reaction cycle [Sulim09]. The cylindrical–like meso–pores of silica–gel (6–20 nm in diameter) [Sulim09] form the main accessible regions for Nitrogen adsorption, contributing strongly to the high S_{BET} values. The initial increase of S_{BET} after the 1st zirconia reaction cycle was suggested to originate mainly from the growth of small zirconia nanoparticles on the external surfaces of Si–60. Therefore, increase in macroporosity (V_{macro}) was observed after the 1st cycle of zirconia reaction (Table 10.1, although absolute values of V_{macro} are low, in general [Gunko13B]), simultaneously with a slight decrease of pore volume by ~2 % for V_p and 9 % for V_{meso} (Table 10.1). The further increase of zirconia content after the 4th reaction cycle resulted in significantly lower S_{BET}, indicating the additional growth of nanozirconia on the walls inside the cylindrical pores of Si–60, suppressing further V_p and V_{meso} by ~21 % and 19 %, respectively (Table 10.1). The pores were not filled fully by zirconia, in any case [Sulim09]. It should be noted that for nanosilicas with mainly textural porosity (e.g. fumed silicas of high S_{BET} 240, 300 and 380 m^2/g [Gunko05, Gunko13B, Klonos10B]), V_p can also be high, in particular V_{macro} (i.e. for *pore diameter* ≥ 50 nm), resulting in high degree of accessibility for both Nitrogen molecules and PDMS chains [Klonos15A, Klonos15B Galaburda14].

10.3.2. Differential scanning calorimetry (DSC)

10.3.2.1. Protocol A (standard crystallization)

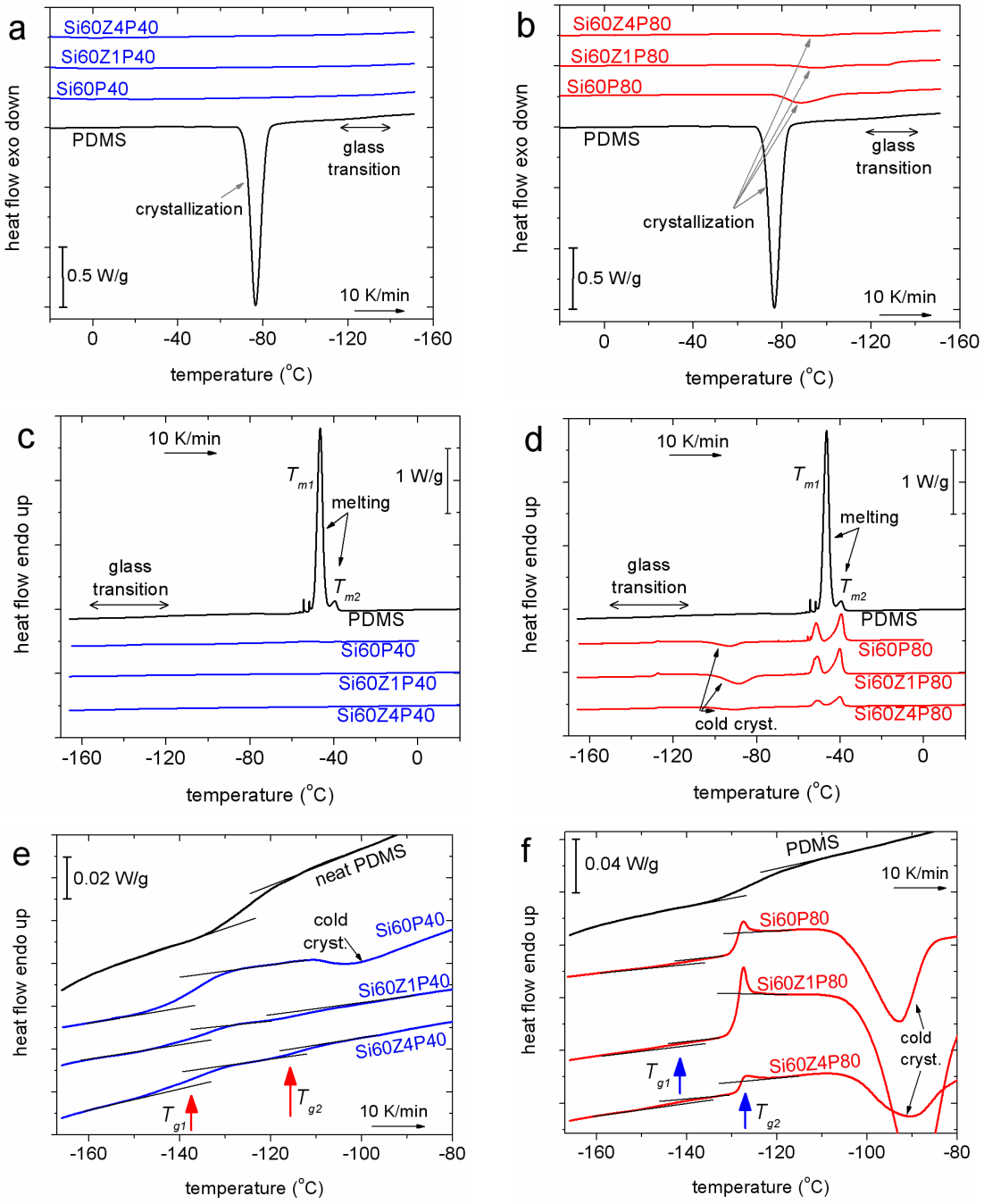

Fig. 10.2. Comparative DSC thermograms during (a,b) cooling and (c,d) the subsequent heating of samples of (a,c) 40 wt% and (b,d) 80 wt% PDMS adsorbed in silica–gel, Si–60, surface modified silica–gel, and for comparison of pure PDMS, for measurements under *Protocol A*. (e,f) show details in the glass transition region during heating. The curves are normalized to sample mass. The drawn lines represent the baselines of the glass transitions, while the arrows mark the glass transitions temperatures (T_{g1}, T_{g2}).

During cooling in DSC in Fig. 10.2a, crystallization of neat PDMS occurs at –76 °C and the respective degree of crystallinity, determined by Eq. (3.2), is equal to 0.65 wt (Table 10.2). No crystallization of PDMS is observed for nanocomposites of 40 wt% PDMS at cooling (Fig. 10.2a). During the subsequent heating (Figs. 10.2c–f) all samples demonstrated glass transition steps in the region between –150 °C and –110 °C, T_{g1} and T_{g2} in the order of increasing temperature (Figs. 10.2e,f, Table 10.2). For neat PDMS and Si60P40 single glass transition steps were observed (T_{g2} and T_{g1}, respectively, Table 10.2), while for Si60Z1P40 and Si60Z4P40 both steps were observed (T_{g1} and T_{g2}). The recorded value for neat PDMS is –126 °C. Interestingly T_{g1} of the nanocomposites is by ~10 K lower than that of neat polymer, and it is slightly reduced on addition of nanozirconia. The normalized change of the heat capacity at glass transition, ΔC_{p1} (Table 10.2), is weaker in the case of modified silica than for the initial Si–60. Next to T_{g1}, an additional weaker glass transition step is recorded in the composites of modified silica–gel at around –118 °C (T_{g2} in Figs. 10.1e,f, Table 10.2). T_{g1} corresponds to the glass transition of the PDMS confined within Si–60 pores, while T_{g2} correspond to the bulk–like mobility of the polymer [Klonos15A].

For Si60P40 nanocomposite an exothermic event above T_{g2} in the region between –110 and –80 °C, representing cold crystallization, was observed during heating (Fig. 10.2e). We recall that, in general, cold crystallization follows uncompleted crystallization during cooling [Gedde95].

Table 10.2

Quantities of interest from DSC measurements for *Protocols A* and *AC*: crystallization temperature, T_c, degree of crystallinity, X_c, glass transition temperatures, T_{g1} and T_{g2}, normalized changes of heat capacity at glass transition, ΔC_{p1} and ΔC_{p2}, temperature maxima of melting, $T_{m1,2}$, fraction of confined polymer, X_{CONF}, rigid and bulk amorphous fractions *RAF* and X_{BULK}, respectively. Note: X_c, *CONF*, *RAF* and X_{BULK} refer to whole polymer mass (i.e. $X_c + X_{BULK} + CONF + RAF = 1$) at ~$T_g$.

	sample	T_c (°C) (±0.5)	T_{g1} (°C) (±1)	ΔC_{p1} (J/gK) (±0.01)	T_{g2} (°C) (±0.5)	ΔC_{p2} (J/gK) (±0.01)	T_{m1} (°C) (±0.5)	T_{m2} (°C) (±0.5)	X_c (wt) (±5%)	X_{BULK} (wt) (±10%)	*CONF* (wt) (±20%)	*RAF* (wt) (±15%)
Protocol A (standard crystallization)	Si60P40	–	–137	0.13	–	–	–54	–39	0.00	0.00	0.39	0.61
	Si60Z1P40	–	–138	0.08	–117	0.02	–	–	0.00	0.06	0.24	0.70
	Si60Z4P40	–	–140	0.08	–118	0.03	–	–	0.00	0.09	0.24	0.67
	Si60P80	–89	–142	0.03	–129	0.16	–51	–40	0.24	0.37	0.07	0.32
	Si60Z1P80	–96	–144	0.02	–128	0.24	–51	–40	0.08	0.67	0.06	0.19
	Si60Z4P80	–94	–145	0.02	–128	0.07	–51	–40	0.07	0.20	0.06	0.67
	PDMS	–76	–	0.00	–126	0.22	–47	–40	0.65	0.23	0.00	0.12
Protocol AC (annealed crystallization)	Si60P40	–	–137	0.14	–	–	–52	–39	0.05	0.00	0.40	0.55
	Si60Z1P40	–	–138	0.09	–116	0.03	–	–	0.00	0.09	0.27	0.64
	Si60Z4P40	–	–139	0.08	–117	0.05	–	–	0.00	0.15	0.24	0.61
	Si60P80	–	–142	0.03	–	–	–50	–39	0.46	0.00	0.05	0.49
	Si60Z1P80	–	–144	0.02	–119	0.04	–51	–40	0.58	0.05	0.03	0.34
	Si60Z4P80	–	–145	0.02	–118	0.07	–51	–40	0.24	0.16	0.05	0.55
	PDMS	–	–	0.00	–126	0.15	–46	–40	0.67	0.15	0.00	0.18

At higher temperatures, complex endothermic melting peaks are observed between –54 and –39 °C (T_{m1}, T_{m2} in Table 10.2) for neat PDMS and a very weak one for Si60P40. Melting events are completely absent for Si60Z1P40 and Si60Z4P40. Complex and double melting peaks are typical for systems containing PDMS [Aranguren98, Klonos1oA, Galaburda14], involving also melting and recrystallization of metastable crystals [Aranguren98, Klonos12].

In the case of higher polymer adsorption (80 wt% PDMS), weak crystallization peaks are observed during cooling (Fig. 10.2b). The presence of Si–60 and, furthermore, the surface modification of Si–60 shift the peak of crystallization towards lower temperatures (T_c between –96 and –89 °C, in Table 10.2), while the degree of crystallinity is strongly suppressed in the composites, varying between 0.07 (for Si60Z4P80) and 0.24 (for Si60P80). During heating, in Fig. 10.2f, double glass transition steps are clearly recorded for the composites based on modified silica (Table 10.2). The first step (polymer confined in mesopores) is relatively weak (ΔC_{p1}~ 0.02 J/gK in Table 10.2) and T_{g1} is by 4–8 K lower than for the lower polymer content nanocomposites. T_{g1} reduces with surface modification (Table 10.2). The second glass transition step is quite strong and sharp shaped in Fig. 10.2f, recorded at around –128 °C (T_{g2} in Table 10.2). We have suggested in previous results (Chapters 4–6) that this sharp shaped glass transition step corresponds to bulk PDMS, and it is characteristic for samples with X_c < 0.40 wt. We will discuss further glass transition properties later in relation to results by DRS. As temperature increases, strong cold crystallization peaks are recorded at about –90 °C for all nanocomposites in Fig. 10.2f. Complex melting peaks are recorded, for all samples of high polymer loading, between –54 and –39 °C (T_{m1}, T_{m2} in Table 10.2).

10.3.2.2. Protocol AC (annealed crystallization)

Concerning measurements under *Protocol AC*, we do not show all raw data, however, we present a comparative thermogram in the glass transition region in Fig. 10.3. All results were analyzed and evaluated (details in section 3.2), and the respective values of interest are shown in Table 10.2 comparatively to those of *Protocol A*.

Crystallization annealing leaded to slight increase of X_c for Si60P40 (from 0 to 0.05 wt, Table 10.2) and stronger increase for all the samples of high polymer content (80 wt%).

The low–temperature glass transition step remained almost unaffected (both T_{g1} and ΔC_{p1} in Table 10.2). On the other hand, the higher–temperature glass transition step (T_{g2}) was again absent for Si60P40, while for Si60Z1P40 and Si60Z4P40 T_{g2} was almost unaffected and ΔC_{p2} was increased. For the samples of 80 wt% PDMS, T_{g2} was increased (as representative,

please compare the changes on Si60Z1P80 in Figs. 10.3a,b) and the respective heat capacity change (ΔC_{p2}) was suppressed for Si60P80 and Si60Z1P80 (Table 10.2), while it remained unchanged for Si60Z4P80.

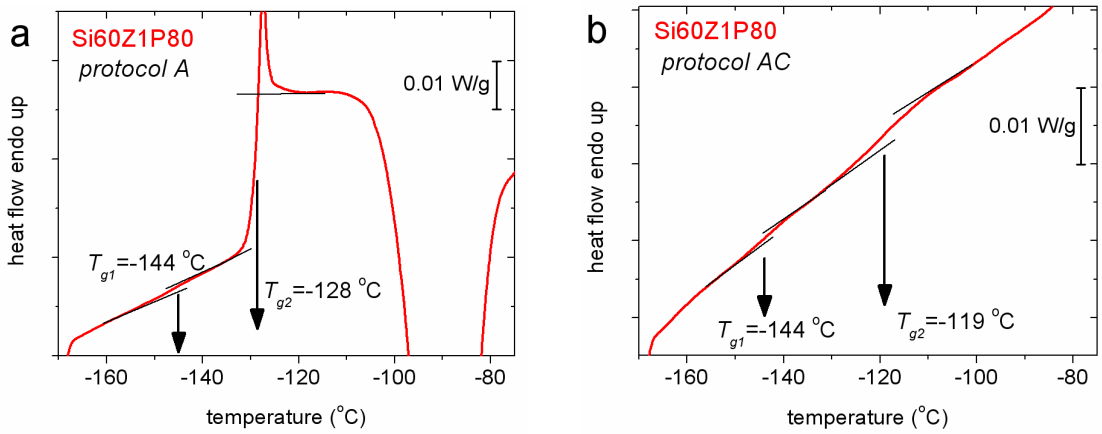

Fig. 10.3. DSC thermogram in the glass transition region for the sample Si60Z1P80 during heating, under (a) *Protocol A* and (b) *Protocol AC*. Curves are normalized to sample mass. Indicated are two well separated glass transition steps (T_{g1}, T_{g2}).

10.3.2.3. Evaluation in terms of models

As discussed in Experimental Techniques (Section 3.2), we may evaluate the various polymer fractions in polymer nanocomposites from the results of DSC measurements according to multi–phase models. Here we employ a '4–*phase model*', namely *CF* + *MAF* + *RAF* + *CONF*. In this model *CF*, *MAF* and *RAF* have been previously described (section 3.2.2), while *CONF* is added to represent the fraction of polymer confined in the cylindrical–like pores of Si–60. Thus, in the following we evaluate the different polymer fractions with respect to the type of their contribution to glass transition. We first estimate the amount of polymer which contributes to bulk–like mobility, X_{BULK}, and to mobility confined within Si–60 mesopores, *CONF*, according to Eqs. (10.1 and 10.2), respectively.

$$X_{BULK} = \frac{\Delta C_{p2}}{\Delta C_{p,amorphous}^{PDMS}}\left(1 - X_c\right) \tag{10.1}$$

$$CONF = \frac{\Delta C_{p1}}{\Delta C_{p,amorphous}^{PDMS}}\left(1 - X_c\right) \tag{10.2}$$

We remind that $\Delta C_{p,amorphous}^{PDMS}$ is the heat capacity step of fully amorphous unaffected PDMS and was found equal to 0.33 J/gK from fast cooling measurements (chapter 5, Fig. 5.1c, [Klonos15C]).

The sum of these two fractions makes the total fraction of mobile amorphous polymer in DSC, *MAF* (Eq. (10.3)).

$$MAF = CONF + X_{BULK} = \frac{\Delta C_{p1} + \Delta C_{p2}}{\Delta C_{p,amorphous}^{PDMS}}\left(1 - X_c\right) \tag{10.3}$$

According to our calculations (Table 10.2), the sum of mobile amorphous and crystallized polymer fractions ($MAF + X_c$) is lower than 1 in the nanocomposites, suggesting that, in agreement with the *4–phase model*, one part of the response is missing from the calculated fractions. This deviation is thought to represent *RAF*, which can be easily calculated by Eq. (10.4).

$$RAF = 1 - X_c - CONF - X_{BULK} = 1 - X_c - MAF \tag{10.4}$$

All the above quantities (fractions of various polymer phases) are included in Table 10.2, for measurements under both thermal protocols.

CONF is reduced with zirconia modification and does not seem to change after annealing of crystallization (Table 10.2). *CONF* values are in general higher for 40 wt% than for 80 wt% PDMS.

The sum of X_c and X_{BULK} is higher for 80 wt% PDMS, while, as expected, *RAF* is higher for samples of 40 wt% PDMS. In addition, X_c, X_{BULK} and *RAF* in Table 10.2 do not change systematically with zirconia modification, while, changes on *RAF*, especially for low polymer adsorption (no interference of crystallinity), seem to follow the respective changes on S_{BET} (Table 10.1). These effects will be discussed later in comparison with respective DRS findings.

Summarizing the findings from DSC, the interactions between Si–60 and the polymer in the nanocomposites suppress highly the crystallization ability of PDMS, which is in general absent for the 40 wt% PDMS content. The effect is stronger in the case of zirconia modification. T_{g1} and ΔC_{p1} of the confined polymer become slightly lower with the growth of zirconia onto the inner interfaces of Si–60 pores (Table 10.1). Thermal annealing does not seem to affect the confined mobility (Fig. 10.3, Table 10.2), whereas, it suppresses significantly bulk mobility (T_{g2} and ΔC_{p2}) and rigid amorphous polymer fraction (*RAF*).

10.3.3. Dielectric relaxation spectroscopy (DRS)

10.3.3.1. Raw data and analysis

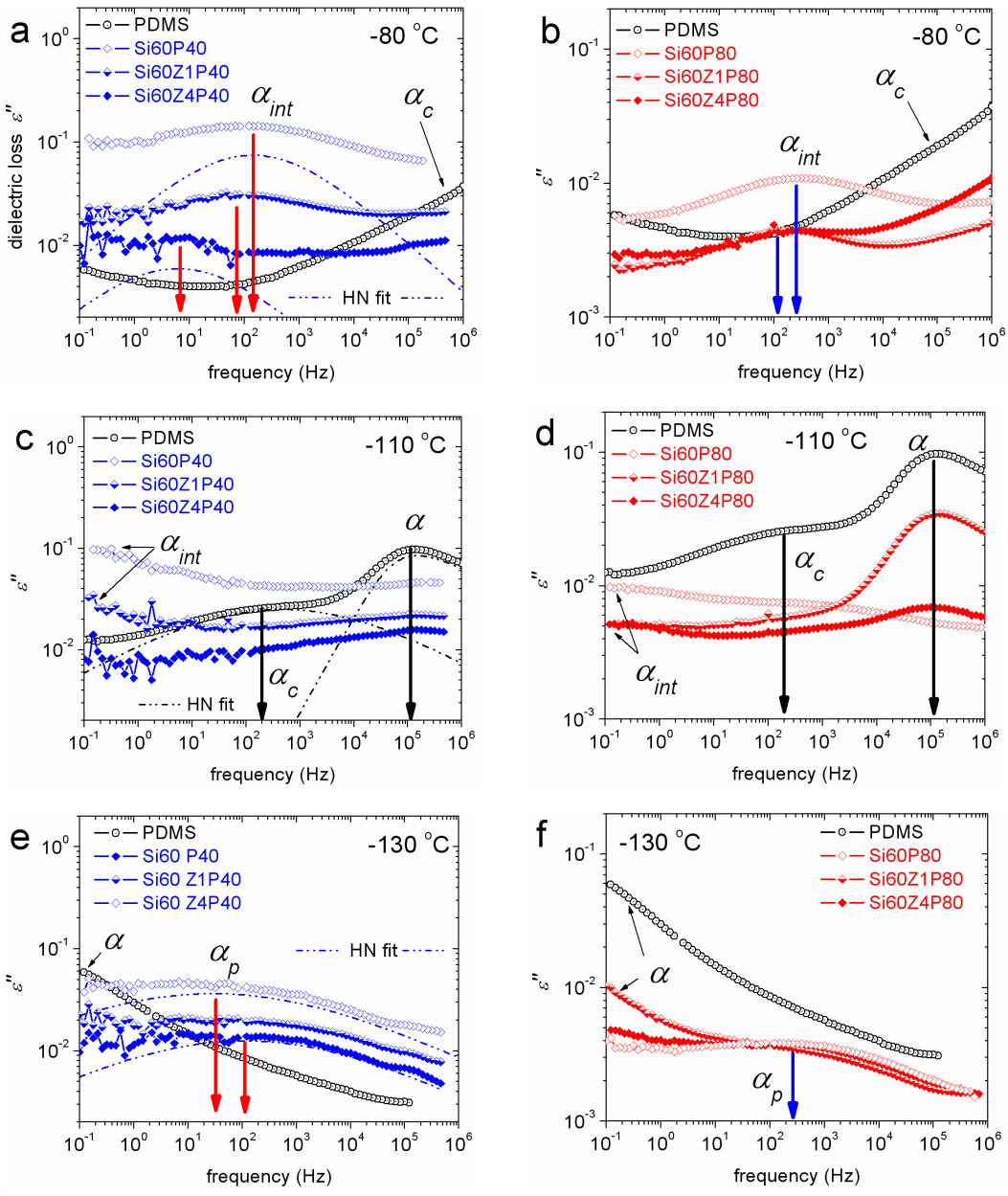

Fig. 10.4. Isothermal DRS plots of the imaginary part of dielectric permittivity (dielectric loss), ε'', vs frequency for PDMS and the composites with (a,b,e) 40 wt% and (b,d,f) 80 wt% PDMS adsorbed in silica gel, at (a,b) –80 °C, (c,d) –110 °C, and (e,f) –130 °C. The results refer to measurements by *Protocol A*. Included are selected analysis results in terms of individual Havriliak–Negami components (Eq. (3.6)) for each of the segmental relaxations (α_{int}, α_c, α, α_p).

The dielectric response (imaginary part of dielectric permittivity, ε'', Fig. 10.4) of the nanocomposites was found significantly higher (by about ten times) for the samples containing 40 wt% PDMS (Figs. 10.4a,c,e) as compared to 80 wt% PDMS (Figs. 10.4b,d,f). This difference was also confirmed by the data for the real part of dielectric permittivity, ε', and conductivity, σ_{AC}, (not shown) and can be explained in terms of chain conformations with higher orientation (polarizability) of interfacial polymer (Chapter 7), which is the majority at low PDMS content (40 wt%) and dominates the dielectric response.

The DRS results will be comparatively presented here in the form of frequency dependence of the imaginary part of dielectric permittivity, ε'' (Fig. 10.4, isothermal plots) at selected temperatures. The focus is again on segmental dynamics, namely on the dielectric relaxations α_p, α, α_c and α_{int} corresponding to the DSC response in the temperature range from –150 to –110 ^{o}C in Figs. 10.2e,f. After analysis of the complex DRS spectra (details in section 3.4.2, selected examples are shown in Figs. 10.4a,c,e) and by plotting the frequency of maximum of ε'' and $\Delta\varepsilon$, from Eq. (3.6), for the four segmental relaxations against reciprocal temperature the plots of Figs. 10.5–7 were constructed. Included in the Arrhenius plots of Figs. 10.5a,10.6a,10.7a are also Thermally Stimulated Depolarization Currents (TSDC, raw data in Appendix A.10.1) and DSC data, peak temperatures and glass transition temperatures, respectively, at the equivalent frequencies of TSDC and DSC (1.6 mHz and 20 mHz, respectively [Fragiadakis05]).

After fitting the Vogel–Tammann–Fulcher–Hesse (VTFH) equation, Eq. (3.7), [VTFH, Richert98] we obtained values for the Vogel temperature, T_0, and fragility strength parameter, D [Boehmer93]. Next to that, we calculated the fragility index, m, according Eq. (3.8). Fragility (cooperativity) index values for the relaxations which follow VTFH equation are listed in Table 10.3.

From a first glance at the Arrhenius plots (Figs. 10.5a and 10.6a), the time–scale of α_p relaxation seems to tend to more linear–like (Arrhenius, temperature–independent activation energy) behavior as compared to α and α_c. Thus, in order to have a rough estimation of the average activation energy (average over temperatures, Table 10.3) of α_p, we employed the Arrhenius equation (Eq. (3.11), [Arrhenius1889]).

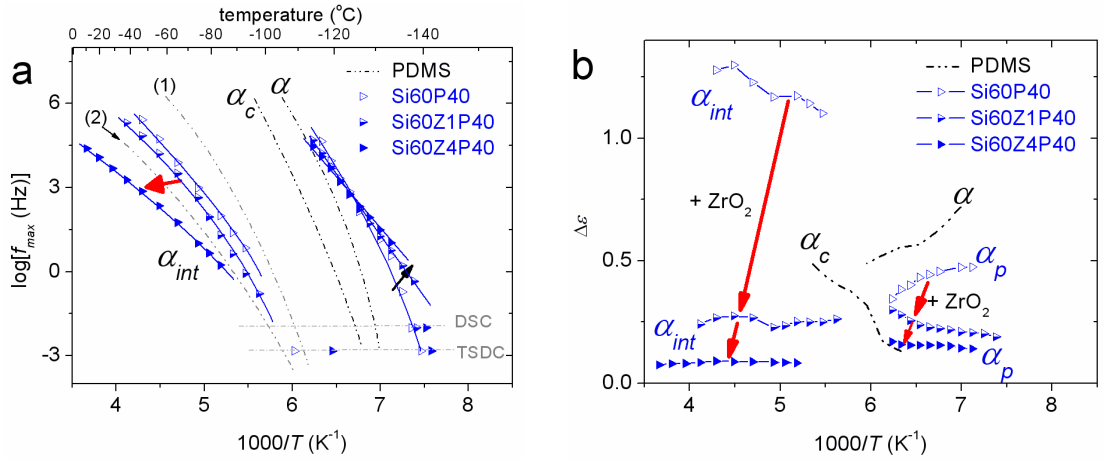

Fig. 10.5. (a) Arrhenius plots and (b) dielectric strength vs reciprocal temperature of the segmental dynamics confined in pores (α_p) and semi–bound at interfaces (α_{int}) for Si60P40, Si60Z1P40 and Si60Z4P40 composites, as recorded in isothermal DRS measurements of ε'' under thermal *Protocol A*. Respective points from DSC and TSDC measurements have been added in (a). The lines in (a) are fittings of the Arrhenius and the VTFH equations to the data for the segmental relaxations. The black dash–dotted lines represent the typical bulk (α) and bulk–like (α_c) behavior of initial PDMS, while the grey dash–dotted lines (1,2) correspond to the interfacial relaxation in *conventional* (1) PDMS/silica and (2) PDMS/titania nanocomposites [Klonos10A]. The arrows mark changes in α_{int} and α_p relaxations imposed by the addition of zirconia in the initial Si–60 particles.

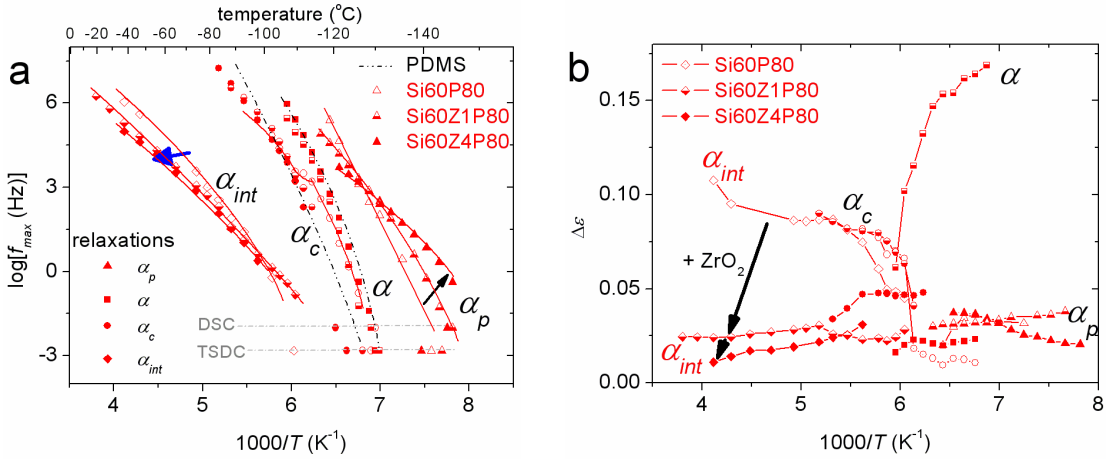

Fig. 10.6. (a) Arrhenius plots and (b) dielectric strength vs reciprocal temperature of the segmental bulk (α), constrained between polymer crystals (α_c), confined in pores (α_p) and interfacial (α_{int}) dynamics for Si60P80, Si60Z1P80 and Si60Z4P80 composites, as recorded in isothermal DRS measurements of ε'' under thermal *Protocol A*. Respective points from DSC and TSDC measurements have been added in (a). The lines in (a) are fittings of the Arrhenius and the VTFH equations to the data for the segmental relaxations. The black dash–dotted lines in (a) represent the typical behavior of initial PDMS. The arrows mark changes in α_{int} and α_p relaxations imposed by the addition of zirconia in the initial Si–60 particles.

Table 10.3

Evaluation of DRS data: shape parameters of the fitted Havriliak–Negami equation, a_{HN} and β_{HN}, (average values over the temperature range of measurements), activation energy, E_{act}, and fragility index, m, for the recorded dielectric relaxations, confined and interfacial polymer fractions $CONF$, RAF_{int}, respectively, and the apparent thickness and density of the interfacial polymer layer, d_{int} and ρ_{int}, respectively, for all the samples. Results are shown for both *Protocols A* and *AC*. *Note*: (*) corresponds to relaxations which do not obey VTFH equation.

Process	α_p					α			α_c			α_{int}						α_{int}					
Protocol	*A and AC*					*A and AC*			*A and AC*			*A*						*AC*					
parameter	a_{HN}	β_{HN}	E_{act} (eV)	m	$CONF$ (*vol*)	a_{HN}	β_{HN}	m	a_{HN}	β_{HN}	m	a_{HN}	β_{HN}	m	RAF_{int} (*vol*)	d_{int} (nm)	ρ_{int} (g/cm^3)	a_{HN}	β_{HN}	m	RAF_{int} (*vol*)	d_{int} (nm)	ρ_{int} (g/cm^3)
Si60P40	0.25	1	0.99	32	0.32	–	–	–	–	–	–	0.41	1	49	0.68	0.7	0.272	0.40	1	32	0.39	0.4	0.156
Si60Z1P40	0.23	1	0.87	*	0.40	–	–	–	–	–	–	0.32	1	39	0.60	0.6	0.238	0.44	1	29	0.34	0.4	0.135
Si60Z4P40	0.25	1	0.78	*	0.53	–	–	–	–	–	–	0.30	1	36	0.47	0.5	0.204	0.43	1	28	0.33	0.4	0.143
Si60P80	0.25	1	1.16	35	0.14	0.50	1	100	0.25	1	86	0.40	1	34	0.30	1.9	0.080	0.40	1	33	0.28	1.8	0.075
Si60Z1P80	0.25	1	0.89	40	0.21	0.85	0.45	113	0.35	1	99	0.42	1	29	0.27	1.7	0.071	0.41	1	31	0.25	1.6	0.066
Si60Z4P80	0.28	1	0.62	62	0.29	0.87	0.40	118	0.34	1	90	0.42	1	30	0.26	1.8	0.075	0.42	1	30	0.25	1.7	0.072
PDMS	–	–	–	–	–	0.89	0.43	106	0.30	1	96	–	–	–	–	–	–	–	–	–	–	–	–

10.3.3.2. Confined polymer relaxation (α_p)

α_p relaxation (characterized by mean values of the shape parameters over the temperature range of the relaxation α_{HN}~0.25, β_{HN}=1) is recorded for both PDMS contents at –130 °C in Figs. 10.4e,f, at around 100 Hz. Comparing Figs. 10.5,10.6 we can easily conclude that α_p relaxation is not significantly affected by the polymer content, although α_p seems slightly faster and weaker ($\Delta\varepsilon$) for 80 wt% PDMS loading. Interestingly, the relaxation becomes faster, immigrating towards higher frequencies / lower temperatures with the addition of nanozirconia (Figs. 10.5a,10.6a). Additionally, zirconia modification imposes reduction of the activation energy of α_p, while its fragility, m, decreases in 40 wt% PDMS samples and increases for 80 wt% PDMS (Table 10.3). Finally, α_p remains completely unaffected by thermal annealing in Fig. 10.7, in close agreement to DSC (T_{gI} in Table 10.2) and TSDC (in Appendix A.10.1).

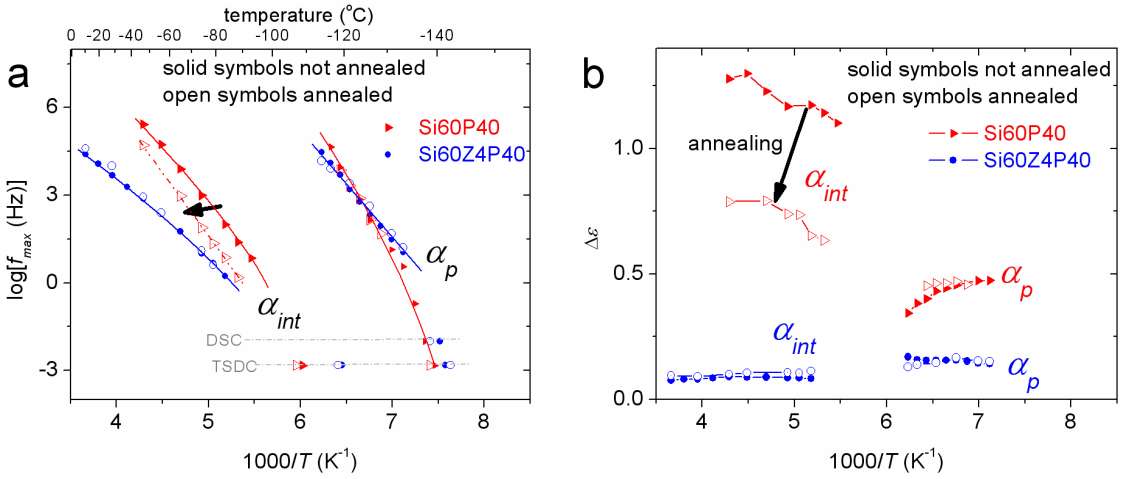

Fig. 10.7. Comparative (a) Arrhenius plots and (b) dielectric strength vs reciprocal temperature of the confined in pores (α_p) and interfacial (α_{int}) dynamics for Si60P40 (red triangles) [Klonos15A] and Si60Z4P40 (blue cycles) composites, as recorded in isothermal DRS measurements of ε'' under thermal *Protocols A* (solid symbols) and *AC* (open symbols). Respective points from DSC and TSDC measurements have been added in (a). The lines in (a) are fittings of the Arrhenius and the VTFH equations (details in section 3.4) to the data for the segmental relaxations. The arrows mark changes imposed by thermal annealing.

10.3.3.3. Bulk–like relaxations (α and α_c)

Recorded at –110 °C, one can observe in Figs. 10.4c,d α_c (α_{HN}~0.25–0.35, β_{HN}=1) and α (α_{HN}~0.50–0.89, β_{HN}~0.40–1.00) relaxations of PDMS and the majority of nanocomposites with 80 wt% PDMS at around 200 Hz and 100 kHz, respectively. Both relaxations are absent in samples of 40 wt% (Fig. 10.5a). The effects of nanozirconia on these relaxations are

indirect and are mainly expressed via the changes in the degree of crystallinity (Table 10.2), in agreement to previous studies on dielectric behavior of PDMS [Lund08, Klonos12, Klonos15A].

10.3.3.4. Interfacial relaxation (α_{int})

In Fig. 10.4a we follow the isothermal ε'' spectra at –80 °C for PDMS and the composites with 40 wt% PDMS. α_{int} relaxation (α_{HN}~0.30–0.42, β_{HN}=1) is recorded exclusively in the composites and is located at around 100 Hz for Si60P40 and Si60Z1P40 and at lower frequencies (~10 Hz) for Si60Z4P40. Being the slowest of the segmental relaxations, α_{int} relaxation monitors polymer dynamics at the polymer–particle interfaces [Fragiadakis07, Klonos10A, Klonos15A–C].

α_{int} becomes slower (Figs. 10.5a,10.6a) and its strength (Figs. 10.5b,10.6b) and cooperativity (*m* in Table 10.3) are reduced with zirconia modification. α_{int} for composites with 80 wt% PDMS is recorded weaker in strength (Fig. 10.4b), as compared to 40 wt% PDMS. The respective changes with zirconia modification (Fig. 10.6) are qualitatively similar, although less pronounced, than those of the low polymer fraction.

10.3.3.5. Evaluation of polymer fractions according to dielectric response

Having clear evidence about the origins of the relaxations described above and in combination with DSC results, we may calculate the various fractions of polymer from the dielectric response of each fraction. To that aim we employ a model analogue to the one used previously for DSC (i.e. Eqs. (10.1–4)) and calculate the fractions of PDMS confined in pores, *CONF*, and interfacial, RAF_{int}, according to the following equations,

$$CONF = \frac{\Delta\varepsilon_{\alpha p}}{\Delta\varepsilon_{total}}(1-X_C) = \frac{\Delta\varepsilon_{\alpha p}(1-X_C)}{\Delta\varepsilon_{\alpha p}+\Delta\varepsilon_{\alpha}+\Delta\varepsilon_{\alpha c}+\Delta\varepsilon_{\alpha\,\mathrm{int}}} \tag{10.6}$$

$$RAF_{\mathrm{int}} = \frac{\Delta\varepsilon_{\alpha\,\mathrm{int}}}{\Delta\varepsilon_{\alpha p}+\Delta\varepsilon_{\alpha}+\Delta\varepsilon_{\alpha c}+\Delta\varepsilon_{\alpha\,\mathrm{int}}}(1-X_C) \tag{10.7}$$

where $\Delta\varepsilon$ is the dielectric strength [Kremer02] of the segmental relaxations and X_c is the degree of crystallinity (obtained from DSC, Table 10.2). Bearing in mind that the dielectric strength of all recorded relaxations changes with temperature, for the sake of clarity, we employed DRS results at the same temperature –95 °C for RAF_{int} calculation and –140 °C for *CONF*. Results are shown in Table 10.3.

Results for the different polymer fractions in Table 10.3 reveal that RAF_{int} decreases (from 0.68 to 0.47 wt) and *CONF* increases (from 0.32 to 0.53 wt) with surface modification,

in particular for 40 wt%, interplaying at the expenses of each other. *CONF* and RAF_{int} are reduced by a factor of about 2 in the 80 wt% polymer nanocomposites. However, also here *CONF* increases (from 0.14 to 0.29 wt) and RAF_{int} decreases (from 0.30 to 0.26 wt) with surface modification. The results will be discussed later comparatively with those obtained from DSC.

We now draw attention to the effects of crystallization annealing on α_{int} relaxation. By comparing results by the two protocols, it becomes clear that annealing of crystallization leads in general to slower α_{int} relaxation (Fig. 10.7a), with lower dielectric strength (Fig. 10.7b), suppressed fragility (*m*) and RAF_{int} (Table 10.3) for both polymer loadings. The effects imposed by annealing on α_{int} become gradually weaker with increasing of surface modification, for example in the case of Si60Z4P40 in Fig. 10.7, where α_{int} is the slowest and weakest among the 40 wt% samples, annealing does not imply any further suppression to interfacial dynamics.

10.4. Discussion

10.4.1. Glass transition (bulk and in pores)

Glass transition of bulk is extremely weak or, even, absent for samples of low PDMS adsorption (40 wt%). Changes in the glass transition temperature T_{g2}, which corresponds to glass transition outside the pores, are dominated by X_c. For samples of high PDMS adsorption (80 wt%), T_{g2} increases with X_c in Table 10.2, as expected for a highly crystallizable polymer, such as PDMS (X_c ~0.6–0.8) [Aranguren98, Klonos10A], as physical and spatial constraints, imposed by the spherulites [Sundararajan02], hinder the diffusion of polymer chains during glass transition [Gedde95]. Furthermore, crystallization annealing suppresses bulk dynamics, increasing X_c and T_{g2}, and, furthermore, eliminates the event of glass transition for Si60P80 (Table 10.2). The results could be also discussed in terms of rearrangements of the quite large Si–60 globules (~1 μm, Fig. 10.1), imposed by the growing of the larger PDMS spherulites [Sundararajan02] (~10^2 μm in size) [Khan09].

At lower temperatures, more than 10 K lower than T_{g2}, an additional glass transition step was revealed for the composites. This is the case of glass transition of PDMS confined in the 6–20 nm (in diameter) cylidrical–like intraparticle pores of silica–gel. Recorded in the range between –145 °C and –134 °C, T_{g1} decreases systematically with the addition of zirconia or, in other words, with the suppression of mesopores volume, V_{meso} (Table 10.1). Being a clear effect of spatial 2–D confinement [Schönhals03, Krutyeva13], the reduction of T_{g1} is

accompanied with respective suppression of confined polymer fraction *CONF* (Fig. 10.8, Table 10.2). A glance at Table 10.2 confirms that annealing of crystallization imposes no serious changes on neither T_{g1} nor *CONF*.

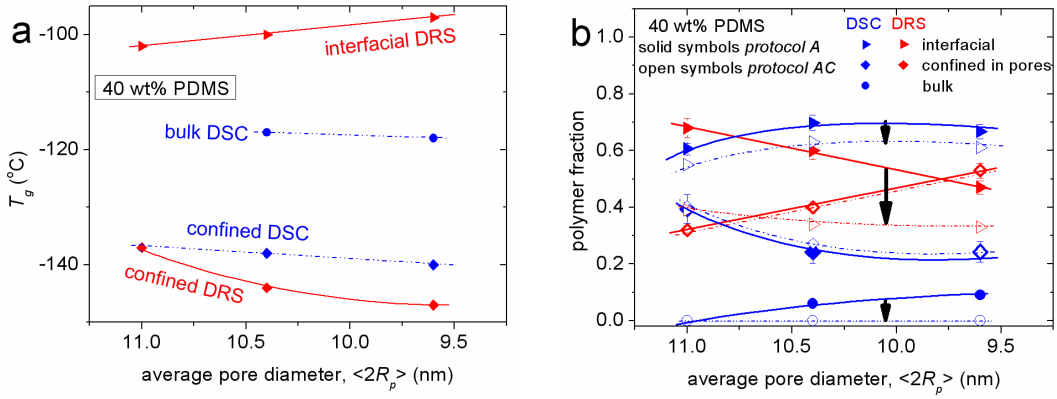

Fig. 10.8. (a) Calorimetric and dielectric glass transition temperature and (b) fraction of polymer confined in pores and in the interfacial layer against the estimated average pore diameter (<2R_p>, Table 10.1) for samples of 40 wt% PDMS loading. Results are shown comparatively from DSC and DRS measurements (details in text). The lines are used as guides for the eyes. The arrows in (b) mark changes imposed by thermal annealing.

10.4.2. Bulk–like dynamics (α and α_c relaxations)

Expoiting the high resolving power of DRS, in combination with DSC (X_c in Table 10.2), the various polymer fractions could be further distinguished in the nanocomposites (Table 10.3, Fig. 10.8).

Bulk–unaffected mobility of PDMS is monitored by α relaxation, characterized by an almost universal time scale in the Arrhenius Plots of Fig. 10.6a, as compared to different types of PDMS [Kirst93, Lund08, Klonos10A, Klonos15A–C]. The relaxation was present only in the high PDMS loadings (i.e. 80 wt%) and neat PDMS. α is the only asymmetric in shape ($\beta_{HN} < 1$) relaxation recorded in the present work (Table 10.3), while its strength, $\Delta\varepsilon$, decreases with temperature (Fig. 10.6b), as expected for bulk–unconstrained segmental dynamics [Kremer02, Donth01].

Standard is also the time scale of α_c relaxation (Fig. 10.6a), which describes the retarded dynamics of polymer chains restricted between PDMS crystals [Klonos10A, Klonos15A, Lund08, Floudas14], recorded, again, only in the samples of high polymer loading (80 wt% PDMS) and in neat PDMS. Its $\Delta\varepsilon$ increases with temperature (Fig. 10.6b), as the constraints imposed by the crystals are gradually loosened [Gedde95, Lund08, Huo92]. In

case of measurements after crystallization annealing, α_c relaxation is enhanced at the expenses of α, without significant changes in fragility and shape parameters.

Any effects of zirconia modification on the evolution of α and α_c relaxations are again indirect, depending on the degree of crystallinity.

10.4.3. Interfacial dynamics (α_{int} relaxation)

Focusing now on interfacial mobility, quite interesting changes were recorded in α_{int} relaxation. α_{int} tends to become slower and less fragile (less cooperative [Donth01]) with zirconia modification (Figs. 10.5a,10.6a and Table 10.3). The changes recorded by DRS could be better related with V_p values in Table 10.1, rather than with the respective changes in S_{BET}. The dielectric strength of α_{int} in Figs. 10.5b,10.6b is higher for the cases of unmodified Si–60, for both amounts of adsorbed PDMS.

According to the surface characterization of samples (section 10.3.1) [Sulim09] the changes in S_{BET} (Table 10.1) were interpreted in terms of (i) an initial growth of zirconia nanoparticles in the cylindrical pores of Si–60 and (ii) the subsequent growth of nanozirconia on the external surfaces. Case (i) dominates changes in S_{BET} for Si60Z1 while (ii) is more significant for the lower S_{BET} of Si60Z4. In both cases one should expect an increasing in the roughness of the inner surfaces (walls of pores) and, consequently, increased concentration of contact points between silica and the adsorbed PDMS. This assumption proves weak on the basis of DRS results in the case of Si60Z1P40 and Si60Z1P80, as α_{int} relaxation was weaker than in the unmodified silica samples. Our results suggest that both the fraction and dynamics of interfacial polymer is reduced in silica–gel (in pores and on outer surfaces) (Table 10.3, Figs. 10.5,10.6). It is likely that the method of adsorption of the gas molecules in cavities of the nanometric scale is not representative of the respective polymer chains adsorption in the same cavities. However, the opposite is true in the case of polymer adsorption on external (free) surfaces, even if those are of nanometric roughness (e.g. textural porosity of ~100 nm in diameter, Chapters 5–6).

Another point of interest is the temperature dependence of $\Delta\varepsilon$ for α_{int} relaxation. We follow in Figs. 10.5b,10.6b that for the strong α_{int} relaxation of Si60P40 and Si60P80 (i.e. unmodified samples) $\Delta\varepsilon$ increases with temperature. Simultaneously with the weakening of α_{int} relaxation with zirconia modification, $\Delta\varepsilon$ tends to decrease with temperature (Figs. 10.5b,10.6b). As discussed in previous chapters, this behavior resembles that of conventional nanocomposites of crosslinked PDMS (Chapter 4) and of natural rubber [Fragiadakis11] filled with *in situ* generated silica particles (~5 nm in diameter) at low amounts (up to ~10 wt%), as

well as that of *core–shell* nanocomposites based on PDMS and silica of low textural porosity (Chapter 6), where $\Delta\varepsilon$ of α_{int} relaxation was lower than that of α and decreased with increasing temperature.

10.4.4. Interpretation in terms of models

For the interpretation of our results on interfacial dynamics, we once again employ the model which involves bimodal conformations of polymer chains at the interfacial layer (Section 5.4.5) [Koga12, Klonos15A], namely the existence of (a) extended tails (Scheme 10.1a) with bulk like density but reduced mobility, and (b) flattened chain segments which form the inner quite dense region due to multiple contact points with the silica surface (loops, Scheme 10.1a). We assume that in our nanocomposites the high S_{BET} values of Si–60 particles lead to a successful adsorption of PDMS chains with a high ratio of loops / tails. Especially for the nanocomposites with low PDMS content (40 wt%) we can suppose that the majority of polymer chains are at the interfacial zone exhibiting high numbers of loops and tails, as well [Klonos15A, Klonos15B]. In agreement with the latter, both DRS and DSC calculations showed higher values for the interfacial polymer fraction (RAF_{int} and RAF in Tables 10.2,10.3, respectively) for samples of low polymer content (40 wt%).

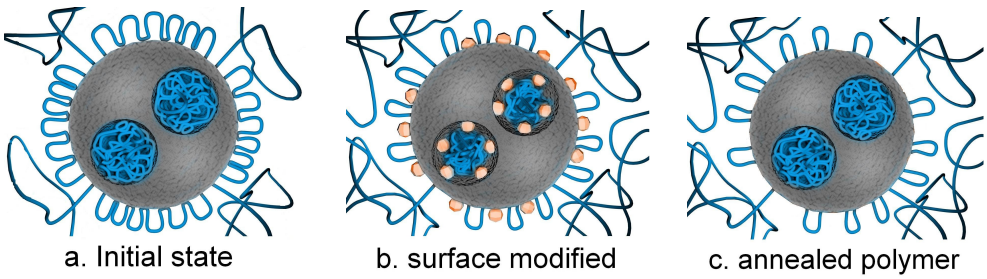

Scheme 10.1. Proposed 2–D schematic models for describing interfacial and confined polymer dynamics for (a) unmodified Si–60 particles, (b) surface modified Si–60 and (c) thermally annealed systems.

Concerning the increase / decrease of $\Delta\varepsilon$ of α_{int} relaxation with temperature, for samples of respectively high / low interfacial polymer fraction (RAF_{int}), we suggest that according to the model described above, the loop–like conformed chains onto a solid surface are weakly attached [Koga12, Rotella11, Klonos15A] on the surface and can increase in concentration, without simultaneous change of interfacial polymer density (Fig. 1.3b) [Koga12]. On the other hand, in case of higher tail / loop ratio (i.e. case of low RAF_{int} and,

respectively, lower $\Delta\varepsilon$ of α_{int}) the mobility of the tails (bulk–like density) can gradually increase, drifted by the increasing of bulk polymer mobility.

The extent of polymer–filler interactions can be also discussed in terms of the thickness of the interfacial polymer layer [Harton10, Gong14]. Thus, assuming that the whole oxide surface area (S_{BET}) is accessible to PDMS chains, we estimate the *apparent interfacial layer thickness*, d_{int}, employing Eq. (5.1). The results are listed in Table 10.3 and show that d_{int} decreases with zirconia modification (from 0.73 to 0.54 nm and from 1.9 to 1.7 nm for 40 wt% and 80 wt% PDMS, respectively). In agreement with the suppression of RAF_{int} after thermal annealing, d_{int} reduces also varying between 0.42 and 0.38 nm and between 1.8 and 1.6 nm for 40 wt% and 80 wt% PDMS, respectively (Fig. 10.9a, Table 10.3). The absolute values of d_{int} seem relatively low for the low polymer contents, but most probably results could be rationalized in the sense of the above assumption for the real accessible interaction area, which should be lower than S_{BET}. d_{int} is significantly higher for 80 wt% as compared to 40 wt% PDMS. The origin of this difference is yet not clear, being also inconsistent with the preparation procedure of the nanocomposites (Section 10.2.1). Moreover, the absolute values of d_{int} for samples with 40 wt% PDMS seem rather low, while they seem realistic for 80 wt% comparing with findings in previous works in PDMS (~2 nm in PDMS/silica nanocomposites [Fragiadakis07, Klonos10A] and 2.5−3.5 nm for PDMS adsorbed in solid surfaces [Schönhals03, Krutyeva13]).

In the next step, it is worthy to compare with the discussion by Kumar and coworkers [Gong14] about the relation between d_{int} and the *Kuhn segment length* of the respective polymer, where the latter should be at the upper limit of d_{int}. Combining this last statement with the changes in interfacial polymer chain conformations (Scheme 10.1), which explain our overall findings by DRS, we proceed with the estimation of the interfacial polymer density. Assuming again that the whole oxide surface area (S_{BET}) is accessible to PDMS chains and that d_{int} is constant and equal to Kuhn segment length (~1.56 nm [Gilra11]) for all nanocomposites, we estimate the *apparent interfacial layer density*, ρ_{int}, by Eq. (7.2). The results are shown in Fig. 10.9b and demonstrate that ρ_{int} decreases with zirconia modification (from 0.272 to 0.204 g/cm^3 and from 0.080 to 0.075 g/cm^3 for 40 wt% and 80 wt% PDMS, respectively, Table 10.3). After thermal annealing, ρ_{int} reduces further varying between 0.152 and 0.143 g/cm^3 and between 0.075 and 0.072 nm for 40 wt% and 80 wt% PDMS, respectively (Fig. 10.9b, Table 10.3).

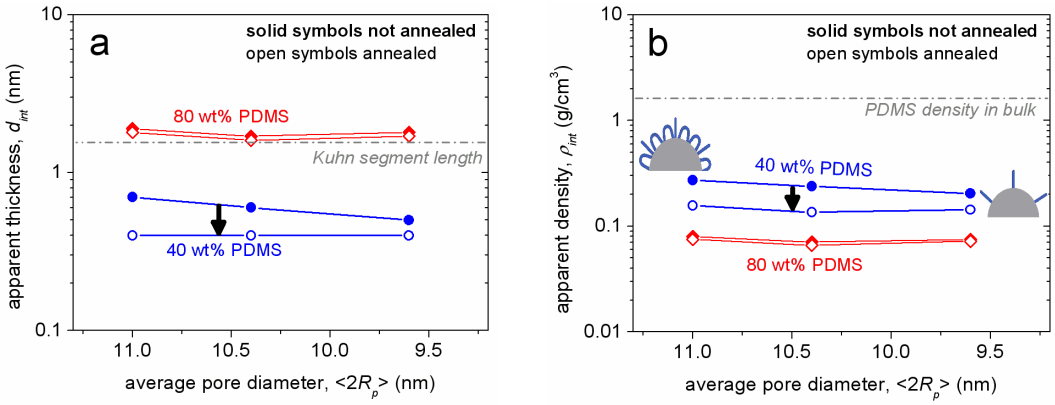

Fig. 10.9. Calculated apparent (a) thickness and (b) density of interfacial polymer layer against the average pore diameter , <2R_p> (Table 10.1). The drawn dash–dotted lines in (a) and (b) represent the *Kuhn segment length* in a PDMS melt [Gilra11] and the density of bulk PDMS [Klonos10A], respectively. The arrows mark changes imposed by thermal annealing.

Results for the samples of 40 wt% PDMS show that the estimated d_{int} is lower than *Kuhn length* by a factor of ~3, while ρ_{int} is lower than bulk PDMS density by a factor of ~6. Thus, for rationalizing results by these equations we should take the real accessible oxide surface area equal to about 3 − 6 times lower than S_{BET} (as determined by Nitrogen adsorption–desorption measurments), as shown also in Chapter 7. In future work measurements of changes in density of the interfacial polymer (e.g. employing Small Angle X-ray Scattering, SAXS), which has been found higher than that in bulk in previous work on polystyrene (PS) [Koga12,Vogiatzis13], are expected to clarify these issues. To further clarify this point, measurements employing small angel X-ray scattering (SAXS) [Grünewald15, Holt14] on similar systems are in progress.

10.4.4.1. Effects of surface modification

The suppression of V_p, RAF_{int} and ρ_{int} induced by surface modification and, at the same time, the suppression of interfacial dynamics and cooperativity suggest strongly that according to the model described above the loops / tails ratio on Si–60 is lower for modified samples (Scheme 10.1b). This result can be explained in terms of decreasing of polymer–silica contact points due to the smoothening of interfaces, in general (Chapter 5).

10.4.4.2. Effects of thermal (crystallization) annealing

In the samples of unmodified silica (i.e. Si60P40 and Si60P80) which have suffered thermal annealing, α_{int} relaxation (a) immigrated towards higher temperatures / lower frequencies

(Fig. 10.7a) and (b) $\Delta\varepsilon$ was suppressed (Fig. 10.7b). On the other hand, for the samples of modified Si–60, effects of thermal annealing are not significant (Fig. 10.7, Table 10.3). Similarly to surface modification effects, annealing procedure seems that could also lead to reorganization of chain distribution in the interfacial layer. Moreover, some of the chains could be detached, resulting in the restriction of the concentration and mobility of the loops (Scheme 10.1c), which are probably more loosely attached on the surfaces of Si–60 as compared to the tails [Koga12, Rotella11]. Interestingly, the case of Si60Z4P40 seems to be at the limit of low polymer adsorption, in particular the case of lowest loop / tail ratio, as α_{int} was the weakest and the less cooperative interfacial relaxation and, at the same time, it was not further affected by thermal annealing. Similar results were reported in Chapter 5 for core–shell systems based on fumed silicas and PDMS, same as in this chapter. Mechanisms like diffusion of free volume holes at the interfaces between the polymer and nanoparticles [Colmenero13SM] or redistribution of interfacial free polymer volume [Napolitano12] can be the driving force for effects of annealing of these systems.

10.4.5. Changes in dynamics confined in pores (α_p relaxation)

We focus now on polymer dynamics confined inside the mesopores of Si–60. Much evidence was provided in the previous sections concerning the origin of α_p relaxation. The dynamics and fraction of confined polymer were not affected by crystallization annealing, in close agreement with DSC (please compare Schemes 10.1a,c). Interestingly, we recorded tremendous changes directly affiliated to the nanozirconia modifications, also significant in DSC, but with opposite trend (Fig. 10.8b). More specifically, the addition of zirconia resulted to even faster α_p (Fig. 10.10) as compared to the unmodified Si–60. Additionally, lower fragility and lower average activation energy (Table 10.3) were obtained. Structural characterization of the initial silicas showed that spherical nanozirconia particles were formed both on the outer surfaces and inside the pores (6–20 nm in diameter) of Si–60 [Sulim09]. The results described above are similar to those obtained previously for PDMS in mesoporous glasses and spherical cavities ([Schönhals03, Colmenero10], Fig. 10.10), providing further proof that zirconia was indeed developed onto the internal walls of Si–60 pores, and, thus, the available volume (average pore diameter, $<2R_p>$, Table 10.1) for polymer adsorption is reduced (Scheme 10.1b). The 9% and 23% of restriction in pore volume (V_p in Table 10.1) for Si60Z1 and Si60Z4, respectively, imposed by nanozirconia, resulted in 50% and 70% increase of the amount of confined polymer, as compared to unmodified Si–60 (Fig. 10.8).

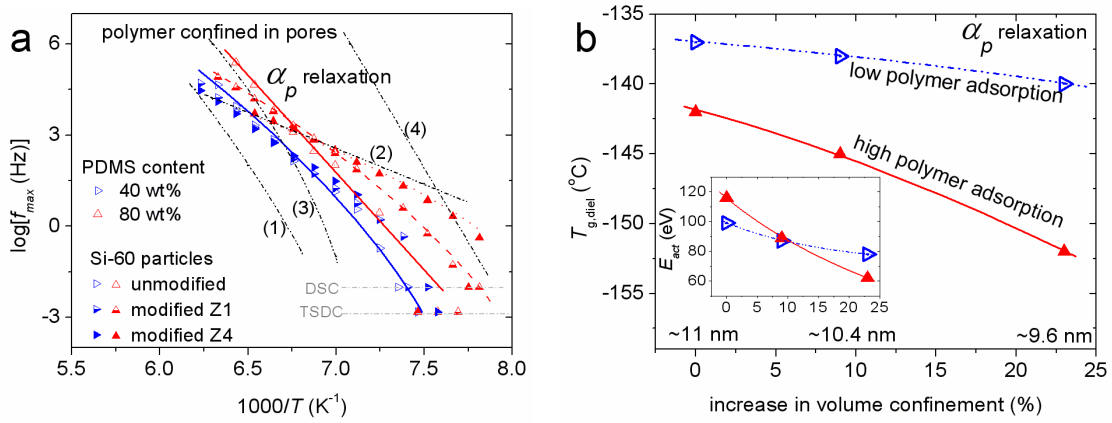

Fig. 10.10. (a) Arrhenius plots for polymer dynamics confined in pores (α_p) of Si60, for low (40 wt%) and high (80 wt%) contents of PDMS, adsorbed in unmodified and modified Si60. Lines (1) and (2) correspond to dynamics of PDMS confined in silica based mesopores of 20 and 5 nm in diameter, respectively [Schönhals03]. Lines (3) and (4) correspond to PDMS confined in spherical cavities of 15.5 nm (3–D) and in cylindrical pores of 9.8 nm (2–D), respectively [Colmenero10]. (b) Comparative diagrams of dielectric glass transition at 10^{-2} Hz, $T_{g,dieb}$ estimated from α_p relaxation, against the % change in volume confinement for low (40 wt%) and high (80 wt%) adsorbed PDMS. The inset in (b) shows the respective effects on the activation energy, E_{act}, of α_p relaxation.

As mentioned previously, *CONF* and RAF_{int} (*vol*) fractions in DRS were determined through the additive contributions of the confined (α_p) and interfacial (α_{int}) polymer fraction to total polarization (Eqs. (10.6, 10.7)). On the other hand, in the case of DSC, *CONF* and *RAF* (*wt*) fractions were extracted through an additional (ΔC_{p1}) and a missing part, respectively, of the corresponding contribution to the heat capacity jump at glass transition. Additionally, we recall that for both Si60Z1P40 and Si60Z4P40 we recorded bulk–like glass transition steps in DSC (T_{g2} in Fig. 10.2, Table 10.2), whereas in DRS no bulk–like relaxations (α or α_c) were recorded. So, the *in principle* different experimental methods can be at the origin of the differences observed in the trends of polymer fractions between DSC and DRS in Fig. 10.8b [Eslami13].

In the case of low polymer adsorption (40 wt%), the sum of confined and interfacial polymer fractions makes 100 % and ~95 % of the polymer response in DRS (Table 10.3) and DSC (Table 10.2), respectively. Despite differences related to calculations, it can be easily obtained from Fig. 10.8b, that there is a clear interplay between *CONF* and RAF_{int}, for the different surface modifications, i.e. different degree of spatial confinement. In the case of high PDMS adsorption (80 wt%) the situation is more complex due to the interference of crystalline fraction (X_c) and the rigid amorphous polymer fraction in close proximity to

polymer crystals (RAF_{cryst}) (details in Section 3.2), rendering more uncertain any further evaluation and comparison of *CONF* and RAF_{int} for the respective samples.

It is interesting, however, to discuss the difference in confined dynamics between low and high polymer content. In Fig. 10.10a, α_p relaxation for the samples of high polymer loading (80 wt%) is in general faster, characterized by lower calorimetric (T_{g1}, Table 10.2) and dielectric T_g ($T_{g,diel}$, Fig. 10.10b), and its E_{act} seems to be more sensitive to changes in spatial confinement (inset to Fig. 10.10b), as compared to lower polymer loading (40 wt%). Combining all the above observations, we conclude that PDMS is under stronger confinement in the pores of Si–60 at the higher polymer loading. This can be further supported by the results for the apparent interfacial density, d_{int} (Table 10.3), estimated higher for 80 wt% as compared to 40 wt% PDMS. Thus, it can be realistic that a thicker interfacial polymer layer probably reduces the intermediate dimension in the cylindrical–like pores and increase the effect of confinement. On the other hand, these results would suggest that lower amount of polymer has penetrated in the mesopores during preparation in case of 80 wt% PDMS, which is not expected according to the preparation procedure of the materials (Section 10.2.1). It is likely that reduction in pore volume of Si–60 occurs during polymer adsorption, possibly higher for 80 wt% PDMS. Unfortunately, this hypothesis cannot be checked by Nitrogen adsorption–desorption isothermal measurements because of the liquid–like character of the samples at 80 wt% PDMS. It is interesting, however, that effects of adsorption of various polymers on porosity and pore size distribution in silica and silica–like fumed particles (quite metastable systems) have been previously demonstrated [Gunko13B]. Finally, we should note that crystallization in polymer nanocomposites may impose significant changes in filler dispersion [Khan09].

10.5. Conclusions

Molecular dynamics and confinement effects of silica–gel/PDMS nanocomposites were in the center of interest in this chapter. The hydrogen bonding developed between the surface hydroxyls of silica and the oxygens of the backbone of PDMS has suppressed both the degree of crystallinity and the segmental dynamics of bulk PDMS. Nanozirconia modification resulted in increase of spatial confinement of the polymer in the intraparticle pores (~6–20 nm in diameter) of silica–gel. At the same time, a second effect of this modification was manifested by the reduction of polymer–particle contact points at the interfaces (external and in pores). As a result, interfacial fraction and dynamics (α_{int} relaxation) were suppressed. Bulk like dynamics was monitored only for high polymer content. Combining results by DSC and

DRS we were able to monitor the suppression of interfacial polymer fraction and dynamics after thermal annealing of the samples (related also to crystallization), while, at the same time, no changes were recorded in the dynamics and the fraction of confined polymer. Moreover, the results by different thermal treatments proved quite useful for understanding better polymer conformations in the interfacial silica/PDMS layer, similarly to chemical and thermal annealing of polymers on solid surfaces [Guiselin91, Koga12, Rotella11]. Therefore, the decreased density of polymer chains and the slowing of dynamics at the interfaces after the annealing, also similar with the effects of zirconia grafting, could be explained by suppression of the polymer–filler interaction surface / volume.

The discussion of the results obtained with these nanocomposites enables to reconsider previous results obtained with conventional polymer nanocomposites of PDMS/silica and PDMS/titania [Klonos10A]. The reported shift of interfacial dynamics to lower frequencies / higher temperatures and the increased interfacial layer thickness in the titania as compared to the silica nanocomposites may not originate exclusively from the higher strength of the PDMS–titania hydrogen bonds (type of particle) [Klonos10A], but determined also by the concentration and density of polymer chains on the available surface of nanoparticles (concentration of contact points) [Klonos15A]. Finally, we gained extra support that confining effects, at least for PDMS, originate mainly from size effects [Kremer14].

APPENDIX A.10

A.10.1. Thermally stimulated depolarization currents (TSDC)

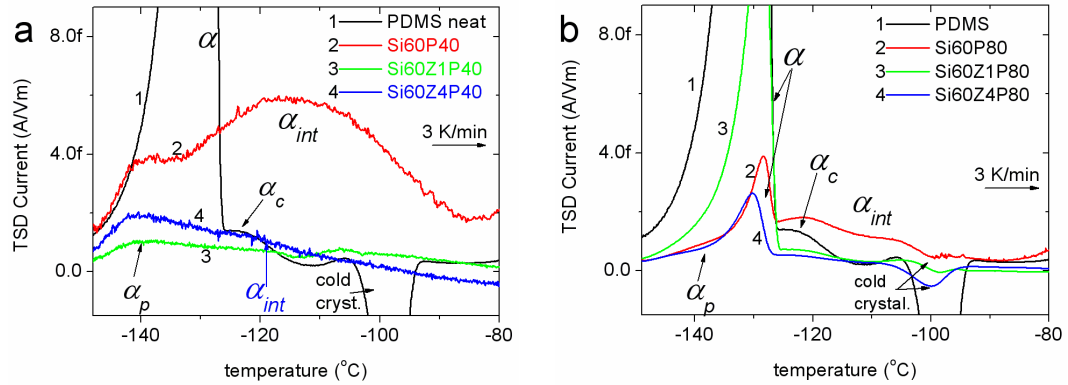

Fig. A.10.1.1. Comparative TSDC thermograms for neat PDMS and nanocomposites of (a) 40 wt% PDMS, (b) 80 wt% PDMS adsorbed in Si–60/ZrO_2 in the glass transition region for measurements of thermal *Protocol A*. Indicated are the dielectric relaxations related to polymer segmental dynamics.

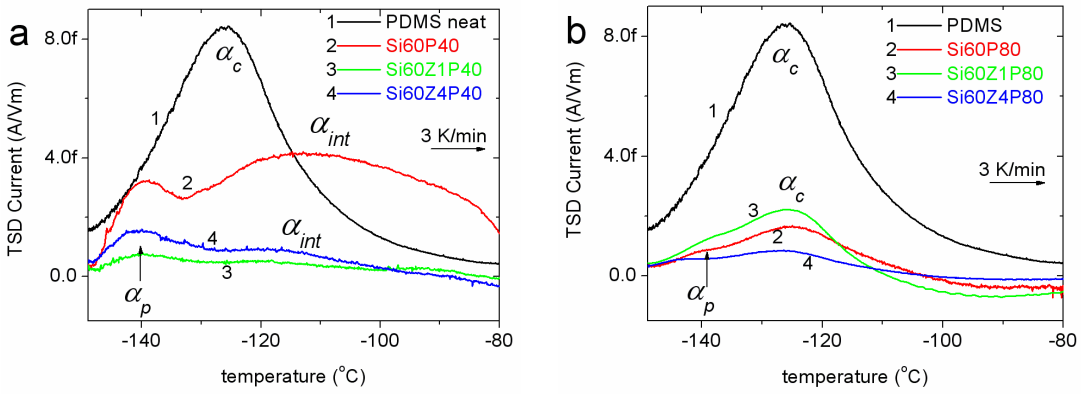

Fig. A.10.1.2. Comparative TSDC thermograms for neat PDMS and nanocomposites of (a) 40 wt% PDMS, (b) 80 wt% PDMS adsorbed in Si–60/ZrO_2 in the glass transition region for measurements of thermal *Protocol AC* (annealed samples).

11. Concluding remarks

In the present PhD Thesis we performed a systematic investigation of effects imposed on molecular dynamics in polymer nanocomposites (NCs) by various physical parameters, summarized in the following sections. Our main focus here was on the study of effects imposed on the fraction and dynamics of the polymer in the interfacial layer with metal oxide fillers, the characteristics of this polymer fraction being in the center of interest of nanocomposite materials science for the last decades. To that aim, we have chosen to study polymer NCs based on one type of polymer, namely polydimethylsiloxane (PDMS). This choice of polymer was made mainly due to four characteristics, i.e. due to (i) the easy and mild processing for preparation of materials based on PDMS, (ii) the rather simple chemical type of PDMS macromolecule, as compared to other types of polymers, a useful characteristic regarding the comparison with already studied simple model systems and with computer simulations in future, (iii) the exceptional dielectric response of PDMS which, in contrast to the majority of other polymers studied by similar techniques, offers the great benefit of studying directly the interfacial polymer dynamics in respective NCs [Fragiadakis06, Panagopoulou08], and (iv) the relatively high flexibility of PDMS chains in combination with the low glass transition temperature, which have been found beneficial with regard to the employed experimental techniques. Concerning NCs under investigation, two chemical types of metal-nanooxide fillers are used here, namely silicon dioxide (SiO_2, silica) and titanium dioxide (TiO_2, titania). NCs are categorized in two classes (a) *conventional* NCs consisted of initial nanoparticles generated *in situ* and dispersed in a PDMS network and (b) *core-shell* structured NCs consisted of nanoparticles in the form of aggregates on which linear PDMS is physically adsorbed. The main interaction in both cases of NCs is hydrogen bonding between the hydroxyls on the surface of nanooxides and the oxygens on the backbone of PDMS.

The techniques employed in this PhD Thesis are scanning electron microscopy (SEM), for studying morphology and filler dispersion in the NCs, differential scanning calorimetry (DSC), in order to study the thermal transitions of the polymer (glass transition and crystallization), two dielectric techniques, thermally stimulated depolarization currents (TSDC) and dielectric relaxation spectroscopy (DRS), in order to study polymer dynamics, and equilibrium water sorption / desorption isotherms (ESI/EDI) at room temperature, in order to study effects on molecular dynamics imposed by hydration/dehydration.

11.1. Effects of filler type and loading

Effects of type of nanooxides and filler loading on glass transition, crystallization and molecular dynamics of PDMS were studied with *conventional* NCs based on *in situ* synthesized silica and titania nanoparticles, 5 and 20–40 nm in diameter, respectively. The fraction of nanoparticles in NCs varied between ~5 and 36 wt% for silica and between ~5 and 18 wt% for titania. Nanoparticles were finely dispersed in PDMS networks (crosslinked polymer).

The strong interaction (hydrogen bonding) between the fillers and the polymer suppresses crystallinity and affects significantly the evolution of the glass transition in the NCs in DSC. The suppression of the degree of crystallinity, X_c, was found stronger in the case of titania NCs than for silica. The recorded changes in glass transition temperature, T_g, by filler loading were indirect, depending mainly on changes in X_c. However, significant systematic decrease in heat capacity change, ΔC_p, of glass transition was observed in NCs, this increase being systematic with filler loading. This suggests that a part of amorphous polymer fraction in NCs does not contribute to glass transition, i.e. the so called *rigid amorphous fraction*, *RAF*. Due to the semi-crystalline character of PDMS in NCs, *RAF* consists of immobilized (rigid) polymer segments between condensed crystal regions, RAF_{cryst}, and segments immobilized at the interfaces of polymer with nanoparticles, RAF_{int}. These two fractions cannot be easily distinguished uniquely by DSC results, since there is a still open debate about the extent of influence of crystals and interfacial interactions on molecular mobility, further calculations being based on speculations for the moment. However, in agreement with respective literature, we recorded that for both types of filler the amount of PDMS which shows amorphous properties (mobile amorphous fraction, *MAF*), participating in the glass transition, seems to be constant at ~12 wt% of the nanocomposite, and keeps a balance between different phases in the NCs under investigation.

The situation becomes more clear with results obtained by dielectric techniques. Regarding molecular dynamics, according to DRS and TSDC, next to the α relaxation, associated with the glass transition of the bulk amorphous polymer fraction, two additional segmental relaxations were recorded, originating from amorphous polymer chains restricted between condensed crystal regions (α_c relaxation) and the semi-bound polymer in an interfacial layer with strongly reduced mobility due to interactions with hydroxyls on the nanoparticle surface (α_{int} relaxation), respectively. We focused on the characteristics of α_{int}, the intensity (dielectric strength, $\Delta\varepsilon$) of which increases with filler loading, suggesting a systematic increase of interfacial polymer fraction, RAF_{int}, with nanoparticles fraction. RAF_{int} was calculated by comparing the dielectric strength of α_{int} with the total dielectric response related to segmental mobility ($\alpha + \alpha_c + \alpha_{int}$) at a fixed temperature and the results suggest that RAF_{int} is larger for silica than for titania. Interestingly, the time scale of α_{int} does not vary with filler fraction, as the temperature dependence of the characteristic frequency (f_{max}) for α_{int} is recorded almost identical for the same type of filler. However, α_{int} for titania is slower characterized by lower cooperativity (fragility) than that for silica. These results suggest that the time scale of α_{int} could possibly be the signature of polymer-particle interaction for each type of oxide. Following a widely adopted formalism for evaluating the range of polymer-filler interactions, we calculated the thickness of the interfacial polymer layer for NCs, which was estimated around 2 nm for silica and at least double for titania NCs.

Combining the above results we concluded that the hydrogen bond between titania and PDMS should be stronger than that between silica and PDMS, this resulting to thicker interfacial layer and slower dynamics in the case of titania/PDMS. Such explanation is reasonable, since the surface hydroxyl (-OH) of titania is more acidic than that on the surface of silica [Bokobza10]. On the other hand, according to recent work [Gong14] these differences between titania/PDMS and silica/PDMS can be due to the size of particles (~30 nm for titania and ~5 nm for silica) and/or due to the surface curvature of the particles.

In a next step, we observed that $\Delta\varepsilon$ of α_{int} decreases with temperature, T, for all titania based NCs and for the low silica loaded NCs. In addition, we performed thermal annealing experiments, aiming to increase crystallinity in NCs, which resulted in unchanged α_{int}, with the exception of silica/PDMS NCs of high filler loading (~30 and 36 wt%). For the latter samples, α_{int} became slower and weaker after annealing, these changes being accompanied by reduction in cooperativity. The after-annealing characteristics of α_{int} for silica/PDMS resemble those of α_{int} for titania/PDMS. Thus, a new question arose, namely as to whether the $\Delta\varepsilon(T)$ behavior and the effects imposed by the different type of nanoparticle and by thermal

annealing originate, on the one hand, from the strength of interaction and/or the geometrical characteristics of nanoparticles or, on the other hand, from changes in the polymer conformations in the interfacial layer and/or other characteristics of nanoparticles (e.g. the available contact points on the surfaces).

11.2. Effects of surface roughness of nanooxides

In order to investigate further interfacial dynamics of PDMS at the interfaces with silica and silica-like particles and other relative effects, as reported in the previous section, we employed a combination of structure (SEM), thermal (DSC), and dielectric (DRS) techniques on *core–shell* structured NCs of PDMS adsorbed onto fumed silica nanoparticles of low (~55 m^2/g) and high (~340 m^2/g) specific surface area, S_{BET}. S_{BET} is estimated via nitrogen adsorption–desorption (IPSD) and is affiliated mainly to textural porosity of nanooxides, thus, it can describe the nanometric surface roughness. The initial particles (8–150 nm in diameter) were found to aggregate (200-600 nm in diameter) and disperse well in the volume of NCs. In order to manipulate the oxide surfaces, these were chemically modified by grafting of small nanozirconia (ZnO) particles (3-10 nm in diameter). For oxides of low S_{BET} (smooth surfaces) nanozirconia grafting resulted in slightly increased roughness, while for the high S_{BET} oxides (rough surfaces) the same modification resulted in smoothened surfaces (lower S_{BET}).

PDMS was adsorbed both onto external surfaces and in the inner space of the voids of the aggregates. According to DRS and DSC the fraction of interfacial polymer, RAF_{int}, increases systematically with S_{BET}. In addition, we observe in DRS that with increasing of S_{BET} the respective dynamics (α_{int} relaxation) and cooperativity are enhanced.

Furthermore, in order to clarify further that these effects on α_{int} by S_{BET} do not arise from the presence of different type of oxide (zirconia), we studied interfacial dynamics of PDMS adsorbed on homogeneous silica and titania nanoparticles of a wide range of specific surface area (S_{BET}, 25 – 342 m^2/g) by the same combination of DSC and DRS. Both techniques revealed an increase of RAF_{int} with increasing of S_{BET} (surface roughness), accompanied by an enhancement of dynamics and cooperativity of α_{int}. At the same time, bulk dynamics (glass transition temperature, T_g, and time scale of α relaxation) was not significantly affected.

For explaining changes in specific characteristics of α_{int} and RAF_{int} we employed a model from the literature, which suggests that a polymer melt adsorbed on an attractive solid surface can adopt different types of conformations, for example loop- and tail-like. Such

models have gained support also by computer simulations [Mansfield89, Daoulas05] and have been examined experimentally [Guiselin91, Rotella11, Koga12]. The extended tails are characterized by bulk–like density but reduced mobility and cooperativity, while the flattened loop-like chain segments form the inner quite dense region due to multiple contact points with the hosting solid surface. The adoption of multiple contact points is favored in the case of polymer with flexible chains, such as those of PDMS, and further in the case of more densely distributed contact points on the surface (e.g. –OH groups) of nanooxide, the latter resembling the increasing in surface roughness (S_{BET}). In addition, in the case of densification of the particle-polymer contact points we expect a decrease in the average cooperativity length, which, in the frame of Adam-Gibbs theory would suggest increase in cooperativity of α_{int}. This was found true here, as the fragility of α_{int} increases with S_{BET}. Additionally, for samples of respectively high/low interfacial polymer fraction (RAF_{int}) we may interpret the respective increase/decrease of $\Delta\varepsilon$ of α_{int} with temperature as follows. According to the model described above, the loop–like conformed chains are weakly attached on the solid surfaces and their concentration can increase as temperature increases, without change in interfacial polymer density, e.g. by simultaneous decrease of loops' maximum distance (height) from the adsorbing surface. On the other hand, in the case of higher tail/loop ratio (i.e. the case of lower RAF_{int} and, respectively, lower $\Delta\varepsilon$ of α_{int}) the mobility of the tails (bulk–like density) can gradually increase, drifted by the increasing of bulk–like polymer mobility. Thus, the degree of immobilization of the tails at the interfaces is suppressed, leading to lowering of $\Delta\varepsilon$ for α_{int} with temperature.

Finally, it is likely that the shift of α_{int} to lower frequencies/higher temperatures in the titania as compared to the silica conventional NCs, reported in the previous section, originates, most probably, from the different concentration of contact points on the surfaces of nanoparticles. This is consistent with the observed rather diffused surfaces of silica (high surface area, ~453 m^2/g) as compared to titania (smoothed surfaces, low surface area, ~47 m^2/g) and the recorded differences in mechanical and swelling properties in conventional NCs [Bokobza10].

11.3. Effects of thermal annealing

In the PDMS based NCs which have suffered thermal annealing (a) α_{int} relaxation has immigrated towards higher temperatures / lower frequencies and (b) $\Delta\varepsilon$ of α_{int} has been suppressed. The effects of annealing on α_{int} become more weak on decreasing of S_{BET} of initial

particles, as α_{int} in theses samples is already weak and slow. Following the model described above (previous section), the changes can be interpreted in terms of reorganization of chain distribution in the interfacial layer. More specifically, some of the chains could be detached during annealing, resulting in the restriction of concentration and mobility of the loops, which are more loosely attached onto the surfaces as compared to the tails. It is important to recall two specific results which give additional support to this explanation. (a) for silica with 40 wt% adsorbed PDMS we recorded by DSC an increase of $\Delta C_{p,n}$ (mobile amorphous fraction, *MAF*) after annealing, without simultaneous increase in X_c (crystalline fraction, *CF*). (b) in DRS for the same sample after annealing, we observed a significant increase in the strength of *S* relaxation, assigned to increase of the concentration of free (not engaged by the polymer) surface hydroxyls, and a slight enhancement of bulk-like relaxation.

Thus, detaching of polymer chains from the solid surface of nanoparticles after annealing, leads to lower amount of interfacial polymer with more sparsely distributed chain segments that demonstrate lower cooperativity (large cooperativity length).

11.4. Effects of hydration / dehydration

DRS in combination with ESI / EDI in polymer NCs based on the hydrophilic silica and titania nanooxides and adsorbed PDMS revealed that the increase of hydration of oxide particles (~0.25 wt% hydration on dry basis in NCs) results in increase of polymer–particle contact points, reflected in enhanced mobility/cooperativity and fraction of the interfacial polymer. Effects on interfacial polymer relaxation (α_{int}) by hydration were found qualitatively similar to effects imposed by changes in the surface roughness of nanooxides and by thermal annealing. Results were found consistent with observations from the literature, in the sense of increased adhesion of the polymer onto the hydrophilic surface in the presence of moisture. Thus, we propose that the additional water molecules bond with the attractive surface hydroxyls and make additional accessible contact points with the polymer.

11.5. Effect of polymer chain length – molecular weight

Effects of chain length on interfacial polymer fraction and dynamics were studied by employing SEM, DSC and DRS on nanocomposites based on low specific surface area (25 m^2/g) spherical–like titania (TiO_2) nanoparticles and physically adsorbed PDMS of two molecular weights (*MW* ~2000 and ~8000). The initial titania particles (40–140 nm in

diameter) were found to aggregate (~500 nm in diameter) forming voids in the nanometric scale.

With nanoparticles content increasing gradually from 20 to 95 wt%, an increase in the glass transition temperature, T_g, is observed in DSC, accompanied by a broadening of the glass transition step and a decrease in the change in heat capacity, ΔC_p. The decrease in ΔC_p was used to estimate RAF_{int}, which was found similar for the two types of PDMS. On the other hand, according to DRS the interfacial polymer layer was estimated thicker in the case of shorter PDMS chains (~22 monomers/chain) and demonstrated slower dynamics (α_{int} relaxation) as compared to longer chains (~105 monomers/chain). Changes in the interfacial polymer fraction, as estimated by DRS, were found consistent with the changes in the specific surface area of the aggregates, as recorded by the gas molecules adsorption–desorption and results by SEM. The comparison with previous results in PDMS–based NCs revealed the importance of the concentration of polymer–particle contact points for the interfacial interactions over the strength of the respective physical bonds. In particular, in the case of shorter chains there is increased concentration of free chain ends. Thus, PDMS of short polymer chains can engage more hydroxyls on the surface of titania (contact points) during adsorption, as compared to PDMS of longer chains.

11.6. Effects imposed by 2D spatial confinement on polymer dynamics

We employed DSC and DRS in combination with different thermal treatments and monitored the interplay between confined, interfacial, and bulk polymer dynamics, all coexisting in silica–gel / PDMS systems.

Confined and bulk mobility could be distinguished by recording two well separated glass transition steps in DSC. For low content of adsorbed PDMS (40 wt%), we detected in DRS two contributions to segmental dynamics, arising from the interfacial polymer layer on the surfaces of nanoparticles (α_{int} relaxation) and from polymer chains confined in 6–20 nm, in diameter, cylindrical-like pores of silica–gel (α_p relaxation). α_{int} is the slowest while α_p is the fastest relaxation that represent segmental mobility for PDMS. Interestingly, no bulk segmental relaxation was detected for low polymer loading.

In order to manipulate both the surface and porosity properties of silica-gel and study in more-depth phenomena induced by changes at interfaces (surface-polymer interaction) and by the spatial 2D confinement in the pores, nanozirconia particles were grafted onto inner and external surfaces of initial silica–gel before polymer adsorption. This modification resulted in

decrease in RAF_{int} and in slower and less cooperative α_{int} in the NCs. These effects on interfacial polymer were interpreted by a loss of polymer–filler contact points with modification, due to smoothening of silica-gel surfaces, in general.

On the other hand, nanozirconia developed in the cylindrical-like pores of silica-gel led to decrease in the average pore diameter and, thus, to more severe spatial confinement of the polymer in pores. The latter was monitored via characteristic changes in α_p, i.e. a decrease in fragility (cooperativity), a decrease in the average activation energy, and an acceleration of α_p. The changes are systematic with increasing of zirconia content.

Crystallization annealing led to suppressed interfacial polymer dynamics (weakening and slowing down of α_{int}). On the contrary, it is remarkable that the confined polymer dynamics (α_p) remained completely unaffected by the same annealing. The latter suggests that interfacial effects are ruled by changes in the strength of interactions and changes in adopted conformations (energetic and entropic reasons), whereas confinement is dominated by dimensionality (size effects).

Bulk dynamics was observed only for the higher polymer loading (80 wt%), via two additional processes which contribute to the dielectric response *(α and α_c* relaxations).

Literature

[Adam65] Adam G, Gibbs JH. J Chem Phys 1965;43:139–46.

[Akcora09] Akcora P, Liu H, Kumar SK, Moll J, Ki Y, Benicewicz BC, Schadler LS, Acehan D, Panagiotopoulos AZ, Pryamitsyn V, Ganesan V, Ilavsky J, Thiyagarajan R, Colby RH, Douglas JF. Nat Mater 2009;8:354–9.

[Akcora10] Akcora P, Kumar SK, Sakai VG, Li Y, Benicewicz BC, Schadler LS. Macromolecules 2010;43:8275–81.

[Alaghemandi11] Alaghemandi M, Müller–Plathe F, Böhm MC. The J Chem Phys 2011;135:184905.

[Allegra08] Allegra G, Raos G, Vacatello M. Prog Polym Sci 2008;33:683–731.

[Antonelli15] Antonelli C, Serrano B, Baselga J, Ozisik R, Cabanelas JC. Eur Poly J 2015;62:31–42.

[Aranguren98] Aranguren M. Polymer 1998;39:4897–903.

[Arrhenius1889] Arrhenius SA. Z. Physik Chem 1889;4:96–116.

[Arrighi98] Arrighi V, Higgins J, Burgess A, Floudas G. Polymer 1998;39:6369–76.

[Arrighi03] Arrighi V, McEwen I, Qian H, Prieto M. Polymer 2003;44:6259–66.

[Balmer11] Balmer JA, Mykhaylyk OO, Schmid A, Armes SP, Fairclough JPA, Ryan AJ. Langmuir 2011;27:9075–89.

[Barroso13] Barroso–Bujans F, Cerveny S, Alegría Á, Colmenero J. Macromolecules 2013;46:7932–9.

[Berriot02] Berriot J, Montes H, Lequeux F, Long D, Sotta P. Macromolecules 2002;35:9756–62.

[Bershtein02] Bershtein VA, Egorova LM, Yakushev PN, Pissis P, Sysel P, Brozova L. J Polym Sci, Part B: Polym Phys 2002;40:1056–69.

[Bershtein09] Bershtein V, Gun'ko V, Egorova L, Guzenko N, Pakhlov E, Ryzhov V, Zarko V. Polymer 2009;50:860–71.

[Bilotti08] Bilotti E, Fischer HR, Peijs T. Appl Polym Sci 2008;107:1116–23.

[Binder96] Binder K, Milchev A, Baschnagel. Annu Rev Mater Sci 1996;26:107–34.

[Binder12] Binder K, Milchev A. J Pol Sci B Pol Phys 2012;50:1515–55.

[Bitsanis93] Bitsanis IA, Brinke G. J Chem Phys 1993;99:3100.

[Boehmer93] Boehmer R, Ngai K, Angell CA, Plazek DJ. J Chem Phys 1993;99:4201–9.

[Bokobza05] Bokobza L, Chauvin JP. Polymer 2005;46:4144–51.

[Bokobza10] Bokobza L, Diop AL. Express Polym Lett 2010;4:355–63.

[Bolbukh12] Bolbukh Yu, Tertykh V, Klonos P, Pissis. J Therm Anal Calorim 2012;108:1111–9.

[Bolhuis75] Bolhuis HH, Pennings AJ. J Macromol Sci B Phys 1975;11:455–73.

[Borodin03] Borodin O, Smith GD, Bandyopadhyaya R, Byutner O. Macromolecules 2003;36:7873–83.

[Boucher] Boucher VM, Cangialosi D, Alegría A, Colmenero J, González–Irun J, Liz–Marzan LM. Soft Matter 2010;6:3306–17.

[Brauenlich79] Brauenlich P. Thermally Stimulated Relaxation in Solids. Berlin: Springer; 1979.

[Brunauer38] Brunauer S, Emmett PH, Teller E. J Am Chem Soc 1938;60:309–19.

[Brunauer40] Brunauer S, Deming LS, Deming WE, Teller E. J Am Chem Soc 1940;62:1723–32.

[Capponi12] Capponi S, Napolitano S, Wübbenhorst M. Nat Commun 2012;3:1233.

[Carlberg04] Carlberg M, Colombini D, Maurer FH. J Appl Polym Sci 2004;94:2240–9.

[Cebe14A] Huang W, Krishnaji S, Rabotyagova Tokareva O, Kaplan D, Cebe P. Macromolecules 2014;47:8098–106.

[Cebe14B] Huang W, Krishnaji S, Rabotyagova Tokareva O, Kaplan D, Cebe P. Macromolecules 2014;47:8107–14.

[Chai14] Chai Y, Salez T, McGraw JD, Benzaquen M, Danloki–Veress K, Raphaël E, Forrest JA. Science 2014;343:994.

[Chao13] Chao H, Riggleman RA. Polymer 2013;54:5222–9.

[Chandran14] Chandran S, Begam N, Padmanabhan V, Basu JK. Nat Commun 2013;5:3697.

[Chen15] Chen F, Shangguan Y, Jiang Y, Qiu B, Luo G, Zheng Q. Polymer 2015;65:81–92.

[Chow78] Chow TS. J Polym Sci 1978;16:959–65.

[Chrissopoulou11] Chrissopoulou K, Andrikopoulos KS, Fotiadou S, Bollas S, Karageorgaki C, Christofilos D, Voyiatzis GA, Anastasiadis SH. Macromolecules 2011;44:9710–22.

[Chrissopoulou13] Fotiadou S, Karageorgaki C, Chrissopoulou K, Karatasos K, Tanis I, Tragoudaras D, Frick B, Anastasiadis SH. Macromolecules 2013;46:2842–2855.

[Clarson85] Clarson SJ, Dodgson K, Semlyen JA. Polymer 1985;26:930–4.

[Coleman06] Coleman JN, Cadek M, Ryan KP, Fonseca A, Nagy JB, Blau WJ, Ferreira MS. Polymer 2006;47:8556–61.

[Colmenero10] Del Valle–Carrandi L, Alegría A, Colmenero J. Eur Phys J 2010;189:257–261.

[Colmenero13SM] Barroso–Bujans F, Palomino P, Cerveny S, Fernandez–Alonso F, Rudić S, Alegría A, Colmenero J, Enciso E. Soft Matter 2013;9:10690–5.

[Colmenero14] Maiz J, Zhao W, Lawrence J, Arbe A, Alegría A, Emrick T, Colmenero J, Russel TP, Mijangos C. Polymer 2014;55:4057–4066.

[Coto13] Coto B, Antia I, Barriga J, Blanco M, Sarasua JR. Comput Mater Sci 2013;79:99–104.

[Couderc14] Couderc H, David E, Frechette M. Transact Electric Electron Mater 2014;15:291–6.

[Daoulas05] Daoulas KC, Harmandaris VA, Mavrantzas VG. Macromolecules 2005;38:5780–95.

[DeMaggio97] DeMaggio GB, Frieze WE, Gidley DW, Zhu M, Hristov HA, Yee AF. Phys Rev Lett 1997;78:1524–27.

[Dewimille05] Dewimille L, Bresson B, Bokobza L. Polymer 2005;46:4135–43.

[Dobbertin96] Dobbertin J, Hensel A, Schick C. J Thermal Anal Calorimet 1996;47:1027–40.

[Dodd12] Dodd PM, Jayaraman A. J Polym Sci B Polym Phys 2012;50:694–705.

[Dong11] Dong A, Huang J, Lan S, Wang T, Xiao L, Wang W, Zhao T, Zheng X, Liu F, Gao G, Chen Y. Nanotechnology 2011;22:295602.

[Donth01] Donth E, editor. The glass transition: relaxation dynamics in liquids and disordered materials. Vol 48 Springer series in materials science, vol 48. Berlin: Springer; 2001.

[Doxastakis14] Pandey YN, Brayton A, Burkhart C, Papakonstantopoulos GJ, Doxastakis M. Multiscale modeling of polyisoprene on graphite. J Chem Phys 2014;140:054908. (doi: 10.1063/1.4863918)

[Dutcher97] Forrest JA, Dalnoki–Veress K, Dutcher JR. Phys Rev E 1997;56:5.

[Ediger14] Ediger M, Forrest JA. Macromolecules 2014;47:471–8.

[Ellison03] Ellison CJ, Torkelson JM. Nature Mater 2003;2:695–700.

[Eslami13] Eslami H, Rahimi M, Müller–Plathe F. Macromolecules 2013;46:8680–92.

[Ezquerra04] Alvarez C, Šics I, Nogales A, Denchev Z, Funari SS, Ezquerra TA. Polymer 2004;45:3953–9.

[Fakhraai08] Fakhraai Z, Forrest JA. Science 2008;319:600–4.

[Feldman01] Raybov Ya, Gutina A, Arkhipov V, Feldman Yu. J Phys Chem B 2001;105:1845–50.

[Ferdous13] Ferdous SF, Sarker MF, Adnan A. Polymer 2013;54:2565–76.

[Fischer99] Fischer E, Kimmich R, Beginn U, Möller M, Fatkullin N. Phys Rev E 1999;59:4.

[Floudas97] Petychakis L, Floudas G, Fleischer G. Europhys Lett 1997;40:685–690.

[Floudas13] Suzuki Y, Duran H, Steinhart M, Butt HJ, Floudas G. Soft Matter 2013;9:2621–8.

[Floudas14] Suzuki Y, Duran H, Steinhart M, Butt HJ, Floudas G. Macromolecules 2014;47:1793–1800.

[Fontanella09] Fontanella JJ, Wintersgill MC, Edmondson CA, Lomax JF. J Phys D Appl Phys 2009;42:042003.

[Fornes03] Fornes TD, Paul DR. Polymer 2003;44:4993.

[Forrest01] Forrest JA, Dalnoki–Veress K. Adv Colloid Interf Sci 2001;94:167–96.

[Forrest02] Forrest JA. Eur Phys J E 2002;8:261–6.

[Fragiadakis05] Fragiadakis D, Pissis P, Bokobza L. Polymer 2005;46:6001–8.

[Fragiadakis06] Fragiadakis D. PhD Thesis, Experimental study of structure-properties relationship in nanocomposite polymeric materials. Athens: National Technical University of Athens; 2006.

[Fragiadakis07] Fragiadakis D, Pissis P. J Non–Cryst Solids 2007;353:4344–52.

[Fragiadakis11] Fragiadakis D, Bokobza L, Pissis P. Polymer 2011;52:3175–82.

[FragiadakisSW] Data analysis software made by Dr. Daniel Fragiadakis, http://grafitylabs.com/.

[Frielinghaus13] Frielinghaus H, Frielinghaus X, Ruocco N, Allgaier J, Pychhout–Hintzen W, Richter D. Soft Matter 2013;9:10484–92.

[Fukao00] Fukao K, Miyamoto Y. Phys Rev E 2000;61:1743–1754.

[Fullbrant13] Füllbrandt M, Purohit PJ, Schönhals A. Macromolecules 2013;46:4626–32.

[Galaburda14] Galaburda MV, Klonos P, Gun'ko VM, Bogatyrov, VM, Borysenko MV, Pissis P. Appl Surf Sci 2014;305:67–76.

[Ganesan14] Ganesan V, Jayaraman A. Soft Matter 2014;10:13–38.

[Gedde95] Gedde UW. Polymer Physics. London: Chapman & Hall; 1995.

[Gedde11] Nordell P, Nilsson F, Hedenqvist MS, Hillborg H, Gedde UW. Eur Polym J 2011;47:2208–15.

[Gee04] Gee R, Maxwell RS, Balazs B. Polymer 2004;45:3885–91.

[Giannelis10] Rodriguez R, Herrera R, Bourlinos AB, Li R, Amassian A, Archer LA, Giannelis EP. Appl Organometal Chem 2010;24:581–9.

[Giannelis11] Vo LT, Anastasiadis SH, Giannelis EP. Macromolecules 2011;24:6162–71.

[Gilra11] Gilra N, Cohen C, Briber RM, Bauer BJ, Hedden RC, Panagiotopoulos AZ.

Macromolecules 2001;34:7773–82.

[Ginzburg13] Ginzburg VV. Macromolecules 2013;46:9798–805.

[Gong14] Gong S, Chen Q, Moll JF, Kumar SK, Colby RH. ACS Macro Lett 2014;3:773–7.

[Gorelik70] Gorelik SS, Rastorguev LN, Skakov YA. Radiographic and Electron–Optical Analysis. Moscow; Metallurgy: 1970

[Goswami09] Goswami M, Sumpter BG. The J Chem Phys 2009;130:134910.

[Greegg82] Gregg SJ, Sing KSW. Adsorption, Surface Area and Porosity, second ed. London; New York: Academic Press: 1982.

[Greenspan77] Greenspan L. J Res Natl Bur Stand A Phys Chem 1977;81:89–96.

[Grünewald15] Grünewald TA, Lassinberger A, van Oostrum PDJ, Rennhofer H, Zirbs R, Capone B, Vonderhaid I, Amenitsch H, Lichtenegger HC, Reimhult E. Chem Mater 2015;27: 4763–71.

[Guiselin91] Lee LT, Guiselin O, Lapp A, Farnoux B. Phys Rev Lett 1991;67:20.

[Gunko05] Gun'ko VM, Turov VV, Bogatyrev VM, Zarko VI, Leboda R, Goncharuk EV, Novza AA, Turov AV, Chuiko AA. Adv Colloid Interf Sci 2005;118:125–172.

[Gunko07] Gun'ko VM, Borysenko MV, Pissis P, Spanoudaki A, Shinyashiki N, Sulim IY, Kulik TV, Palyanytsya BB. Appl Surf Sci 2007;253:7143–56.

[Gunko13] Gun'ko VM, Turov VV, Ruban AN, Kazanets AI, Leboda R, Skubiszewska–Zięb Colloid Interf Sci 2013;394:467–74.

[Gunko13B] Gun'ko VM, Turov VV. Nuclear Magnetic Resonance Studies of Interfacial Phenomena. Boca Raton: CRC Press; 2013.

[Gunko14] Gun'ko VM, Turov VV, Turova AA, Krupska TV, Pissis P, Leboda R, Skubiszewska–Zieba. J Colloids Interf Sci 2014;426:48–55.

[Gunko14B] Gun'ko VM. Appl Surf Sci 2014;307:444–54.

[Hanakata14] Hanakata PZ, Douglas JG, Starr FW. Nat Commun 2014;5:4163.

[Harmandaris05] Harmandaris VA, Daoulas KC, Mavrantzas VG. Macromolecules 2005;38:5796–809.

[Harmandaris14] Rissanou AN, Harmandaris V. Soft Matter 2014;10:2876–88.

[Harmandaris15] Rissanou AN, Harmandaris V. Macromolecules 2015;48:2761–72.

[Harton10] Harton SE, Kumar SK, Yang H, Koga T, Hicks K, Lee HK, Mijovic J, Liu M, Vallery RS, Gidley DW. Macromolecules 2010;43:3415–3421.

[Havriliak67] Havriliak S, Negami S. Polymer 1967;8:161–210.

[He07] He F, Wang LM, Richert R. Eur Phys J Spec Top 2007;141:3–9.

[Hedvig77] Hedvig P. Dielectric spectroscopy of polymers. Bristol: Adam Hilger; 1977.

[Hintermeyer08] Hintermeyer J, Hermann A, Kahlau R, Goiceanu C, Rössler EA.

Macromolecules 2008;41:9335–44.

[Hodge97] Hodge IM. J. Res Natl Inst Stand Technol 1997;102:195–205.

[Hongbin03] Hongbin L, Steven N. Macromolecules 2003;36:4010–6.

[Holt13] Holt AP, Sangoro JR, Wang Y, Agapov AL, Sokolov AP. Chain and segmental dynamics of poly(2-vinylpyridine) nanocomposites. Macromolecules 2013;46:4168–73.

[Holt14] Holt AP, Griffin PJ, Bocharova V, Agapov AL, Imel AE, Dadmun MD, Sangoro JR, Sokolov AP. Macromolecules 2014;47:1837–43.

[Huang14] Huang C, Bai H, Xiu H, Zhang Q, Fu Q. Compos Sci Technol 2014;102:20–7.

[Huo92] Huo P, Cebe P. Macromolecules 1992;25:902–9.

[Jancar10] Jancar J, Douglas JF, Starr FW, Kumar SK, Cassagnau P, Lesser AJ, Sternstein SS, Buehler MJ. Polymer 2010;51:3321–43.

[JCPDS01] JCPDS Database. International Center for Diffraction Data PA 2001; PDF 79–1769.

[Jhon73] Jhon JS, Andrade JD. J Biomed Mater Res 1973;7:509–22.

[Johnston13] Johnston K, Harmandaris V. Macromolecules 2013;46:5741–50.

[Johnston13R] Johnston K, Harmandaris V. Soft Matter 2013;9:6696–710.

[Jouault13] Jouault N, Moll JF, Meng D, Windsor K, Ramcharan S, Kearney C, Kumar S. ACS Macro Lett 2013;2:371–4.

[Kalathi12] Kalathi JT, Grest GS, Kumar SK. Phys Rev Lett 2012;109:198301.

[Kalathi14] Kalathi JT, Yamamoto U, Schweizer S, Grest GS, Kumar SK. Phys Rev Lett 2014;112:108301.

[Karatasos14] Karatasos K. Macromolecules 2014;47:8833–45.

[Karatrantos13] Karatrantos A, Clarke N, Composto RJ, Winey KI. Soft Matter 2013;9:3877–84.

[Karatrantos15] Karatrantos A, Clarke N, Composto RJ, Winey KI. Soft Matter 2015;11:382–8.

[Karul09] Karul A, Tan KT, White CC, Hunston DL, Marshall ST, Akgun B, Satija SK, Soles CL, Vogt BD. Polymer 2009;50:3234–9.

[Khan09] Khan J, Harton SE, Ackora P, Benicewicz BC, Kumar SK. Macromolecules 2009;42:5741–4.

[Khodadadi15] Khodadadi S, Sokolov AP. Soft Matter 2015;11:4984–98.

[Kickelbick12] Wisser FM, Abele M, Gasthauer M, Müller K, Moszner N, Kickelbick GJ. Colloid Interf Sci 2012;374:77–82.

[Kim91] Kim KS, Kim HS, Jang JH, Kim HS, Mhin BJ, Xie Y, Schaefer HF. J Chem Phys 1991;94:2057–62.

[Kim12] Kim SY, Meyer HW, Saalwächter K, Zukoski CF. Macromolecules 2012;45:4225–37.

[Kim13] Kim KD, Seo HO, Sim, CW, Jeong MG, Kim YD, Lim DC. Progr Org Coat 2013;76:596–600.

[Kim15] Kim B, Choi J, Yang S, Yu S, Cho M. Polymer 2015;60:186–97.

[Kirst93] Kirst KU, Kremer F, Litvinov VM. Macromolecules 1993;26:975–80.

[Klonos10A] Klonos P, Panagopoulou A, Bokobza L, Kyritsis A, Peoglos V, Pissis P. Polymer 2010;51:5490–99.

[Klonos10B] Klonos P, Pissis P, Gun'ko VM, Kyritsis A, Guzenko NV, Pakhlov EM, Zarko VI, Janusz W, Skubiszewska–Zieba J, Leboda R. Colloids Surf A 2010;360:220–31.

[Klonos11] Klonos P, Panagopoulou A, Kyritsis A, Bokobza L, Pissis P. J Non–Cryst Solids 2011;357:610–4.

[Klonos12] Klonos P, Pandis Ch, Kripotou S, Kyritsis A, Pissis P. IEEE Transact Diel Electr Insul 2012;19:1283–90.

[Klonos13] Klonos P, Kaprinis S, Zarko VI, Peoglos V, Pakhlov EM, Pissis P, Gun'ko VM. J Appl Polym Sci 2013;128:1601–15.

[Klonos15A] Klonos P, Sulym IY, Borysenko MV, Gun'ko VM, Kripotou S, Kyritsis A, Pissis P. Polymer 2015;58:9–21.

[Klonos15B] Klonos P, Sulym IY, Kyriakos K, Vangelidis I, Zidropoulos S, Sternik D, Borysenko MV, Kyritsis A, Deryło–Marczewska A, Gun'ko VM, Pissis P. Polymer 2015;68:158–67.

[Klonos15C] Klonos P, Kyritsis A, Pissis P. Eur Polym J 2015;70:342–59.

[Klonos15D] Klonos P, Kyritsis A, Pissis P. *Interfacial dynamics of polydimethylsiloxane adsorbed on fumed metal oxide particles of a wide range of specific surface area*. Polymer 2015;77:10-13.

[Klonos15TA] Klonos P, Kripotou S, Kyritsis A, Papageorgiou GZ, Bikiaris D, Gournis D, Pissis P. Thermochimica Acta 2015;617:44–53.

[Kochumalayil13] Kochumalayil JL, Bergenstrahle–Wohlert M, Utsel S, Wagberg L, Zhou Q, Berglund A. Biomacromolecules 2013;14:84–91.

[Kofinas11] Yang TI, Brown RNC, Kempel LC, Kofinas P. Nanotechnology 2011;22:105601.

[Koga12] Gin P, Jiang N, Liang C, Taniguchi T, Akgun B, Satija SK, Endoh MK, Koga T. Phys Rev Lett 2012;109:265501.

[Koga14] Jiang N, Shang J, Di X, Endoh MK, Koga T. Macromolecules 2014;47:2682–9.

[Koski13] Koski J, Chao H, Riggleman RA. The J Chem Phys 2013;139:244911.

[Kramarenko05] Fragiadakis D, Logakis E, Pissis P, Kramarenko VYu, Shantalii TA, Karpova IL, Dragan KS, Privalko EG, Usenko A, Privalko VP. J Phys: Conf Ser

2005;10**:**139–42.

[Kremer02] Kremer F, Schoenhals A, editors. Broadband dielectric spectroscopy. Berlin: Springer; 2002.

[Kremer14] Kremer F, editor. Dynamics in Geometrical Confinement, Advances in Dielectrics, vol 8. Switzerland: Springer International; 2014.

[Kripotou10] Kripotou S, Pissis P, Savelyev YV, Robota LP, Travinskaya TV. J Macrom Sci, Part B: Phys 2010;49:86–110.

[Kritikos13] Kritkos G, Terzis AF. Eur Polym J 2013;49:613–29.

[Kruk01] Kruk M, Jaroniec M. Chem Mater 2001;13:3169–83.

[Krutyeva13] Krutyeva M, Wischnewski A, Wilner L, Maiz J, Mijangos C, Arbe A, Colmenero J, Radulescu A, Holderer O, Ohl M, Richter D. Phys Rev Lett 2013;110:108303.

[Kumar99N] Jones RL, Kumar SK, Ho DL, Briber RM, Russell TP. Nature 1999;400:146–9.

[Kumar05] Kumar KV, Sivanesan S. J Hazard Mater 2005;126:198–201.

[Kumar10] Kumar SK, Krishnamoorti R. Annu Rev Chem Biomol Eng 2010;1:37–58.

[Kumar13] Kumar SK, Jouault, Benicewicz B, Neely T. Macromolecules 2013;46:3199–24.

[Kutvonen12] Kutvonen A, Rossi G, Puisto SR, Rostedt NK, Ala–Nissila T. The J Chem Phys 2012;137:214901.

[Kyritsis95] Kyritsis A, Pissis P, Gomez Ribelles JL, Monleon Pradas M. Polym Gels Netw 1995;3:445–69.

[Lacabanne11] Capsal JF, Dantras E, Dandurand J, Lacabanne C. J Non–Cryst Solids 2011;357:587–93.

[Lang14] Lang RJ, Merling WL, Simmons DS. ACS Macro Lett 2014;3:758–62.

[Lee05] Lee KY, Paul DR. Polymer 2005;46:9064.

[Leng15] Leng J, Purohit PJ, Kang N, Wang DY, Falkenhagen J, Emmerling F, Thünemann AF, Schönhals A. Eur Polym J 2015;68:338–54.

[Li14] Li L, Zhou D, Huang D, Xue G. Macromolecules 2014;47:297–03.

[Li15] Li L, Chen J, Deng W, Zhang C, Sha Y, Cheng Z, Xue G, Zhou D. J Phys Chem B 2015;119:5047–54.

[Liao12] Liao B, Zebarjadi M, Esfarjani K, Chen G. Phys Rev Lett 2012;109:126806.

[Lin15] Lin Y, Liu L, Xu G, Zhang D, Guan A, Wu G. J Phys Chem C 2015;119:12956–66.

[Lincoln01] Lincoln DM, Vaia RA, Wang ZG, Hsiao BS. Polymer 2001;42:1621–31.

[Litvinov91] Litvinov V, Spiess H. Macromol. Chem Phys 1991;192:3005–19.

[Liu10] Liu YL, Chen E. Coord Chem Rev 2010;254:1011–37.

[Liu11] Liu J, Gao Y, Cao D, Zhang L, Guo Z. Langmuir 2011;27:7926–33.

[Logakis09] Logakis E, Pandis C, Peoglos V, Pissis P, Stergiou C, Pionteck J, Poetschke P, Micusik M, Omastova M. J Polym Sci, Part B: Polym Phys 2009;47:764–74.

[Lorthioir04] Lorthioir C, Alegria A, Colmenero J, Deloche B. Macromolecules 2004;37:7808–17.

[Lund08] Lund R, Alegría A, Goitandia L, Colmenero J, Gonzaalez MA, Lindner P. Macromolecules 2008;41:1364–76.

[Luo11] Luo T, Esfarjani K, Shiomi J, Henry A, Chen G. J Appl Phys 2011;109:074321.

[Mai12] Mai DJ, Brockman C, Schroeder. Soft Matter 2012;8:10560–72.

[Mansfield89] Mansfield KF, Theodorou DN. Macromolecules 1989;22:3143–52.

[Mark96] Mark J. Polym Eng Sci 1996;36:2905–20.

[Matejka00] Matejka L, Dukh O, Kolarik J. Polymer 2000;41:1449–59.

[Melnichenko03] Melnichenko YB, Wingnall GD, Schwahn D. Fluid Phase Equilibria 2003;212:209–19.

[Merino13] Merino EG, Neves PD, Fonseca IM, Danéde F, Idrissi A, Dias CJ, Dionísio M, Correia N. J Phys Chem C 2013;117:21516–28.

[Mijovic06] Mijovic J, Lee H, Kenny J, Mays J. Macromolecules 2006;39:2172.

[Miwa04] Miwa Y, Sugino Y, Yamamoto K, Tanabe T, Sakaguchi M, Sakai M, Shimada S. Macromolecules 2004;37:6061–8.

[Miwa06] Miwa Y, Drews AR, Schlick S. Macromolecules 2006;39:3304–31.

[Miyazaki02] Miyazaki T, Kaneko T, Gong JP, Osada Y, Demura M, Suzuki M. Langmuir 2002;18:965–7.

[Moll12] Moll J, Kumar SK. Macromolecules 2012;45:1131–4.

[Moniruzzaman06] Moniruzzaman M, Winey KI. Macromolecules 2006;39:5194–205.

[Morks08] Morks MF, Kobayashi A. J Mech Behav Biomed Mater 2008;1:165–71.

[Muthkumar12] Muthkumar M. Polymers under Confinement, in Advances in Chemical Series, vol 149. New Jersey: John Wiley & Sons; 2012.

[Nakabayashi12] Nakabayashi K, Oya H, Mori H. Macromolecules 2012;45:3197–204.

[Nan12] Nan A, Turcu R, Liebscher J. J Polym Sci A Polym Chem 2012;50:1485–90.

[Napolitano06] Napolitano S, Wübbenhorst M. Macromolecules 2006;39:5967–70.

[Napolitano07] Napolitano S, Wübbenhorst M. J Non–Cryst Solids 2007;353:4357–61.

[Napolitano08] Napolitano S, Lupascu V, Wübbenhorst M. Macromolecules 2008;41:1061–3.

[Napolitano10] Napolitano S, Wübbenhorst M. ACS Nano 2010;4:841–48.

[Napolitano11] Napolitano S; Wübbenhorst M. Nature Commun 2011;2:260.

[Napolitano12] Napolitano S, Rotella C, Wübbenhorst M. ACS Macro Lett 2012;1:1189–93.

[Napolitano14] Housmans C, Sferrazza M, Napolitano S. Macromolecules 2014;47:3390–3393.

[Ngai98] Ngai KL. J Chem Phys 1998;109:6982–94.

[Nikaj10] Nikaj E, Stevenson–Royaud I, Seytre G, David L, Espuche E. J Non–Cryst Solids 2010;356:589–96.

[Nodera06] Nodera A, Toshitaka K. J Appl Polym Sci 2006;101:3862–8.

[O'Connell05] O'Connell PA, McKenna GB. Science 2005;307:1760–3.

[Okada06] Okada A, Usuki A. Macromol Mater Eng 2006;291:1449–76.

[Paeng11] Paeng K, Swallen SF, Ediger MD. J Am Chem Soc 2011;133:8444–7.

[Page06] Page KA, Adachi K. Polymer 2006;47:6406–13.

[Pahlavanpour13] Pahlavanpour M, Moussaddy H, Chossein E, Hubert P, Lévesque M. Comput Mater Sci 2013;79:206–15.

[Panagopoulou08] Panagopoulou A. MSc Thesis, Study of molecular dynamics and properties in polydimethylsiloxane/titania nanocomposites. Athens: National Technical University of Athens; 2008.

[Panagopoulou12] Panagopoulou A, Kyritsis A, Shinyashiki N, Pissis P. J Phys Chem B 2012;116:4593–602.

[Pandis11] Pandis C, Spanoudaki A, Kyritsis A, Pissis P, Rodríquez Hernández JC, Gómez Ribelles JL, Monleón Pradas M. J Polym Sci B Polym Phys 2011;49. 657–68.

[Papageorgiou14] Papageorgiou GZ, Terzopoulou Z, Bikiaris D, Triantafyllidis KS, Diamanti E, Gournis D, Klonos P, Giannoulidis E, Pissis P. Thermochimica Acta 2014;597:48–57.

[Papakonstanto–poulos05] Papakonstantopoulos GJ, Yoshimoto K, Doxastakis M, Nealey PF, de Pablo JJ. Phys Rev E 2005;72: 031801.

[Papon11] Papon A, Saalwächter K, Schäler K, Guy L, Lequeux F, Montes H. Macromolecules 2011;44:913–22.

[Paul08] Paul DR, Robenson LM. Polymer 2008;49:3187–204.

[Pavlidou08] Pavlidou S, Papaspyrides CD. Prog Polym Sci 2008;33:1119–98.

[Pelster99] Pelster R, Simon U. Colloid Polym Sci 1999;277:2–14.

[Pelster01] Spanoudaki A, Pelster R. Phys Rev B 2001;064205:642051–6.

[Pfaller13] Pfaller S, Rahimi M, Possart G, Steinmann P, Müller–Plathe F, Böhm MC. Comput Methods Appl Mech Engrg 2013;260:109–29.

[Pissis08] Pissis P, Fragiadakis D, Kanapitsas A, Delides K, Macromol Symp 2008;265:12.

[Pissis13] Pissis P, Kyritsis A. J Polym Sci B Polym Phys 2013;51:159–75.

[Plueddeman82] Plueddeman EP. Silane Coupling Agent. Plenum Press;New York:1982.

[Priestley07] Priestley RD, Rittigstein P, Broadbelt LJ, Fukao K, Torkelson JM. J Phys: Condens Matter 2007;19:205120.

[Purohit14] Purohit PJ, Wang D, Wurm A, Schick C, Schönhals A. Eur Polym J 2014;55:48–56.

[Qiao11] Qiao R, Deng H, Putz KW, Brinson C. J Polym Sci B Polym Phys 2011;49:740–8.

[Quan15] Quan D, Ivankovic A. Polymer 2015;66:16–28.

[Raftopoulos10] Raftopoulos KN, Pandis Ch, Apekis L, Pissis P, Janowski B, Pielichowski K, Jaczewska J. Polymer 2010;51:709–18.

[Ramanathan08] Ramanathan T, Abdala AA, Stankovich S, Dikin DA, Herrera–Alonso M, Piner RD, Adamson DH, Schniepp HC, Chen X, Ruoff RS, Nguyen ST, Aksay IA., Prud'Homme RK, Brinson LC. Nature Nanotech 2008;3:327–31.

[Ray03] Ray SS, Okamoto M. Prog Polym Sci 2003;28:1539–641.

[Redeker13] Redeker ND, Danesh CD, Ding Y, Zhang S. Polymer 2013;54:7004–8.

[Richardson77] Richardson MOW, editor. Polymer engineering composites. London: Applied Science Publishers LTD; 1977.

[Richter89] Richter D, Ewen B, Farago B, Wagner T. Phys Rev Lett 1989;62:18.

[Richert98] Richert R, Angell CA. J Chem Phys 1998;108(21):9016–26.

[Righetti14] Righetti MC, Laus M, Di Lorenzo ML. Eur Polym J 2014;58:60–8.

[Rittigstein06] Rittigstein P, Torkelson JM. J Polym Sci, Part B: Polym Phys 2006;44:2935–43.

[Robertson08] Robertson CG, Lin CJ, Rackaitis M, Roland CM. Macromolecules 2008;41:2727–31.

[Rodriguez08] Rodriguez Hernandez JC, Monleon Pradas M, Gomez Ribelles JL. J Non–Cryst Solids 2008;354:1900–8.

[Rotella11] Rotella C, Napolitano S, Vandendriessche S, Valev VK, Verbiest T, Larkowska M, Kucharski S, Wübbenhorst M. Langmuir 2011;27:13533–8.

[Saiter13] Saiter A, Prevosto D, Passaglia E, Counderc H, Delbreilh L, Saiter JM. Phys Rev Lett E 2013;88:042605.

[Sappelt93] Sappelt D, Jackle J. J Phys A: Math Gen 1993;26:7325–41.

[Sargsyan07] Sargsyan A, Tonoyan A, Davtyan S, Schick C. Eur Polym J 2007;43:3113–27.

[Scheutjens79] Scheutjens JMHM, Fleer GJ. J Phys Chem 1979;83:1619–35.

[Schönhals02] Frunza L, Kosslick H, Frunza S, Schönhals A. J Phys Chem B 2002;106:9191–4.

[Schönhals03] Schönhals A, Goering H, Schick Ch, Frick B, Zorn R. Eur Phys J 2003;E12:173–178.

[Schönhals15] Leng J, Purohit PJ, Kang N, Wand DY, Falkenhagen J, Emmerling F, Thünemann AF, Schönhals A. Eur Polym J 2015;68:338–54.

[Schmidt10] Schmidt DF, Giannelis EP. Chem Mater 2010;22:167–74.

[Schwartz04] Schwartz GA, Bergman R, Swenson J. J Chem Phys;22:5736–44.

[Sen07] Sen S, Thomin JD, Kumar SK, Keblinski P. Macromolecules 2007;40:4059–67.

[Shinyashiki07] Capaccioli S, Ngai KL, Shinyashiki N. J Phys Chem B 2007;111:8197–209.

[Shinyashiki07B] Shinyashiki N, Sudo S, Yagihara S, Spanoudaki A, Kyritsis A, Pissis P. J Phys Condens Matter 2007;19:205113.

[Si06] Si M, Araki T, Ade H, Kilcoyne ALD, Fisher R, Sokolov JC, et al. Macromolecules 2006;39:4793–801.

[Siengchin08] Siengchin S, Karger–Kocsis J, Psarras GC, Thomann R. J Appl Polym Sci 2008;110:1613.

[Singha14] Singha S, Jana T. ACS Appl Mater Interf 2014;6:21286–96.

[Sohrabi13] Sohrabi A, Shaibani PM, Etayash H, Kaur K, Thundat T. Polymer 2013;54:2699–705.

[Sorai04] Sorai M, editor. Comprehensive Handbook of Calorimetry and Thermal Analysis. West Sussex: Wiley; 2004.

[Soutzidou98] Soutzidou M, Panas A, Viras K. J Polym Sci B 1998;36:2805–10.

[Sperling06] Sperling LH. Introduction to physical polymer science. New Jersey: Wiley; 2006.

[Spiess02] Dollase T, Spiess HW, Gottlieb M, Yerushalmi–Rozen R. Europhys Lett 2002;60:390–6.

[Srivastava07] Srivastava S, Basu JK. Phys Rev Lett 2007;98:165701.

[Stamatopoulou14] Stamatopoulou C, Klonos P, Koutsoumpis S, Gun'ko VM, Pissis P, Karabanova L. J Appl Polym Sci B Polym Phys 2014;52:397–408.

[Stathopoulos10] Stathopoulos A, Klonos P, Kyritsis A, Pissis P, Christodoulides C, Rodriquez Hernández JC, Monleón Pradas M, Gómez Ribelles JL. Eur Polym J 2010;46:101–11.

[Starr01] Starr FW, Schrøder TB, Glotzer SC. Phys Rev E 2001;64:218021–5.

[Stirnemann11] Stirneman G, Castrillon SRV, Hynes JT, Rossky PJ, Debenedetti PG, Laage D. Phys Chem Chem Phys 2011;13:19911–7.

[Sulim09] Sulim IY, Borysenko MV, Korduban OM, Gun'ko VM. Appl Surf Sci 2009;255:7818–24.

[Sulym14] Sulym I, Klonos P, Borysenko M, Pissis P, Gun'ko VM. J Appl Polym Sci 2014;131:10.1002. (doi: 10.1002/app.41154)

[Sundararajan02] Sundararajan PR. Polymer 2002;43:1691–3.

[Sen07] Sen S, Xie Y, Kumar SK, Yang H, Bansal A, Ho DL, Hall L, Hooper JB, Schweizer KS. Phys Rev Lett 2007;98:128302.

[Starr13] Pazmino Betancourt BA, Douglas JF, Starr FW. Soft Matter 2013;9:241–54.

[Syunyaev07] Syunyaev RZ, Balabin RM. J Dispers Sci Technol 2007;28:419–24.

[Takakashi06] Takakashi S, Paul DR. Polymer 2006;47:7519–34.

[Tavares14] Tavares MTS, Santos ASF, Santos LMG, Silva MRS, Bomio MRD, Longo E,

Paskocimas CA, Motta FV. Surf Coat Technol 2014;239:16–9.

[Termonia09] Termonia Y. Polymer 2009;50:1062–66.

[Theodorou14] Theodorou DN, Vogiatzis GG, Kritikos G. Macromolecules 2014;47:6964–81.

[Tigges11] Tigges B, Popescu C, Weichold O. Soft Matter 2011;7:5391–6.

[Timmermann89] Timmermann EO. J Chem Soc Faraday Trans 1 1989;85:1631–45.

[Tress10] Tress M, Erber M, Mapesa EU, Huth H, Müller J, Serghei A, Schick C, Eichhorn KJ, Voit B, Kremer F. Macromolecules 2010;43:9937–44.

[Tress13] Tress M, Mapesa EU, Kossack W, Kipnusu WK, Reiche M, Kremer F. Science 2013;341:1371–4.

[Tsagaropoulos95] Tsagaropoulos G, Eisenberg A. Macromolecules 1995;28:6067–77.

[Tuteja07] Tuteja A, Duxbury PM, Mackay ME. Macromolecules 2007;40:9427–34.

[Vanroy13] Vanroy B, Wübbenhorst W, Napolitano S. ACS Macro Lett 2013;2:168–72.

[Vatalis01] Vatalis AS, Kanapitsas A, Delides CG, Pissis P. Thermochim Acta 2001;372:33–38.

[Vogiatzis11] Vogiatzis GG, Voyiatzis E, Theodorou DN. Eur Polym J 2011;47:699–712.

[Vogiatzis13] Vogiatzis GG, Theodorou DN. Macromolecules 2014;44:387–404.

[Vralstad09] Vralstad H, Spets Ø, Lesaint C, Lundgaard L, Sjoblom J. Energy Fuels 2009;23:5596–602.

[VTFH] Vogel H. Phys Z 1921;22:645–6. Fulcher GS. J Am Ceram Soc 1925;8:339–55. Tammann G, Hesse W. Z Anorg Allg Chem 1926;156:245–57.

[Wang03] Wang Y, Zhang Q, Fu Q. Macrom Rapid Commun 2003;24:231–5.

[Wang06] Wang Y, Gao S, Ye W, Yoon HS, Yang Y. Nature Mater 2006;5:791–6.

[Wang14] Wang Y, Wohlet J, Berglund LA, Tu Y, Agren H. J Mater Chem A 2014;2:9541–7.

[Wang15] Wang Y, Wohlert J, Bergenstrahle–Wohlert M, Kochumalayil JL, Berglund LA, Tu Y, Agren H. Biomacromolecules 2015;16:257–65.

[Wolf12] Wolf M, Gulich R, Lunkenheimer P, Loidl A. Biochim Biophys Acta 2012;1824:723–30.

[Wu10] Wu C. Polymer 2010;51:4452–60.

[Wunderlich95] Wunderlich B. Pur Appl Chem 1995;67:1019. (See also on WWW URL http://athas.prz.edu.pl/Default.aspx?op=db)

[Wunderlich03] Wunderlich B. Prog Polym Sci 2003;28:383–450.

[Wurm03] Wurm A, Soliman R, Schick C. Polymer 2003;44:7467–76.

[Wurm10] Wurm A, Ismail M, Kretzschmar B, Pospiech D, Schick C. Macromolecules 2010;43:1480–7.

[Xu04] Xu H, Cebe P. Macromolecules 2004;37:2797–806.

[Yabu14] Yabu H, Hiquchi T, Jinnai H. Soft Matter 2014;10:2919–2931.

[Yan13] Yan LT, Xie XM. Prog Polym Sci 2013;38:369–405.

[Yang12] Yang S, Choi J, Cho M. ACS Appl Mater Interfaces 2012;4:4792–9.

[Yang14] Yang J, Wang X, Zhao H, Zhang W, Xu M. IEEE Transact Diel Electr Insul 2014;21:1957–64.

[Yin15] Yin H, Madkour S, Schönhals A. Macromolecules 2015;doi: 10.1021/acs.macromol.5b01259.

[Yu09] Yu L, Cebe P. J Polym Sci, Part B: Polym Phys 2009;47:2520–32.

[Zhuravlev14] Zhuravlev E, Wurm A, Pötschke P, Androsch R, Schmelzer JWP, Schick C. Eur Polym J 2014;52:1–11.

[Zou08] Zou H, Wu S, Shen J. Chem Rev 2008;108:3893–957.

Εκτενής περίληψη

Στην παρούσα διδακτορική διατριβή, με τίτλο '*Διεπιφανειακές αλληλεπιδράσεις και μοριακή δυναμική σε οργανικά-ανόργανα νανοσύνθετα πολυμερικά υλικά*', πραγματοποιείται μία συστηματική μελέτη της επίδρασης των διεπιφανειακών αλληλεπιδράσεων μεταξύ ενός πολυμερούς (συγκεκριμένα, του πολυδιμεθυλοσιλοξανίου, PDMS) (Εικόνα 1) και της στερεάς επιφάνειας διαφόρων τύπων νανοσωματιδίων μεταλλικών οξειδίων (πυριτίας, τιτανίας, Εικόνα 2) στη μοριακή δυναμική και της θερμικές μεταβάσεις του πολυμερούς. Μελετούμε κυρίως τα χαρακτηριστικά του πολυμερούς που αλληλεπιδρά απευθείας με τα νανοσωματίδια. Το κύριο μέσον αλληλεπίδρασης πολυμερούς-σωματιδίων είναι η ανάπτυξη ισχυρών δεσμών υδρογόνου μεταξύ των υδροξυλίων (-OH) στην επιφάνεια των οξειδίων (Εικόνα 2) και των οξυγόνων (-O-) της πολυμερικής αλυσίδας (Εικόνα 1).

Το κλάσμα του πολυμερούς που αλληλεπιδρά απευθείας με τα νανοσωματίδια ονομάζεται '*διεπιφανειακό πολυμερές*' ή '*διεπιφανειακό στρώμα*' και θεωρείται ευρέως ότι η παρουσία του ευθύνεται για τις σημαντικώς βελτιωμένες ιδιότητες που χαρακτηρίζουν τα νανοσύνθετα (ΝΣ) πολυμερικά υλικά, σε σύγκριση με τα παραδοσιακά σύνθετα υλικά (μικροσύνθετα). Τα τελευταία χρόνια έχει προταθεί ότι οι τροποιημένες ιδιότητες του διεπιφανειακού πολυμερούς κυριαρχούν επί των τελικών ιδιοτήτων του ΝΣ. Εκτός των φυσικών ιδιοτήτων του εκάστοτε πολυμερούς (π.χ. τη δομή του), τα χαρακτηριστικά της προς αλληλεπίδραση στερεής επιφάνειας παίζουν σημαντικό ρόλο στην ανάπτυξη των διεπιφανειακών αλληλεπιδράσεων. Έχει επίσης αναφερθεί ότι το μέγεθος και η επιφανειακή καμπυλότητα των νανοσωματιδίων επηρεάζουν την ισχύ της αλληλεπίδρασης. Πιο συγκριμένα, φαίνεται ότι το πάχος του διεπιφανειακού πολυμερικού στρώματος αυξάνεται όσο αυξάνει το μέγεθος σφαιρικών σωματιδίων ή, ισοδυνάμως, όσο περιορίζεται η καμπυλότητα της επιφάνειας των σωματιδίων. Στην παρούσα μελέτη, παρουσιάζουμε αποτελέσματα που αναδεικνύουν πώς η *επιφανειακή τραχύτητα νανομετρικής κλίμακας* των

νανοσωματιδίων και η *ευκαμψία* της πολυμερικής αλυσίδας κυριαρχούν στον καθορισμό των διεπιφανειακών αλληλεπιδράσεων συγκριτικά με άλλες παραμέτρους, όπως ο τύπος και το μέγεθος των νανοσωματιδίων, τουλάχιστον για τα ΝΣ που βασίζονται στο PDMS. Η επιφανειακή τραχύτητα των σωματιδίων δεν έχει μελετηθεί έως τώρα στη βιβλιογραφία, ως ιδιότητα-παράμετρος σχετική με την αλληλεπίδραση πολυμερούς-εγκλείσματος στα ΝΣ.

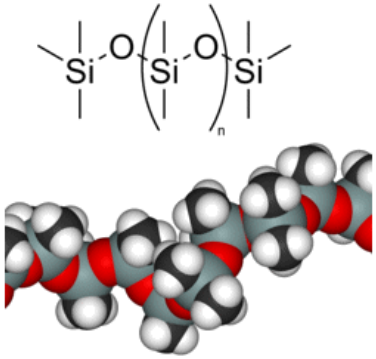

Εικόνα 1. Μοριακή δομή και σχηματική αναπαράσταση της πολυμερικής αλυσίδας του πολυδιμεθυλοσιλοξανίου (polydimethylsiloxane, PDMS)

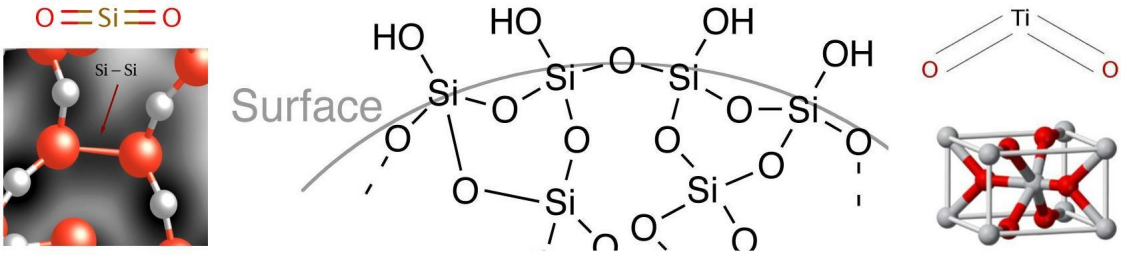

Εικόνα 2. Σχηματική αναπαράσταση της μοριακής δομής της πυριτίας (silica, αριστερά και μέση) και της τιτανίας (titania, δεξιά).

Η παρούσα μελέτη περιλαμβάνει μετρήσεις μορφολογίας, θερμικών μεταβάσεων και διηλεκτρικής συμπεριφοράς σε ΝΣ συστήματα PDMS/πυριτίας και PDMS/τιτανίας (α) διαφόρων περιεκτικοτήτων σε σωματίδια, (β) μεγάλου εύρους επιφανειακής τραχύτητας και μεγέθους σωματιδίων, (γ) διαφόρων μοριακών βαρών και δομής του πολυμερούς (γραμμικό/σταυροδεμένο), και (δ) σε διάφορα επίπεδα υδάτωσης των υλικών. Για την αποτίμηση των επιπέδων υδάτωσης εφαρμόσθηκαν τεχνικές ισόθερμης υδάτωσης–αφυδάτωσης σε ισορροπία (σε θερμοκρασία δωματίου).

Τα προς μελέτη υλικά μπορούν να κατηγοριοποιηθούν σε δύο σειρές. Τα υλικά της πρώτης σειράς θεωρούνται '*συμβατικά*' νανοσύνθετα (ΝΣ) και είναι δοκίμια στα οποία έχουν συντεθεί και διασπαρεί νανοσωματίδια πυριτιας (SiO_2) και τιτανίας (TiO_2), διαμέτρου 5 και

~30 nm, αντιστοίχως, παρουσία (*in situ*) δικτύων PDMS (μοριακού βάρους *MB* ~18000) μέσω τεχνικών λύματος πηκτής (sol–gel technique) (Εικόνα 3). Τα υλικά παρασκευάσθηκαν από την Καθηγήτρια Liliane Bokobza στο Laboratoire PPMD, E.S.P.C.I., στο Παρίσι της Γαλλίας. Τέτοια υλικά σχεδιάζονται για χρήση σε ελαστικά αυτοκινήτων. Τα υλικά της δεύτερης σειράς θεωρούνται ΝΣ τύπου '*πυρήνα–φλοιού*' και είναι συστήματα στα οποία γραμμικό PDMS (*MB* ~2000 και ~8000) έχει προσροφηθεί με φυσικό τρόπο (ανάπτυξη δεσμών υδρογόνου) σε συσσωματώματα νανοσωματίδιων μεταλλικών οξειδίων (Εικόνες 4,5), οι επιφάνειες των οποίων χαρακτηρίζονται από μεγάλο εύρος νανομετρικής τραχύτητας (ειδική επιφάνεια, S_{BET}). Τα συσσωματώματα αποτελούνται από νανοσωματίδια τιτανίας (αρχικά σωματίδια διαμέτρου ~70 nm, συσσωματώματα ~800 nm, S_{BET} ~25 m^2/g) και διαφόροι τύποι νανοσωματιδίων πυριτίας (αρχικά σωματίδια 8–85 nm, συσσωματώματα 300–600 nm, S_{BET} ~55–342 m^2/g). Τα υλικά αυτής της κατηγορίας παρασκευάσθηκαν από την ερευνητική ομάδα του Καθηγητή Vladimir M. Gun'ko στο Institute of Surface Chemistry, National Academy of Sciences of Ukraine στο Κίεβο της Ουκρανίας. Η τροποποίηση (tuning) των ιδιοτήτων τέτοιων σωματιδίων (πορωσιμότητα, υδροφιλικότητα) μέσω της επιφανειακής προσρόφησης πολυμερούς στοχεύει στη χρήση τέτοιων υλικών σε χημικές, βιολογικές και βιοϊατρικές εφαρμογές.

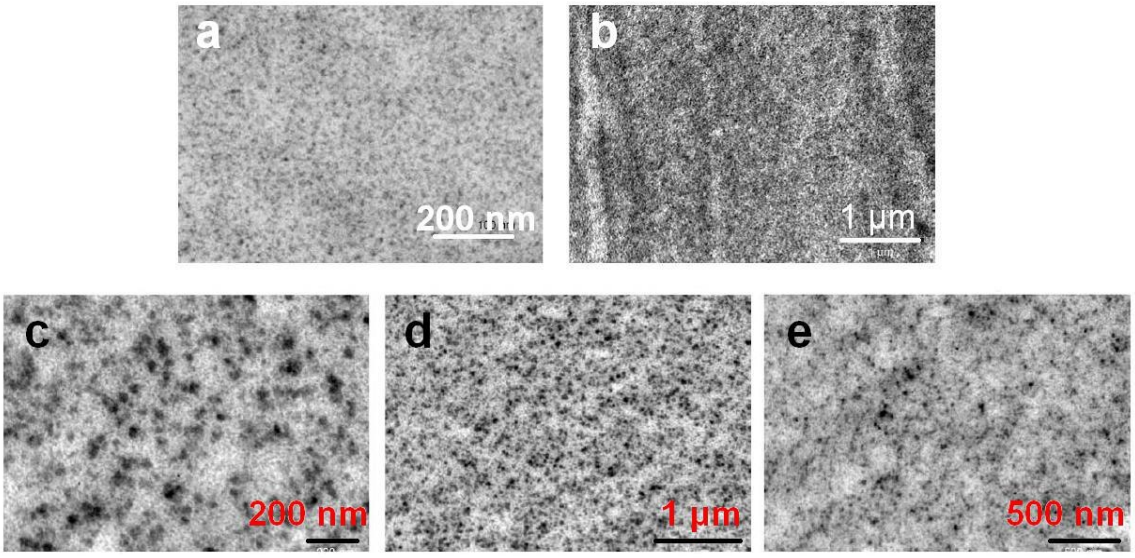

Εικόνα 3. Εικόνες TEM για συμβατικά ΝΣ συστήματα με βάση μήτρα PDMS και διασπαρμένα σωματίδια: (a) 9 wt% πυριτία, (b) 22 wt% πυριτία, (c) 11 wt% τιτανία, (d) 11 wt% τιτανία, και (e) 20 wt% τιτανία [Bokobza L, Diop AL. Express Polym Lett 2010;4:355–63]

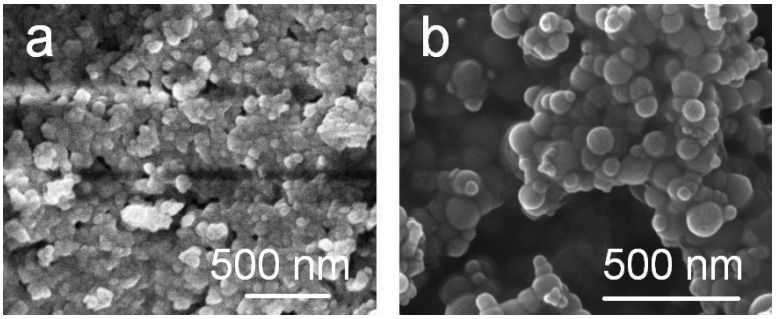

Εικόνα 4. Εικόνες SEM για δοκίμια καθαρών οξειδίων (a) πυριτίας και (b) τιτανίας

Μελετήθηκαν, επίσης, φαινόμενα χωρικού περιορισμού του πολυμερούς (spatial confinement effects) σε δοκίμια στα οποία το PDMS είναι προσφοφημένο σε πόρους κυλινδρικού τύπου (διαμέτρων 6-20 nm) silica–gel υψηλής ειδικής επιφάνειας (S_{BET} ~384 m^2/g). Για επιλεγμένα δοκίμια, οι επιφάνειες τροποποιήθηκαν μερικώς μέσω χημικής ανάπτυξης μικρών νανοσωματιδίων ζιρκονίας (ZrO_2) με σκοπό την χειραγώγηση της αλληλεπίδρασης σωματιδίου-πολυμερούς.

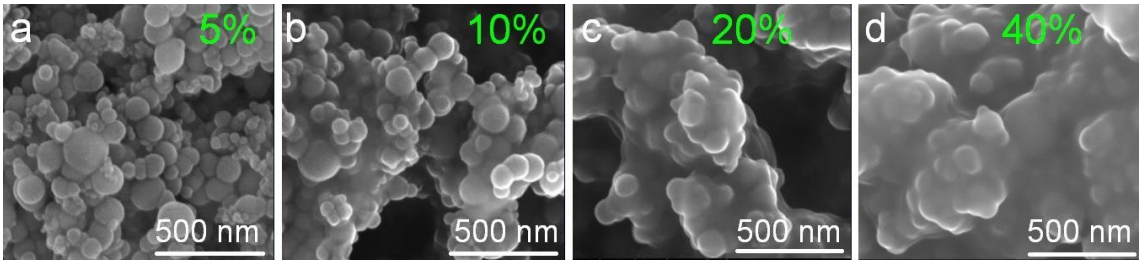

Εικόνα 5. Εικόνες SEM για ΝΣ συστήματα TiO_2/PDMS τύπου *core–shell* για περιεκτικότητες σε PDMS από 5 έως 40 wt%

Η μορφολογία των υλικών εξετάσθηκε με χρήση μικροσκοπίας ηλεκτρονιακής σάρωσης (SEM) (Εικόνες 4,5). Οι θερμικές μεταβάσεις (με έμφαση στην υαλώδη μετάβαση) καταγράφηκαν εφαρμόζοντας την τεχνική της διαφορικής θερμιδομετρίας σάρωσης (DSC), ενώ η μοριακή δυναμική εξετάσθηκε λεπτομερώς με τη χρήση δύο τεχνικών διηλεκτρικής φασματοσκοπίας, των θερμικώς διεγειρόμενων ρευμάτων αποπόλωσης (TSDC) και της διηλεκτρικής φασματοσκοπίας εναλλασομένου πεδίου (DRS), σε ευρεία περιοχή συχνοτήτων (10^{-4} to 10^6 Hz) και θερμοκρασιών (–150 to 60 ^oC). Οι παραπάνω μετρήσεις διεξήχθησαν χρησιμοποιώντας πειραματικές διατάξεις στον Τομέα Φυσικής του Εθνικού Μετσόβιου Πολυτεχνείου (ΕΜΠ). Τα αποτελέσματά μας διερευνώνται και σε σχέση με αποτελέσματα μετρήσεων ισόθερμης ρόφησης-εκρόφησης αερίου αζώτου/αργού (Incremental Pore Size

Distribution analysis, IPSD), σκέδασης ακτίνων-Χ υπό ευρεία γωνία (WAXD) και φασματοσκοπίας υπερύθρου (FTIR), οι οποίες πραγματοποιήθηκαν στα εν λόγω υλικά στα εργαστήρια που παρασκευάσθηκαν.

Τα σημαντικότερα αποτελέσματα αυτής της διδακτορικής διατριβής συζητούνται αναλυτικά, σε συσχέτιση με σημαντικά ανοιχτά θέματα της πρόσφατης βιβλιογραφίας. Διεξοδικές μετρήσεις υπό διάφορα θερμικά πρωτόκολλα δείχνουν ότι η καλή διασπορά των νανοσωματιδίων εντός της πολυμερικής μήτρας και οι ισχυρές αλληλεπιδράσεις πολυμερούς/νανοσωματιδίων περιορίζουν τις θερμικές μεταβάσεις (κρυστάλλωση, υαλώδης μετάβαση) αλλά και τις συνεργασιακές κινήσεις του πολυμερούς (πολυμερική δυναμική σχετιζόμενη με την υαλώδη μετάβαση).

Επιρροή του τύπου και του κλάσματος βάρους των νανοεγκλεισμάτων στα χαρακτηριστικά του διεπιφανειακού πολυμερούς

Σύμφωνα με τα αποτελέσματα των μετρήσεων DSC, φαίνεται ότι η ανάπτυξη ισχυρών δεσμών υδρογόνου μεταξύ των υδροξυλίων στην επιφάνεια των νανοσωματιδίων (Εικόνα 2) και των οξυγόνων στην κεντρική πολυμερική αλύσιδα του PDMS (Εικόνα 1) οδηγούν στην ανάπτυξη ενός διεπιφανειακού στρώματος δέσμιου/ακίνητοποιημένου πολυμερούς, πάχους λίγων nm. Τα αποτελέσματα δείχνουν μία σημαντική μείωση του βαθμού κρυσταλλικότητας του πολυμερούς (Εικόνα 6) με μία παράλληλη ελάττωση της θερμοκρασίας κρυστάλλωσης (Εικόνα 7). Ο συνδυασμός των παραπάνω αποτελεσμάτων συνιστά σημαντική απόδειξη ότι η ύπαρξη των νανοσωματιδιών και του διεπιφανειακού πολυμερικού στρώματος (α) ευθύνεται για τον περιορισμό του πλήθους των πυρήνων κρυστάλλωσης στο ΝΣ σύστημα και (β) οδηγεί στην ανάπτυξη των κρυσταλλιτών μακρυά από τις διέπιφανειες πολυμερούς/νανοσωματιδίων.

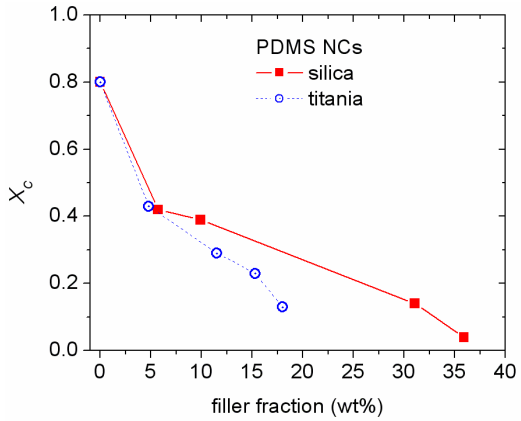

Εικόνα 6. Μείωση του βαθμού κρυσταλλικότητας, X_c, του PDMS με την περιέκτικοτητα σε νανοσωματίδια (πυριτίας και τιτανίας)

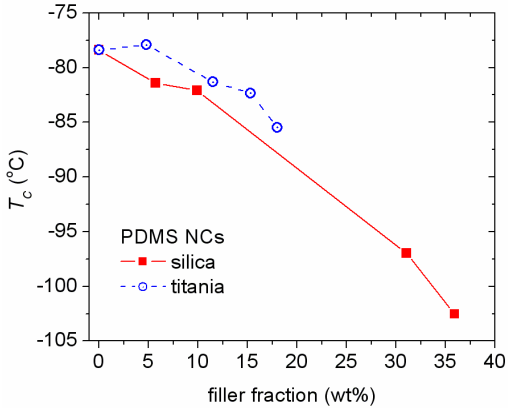

Εικόνα 7. Ελάττωση της θερμοκρασίας κρυστάλλωσης, T_c, του PDMS με την περιέκτικοτητα σε νανοσωματίδια (πυριτίας και τιτανίας)

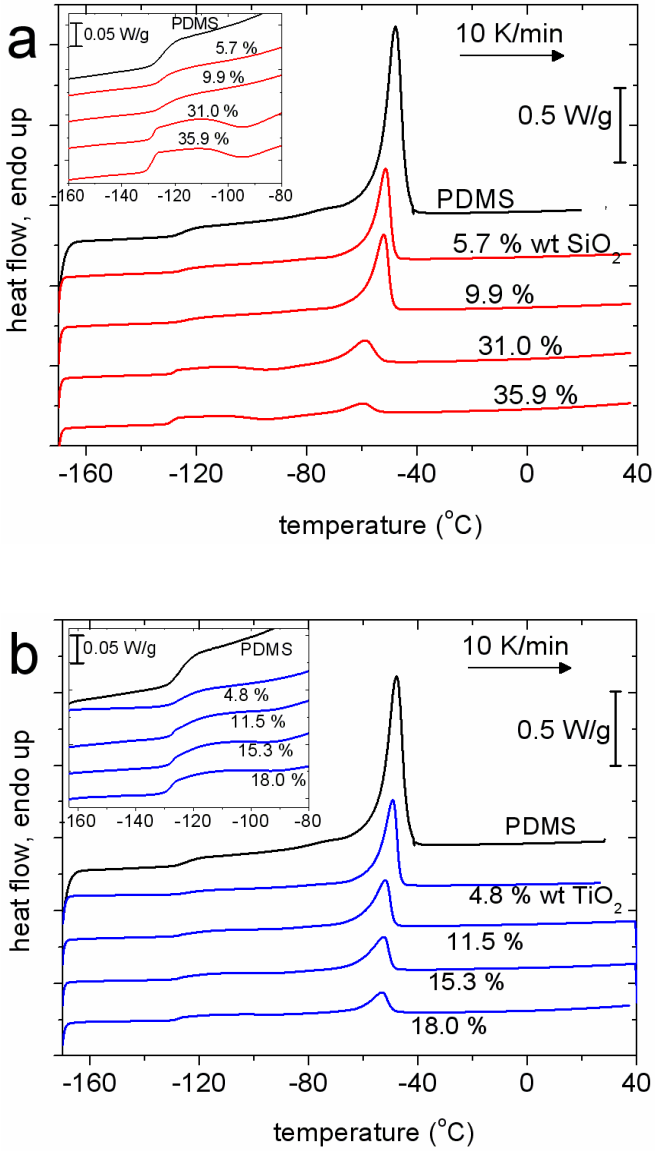

Εικόνα 8. Συγκριτικά θερμογράμματα DSC για το καθαρό PDMS και ΝΣ (a) PDMS/silica και (b) PDMS/titania, κατά τη διάρκεια της θέρμανσης. Στα ένθετα φαίνονται τα βήματα της υαλώδους μετάβασης σε μεγαλύτερη λεπτομέρεια.

Η παρουσία των νανοσωματιδίων στην πολυμερική μήτρα φαίνεται να περιορίζει τις συνεργασιακές κινήσεις του πολυμερούς κατά τη διάρκεια της εξέλιξης της υαλώδους ματάβασης σε χαμηλότερες θερμοκρασίες. Η θερμοκρασία υαλώδους μετάβασης του πολυμερούς, T_g, τείνει να αυξηθεί με την προσθήκη εγκλεισμάτων, ενώ, ταυτοχρόνως, το βήμα της υαλώδους μετάβασης διευρύνεται στην κλίμακα της θερμοκρασίας (αύξηση της

μοριακής ανομοιογένειας) και περιορίζεται στην κλίμακα της παρεχόμενης ισχύος, ΔC_p, (περιορισμός του κλάσματος ελεύθερου πολυμερούς) (Εικόνα 8).

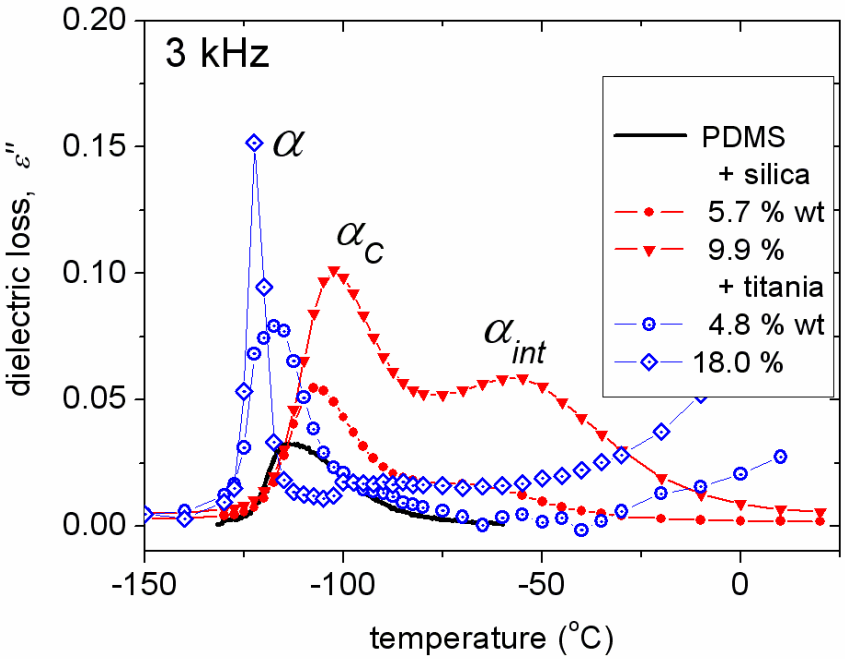

Εικόνα 9. Αντιπροσωπευτικά ίσοχρονα διαγράμματα του φανταστικού μέρους της διηλεκτρικής συνάρτησης (διηλεκτρικές απώλειες), *ε΄΄*, συγκριτικά στη συχνότητα των 3 kHz για ΝΣ PDMS/silica και PDMS/titania

Παράλληλα με τη θερμιδομετρία (DSC), οι διηλεκτρικές τεχνικές προσέφεραν σημαντικές πληροφορίες σχετικά με την συνολική συνεργασιακή δυναμική του πολυμερούς (δυναμική υαλώδους μετάβασης), η οποία βρέθηκε να εκφράζεται από τρεις διακριτές συνεισφορές (τρεις μηχανισμοί διηλεκτρικής αποκατάστασης/χαλάρωσης) (Εικόνα 9). Αυτές οι συνεισφορές προέρχονται από διαφορετικά τμήματα του πολυμερούς, δηλαδή (α) του αμόρφου ανεπηρέαστου (bulk) πολυμερούς (μηχανισμός *α*), (β) του πολυμερούς περιορισμένης κινητικότητας μεταξύ κρυσταλλικών περιοχών (μηχανισμός α_c), και (γ) του διεπιφανειακού πολυμερούς με συνεργασιακή, αλλά καθυστερημένη, δυναμική (μηχανισμός α_{int}) (Εικόνα 9).

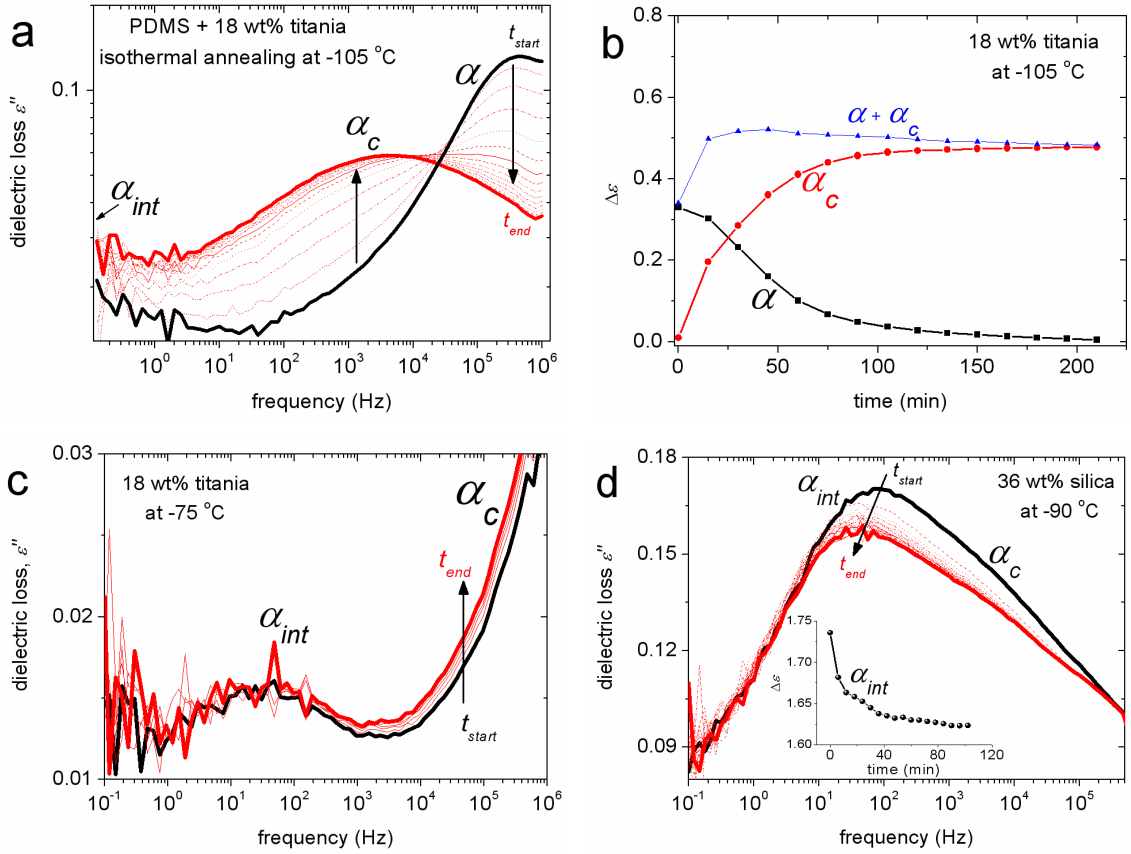

Εικόνα 10. Ισόθερμα φάσματα διηλεκτρικών απωλειών (DRS) για ΝΣ (a-c) PDMS + 18 wt% titania και (d) PDMS + 36 wt% silica, κατά τη διάρκεια της ισόθερμης ανόπτησης της κρυστάλλωσης

Η κινητικότητα του πολυμερούς μακρυά από τη διεπιφάνεια με το έγκλεισμα (bulk polymer) φαίνεται να επηρεάζεται κυρίως από τις μεταβολές στο βαθμό κρυσταλλικότητας. Αυτό ελέγθηκε με πειράματα θερμικής ανόπτησης, που στόχευαν στην ενίσχυση της κρυσταλλικότητας στα ΝΣ (Εικόνα 10). Όπως αναμενόταν, ο μηχανισμός διηλεκτρικής αποκατάστασης που σχετίζεται με τη συνεργασιακή δυναμική του πολυμερούς (υαλώδης μετάβαση) μεταβαίνει από τη συμεριφορά α προς τη συμεριφορά α_c στα ΝΣ (Εικόνες 10a,b). Όσον αφορά τη δυναμική του διεπιφανειακού πολυμερούς, η θερμική ανόπτηση οδήγει σε καταπίεση του μηχανισμού α_{int} μόνο για ΝΣ μεγάλης περιέκτικοτητας σε πυριτία, ενώ για τα υπόλοιπα συστήματα η ίδια θερμική διαδικασία αφήνει εντελώς ανεπηρέαστο το μηχανισμό α_{int} (σύγκριση μεταξύ Εικόνων 10c,d).

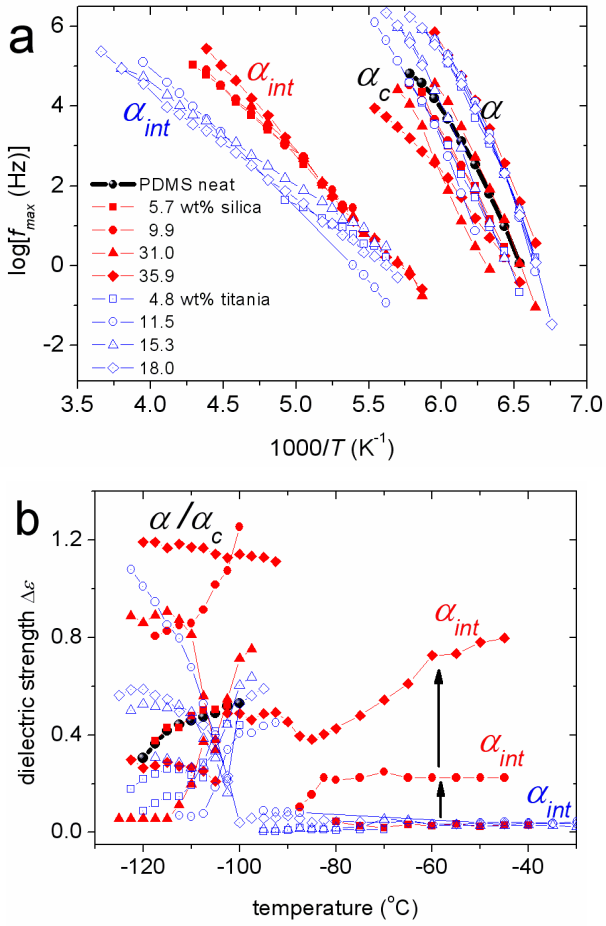

Εικόνα 11. (a) Διηλεκτρικός χάρτης (Arrhenius plots) και (b) θερμοκρασιακή εξάρτηση της διηλεκτρικής ισχύος των μηχανισμών συνεργασιακής αποκατάστασης για το καθαρό PDMS και τα αντίστοιχα ΝΣ PDMS/silica και PDMS/titania

Συγκρίνοντας τους δύο τύπους εγκλείσματος στα συμβατικά ΝΣ, στα συστήματα PDMS/τιτανίας ο μηχανισμός πολυμερικής αποκατάστασης α_{int} καταγράφεται σε χαμηλότερες συχνότητες / υψηλότερες θερμοκρασίες σε σχέση με τα ΝΣ PDMS/πυριτίας (Εικόνα 11), ενώ το εκτιμώμενο πάχος του διεπιφανειακού στρώματος είναι μεγαλύτερο (2 nm και ~4 nm για τα ΝΣ της πυριτίας και τιτανίας, αντιστοίχως, Εικόνα 12). Οι μεταβολές αυτών των χαρακτηριστικών φαίνεται να μην επηρεάζονται απο την περιεκτικότητα (κλάσμα μάζας) του εγκλείσματος. Οι μεταβολές μεταξύ των διαφορετικών τύπων νανοσωματιδίων σχετίζονται, με την ανάπτυξη δεσμών υδρογόνου μεταξύ πολυμερικής μήτρας και εγκλείσματος, οι οποίοι είναι πιθανώς ισχυρότεροι μεταξύ PDMS και τιτανίας σε σχέση με τους αντίστοιχους δεσμούς PDMS–πυριτίας. Αυτή η πρώτη προσέγγιση μπορεί να αιτιολογηθεί με βάση τη διαφορετική ηλεκτροχημική κατάσταση των επιφανειακών υδροξυλίων στα δύο οξείδια (πιο όξινα –OH στην περίπτωση της τιτανίας).

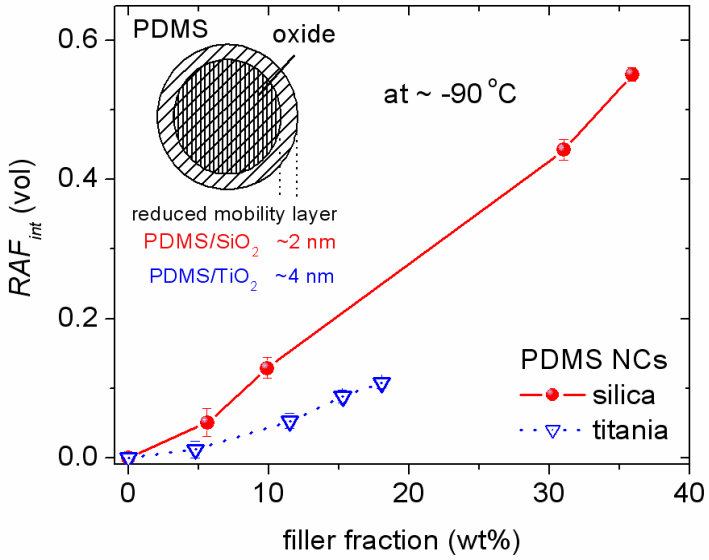

Εικόνα 12. Η περιεκτικότητα του PDMS περιορισμένης κινητικότητας στη διεπιφάνεια με τα νανοσωματίδια, RAF_{int}, συναρτήσει της περιεκτικότητας σε πυριτία (silica) και τιτανία (titania) στους –90 °C. Στο ένθετο παρουσιάζονται αποτελέσματα για την τιμή του εκτιμώμενου πάχους του διεπιφανειακού πολυμερικού στρώματος μέσω γεωμετρικών μοντέλων.

Συγκρίνοντας με την πρόσφατη βιβλιογραφία, τα αποτελέσματά μας (πιο παχύ διεπιφανειακό στρώμα στην περίπτωση των ΝΣ PDMS/τιτανίας) μπορούν να εξηγηθούν επίσης με βάση το μεγαλύτερο μέγεθος των νανοσωματιδίων τιτανίας (σωματίδια διαμέτρου ~30 nm και ~5nm για την τιτανία και την πυριτία, αντιστοίχως). Με στόχο την περαιτέρω διερεύνηση των παραπάνω διαφορών, προχωρούμε στα αποτελέσματα ΝΣ τύπου πυρήνα–φλοιού τιτανίας και πυριτίας. Από αυτά προκύπτει άμεσα η σημαντική επιρροή της νανομετρικής τραχύτητας (roughness) της επιφάνειας των σωματιδίων στον βαθμό της αλληλεπίδρασης πολυμερούς-εγκλείσματος.

Επιρροή της επιφανειακής τραχύτητας στα χαρακτηριστικά του διεπιφανειακού πολυμερούς

Ακολουθούν αποτελέσματα σε ΝΣ τύπου πυρήνα–φλοιού στα οποία PDMS σταθερού κλάσματος (40%) έχει προσροφηθεί στις επιφάνειες συσσωματωμάτων (aggregates) πυριτίας/τιτανίας (Εικόνες 4,5). Οι επιφάνειες των συσσωματωμάτων χαρακτηρίζονται από μεγάλος εύρος νανομετρικής τραχύτητας, η οποία εκφράζεται από το χαρακτηριστικό μέγεθος της '*ειδικής επιφάνειας*', S_{BET}. Οι τιμές S_{BET} στα υπό μελέτη συστήματα ποικίλουν μεταξύ 25 και 342 m^2/g. Το μέγεθος αυτό προκύπτει από μετρήσεις ρόφησης-εκρόφησης αδρανών αερίων (αζώτου ή αργού). Τα μόρια των αερίων προσροφώνται, κυρίως, στις ανοικτές κοιλότητες στην επιφάνεια των συσσωματωμάτων (επιφανειακοί πόροι). Οι κοιλότητες δημιουργούνται στη συναρμογή των αρχικών νανοσωματιδίων κατά τη διάρκεια της συσσωματωμάτωσης (agreegation, Εικόνα 13). Έτσι, αναμένεται ότι ο βαθμός επιφανειακής πορωσιμότητας, ή αλλιώς τραχύτητας, θα αυξάνει όσο μειώνεται η μέση διάμετρος των αρχικών νανοσωματιδίων (Εικόνα 13).

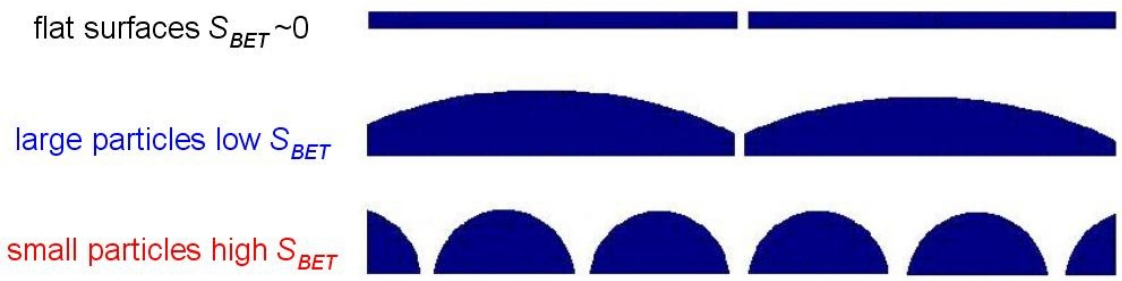

Εικόνα 13. Σχηματική εκτίμηση της επιφανειακής τραχύτητας - πορωσιμότητας στην επιφάνεια συσσωματωμάτων που απαρτίζονται από σωματίδια σφαρικού σχήματος.

Σύμφωνα με τα αποτελέσματα των μετρήσεων DSC σε ΝΣ τύπου πυρήνα–φλοιού (Εικόνα 14), η θερμοκρασία υαλώδους μετάβασης του πολυμερούς, T_g, αυξάνει με την αύξηση της ειδικής επιφάνειας. Ταυτοχρόνως, το βήμα της υαλώδους μετάβασης διευρύνεται στην κλίμακα της θερμοκρασίας (αύξηση της μοριακής ανομοιογένειας) (Εικόνα 14a). Επίσης, από τον αντίστοιχο περιορισμό του βήματος της υαλώδους μετάβασης στην κλίμακα της παρεχόμενης ισχύος, ΔC_p, (περιορισμός του κλάσματος ελεύθερου πολυμερούς) εκτιμούμε την αύξηση του κλάσματος του διεπιφανειακού-ακίνητοποιημένου πολυμερούς (*RAF*). Στην Εικόνα 14b το *RAF* αυξάνει συστηματικά με την αύξηση της ειδικής επιφάνειας.

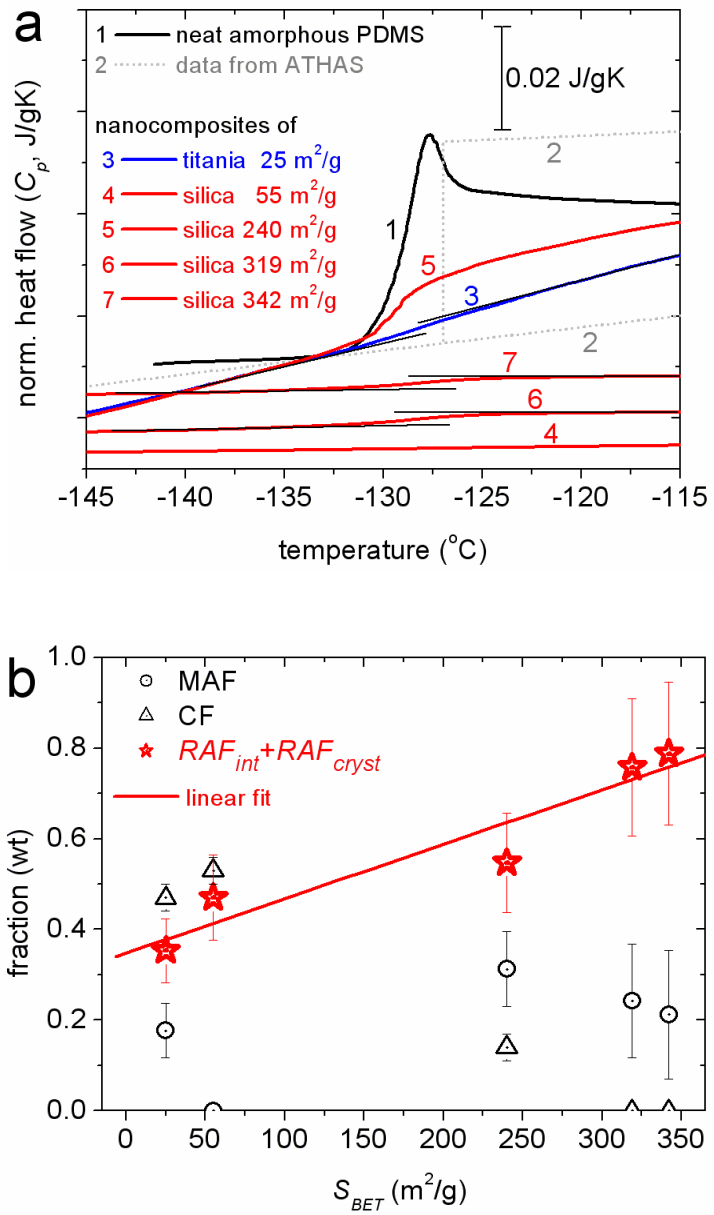

Εικόνα 14. (a) Συγκρτικά θερμογράμματα DSC στην περιοχή της υαλώδους μετάβασης για ΝΣ δοκίμια τύπου πυρήνα-φλοιού στα οποία 40 wt% PDMS είναι προσροφημένο σε σωματίδια silica και titania και, για σύγκριση, για δοκίμιο καθαρού αμόρφου PDMS. (b) Κλάσμα βάρους του ακινητοποιημένου αμόρφου πολυμερούς (rigid amorphous fraction, *RAF*), του ευκίνητου αμόρφου πολυμερούς (mobile amorphous fraction, *MAF*) και του κρυσταλλωμένου πολυμερούς (crystalline fraction, *CF*) συναρτήσει της ειδικής επιφάνειας (τραχύτητας), S_{BET}, των σωματιδίων.

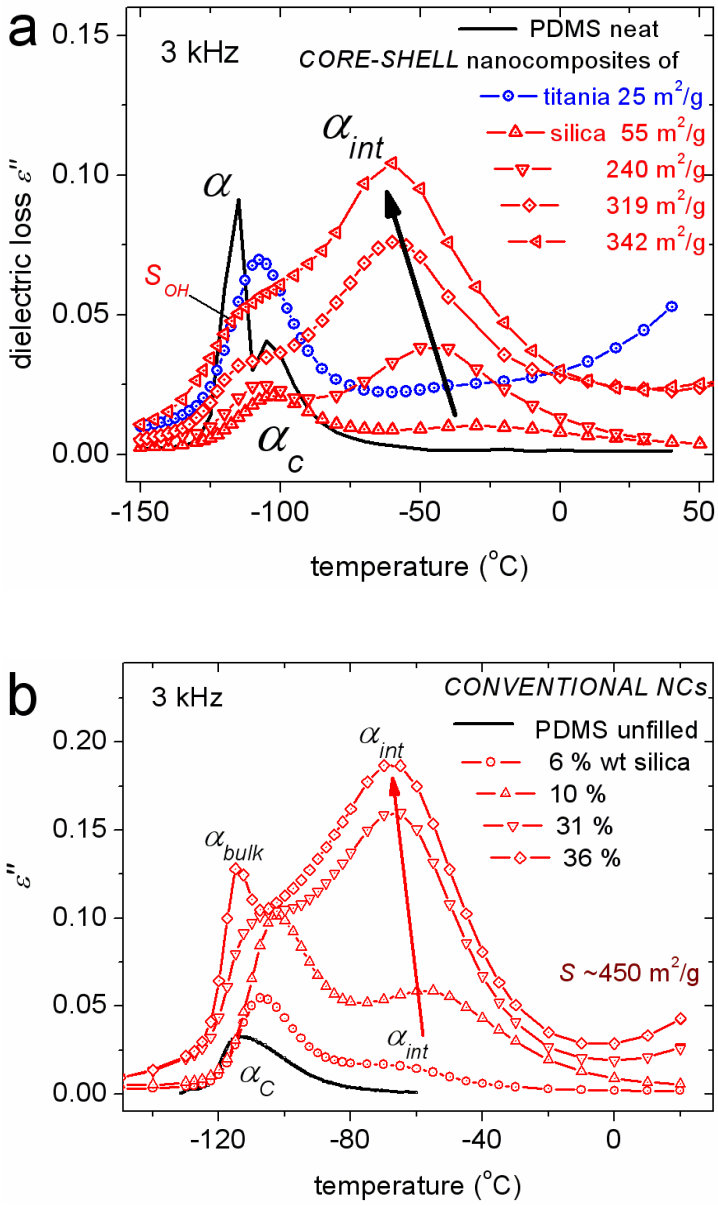

Εικόνα 15. Συγκριτικά ισόχρονα διαγράμματα DRS του φανταστικού μέρους της διηλεκτρικής συνάρτησης (διηλεκτρικές απώλειες), ε'', στη σύχνοτητα των 3 kHz για (a) ΝΣ τύπου πυρήνα-φλοιού (*core–shell NCs*) και (b) συμβατικά ΝΣ (*conventional NCs*) νανοσωματιδίων/PDMS. Τα βέλη στις εικόνες (a) και (b) δείχνουν τις μεταβολές στη δυναμική του διεπιφανειακού πολυμερούς (α_{int}) που επιφέρει η αύξηση στην S_{BET} και στο κλάσμα βάρους των εγκλεισμάτων, αντιστοίχως.

Τα αποτελέσματα των μετρήσεων DRS (Εικόνα 15) σε ΝΣ τύπου πυρήνα–φλοιού τιτανίας και πυριτίας, χαμηλής τραχύτητας (low S_{BET}) αναδεικνύουν ομοιότητες στα χαρακτηριστικά του μηχανισμού α_{int} (δυναμική, ισχύς, συνεργασιμότητα) (Εικόνα 16) με εκείνα των συμβατικών ΝΣ PDMS/τιτανίας, ανεξαρτήτως του μεγέθους των αρχικών σωματιδίων. Η αύξηση της τραχύτητας της προσροφούσας επιφάνειας επιφέρει όμοιο

αποτελέσμα στην διεπιφανειακή κινητικότητα του πολυμερούς (ποιοτικά και ποσοτικά) στα ΝΣ τύπου πυρήνα-φλοιού (Εικόνα 15a) με αυτό της αύξησης της περιεκτικότητας καλώς διασπαρμένων νανοσωματιδίων στα συμβατικά ΝΣ (Εικόνα15b). Αντίστοιχες ομοιότητες παρατηρούνται και στη διεπιφανειακή δυναμική (δυναμική υαλώδους μετάβασης) στην Εικόνα 16.

Είναι, επίσης, ενδιαφέρον ότι η διηλεκτρική ισχύς των μηχανισμών, $\Delta\varepsilon$, ελαττώνεται συστηματικά με τη θερμοκρασία για χαμήλες τιμές S_{BET} και αυξάνει για υψηλές τιμές S_{BET} (Εικόνα 16b). Υπενθυμίζουμε ότι η $\Delta\varepsilon$ περιγράφει τον πληθυσμό των αντίστοιχων ευκίνητων μοριακών ομάδων.

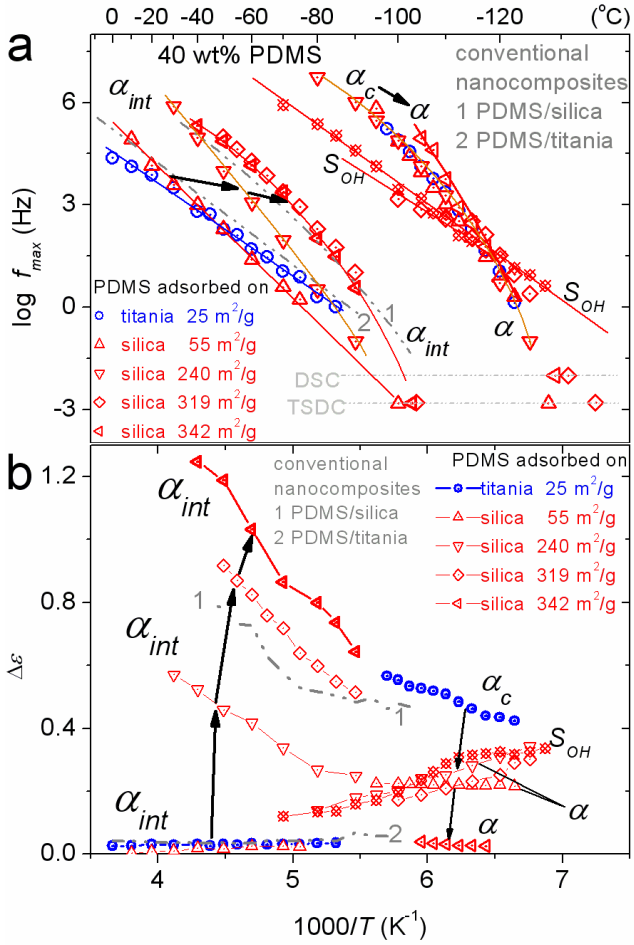

Εικόνα 16. (a) Διηλεκτρικός χάρτης (Arrhenius plots) και (b) διηλεκτρική ισχύς συναρτήσει της αντίστροφης θερμοκρασίας των μηχανισμών συνεργασιακής αποκατάστασης για ΝΣ τύπου πυρήνα-φλοιού στα οποία 40% PDMS έχει προσροφηθεί σε νανοσωματίδια (πυριτίας και τιτανίας) διαφόρων τιμών ειδικής επιφάνειας. Οι γραμμές (1) και (2) στις εικόνες (a) και (b) αντιστοιχούν στη διεπιφανειακή πολυμερική δυναμική στα συμβατικά ΝΣ (1) PDMS/πυριτίας και (2) PDMS/τιτανίας. Τα βέλη δείχνουν τις μεταβολές που επιφέρει η αύξηση στην ειδική επιφάνεια των σωματιδίων, S_{BET}.

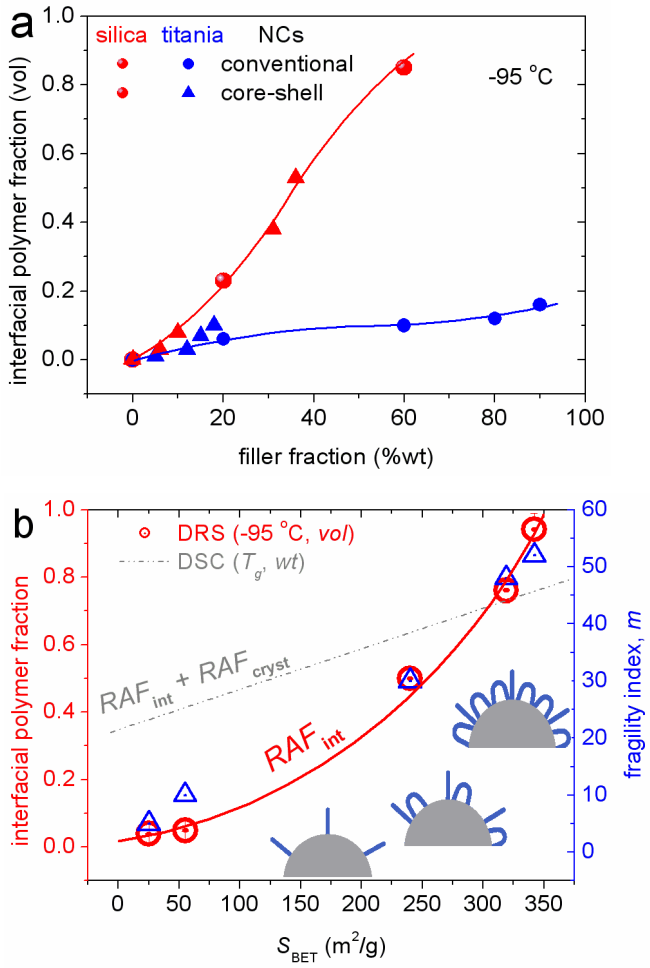

Εικόνα 17. (a) Κλάσμα όγκου του διεπιφανειακού πολυμερούς συναρτήσει της περιεκτικότητας σε έγκλεισμα για ΝΣ silica/PDMS και titania/PDMS τύπου πυρήνα-φλοιού (core–shell) και συμβατικά (conventional) ΝΣ στους –95 °C. (b)(αριστερή κλίμακα) κλάσμα όγκου του διεπιφανειακού πολυμερούς και (δεξιά κλίμακα) δείκτης συνεργασιμότητας (fragility index, *m*) του διεπιφανειακού πολυμερούς συναρτήσει της ειδικής επιφάνειας των νανοσωματιδίων, S_{BET}, στους –95 °C.

Το κλάσμα του διεπιφανειακού πολυμερούς στα ΝΣ αυξάνει με την περιεκτικότητα σε έγκλεισμα, όπως φαίνεται στην Εικόνα 17a. Η αύξηση αυτή είναι μεγαλύτερη για τα ΝΣ PDMS/πυριτίας σε σχέση με τα ΝΣ PDMS/τιτανίας. Είναι ενδιαφέρον, ότι οι μεταβολές φαίνεται να μην εξαρτώνται από τη μέθοδο παρασκευής των ΝΣ, αλλά μόνο από τον τύπο των νανοσωματιδίων. Στην Εικόνα 17b φαίνεται ότι για ΝΣ τύπου πυρήνα-φλοιού που βασίζονται σε σταθερή περιεκτικότητα σε πολυμερές (40%) το κλάσμα του διεπιφανειακού πολυμερούς αυξάνει συστηματικά με την ειδική επιφάνεια, ενώ ταυτοχρόνως αυξάνει η συνεργασιμότητα της αντίστοιχης δυναμικής στο διεπιφανειακό πολυμερικό στρώμα στα ΝΣ.

Κατόπιν, επιχειρήσαμε την εκτίμηση του πάχους και της πυκνότητας του διεπιφανειακού στρώματος, d_{int} και ρ_{int}, αντιστοίχως. Η εκτίμηση αυτή βασίζεται στη γνώση (α) της διαθέσιμης προς αλληλεπίδραση επιφάνειας των νανοσωματιδίων (δηλ. των τιμών S_{BET}), (β) της περιεκτικότητας σε διεπιφανειακό πολυμερές (RAF), (γ) της πυκνότητας του πολυμερούς (ρ_{PDMS}), και (δ) της περιεκτικότητας πολυμερους στα ΝΣ (X_{PDMS}). Έτσι κατόπιν απλών παραδοχών σχεδιάσαμε τις εξισώσεις (Α) και (Β) για τον υπολογισμό των μεγεθών d_{int} και ρ_{int}, αντιστοίχως.

$$d_{\text{int}} = \frac{volume_{\text{int}\,erfacial,PDMS}}{surface_{\text{int}\,erfacial}} = \frac{mass_{sample} \cdot X_{PDMS} \cdot RAF_{\text{int}} / \rho_{PDMS}}{mass_{sample} \cdot (1 - X_{PDMS}) \cdot S_{BET}} \qquad \text{(A)}$$

$$\rho_{\text{int}} = \frac{mass_{\text{int}\,erfacial,PDMS}}{volume_{\text{int}\,erfacial,PDMS}} = \frac{mass_{sample} \cdot X_{PDMS} \cdot RAF_{\text{int}\,erfaces}}{mass_{sample} \cdot (1 - X_{PDMS}) \cdot S \cdot 1.56(nm)} \qquad \text{(B)}$$

Πίνακας 1

Ειδική επιφάνεια των αρχικών συσσωματωμάτων, S_{BET}, κλάσμα όγκου του διεπιφανειακού πολυμερούς, RAF_{int}, δείκτης ευθραυστότητας (συνεργασιμότητας), m, πάχος και πυκνότητα μάζας του διεπιφανειακού πολυμερικού στρώματος, d_{int} και ρ_{int}, αντιστοίχως.

τύπος εγκλείσματος	S_{BET} (m^2/g)	RAF_{int} (vol)	m	d_{int} (nm)	ρ_{int} (g/cm^3)
τιτανία	25	0.04	5	0.6	0.23
πυριτία	55	0.05	10	0.4	0.14
πυρίτια	240	0.50	30	0.9	0.32
πυριτία	319	0.76	48	1.0	0.37
πυριτία	342	0.94	52	1.1	0.42

Τα αποτελέσματα των υπολογισμών φαίνονται στον Πίνακα 1 και παρουσιάζουν οτί η αύξηση στην ειδική επιφάνεια οδηγεί στην αύξηση του πάχους και/ή της πυκνότητας του διεπιφανειακού πολυμερικού στρώματος στα ΝΣ. Ειδικά η εκτιμώμενη αύξηση της πυκνότητας του διεπιφανειακού πολυμερούς, μπορεί να είναι συμβατή με το αποτέλεσμα της επιτάχυνσης της διεπιφανειακής δυναμικής (Εικόνα 16a) και την αύξηση του βαθμού συνεργασιμότητας (τιμές δείκτη m, Εικόνα 17b, Πίνακας 1). Ο συνδυασμός των τελευταίων αποτελεσμάτων συνιστά, στα πλαίσια της Θεωρίας Adam-Gibbs, ότι καθώς αυξάνει η ειδική επιφάνεια των νανοσωματιδίων, το μήκος συνεργασιμότητας των πολυμερικών αλυσίδων στη διεπιφάνεια τείνει να μειωθεί ή, ισοδυνάμως, οι προσροφημένες αλυσίδες τείνουν να

πλησιάσουν η μία την άλλη. Οι απόλυτες τιμές των δύο μεγεθών (0.4–1.1 nm για το πάχος και 0.14–0.42) φαντάζουν μικρές σε σχέση με αντίστοιχες τις βιβλιογραφίας (~2 nm και άνω). Είναι πιθανόν οι υπολογισμοί των μεγεθών d_{int} και ρ_{int} να 'βελτιωθούν' με τον περαιτέρω έλεγχο του τρόπου υπολογισμού και των συνοδών παραδοχών αυτού σε περισσότερα ΝΣ συστήματα.

Ένα ενδιαφέρον αποτέλεσμα που προκύπτει είναι ότι η παρουσία του διεπιφανειακού πολυμερούς στα ΝΣ έχει ως αποτέλεσμα την ενίσχυση της ενδογενούς πόλωσης των υλικών (π.χ. αυξημένες τιμές του πραγματικού μέρους της διηλεκτρικής διαπερατότητας, ε', σε χαμηλές θερμοκρασίες, Εικόνα 18) πέραν της προσθετικότητας. Η ενίσχυση αυξάνει στα ΝΣ με την αύξηση του S_{BET} (Εικόνα 18a) και είναι πιο σημαντική όσο αυξάνει η περιεκτικότητα σε σωματίδια (Εικόνα 18b). Συνεπώς, φαίνεται ότι οι μεταβολές στην ενδογενή πόλωση των ΝΣ πηγάζουν από την, εν γένει, ύπαρξη του διεπιφανειακού πολυμερούς. Ωστόσο, η λεπτομερής εξήγηση του φαινομένου δε μπορεί να πραγματοποιηθεί σε αυτό το στάδιο, διότι στα παραπάνω φαινόμενα εμπλέκονται σύνθετοι μηχανισμοί αλληλεπιδράσεων μεταξύ διπόλων (ή ηλεκτρικών φορτίων). Έτσι τα εν λόγω φαινόμενα αποτελούν αντικείμενο περαιτέρω διερεύνησης.

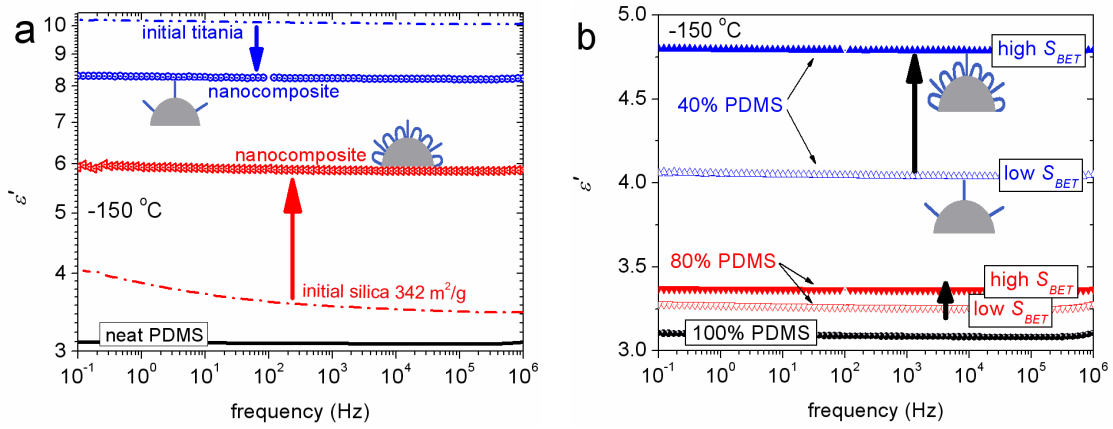

Εικόνα 18. Επιλεγμένα αποτελέσματα για το πραγματικό μέρος της διηλεκτρικής συνάρτησης, ε', συναρτήσει της συχνότητας στους –150 °C. Παρουσιάζεται η επιρροή (a) της αύξησης της ειδικής επιφάνειας και (b) της ταυτόχρονης μεταβολής της σύστασης των ΝΣ (περιεκτικότητα εγκλείσματος).

Επιρροή της θερμικής ανόπτησης της κρυστάλλωσης

Τα αποτελέσματα σε δοκίμια που είχαν υποστεί θερμική ανόπτηση, προς ενίσχυση της κρυσταλλικότητας, κατέδειξαν την υποβάθμιση της κινητικότητας του ανεπηρέαστου (bulk) πολυμερούς (μηχανισμός α, Εικόνα 19a) και, ταυτόχρονως, την ενίσχυση της κινητικότητας του πολυμερούς που βρίσκεται χωρικώς περιορισμένο μεταξύ πυκνών κρυσταλλικών περιοχών (μηχανισμός α_c, Εικόνα 19a). Οι μεταβολές αυτές παρατηρούνται και σε δοκίμια καθαρού πολυμερούς και στα ΝΣ.

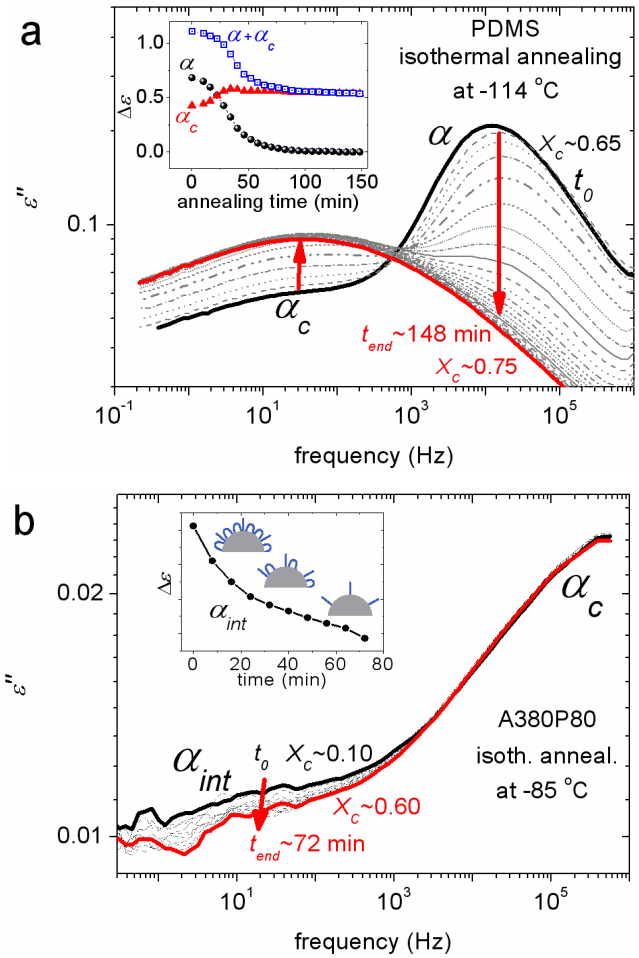

Εικόνα 19. Χρονική εξέλιξη των μηχανισμών διηλεκτρικής αποκατάστασης που σχετίζονται με τη συνεργασιακή δυναμική (υαλώδη μετάβαση) κατά τη διάρκεια της ισόθερμης ανόπτησης της κρυστάλλωσης, για (a) το καθαρό PDMS στους –114 °C και (b) ΝΣ πυριτίας με 80 % PDMS στους –85 °C. Στα (a) και (b) συμπεριλαμβάνονται οι τιμές του βαθμού κρυσταλλικότητας, X_c, σύμφωνα με τα αποτελέσματα DSC, στην αρχή, t_0, και το τέλος, t_{end}, της θερμικής ανόπτησης. Στα ένθετα φαίνεται η αντίστοιχη χρονική εξέλιξη της διηλεκτρικής ισχύος, $\Delta\varepsilon$, των υπό μελέτη μηχανισμών.

Στην περίπτωση των ΝΣ η θερμική ανόπτηση οδηγεί στην καταπίεση της δυναμικής και της ισχύος του διεπιφανειακού πολυμερούς (μηχανισμού α_{int}, Εικόνες 19b, 20). Ο μηχανισμός α_{int} μεταναστεύει προς υψηλότερες θερμοκρασίες / χαμηλότερες συχνότητες (Εικόνα 20a) και ταυτοχρόνως μειώνεται η διηλεκτική ισχύς (Εικόνα 20b) και η συνεργασιμότητα της αντίσοιχης μοριακής κίνησης (Εικόνα 20a). Το αποτέλεσμα της θερμικής ανόπτησης είναι ποιοτικώς και ποσοτικώς παρεμφερές με την επιρροή στη διεπιφανειακή δυναμική που επέφερε η μείωση της τραχύτητας, S_{BET}, της προσροφούσας επιφάνειας (Εικόνα 16).

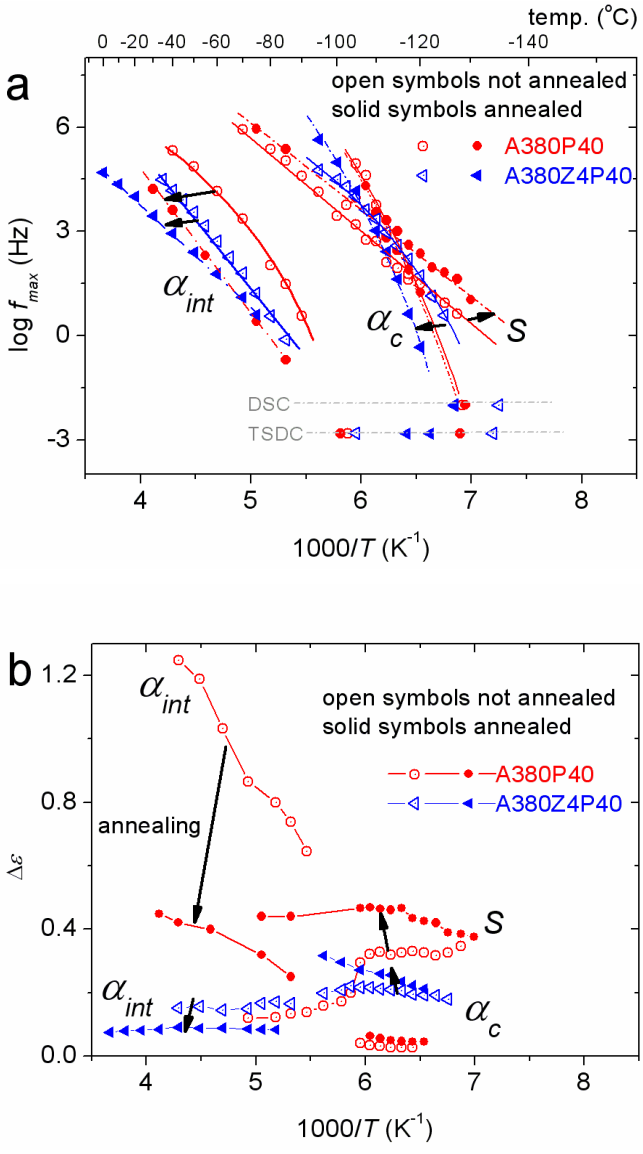

Εικόνα 20. Επιρροή της θερμικής ανόπτησης, προς ενίσχυση του βαθμού κρυσταλλικότητας, (a) στη μοριακή δυναμική και (b) στη διηλεκτρική ισχύ των μηχανισμών διηλεκτρικής αποκατάστασης σε ΝΣ PDMS/πυριτίας

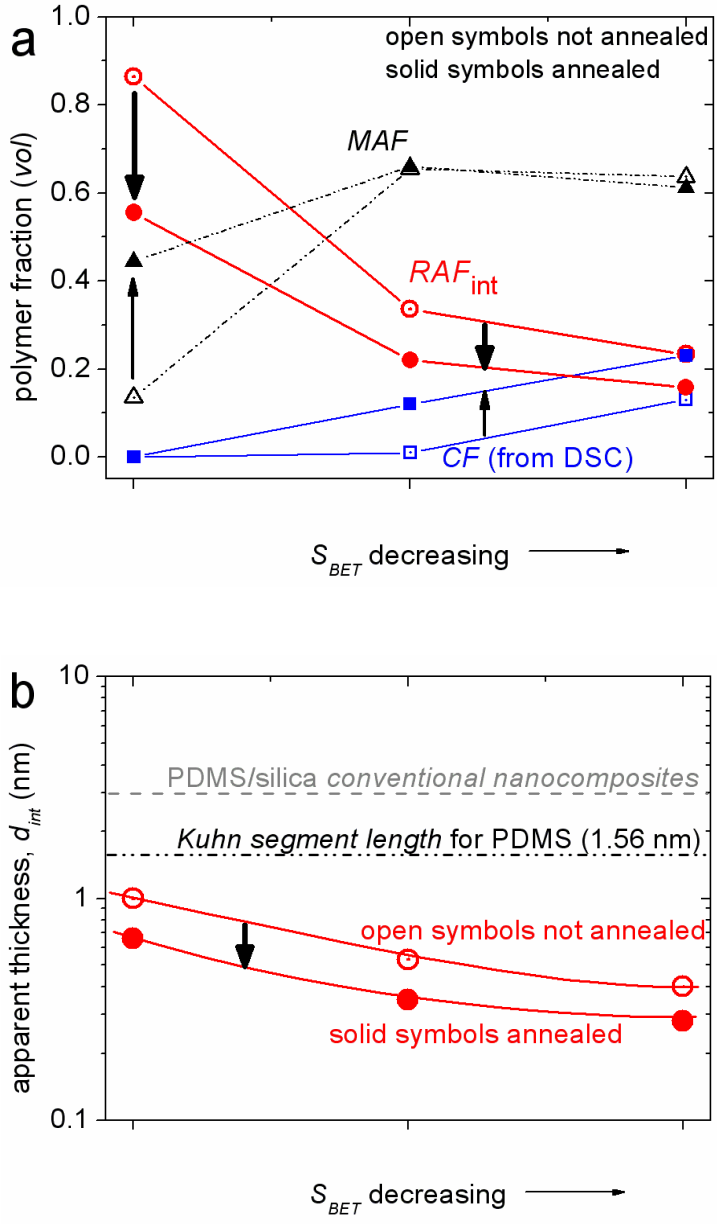

Εικόνα 21. Επιρροή της θερμικής ανόπτησης και της μείωσης της ειδικής επιφάνειας (a) στις διάφορες φάσεις του πολυμερούς στα ΝΣ (διεπιφανειακό πολυμερές, RAF_{int}, ευκίνητο άμορφο πολυμερές, *MAF*, κρυσταλλωμένο πολυμερές, *CF*) και (b) στο πάχος του διεπιφανειακού πολυμερικού στρώματος, d_{int}.

Τα αποτελέσματα ποσοτικοποιούνται, στην Εικόνα 21, με όρους κλάσματος του διεπιφανειακού πολυμερούς (RAF_{int}, Εικόνα 21a,b) και πάχους του διεπιφανειακού στρώματος (d_{int}, Εικόνα 21c), βάσει των μοντέλων-σχέσεων που περιγράφηκαν προηγουμένως.

Η υποβάθμιση της δυναμικής του διεπιφανειακού πολυμερούς συνοδεύεται από την ταυτόχρονη ενίσχυση της δυναμικής και της συγκέντρωσης του ελεύθερου πολυμερούς και των 'ελεύθερων' υδροξυλίων στην επιφάνεια της πυριτίας (μηχανισμός *S* στην Εικόνα 20). Με τον όρο *ελεύθερα υδροξύλια* εννοούμε εκείνα τα επιφανειακά υδροξύλια (-OH) που δεν αλληλεπιδρούν ή απώλεσαν την αλληλεπίδρασή τους με τις πολυμερικές αλυσίδες. Το αποτέλεσμα είναι σύμφωνο με την πρατηρούμενη ενίσχυση του βήματος της υαλώδους μετάβασης (αύξηση της τιμής ΔC_p) στα ίδια δοκίμια κατόπιν της ίδιας θερμικής μεταχείρισης σε μετρήσεις DSC.

Συνδυάζοντας όλες τις παραπάνω πειραματικές ενδείξεις, επιχειρούμε την ποιοτική εξήγηση των αποτελεσμάτων ως εξής. Κατά τη διάρκεια της θερμικής ανόπτησης οι πολυμερικές αλυσίδες πακετάρονται σε κρυσταλλικές-περιοδικές δομές (σφαιρουλίτες). Σύμφωνα με προηγούμενα συμπεράσματα, αυτή η δομική διεργασία στα ΝΣ λαμβάνει χώρα μακρύα από τις διεπιφάνειες πολυμερούς/εγκλείσματος. Συνεπώς, προτείνουμε ότι η 'οδηγός δύναμη' της κρυστάλλωσης κυριαρχεί επί των 'πιο ασθενών' αλληλεπιδράσεων μεταξύ πολυμερούς και στέρεης επιφάνειας των σωματιδίων, με αποτέλεσμα την 'αποκόλληση' μέρους των πολυμερικών αλυσίδων (Εικόνα 22). Έτσι, το διεπιφανειακό στρώμα λεπταίνει (ή αραιώνει, Εικόνες 21a, 22c) και η συνεργασιμότητα και η δυναμική των πολυμερικών αλυσίδων εξασθενούν (Εικόνα 20a).

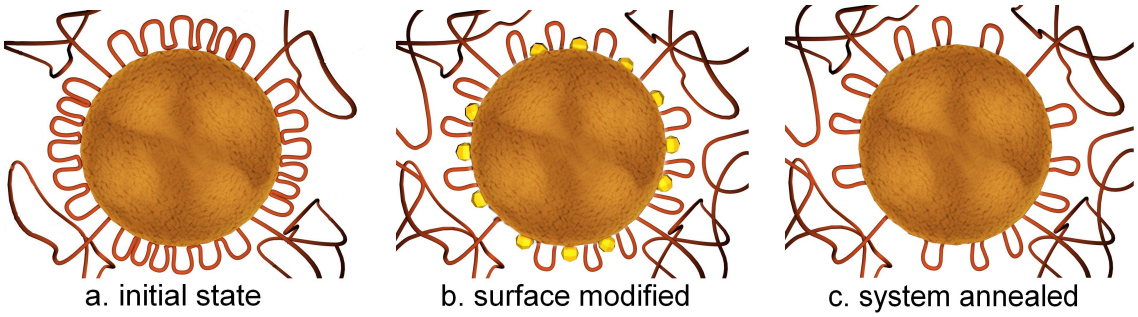

Εικόνα 22. Σχηματική αναπαράσταση για τις προτεινόμενες μεταβολές στην κατανομή των πολυμερικών αλυσίδων στη διεπιφάνεια με τα σωματίδια που επιφέρουν: (b) η τροποποίηση της επιφάνειας και (c) η θερμική ανόπτηση της κρυστάλλωσης.

Ερμηνεία των αποτελεσμάτων βάσει μοντέλων

Συνδυάζοντας τις επιδράσεις στη συνολική διηλεκτρική συμπεριφορά των υλικών (κάτι που δεν γίνεται συνήθως στη βιβλιογραφία), ερμηνεύουμε τα αποτελέσματα επιστρατεύοντας ένα σύγχρονο μοντέλο. Σύμφωνα με αυτό το μοντέλο, το PDMS (πολυμερές με πολύ εύκαμπτες πολυμερικές αλυσίδες) μπορεί να διαμορφωθεί με 2 τρόπους, τουλάχιστον, στη διεπιφάνεια με τα σωματιδια, συγκεκριμένα μέσω (α) διαμορφώσεων τύπου εκτεταμένης ουράς (tail), και (β) διαμορφώσεων τύπου βρόχου (loop) με πολλαπλά σημεία επαφής με τη διεπιφάνεια (Εικόνα 23).

Εικόνα 23. Απλοποιημένο μοντέλο πολλαπλών διαμορφώσεων των πολυμερικών αλυσίδων προσροφημένων σε στερεή ελκτική επιφάνεια

Οι διαμορφώσεις αυτές, ιδίως οι τύπου βρόχου, οδηγούν σε υψηλότερη πυκνότητα και συνεργασιμότητα του διεπιφανειακού πολυμερούς. Είναι προφανές ότι και οι δύο τύποι διαμορφώσεων χαρακτηρίζονται από αυξημένο προσανατολισμό (τάξη) και πολωσιμότητα, συγκρινόμενοι με τις διαμορφώσεις του πολυμερούς μακρυά από τη διεπιφάνεια (bulk). Αυτό εξηγεί πιθανώς την παρατηρούμενη αυξημένη διηλεκτρική απόκριση των ΝΣ πέραν της προσθετικότητας (Εικόνα 18). Ο λόγος των πληθυσμών βρόχοι / ουρές αυξάνει με την τραχύτητα (S_{BET}). Επίσης, η αύξηση στην επιφανειακή τραχύτητα οδηγεί, στην παρούσα μελέτη, στην πύκνωση των προσβάσιμων θέσεων πρόσδεσης / αλληλεπίδρασης μεταξύ πολυμερούς και νανοσωματιδίων (Εικόνα 24), και, έτσι, στη σταδιακά αυξανόμενη πυκνότητα του διεπιφανειακού πολυμερικού στρώματος. Αυτό έχει ως αποτέλεσμα τη μείωση του μήκους συνεργασιμότητας των διεπιφανειακών αλυσίδων, άρα, στο πλαίσιο της θεωρίας Adam–Gibbs, η διεπιφανειακή δυναμική επιταχύνεται, σε συμφωνία με τα αποτελέσματα μας (Εικόνες 16a,20a).

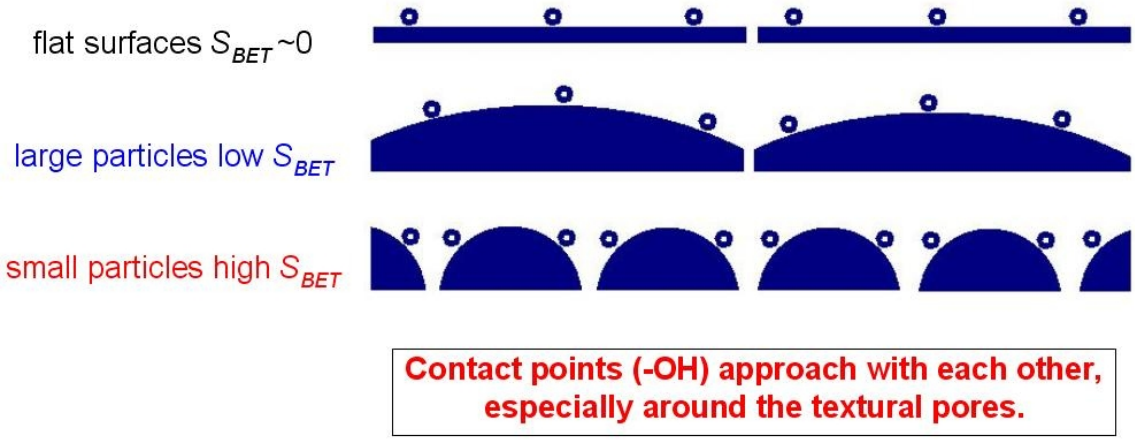

Εικόνα 24. Σχηματική αναπαράσταση της πύκνωσης των επιφανειακών υδροξυλίων (κύκλοι, εν δυνάμει σημεία επαφής πολυμερούς-σωματιδίου) με την αύξηση της ειδικής επιφάνειας (S_{BET}), των συσσωματωμάτων που απαρτίζονται από νανοσωματίδια σφαρικού τύπου.

Επιρροή της υδάτωσης/αφυδάτωσης

Σύμφωνα με τις μετρήσεις ισόθερμης υδάτωσης σε ισσοροπία σε καθαρά οξείδια, ΝΣ και στο καθαρό πολυμερές προκύπτουν τα εξής. Το καθαρό PDMS δεν προσροφά μόρια νερού. Τα νανοσωματίδια είναι ισχυρώς υδρόφιλα συστήματα και προσροφούν σημαντικές ποσότητες νερού (έως 60%, Εικόνα 25a). Είναι ενδιαφέρον ότι η υδάτωση των καθαρών νανοσωματιδίων αυξάνει με την αύξηση της ειδικής επιφάνειας, ειδίως σε συνθήκες υψηλής σχετικής υγρασίας (Εικόνα 25b).

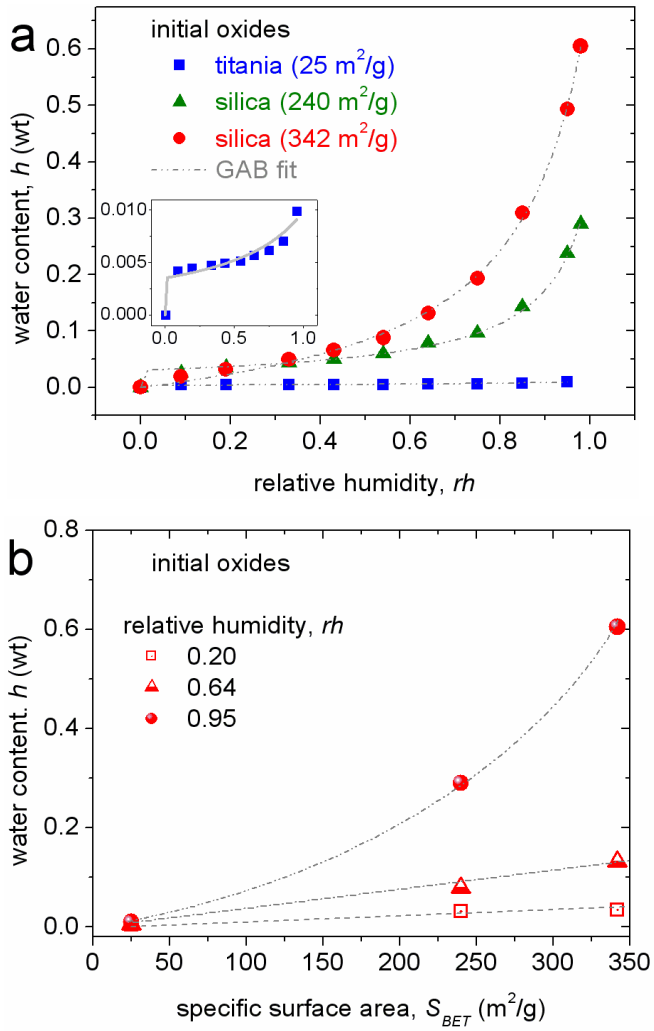

Εικόνα 25. (a) Συκριτικές καμπύλες ισόθερμης υδάτωσης για καθαρά νανοσωματίδια: τιτανίας (S_{BET} ~25 m^2/g) και πυριτίας (S_{BET} ~240 και 342 m^2/g). (b) Υδάτωση συναρτήσει της ειδικής επιφάνειας των νανοσωματίδια για επιλεγμένες τιμές σχετικής υγρασίας (*rh*).

Η υδάτωση των ΝΣ είναι ιδιατέρως χαμηλή, αναφέρουμε ενδεικτικώς ότι η μέγιστη υδάτωση των ΝΣ είναι 0.3 % για την υψηλότερη σχετική υγρασία (95 *rh*%). Είναι ενδιαφέρον ότι η υδάτωση των ΝΣ είναι ανεξάρτητη της περιεκτικότητας σε πολυμερές και οι διαδικασίες υδάτωσης-αφυδάτωσης είναι πλήρως αντιστρεπτές. Αντιθέτως, οι ίδιες διαδικάσίες δεν είναι αντιστρεπτές για τα καθαρά οξείδια (δημιουργία γέλης στην επιφάνεια των δοκιμίων).

Συμπερασματικά, η ισχυρή αλληλεπίδραση πολυμερούς-εγκλείσματος οδηγεί στον περιορισμό των ελεύθερων θέσεων υδάτωσης (υδροξύλια) την επιφάνεια των σωματιδίων. Συνδυάζοντας με τον πλήρως υδροφοβικό χαρακτήρα του PDMS, συμπεραίνουμε ότι οι πιθανές μεταβολές στην υδάτωση των ΝΣ λαμβάνουν χώρα στη διαθέσιμη επιφάνεια των εγκλεισμάτων, δηλαδή στη μη καλυμένη από πολυμερές επιφάνεια.

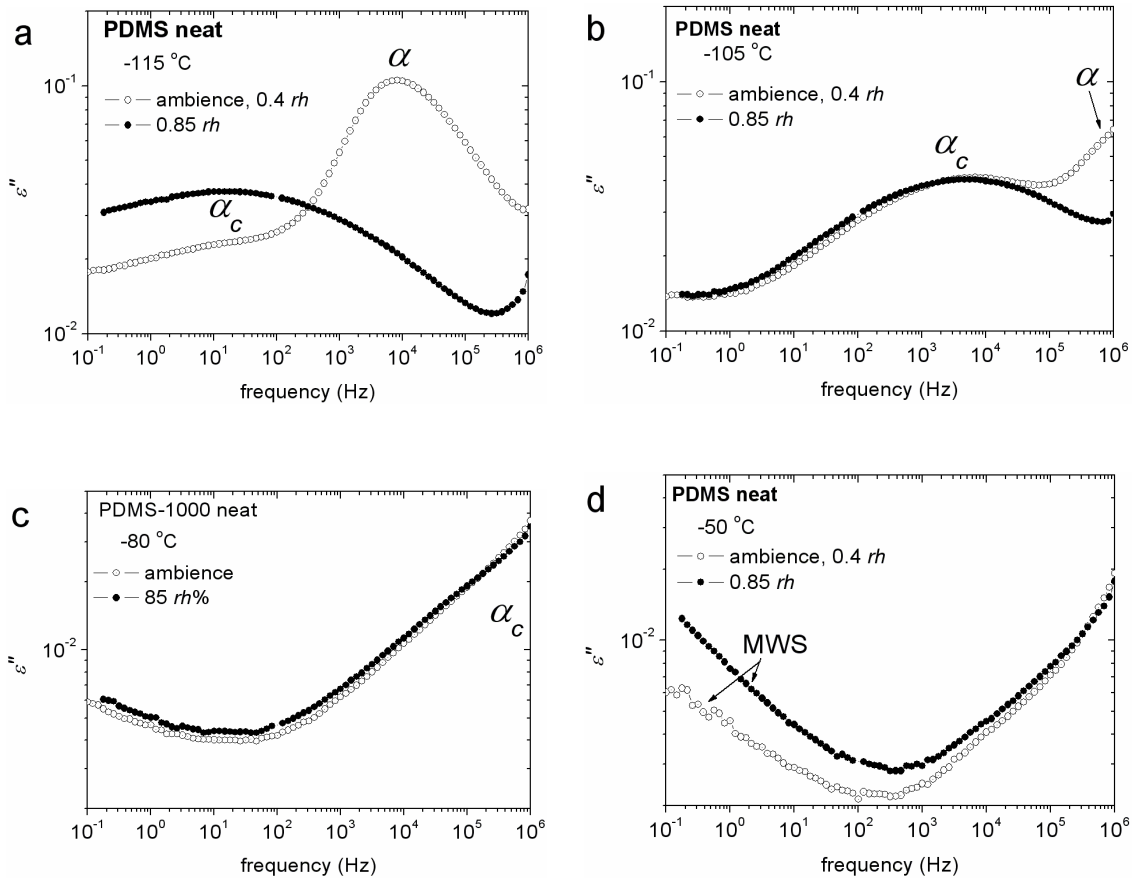

Εικόνα 26. Συγκριτικές ισόθερμες μετρήσεις DRS των διηλεκτρικών απωλειών, *ε΄΄*, σε διάφορες θερμοκρασίες, συναρτήσει της συχνότητας για καθαρό PDMS, που έχει προηγουμένως ισορροπήσει σε σχετική υγρασία περιβάλλοντος (~0.40 *rh*) και υψηλή σχετική υγρασία (0.85 *rh*).

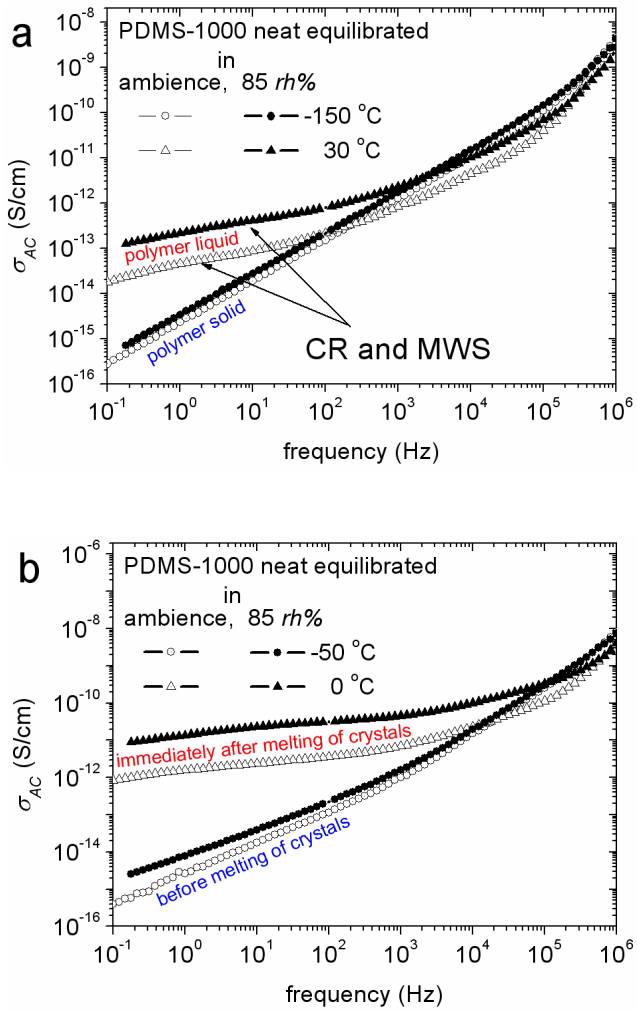

Εικόνα 27. Μετρήσεις αγωγιμότητας σε εναλλασσόμενο ηλεκτρικό πεδίο (AC conductivity), σ_{AC}, συναρτήσει της συχνότητας για καθαρό PDMS που έχει προηγουμένως ισορροπήσει σε σχετική υγρασία περιβάλλοντος (~0.40 *rh*) και υψηλή σχετική υγρασία (0.85 *rh*), στους (a) –150 και 30 °C για σύγκριση μεταξύ πλήρως ακινητοποιημένων και πλήρως ευκίνητων πολυμερικών αλυσίδων και στους (b) –50 και 0 °C για σύγκριση πριν και αμέσως μετά την τήξη των κρυσταλλιτών του πολυμερούς.

Σύμφωνα με τις μετρήσεις διηλεκτρικής φασματοσκοπίας σε δοκίμια καθαρού PDMS (Εικόνες 26,27), στα δοκίμια που έχουν ισορροπήσει σε συνθήκες υψηλής σχετικής υγρασίας η συνεργασιακή δυναμική εκφράζεται μέσω του μηχανισμού α_c, ενώ για δοκίμια ισορροπημένα σε συνθήκες υγρασίας περιβάλλοντος κυριαρχεί ο μηχανισμός α (Εικόνα 26a). Σύμφωνα με τα αποτελέσματα σε υψηλότερες θερμοκρασίας, δηλάδη κατά την εξέλιξη του φαινομένου της ψυχρής κρυστάλλωσης (κρυστάλλωση κατά τη θέρμανση), φαίνεται ότι ο μηχανισμός α_c κυριαρχεί και στις δύο περιπτώσεις (Εικόνα 26b). Έτσι, συμπεραίνουμε ότι η υψηλότερη σχετική υγρασία ευνοεί την κρυστάλλωση, αποτέλεσμα που ελέγθηκε και με

μετρήσεις DSC, και ενισχύει την αγωγιμότητα μέσω φαινομένων πόλωσης ηλεκτροδίων (Εικόνες 26c,d, 27).

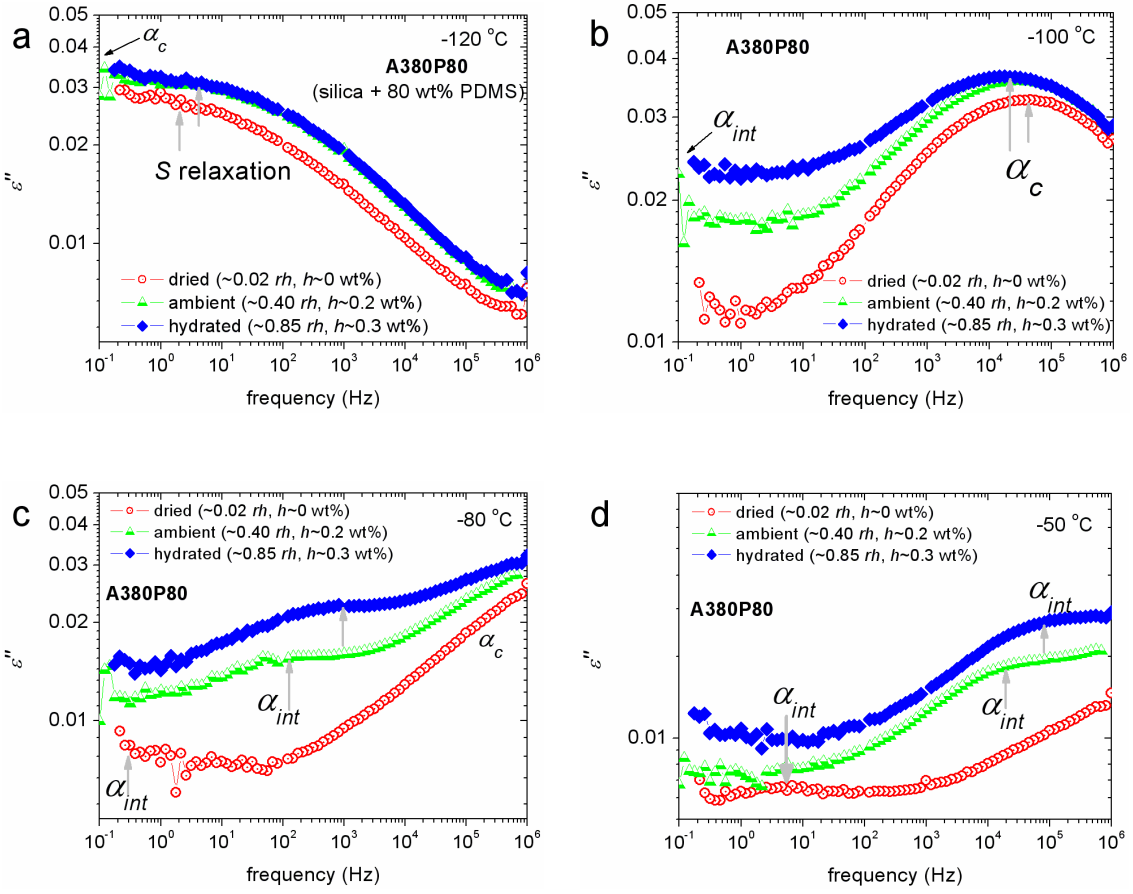

Εικόνα 28. Συγκριτικές ισόθερμες μετρήσεις DRS των διηλεκτρικών απωλειών, ε'', στους (a) –120 °C, (b) –100 °C, (c) –80 °C, και (d) –50 °C, συναρτήσει της συχνότητας για ΝΣ δοκίμιο πυριτίας με 80% PDMS για διάφορα επίπεδα υδάτωσης

Ο συνδυασμός μετρήσεων DRS (Εικόνα 28) και ισοθέρμης υδάτωσης στα ΝΣ συστήματα ανέδειξε την επιτάχυνση της δυναμικής του διεπιφανειακού πολυμερούς με την υδάτωση. Πιο συγκεκριμένα, η αύξηση της υδάτωσης των ΝΣ (~0.25 wt%) οδήγησε στην επιτάχυνση του διηλεκτρικού μηχανισμού αποκατάστασης α_{int} (Εικόνα 28c,d). Ταυτοχρόνως, αυξάνει η συνεργασιμότητα (Εικόνα 29a) και η διηλεκτρική ισχύς του μηχανισμού (Εικονα 29b). Τα αποτελέσματα της αύξησης των επιπέδων υδάτωσης στο μηχανισμό α_{int} είναι αντιστρεπτά, όπως διαπιστώθηκε απο μετρήσεις επαναξήρανσης και επανυδάτωσης των ίδιων δοκιμίων.

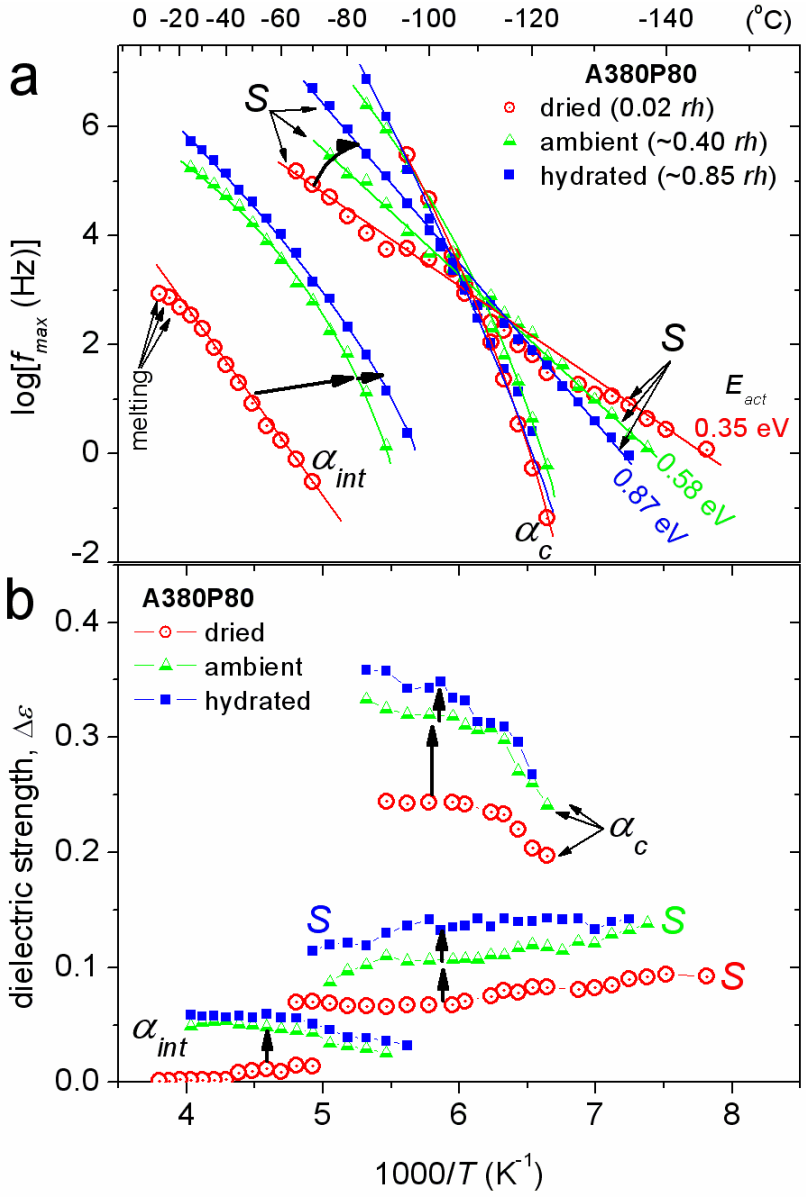

Εικόνα 29. (a) Διηλεκτρικός χάρτης (Arrhenius plots) και (b) διηλεκτρική ισχύς συναρτήσει της αντίστροφης θερμοκρασίας για τους διάφορους μηχανισμούς διηλεκτρικής αποκατάστασης (*S*, α_c και α_{int}) για ΝΣ δοκίμιο πυριτίας με 80% PDMS για διάφορα επίπεδα υδάτωσης.

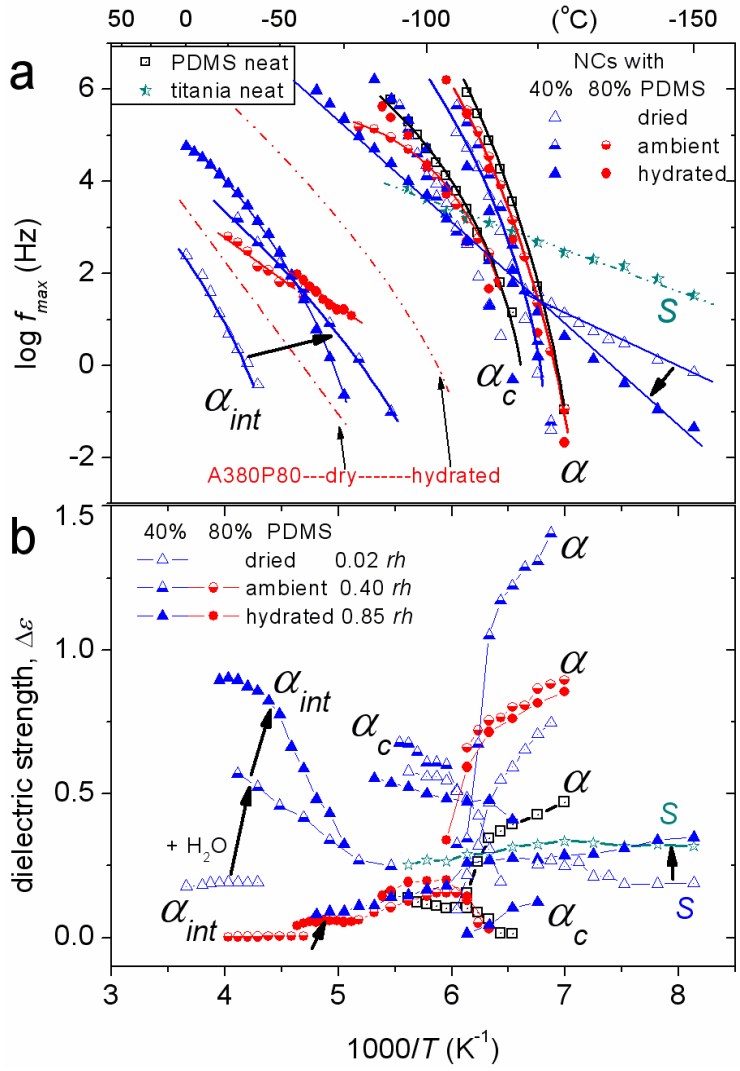

Εικόνα 30. (a) Διηλεκτρικός χάρτης (Arrhenius plots) και (b) διηλεκτρική ισχύς συναρτήσει της αντίστροφης θερμοκρασίας για τους διάφορους μηχανισμούς διηλεκτρικής αποκατάστασης (*S*, *α*, α_c και α_{int}) για ΝΣ δοκίμια τιτανίας με 40% και 80% PDMS για διάφορα επίπεδα υδάτωσης.

Τα αποτελέσματα της αύξησης των επιπέδων υδάτωσης στους μηχανισμούς διηλεκτρικής αποκατάστασης για την περίπτωση ΝΣ τιτανίας/PDMS (Εικόνα 30) είναι ποιοτικώς όμοια και προς την ίδια κατεύθυνση (επιτάχυνση και ενίσχυση της διεπιφανειακής δυναμικής με την υδάτωση) με εκείνα των ΝΣ πυριτίας/PDMS (Εικόνα 29). Στην Εικόνα 31 οι παραπάνω μεταβολές ποσοτικοποιούνται με όρους αύξησης του κλάσματος όγκου του διεπιφανειακού πολυμερούς, RAF_{int}.

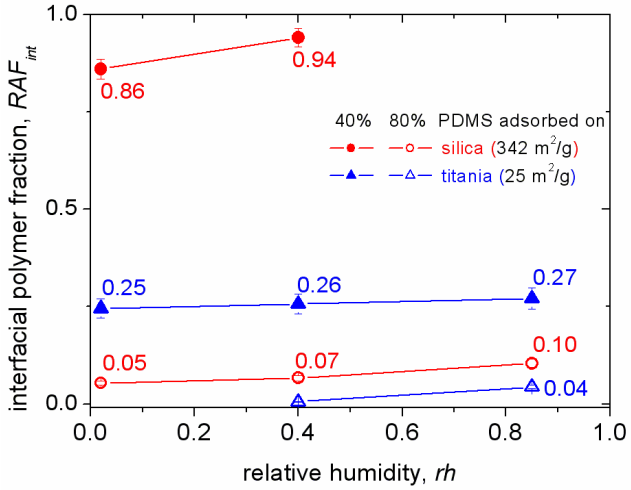

Εικόνα 31. Επιρροή των επιπέδων υδάτωσης στο κλάσμα όγκου του διεπιφανειακού πολυμερούς, RAF_{int}.

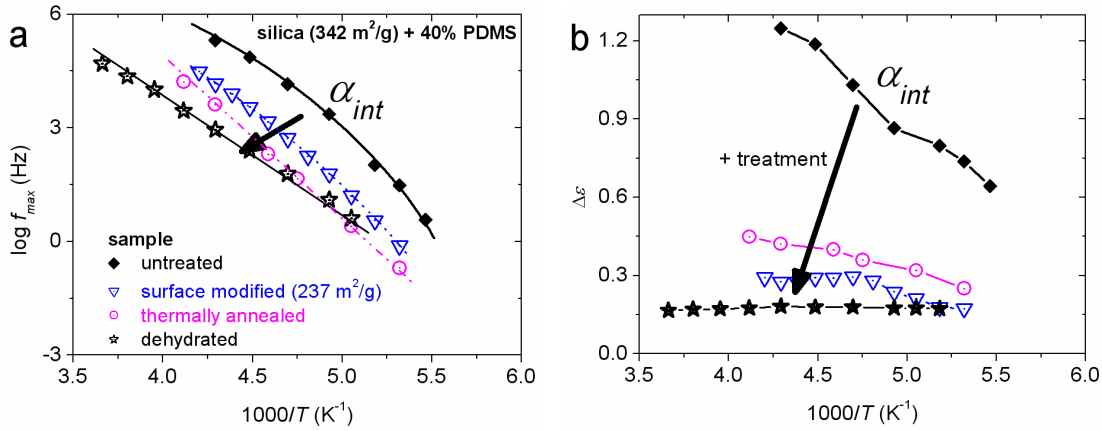

Εικόνα 32. (a) Διηλεκτρικός χάρτης (Arrhenius plots) και (b) διηλεκτρική ισχύς συναρτήσει της αντίστροφης θερμοκρασίας για το μηχανισμό διηλεκτρικής αποκατάστασης του διεπιφανειακού πολυμερούς, α_{int}, για το ΝΣ δοκίμιο πυριτίας υψηλής ειδικής επιφάνειας (342 m^2/g) με 40% προσροφημένο PDMS. Παρουσιάζονται τα αποτελέσματα διαφόρων τύπων μεταχείρισης του δοκιμίου (αφυδάτωση, θερμική ανόπτηση, επιφανειακή τροποποίηση) στη δυναμική του μηχανισμού.

Τα αποτελέσματα των διαφόρων τύπων μεταχείρισης του δοκιμίου, δηλαδή, η αφυδάτωση, η θερμική ανόπτηση και η επιφανειακή τροποποίηση των εγκλεισμάτων, στη δυναμική του μηχανισμού του διεπιφανειακού πολυμερούς, α_{int}, στα ΝΣ είναι ποιοτικώς και ποσοτικώς όμοια μεταξύ τους. Χαρακτηριστικό παράδειγμα των παραπάνω μεταβολών παρουσιάζεται στην Εικόνα 32 για το ΝΣ δοκίμιο πυριτίας υψηλής ειδικής επιφάνειας (342 m^2/g) με 40% προσροφημένο PDMS.

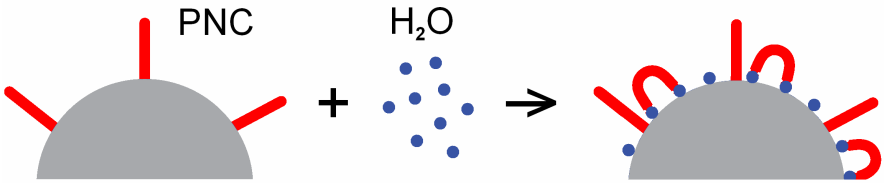

Εικόνα 33. Σχηματική εκτίμηση της επιρροής των μορίων νερού στη διεπιφάνεια πολυμερούς-νανοσωματιδίων στις διαμορφώσεις των πολυμερικών αλυσίδων; πιθανή δράση των μορίων νερού ως επιπλέον σημείων επαφής πολυμερούς-επιφάνειας

Από το συνδυασμό όλων των παραπάνω αποτελεσμάτων εκτιμούμε ότι τα επιπλέον μόρια νερού στην υδρόφιλη επιφάνεια των νανοσωματιδίων δημιουργούν ή συνδράμουν στην ανάπτυξη νέων (δευτερευόντων) θέσεων αλληλεπίδρασης μεταξύ πολυμερικών αλυσίδων και σωματιδίων (Εικόνα 33). Προς στο παρόν, δε μπορούμε να καταλήξουμε οριστικώς στο κατά πόσον τα επιπλέον μόρια νερού δρουν ως επιπλέον 'νέες' θέσεις προσρόφησης ή έαν δρούν επικουρικά (υποβοηθούν) στην προσβάσιμοτητα του πολυμερούς προς διάθεσιμες θέσεις υδάτωσης (υδροξύλια) στην υδρόφιλη στέρεη επιφάνεια.

Παρά ταύτα, τα αποτελέσματα μπορεί να εξηγούνται με όρους διαφορετικών διαμορφώσεων (loops και tails, Εικόνα 33) του πολυμερούς στο διεπιφανειακό στρώμα. Η αραίωση του πολυμερούς ή μείωση του κλάσματος του προσροφημένου πολυμερούς (Εικόνα 31), όπως ερμηνεύεται από τα αποτελέσματα της παρούσας εργασίας, είναι συμβατές με πειραματικά αποτελέσματα χαρακτηρισμού δομής και μοριακών προσομοιώσεων σε αντίστοιχα συστήματα. Η γενικότερη συζήτηση περί της συμπεριφοράς των μορίων νερού στις διεπιφάνειες είναι ένα ανοιχτό και, ήδη, πολυμελετημένο αντικείμενο της βιβλιογραφίας τα τελευταία χρόνια.

Επιρροή του μήκους της πολυμερικής αλυσίδας (μοριακό βάρος)

Πραγαμτοποιήσαμε μετρήσεις DSC και DRS σε ΝΣ τιτανίας/PDMS τύπου πυρήνα/φλοιού. Χρησιμοποιήσαμε PDMS δύο μοριακών βαρών, ~2000 και ~8000, τα οποία αντίτοιχουν σε βαθμούς πολυμερισμού ~22 και ~105 μονομερή/αλυσίδα, αντιστοίχως. Το κλάσμα βάρους του πολυμερούς στα ΝΣ καλύπτει την ευρύα περιοχή από 5 έως 80 % (Εικόνα 34).

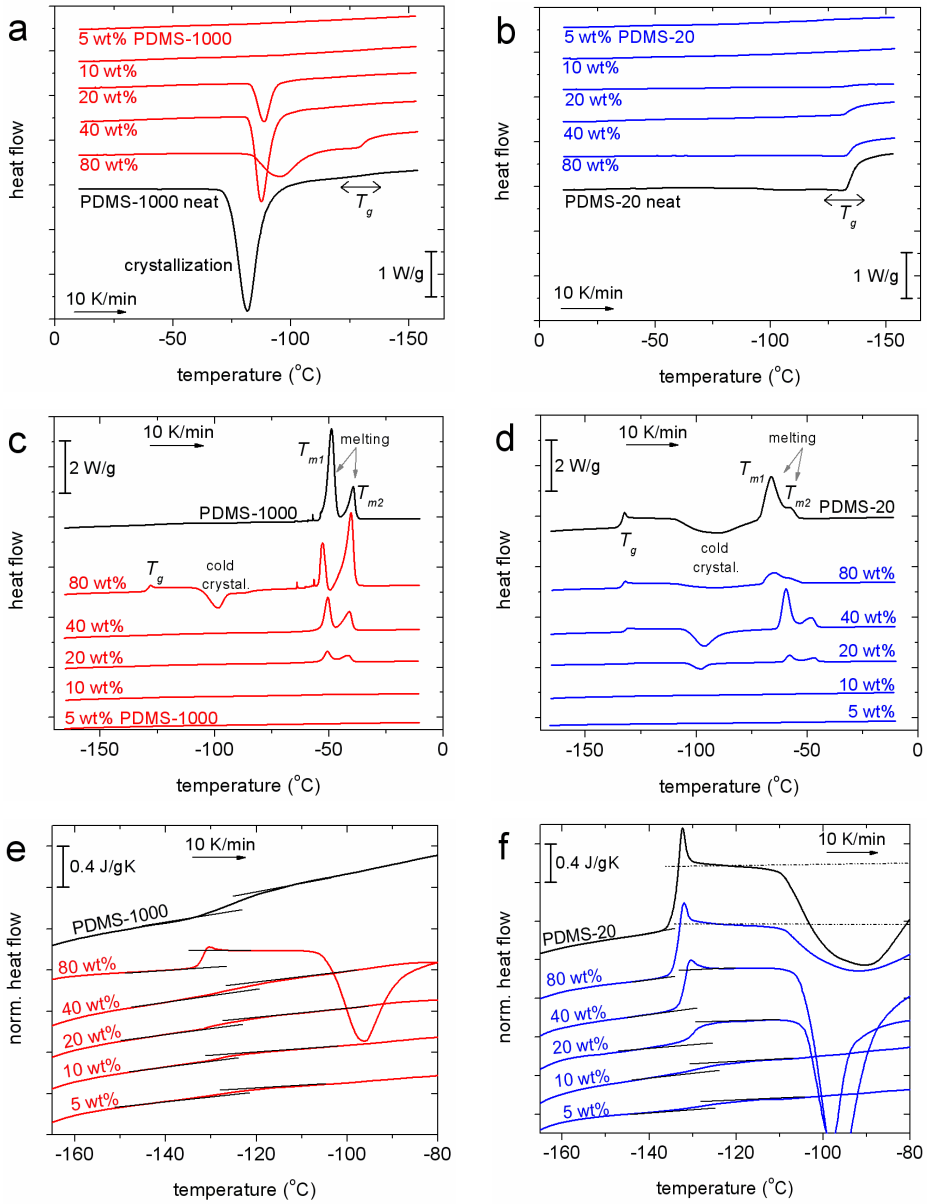

Εικόνα 34. Συγκριτικές μετρήσεις DSC (a,b) ψύξης και (c,d) θέρμανσης ΝΣ τιτανίας/PDMS, για PDMS μεγάλου (a,c,e) και μικρού (b,d,f) μοριακού βάρους, ~8000 και ~2000, αντιστοίχως. Τα (e,f) παρουσιάζουν την περιοχή της υαλώδους μετάβασης σε μεγαλύτερη λεπτομέρεια.

Στην περίπτωση των ΝΣ που βασίζονται στο PDMS μικρότερου μοριακού βάρους, δεν παρατηρήθηκε το φαινόμενο της κρυστάλλωσης κατά την ψύξη (Εικόνα 34b), σε αντίθεση με την περίπτωση του μεγαλύτερου μοριακού βάρους (Εικόνα 34a). Αυτό το αποτέλεσμα είναι σημαντικό, καθώς κατά την ακόλουθηση θέρμανση των ίδιων ΝΣ και ιδίως στην περιοχή της υαλώδους μετάβασης (Εικόνα 34f) γίνεται σαφής η άμεση επιρροή των εγκλεισμάτων στην κινητικότητα του πολυμερούς (υαλώδης μετάβαση). Γίνεται ξεκάθαρο ότι η θερμοκρασία υαλώδους μετάβασης, T_g, αυξάνει στα ΝΣ και το φαινόμενο εξελίσσεται σε αυξημένη θερμοκρασιακή κλίμακα (θερμοκρασιακή διεύρυνση του ενδοθέρμου βήματος) με την αύξηση της περιεκτικότητας σε σωματίδια.

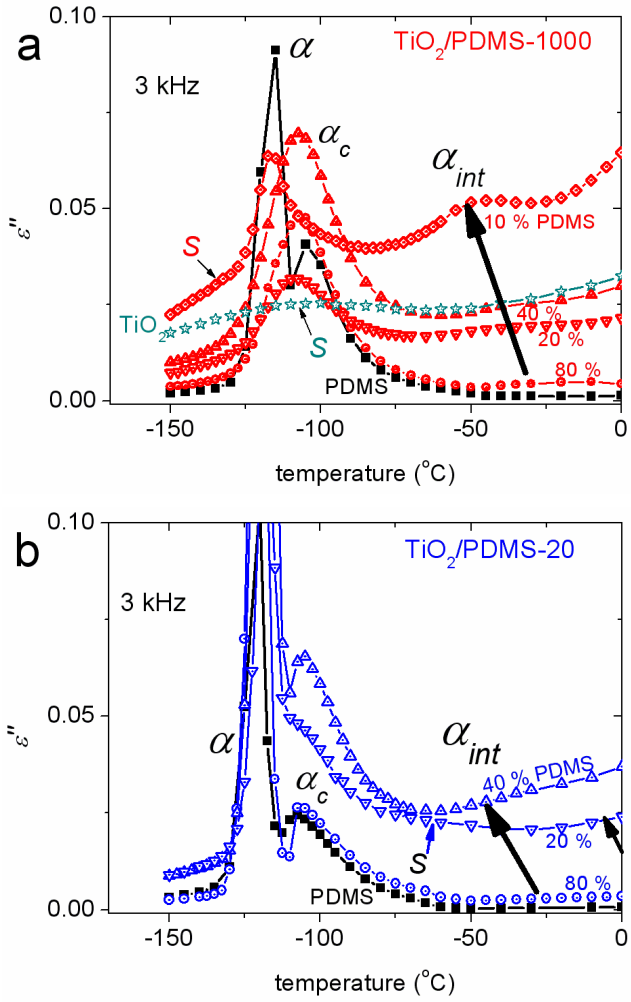

Εικόνα 35. Συγκριτικά ισόχρονα διαγράμματα DRS του φανταστικού μέρους της διηλεκτρικής συνάρτησης (διηλεκτρικές απώλειες), ε'', στη σύχνοτητα των 3 kHz για ΝΣ τύπου πυρήνα-φλοιού (core–shell) τιτανίας/PDMS (a) μεγάλου και (b) μικρού μοριακού βάρους.

Σύμφωνα με τις μετρήσεις DRS (Εικόνα 35) η δυναμική του πολυμερούς μακρυά από τις διεπιφάνειες (μηχανισμοί α και α_c) δεν επηρεάζονται σημαντικά από τη σύσταση των ΝΣ (Εικόνα 35). Αυτό επιβεβαιώνεται και με την αντίστοιχη ανάλυση των αποτελεσμάτων (Διηλεκτρικός Χάρτης, Εικόνα 36a).

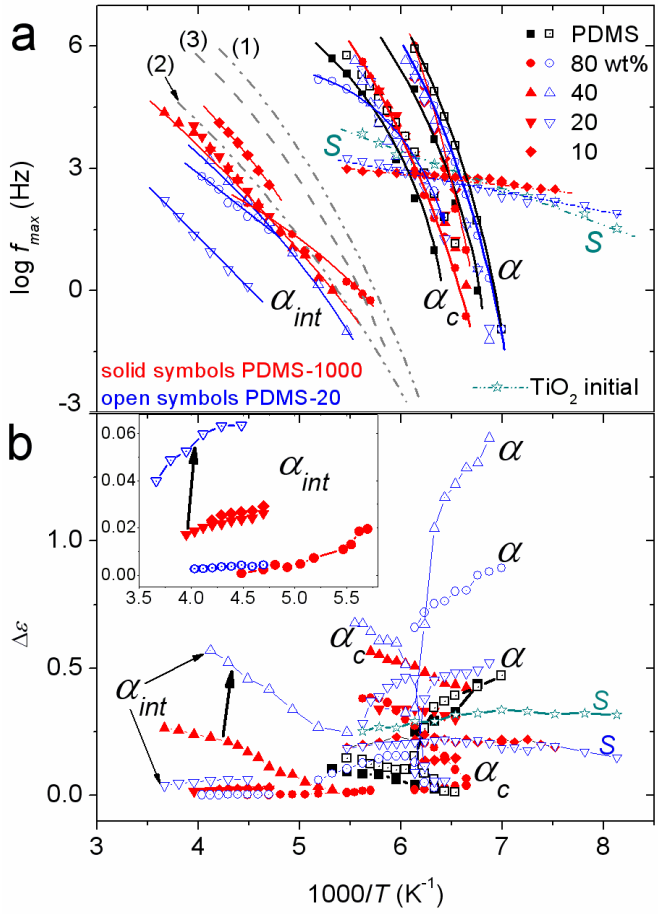

Εικόνα 36. (a) Διηλεκτρικός χάρτης (Arrhenius plots) και (b) διηλεκτρική ισχύς συναρτήσει της αντίστροφης θερμοκρασίας για τους διάφορους μηχανισμούς διηλεκτρικής αποκατάστασης (*S*, α, α_c και α_{int}) για ΝΣ δοκίμια τιτανίας με 10-80% PDMS για δύο μοριακά βάρη του πολυμερούς

Οι πιο ενδιαφέρουσες παρατηρήσεις αφορούν, και εδώ, τις διαφορές που καταγράφονται στη δυναμική του διεπιφανειακού πολυμερούς (μηχανισμός α_{int}). Φάινεται ότι στην περίπτωση του μικρού μοριακού βάρους (κοντές πολυμερικές αλυσίδες) ο μηχανισμός α_{int} καταγράφεται πιο αργός και λιγότερο συνεργασιακού χαρακτήρα (Εικόνα 36a), παραταύτα, με υψηλότερη διηλεκτρική ισχύ (Εικόνα 36b), σε σχέση με τα ΝΣ που βασίζονται σε πολυμερές μεγαλύτερου μοριακού βάρους (μακρύτερες πολυμερικές αλυσίδες).

Ωστόσο, αυξανομένης της περιεκτικότητας σε πολυμερές παρατηρείται η τάση προς αύξηση της συνεργασιμότητας (Εικόνα 36a) και, βάσει των υπολογισμών, αύξηση του πάχους του διεπιφανειακού στρώματος (Εικόνα 37). Επίσης, το πλήθος των πολυμερικών αλυσίδων στο διεπιφανειακό στρώμα εκτιμάται μεγαλύτερο στην περίπτωση των κοντύτερων πολυμερικών αλυσίδων.

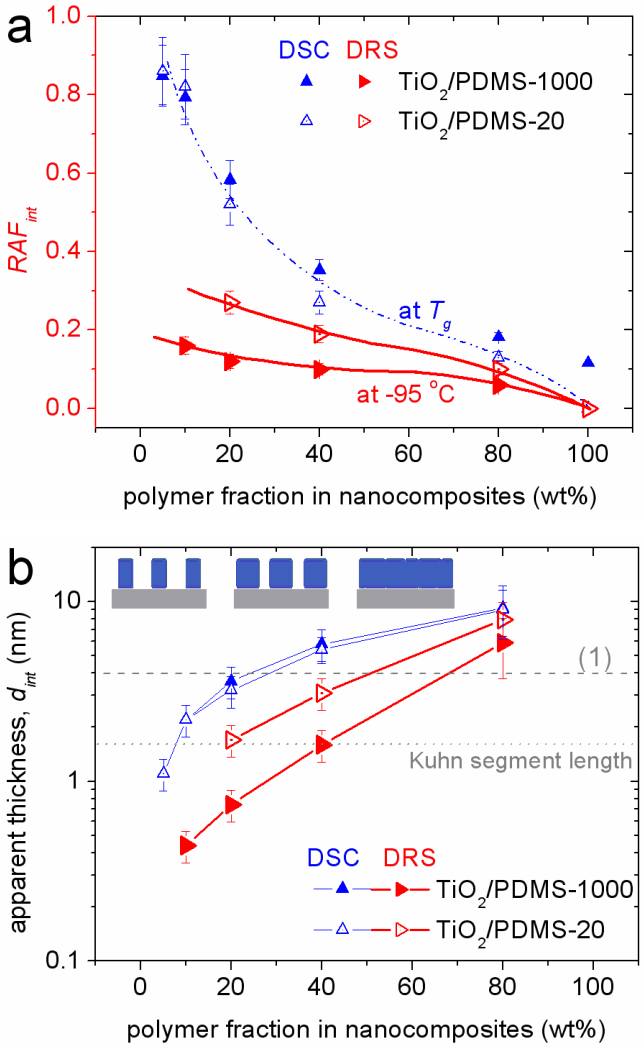

Εικόνα 37. (a) Κλάσματα μάζας/όγκου του διεπιφανειακού πολυμερούς, RAF_{int}, όπως προκύπτουν από τις μετρήσεις DSC/DRS, αντιστοίχως, και (β) πάχος του διεπιφανειακού στρώματος, d_{int}, συναρτήσει της περιέκτικότητας σε πολυμερές για τα ΝΣ τιτανίας/PDMS.

Αξίζει να σημειωθεί ότι η σταθεροποίηση των τιμών του πάχους του διεπιφανειακού στρώματος, d_{int}, σε σχετικώς υψηλές περιεκτικότητες πολυμερούς (>60 % στην Εικόνα 37b) μπορεί να εξηγηθεί με όρους μη ομογενούς κάλυψης της επιφάνειας των σωματιδίων (ένθετο σχήμα στην Εικόνα 37b).

Συνδυάζοντας τα παραπάνω αποτελέσματα προτείνουμε ότι η αυξανομένη προσρόφηση πολυμερούς στη διεπιφάνεια οδηγεί σε αυξανόμενο λόγο loops/stails ιδίως για τα ΝΣ που βασίζονται σε πολυμερές μακρύτερων αλυσίδων (Εικόνα 38).

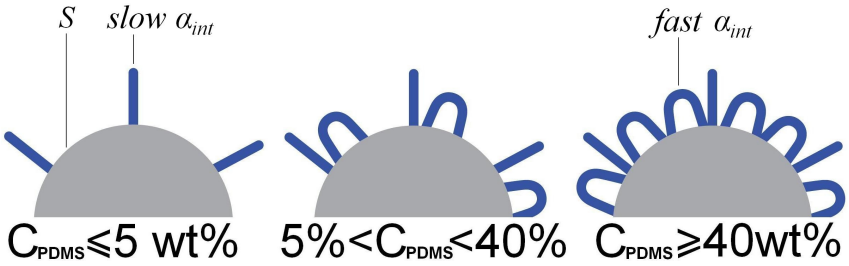

Εικόνα 38. Απλοποιημένο μοντέλο πολλαπλών διαμορφώσεων των πολυμερικών αλυσίδων, που έχουν προσροφηθεί σε στερεή ελκτική επιφάνεια; επιρροή της περιεκτικότητας του διεπιφανειακού πολυμερούς

Επίσης, οι διαφορές μεταξύ ΝΣ που βασίζονται σε πολυμερές με κοντές ή μακρύτερες αλυσίδες, όπως προκύπτουν από τα πειραματικά μας αποτελέσματα, μπορούν να εξηγηθούν ως εξής. Ο λόγος tails/loops είναι, πιθανώς, μεγαλύτερος στην περίπτωση κοντών πολυμερικών αλυσίδων PDMS (μικρό μοριακό βάρος του πολυμερούς), σε σχέση με τις μακρύτερες αλυσίδες, λόγω της μεγαλύτερης συγκέντρωσης ελεύθερων άκρων. Επίσης η ύπαρξη περισσότερων ελεύθερων άκρων οδηγεί στην αυξημένη προσβασιμότητα των διαθέσιμων σημείων αλληλεπίδρασης (επιφανειακά υδροξύλια). Τα παραπάνω απεικονίζονται σχηματικά με απλό τρόπο στην Εικόνα 39.

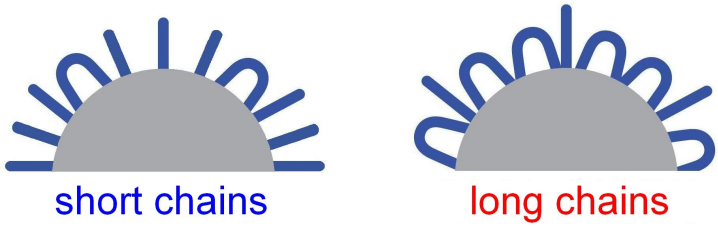

Εικόνα 39. Απλοποιημένο μοντέλο πολλαπλών διαμορφώσεων των πολυμερικών αλυσίδων προσροφημένων σε στερεή ελκτική επιφάνεια, επιρροή του μήκους των αλυσίδων (μοριακού βάρους)

Συμπερασματικά, καταλήγουμε στο ότι ο αριθμός και η προσβασιμότητα των σημείων επαφής (επιφανειακές ιδιότητες των σωματιδίων) και η δομή και ευκαμψία των πολυμερικών αλυσίδων (τοπολογία του πολυμερούς στις επιφάνειες των σωματιδίων) κυριαρχούν στη διαμόρφωση των διεπιφανειακών αλληλεπιδράσεων. Τέλος, από τα παραπάνω αποκομίζουμε τεκμήρια περί μεταβολών στην πυκνότητα του πολυμερούς στο διεπιφανειακό στρώμα. Τέτοιες μεταβολές έχουν μελετηθεί με τη χρήση υπολογιστικών μεθόθων προσομοιώσεων.

Επιρροή του χωρικού περιορισμού (spatial confinement) του πολυμερούς σε κυλινδρικούς πόρους

Τέλος, μελετήσαμε φαινόμενα 2D χωρικού περιορισμού του πολυμερούς σε ΝΣ συστήματα silica-gel (Si-60) με 40% και 80% προσροφημένο γραμμικό PDMS (Εικόνα 40). Η silica-gel απαρτίζεται από συσσωματώματα διαστάσεων μερικών μm (Εικόνα 40a), ενώ κάθε συσσωμάτωμα αποτελείται από πυκνό σύμπλεγμα μικρότερων νανοσωματιδίων που σχηματίζουν εσωτερικούς πόρους κυλινδρικού τύπου (σύραγγες) που ποικίλουν σε διάμετρο μεταξύ 6 και 20 nm. Η ειδική επιφάνεια των εν λόγω συστημάτων είναι υψηλή, περιπου 380 m^2/g, και οφείλεται κυρίως στην εσωτερική πορωσιμότητα και δευτερευόντως στην εξωτερική-επιφανειακή τραχύτητα.

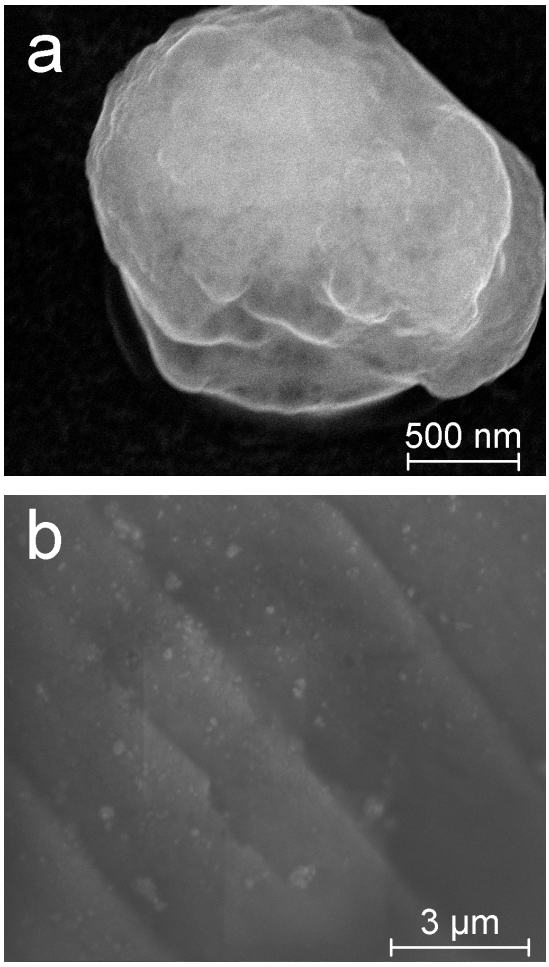

Εικόνα 40. Εικόνες ηλεκτρονικής μικροσκοπίας σάρωσης (SEM) (a) ενός συσσωματώματος Si−60 και (b) του ΝΣ Si-60 με 80% προσροφημένο PDMS

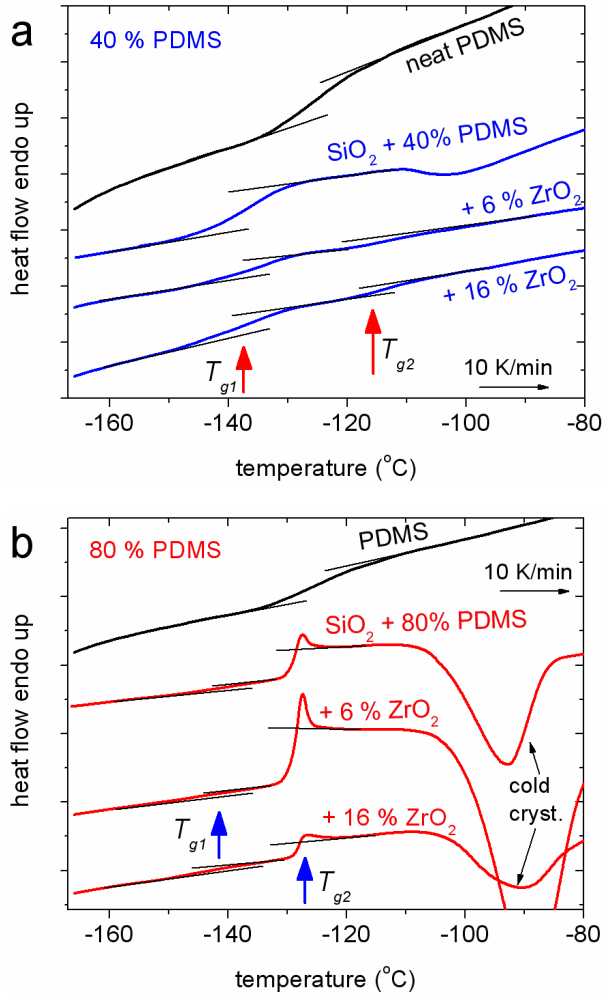

Εικόνα 41. Συγκριτικά θερμογράμματα DSC στην περιοχή της υαλώδους μετάβασης για ΝΣ βασισμένα στη silica-gel Si-60 και προσροφημένο PDMS με κλάσμα μάζας (a) 40% και (b) 80%. Παρουσιάζονται επίσης αποτελέσματα για ΝΣ βασισμένα στη silica-gel τροποποιημένη με μικρότερα νανοσωματίδια ζιρκονίας (ZrO_2).

Σύμφωνα με τα αποτελέσματα DSC, στα ΝΣ καταγράφεται ένα επιπρόσθετο βήμα υαλώδους μετάβασης (DSC) σε χαμηλές θερμοκρασίες, περίπου στους -140 °C (T_{g1}, Εικόνα 41). Η δευτερεύουσα αυτή υαλώδης μετάβαση κυριαρχεί στην απόκριση των υλικών χαμηλής περιεκτικότητας σε πολυμερές (40%, Εικόνα 41a), ενώ στην περίπτωση ΝΣ μεγάλης περιεκτικότητας σε PDMS η κύρια συνεισφορά στην υαλώδη μετάβαση καταγράφεται μεταξύ -130 και -125 °C (T_{g2}, Εικόνα 41b). Η υαλώδης μετάβαση στη χαμηλότερη θερμοκρασιακή περιοχή (T_{g1}) αντιστοιχεί στο τμήμα του πολυμερούς που βρίσκεται χωρικώς περιορισμένο εντός των κυλινδρικών πόρων της silica-gel, ενώ η υαλώδης μετάβαση σε υψηλότερες θερμοκρασίες (T_{g2}) οφείλεται στο τμήμα του ελεύθερου τμήματος του

πολυμερούς (bulk). Είναι ενδιαφέρον ότι κατόπιν επιφανειακής τροποποίησης της καθαρής silica-gel με μικρά νανοσωματίδια ζιρκονίας (zirconia, ZrO_2), η T_{g1} στα ΝΣ μειώθηκε και η μεταβολή στην ειδική θερμότητα, ΔC_{p1}, αυξήθηκε. Το αποτέλεσμα αυτό ερμηνεύεται ώς αυξημένη επιρροή του χωρικού περιορισμού εντός των πόρων, στα τοιχώματα των οποίων αναπτύχθηκαν τα νανοσωματίδια ζιρκονίας (~3 nm σε διάμετρο) και, έτσι περιορίσθηκε η μέση διάμετρος των κυλινδρικών πόρων.

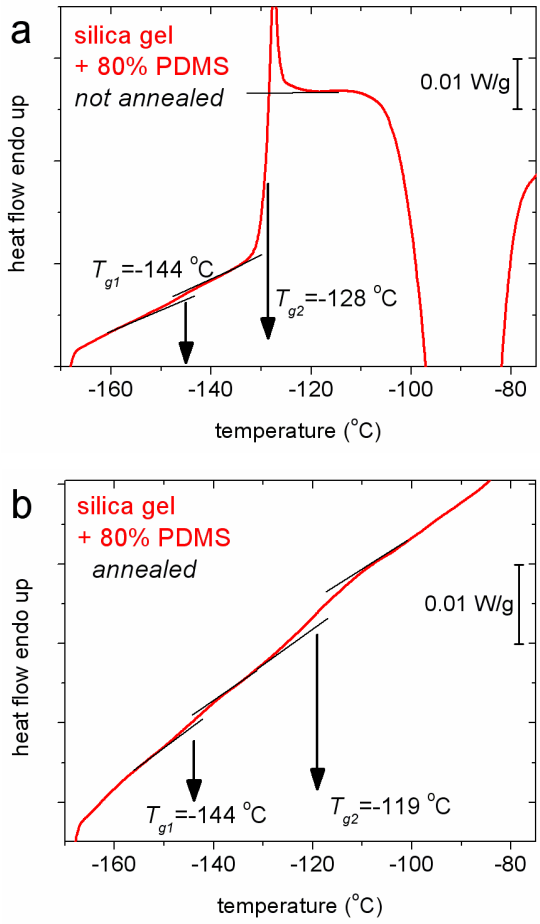

Εικόνα 42. Θερμογράμματα DSC στην περιοχή της υαλώδους μετάβασης για ΝΣ βασισμένο στη silica-gel Si-60 και 80% προσροφημένο PDMS για μέτρηση πριν (a) και μετά (b) τη θερμική ανόπτηση της κρυστάλλωσης (εντός της συσκευής DSC)

Μετά από μετρήσεις δοκιμίων που υπέστησαν θερμική ανόπτηση, προς ενίσχυση του βαθμού κρυσταλλικότητας, παρατηρήθηκε ότι η υαλώδης μετάβαση του χωρικώς περιορισμένου πολυμερούς παρέμεινε τελείως ανεπηρέαστη (σύγκριση μεταξύ Εικόνων 42a,b), σε αντίθεση με την επιβράδυνση και υποβάθμιση της bulk δυναμικής (αύξηση της T_{g2} και ελάττωση της ΔC_{p2}, Εικόνα 42b).

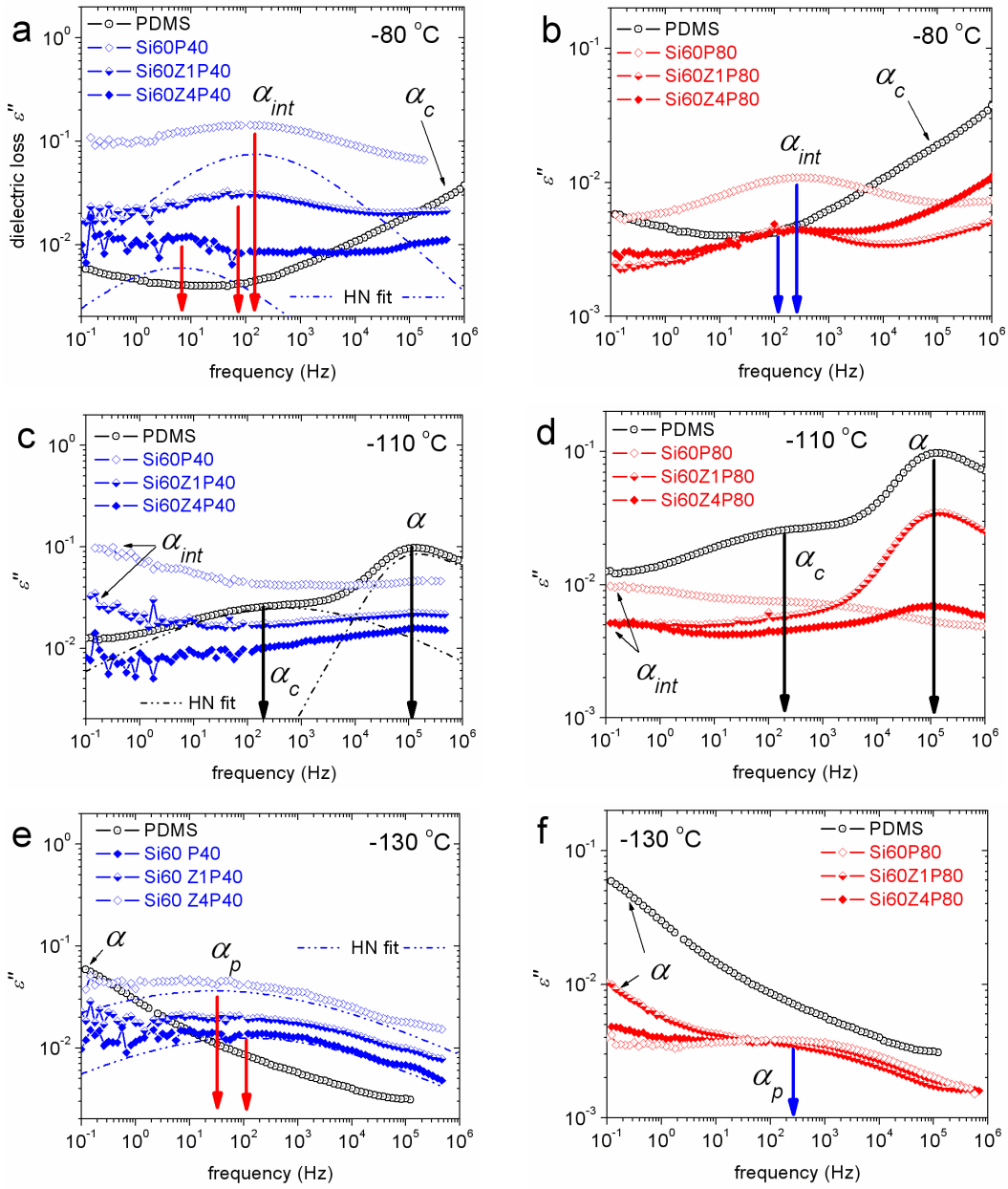

Εικόνα 43. Συγκριτικά ισόθερμα διαγράμματα DRS του φανταστικού μέρους της διηλεκτρικής συνάρτησης (διηλεκτρικές απώλειες), ε'', σε διάφορες θερμοκρασίες για ΝΣ βασισμένα στη silica-gel Si-60 και προσροφημένο PDMS με κλάσμα μάζας (αριστερά) 40% και (δεξιά) 80%.

Από τις μετρήσεις διηλεκτρικής φασματοσκοπίας (DRS) καταγράφεται η συνολική συνεργασιακή δυναμική του πολυμερούς (που σχετίζεται με την υαλώδη μετάβαση, Εικόνα 43), η οποία βρέθηκε να εκφράζεται στα ΝΣ από τέσσερις καλώς διακριτές συνεισφορές. Όπως στα προηγούμενα ΝΣ τύπου πυρήνα-φλοιού, έτσι και εδώ αυτές οι συνεισφορές προέρχονται από διαφορετικά τμήματα του πολυμερούς, δηλαδή (α) του διεπιφανειακού

πολυμερούς με συνεργασιακή αλλά καθυστερημένη δυναμική (μηχανισμός α_{int}, Εικόνα 43a,b), (β) του αμόρφου ανεπηρέαστου (bulk) πολυμερούς (μηχανισμός α, Εικόνα 43c,d), (γ) του πολυμερούς περιορισμένης κινητικότητας μεταξύ κρυσταλλικών περιοχών (μηχανισμός α_c, Εικόνα 43c,d), και (δ) έναν επιπρόσθετο γρήγορο μηχανισμό διηλεκρικής χαλάρωσης (α_p, DRS, Εικόνα 43e,f). Ο τελευταίος αντιστοιχεί στη μοριακή δυναμική του πολυμερούς που βρίσκεται χωρικώς περιορισμένο εντός των κυλινδρικών πόρων της silica-gel.

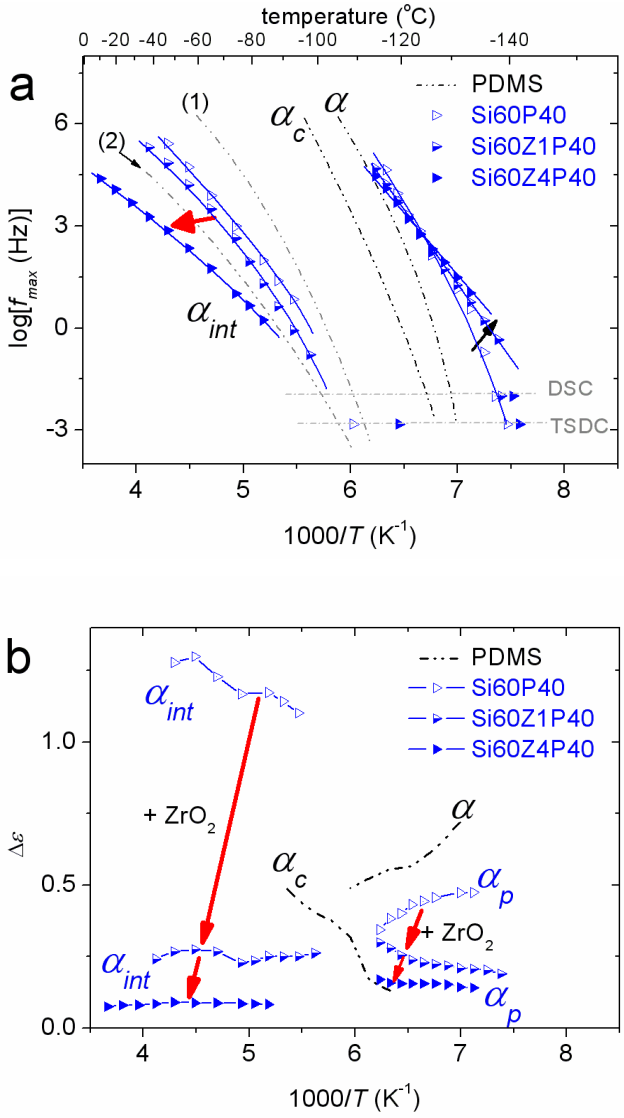

Εικόνα 44. (a) Διηλεκτρικός χάρτης (Arrhenius plots) και (b) διηλεκτρική ισχύς συναρτήσει της αντίστροφης θερμοκρασίας για τους δύο μηχανισμούς διηλεκτρικής αποκατάστασης (α_p και α_{int}) για ΝΣ δοκίμια silica-gel με 40% PDMS. Τα βέλη δείχνουν την επιρροή της επιφανειακής τροποποίησης της silica-gel με μικρά νανοσωματίδια ζιρκονίας στη δυναμική του πολυμερούς.

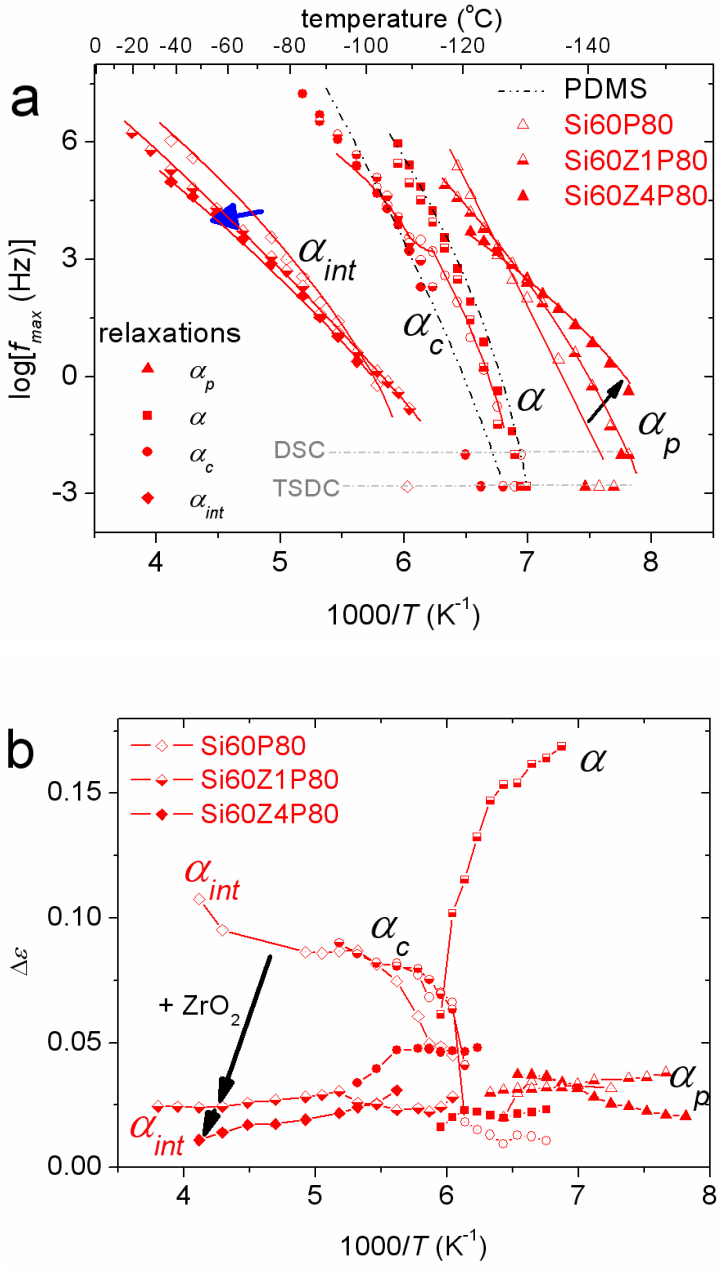

Εικόνα 45. (a) Διηλεκτρικός χάρτης (Arrhenius plots) και (b) διηλεκτρική ισχύς συναρτήσει της αντίστροφης θερμοκρασίας για τους τέσσερις μηχανισμούς διηλεκτρικής αποκατάστασης (α_p, α, α_c και α_{int}) για ΝΣ δοκίμια silica-gel με 80% προσροφημένο PDMS. Τα βέλη δείχνουν την επιρροή της επιφανειακής τροποποίησης της silica-gel με μικρά νανοσωματίδια ζιρκονίας στη δυναμική του διεπιφανειακού και του χωρικώς περιορισμένου πολυμερούς (α_{int} και α_p).

Η επιφανειακή τροποποίηση της silica-gel με μικρά νανοσωματίδια ζιρκονίας οδήγησε στην εξασθένιση της διεπιφανειακής αλληλεπίδρασης πολυμερούς/silica-gel, καθώς παρατηρήθηκε (α) επιβράδυνση της διεπιφανειακής πολυμερικής δυναμικής (Εικόνες 44a,45a), (β) μείωση του βαθμού συνεργασιμότητας (Εικόνες 44a,45a) και (γ) εξασθένιση του μηχανισμού α_{int} (Εικόνες 44b,45b).

Από την άλλη, μετά την επιφανειακή τροποποίηση της silica-gel και την προσρόφηση του πολυμερούς, καταγράφονται σημαντικές μεταβολές στο μηχανισμό α_p, δηλαδή (α) επιτάχυνση της δυναμικής (Εικόνες 44a,45a), (β) περιορισμός της συνεργασιμότητας (Εικόνες 44a,45a) και (γ) εξασθένιση του μηχανισμού α_p (Εικόνες 44b,45b).

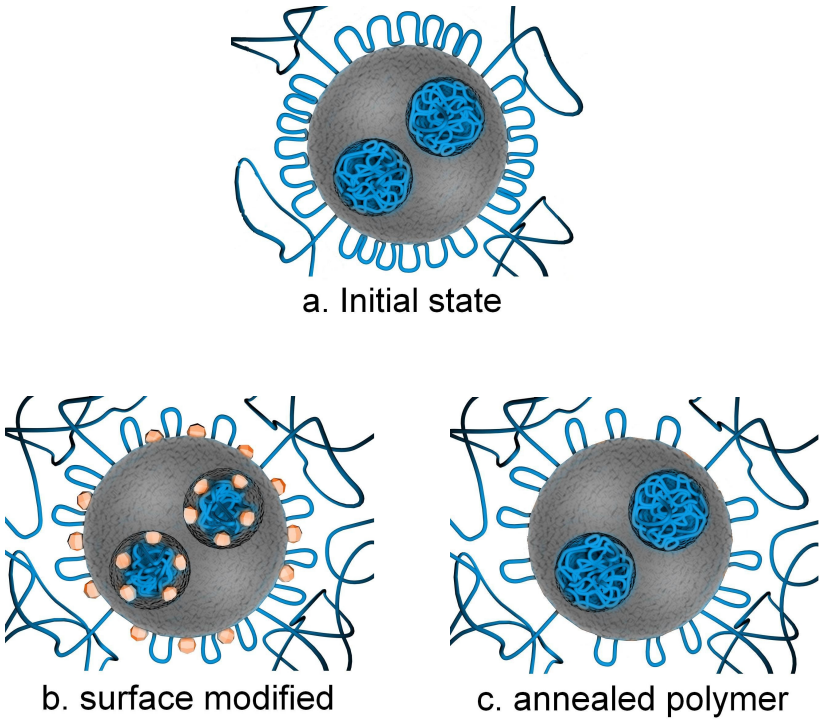

Εικόνα 46. Σχηματική 2D αναπαράσταση για τις προτεινόμενες μεταβολές στην κατανομή των πολυμερικών αλυσίδων στη διεπιφάνεια και τους εσωτερικούς πόρους με τα σωματίδια silica-gel που επιφέρουν: (b) η τροποποίηση της επιφάνειας με μικρά νανοσωματίδια ζιρκονίας και (c) η θερμική ανόπτηση της κρυστάλλωσης.

Συγκρίνοντας με τη σχετική βιβλιογραφία, εκτιμούμε ότι τα νανοσωματίδια ζιρκονίας (~3 nm σε διάμετρο) αναπτύχθηκαν στα τοιχώματα εντός των κυλινδρικών πόρων (Εικόνες 46a,b) και, έτσι περιορίσθηκε η μέση διάμετρος των πόρων. Συνέπεια της μείωσης του διαθέσιμου χώρου εντός των πόρων είναι η περαιτέρω επιρροή του χωρικού περιορισμού του πολυμερούς. Ο περιορισμός της συνεργατικότητας και η επιτάχυνση της περιορισμένης

δυναμικής, εξηγείται στη βιβλιογραφία με όρους μικρότερου πλήθους συνεργαζόμενων πολυμερικών αλυσίδων σε μικρότερο χώρο (χαμηλότερο μήκος συνεργασιμότητας).

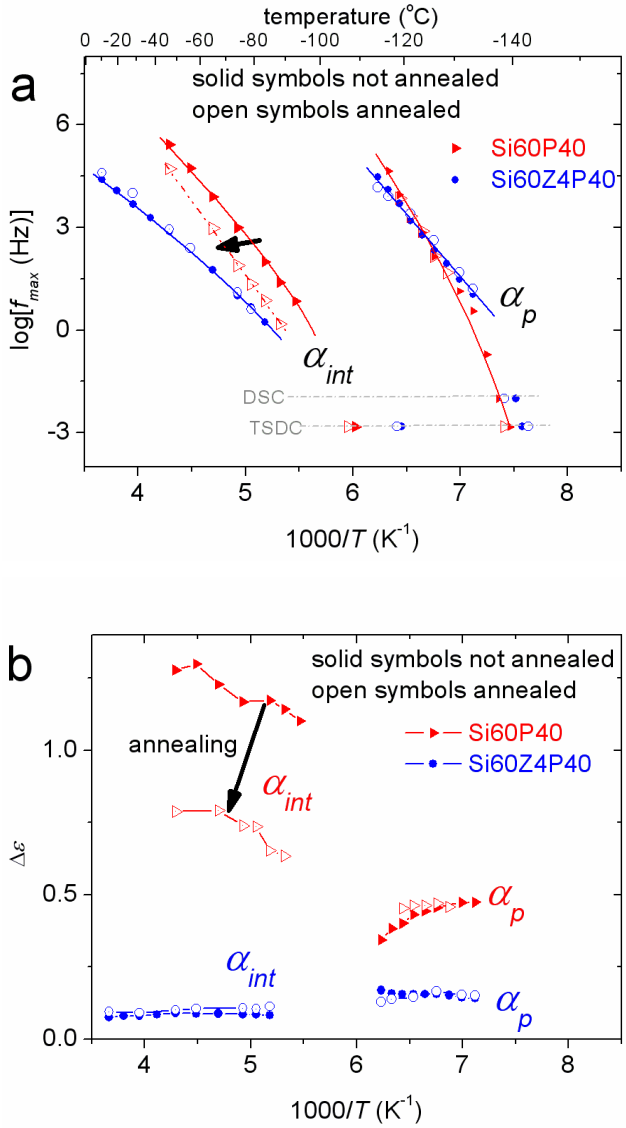

Εικόνα 47. Επιρροή της θερμικής ανόπτησης, προς ενίσχυση του βαθμού κρυσταλλικότητας, (a) στη μοριακή δυναμική και (b) στη διηλεκτρική ισχύ των μηχανισμών διηλεκτρικής αποκατάστασης σε ΝΣ silica-gel/PDMS(40%)

Ενδιαφέρον προκύπτει και από μετρήσεις θερμικής ανόπτησης της κρυσταλλικότητας (crystallization annealing, Εικόνα 47). Αυτή η θερμική μεταχείριση επηρεάζει σημαντικά την κινητικότητα του διεπιφανειακού πολυμερούς, οδηγώντας σε επιβράδυνσης της αντίστοιχης δυναμικής (Εικόνες 47a) και αραίωση του διεπιφανειακού στρώματος (Εικόνες 47b,48b), όπως στα προηγούμενα ΝΣ τύπου πυρήνα φλοιού (σύγκριση μεταξύ Εικόνας 20 και Εικόνας

47). Όμως, η ίδια θερμική μεταχείριση των ΝΣ που βασίζονται στην silica-gel αφήνει εντελώς ανεπηρέαστη τη χωρικώς περιορισμένη δυναμική εντός των πόρων (μηχανισμός α_p, Εικόνες 47,48).

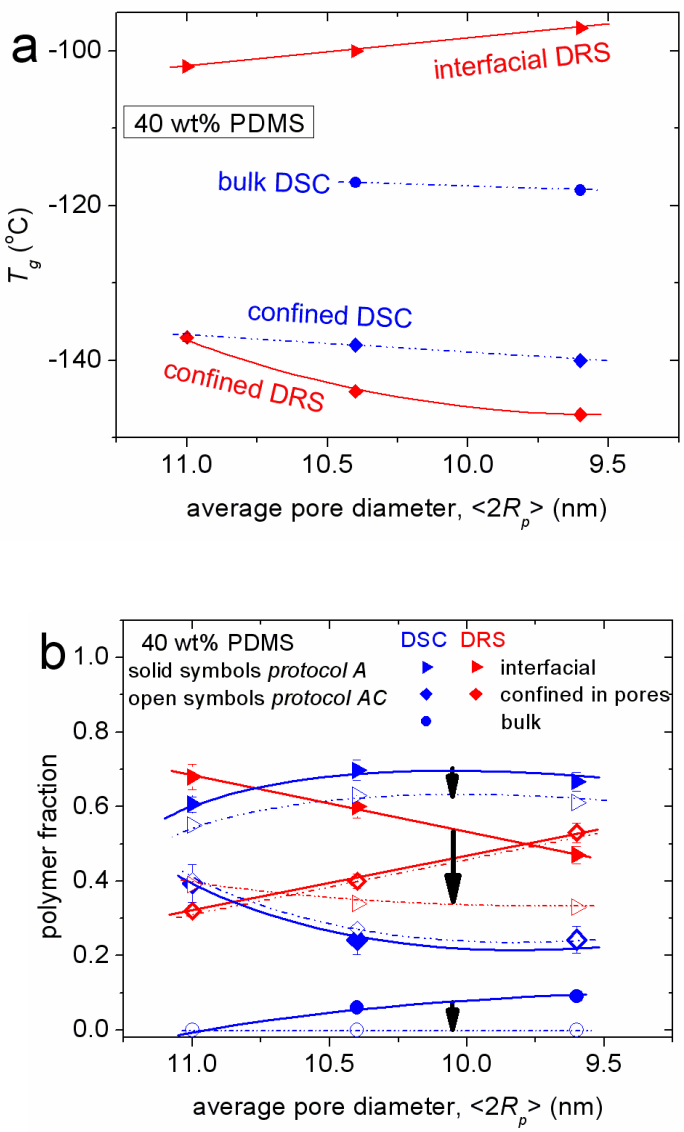

Εικόνα 48. (a) θερμιδομετρική και διηλεκτρική θερμοκρασία υαλώδους μετάβασης και (b) κλάσμα μάζας/όγκου των διάφορων τμημάτων του πολυμερούς στα ΝΣ silica-gel/PDMS συναρτήσει της εκτιμούμενης μέσης διαμέτρου των κυλινδρικών πόρων. Τα βέλη δείχνουν την επιρροή της θερμικής ανόπτησης της κρυστάλλωσης.

Σε συμφωνία με τη βιβλιογραφία, επιβεβαιώνουμε και εδώ ότι ο χωρικός περιορισμός πολυμερούς στην κλίμακα των nm (spatial nano-confinement) κυριαρχούνται από τα φαινόμενα μεγέθους (size effects) παρά από φαινόμενα δυναμικής και αλληλεπιδράσεων. Αντιθέτως η ισχύς της αλληλεπίδρασης μεταξύ του πολυμερούς και της ελκτικής στέρεης

επιφάνειας επηρρεάζονται καθοριστικά από την ισχύ της αντίστοιχης αλληλεπίδρασης (πχ. δεσμός υδρογόνου, οδηγός δύναμη της κρυστάλλωσης), από την τοπολογία του πολυμερούς επάνω σε διαφορετικές επιφάνειες (πχ. τραχύτητα της επιφάνειας και διαμορφώσεις πολλαπλού τύπου στην περίπτωση εύκαμπτων πολυμερικών αλυσίδων) και, πιθανόν, από την επικουρική συμμετοχή των επιφανειακών μορίων νερού στο βαθμό αλληλεπίδρασης πολυμερούς-επιφάνειας.

Ευχαριστία

Η παρούσα έρευνα έχει συγχρηματοδοτηθεί από την Ευρωπαϊκή Ένωση (Ευρωπαϊκό Κοινωνικό Ταμείο - ΕΚΤ) και από εθνικούς πόρους μέσω του Επιχειρησιακού Προγράμματος «Εκπαίδευση και Δια Βίου Μάθηση» του Εθνικού Στρατηγικού Πλαισίου Αναφοράς (ΕΣΠΑ) – Ερευνητικό Χρηματοδοτούμενο Έργο: Ηράκλειτος ΙΙ. Επένδυση στην κοινωνία της γνώσης μέσω του Ευρωπαϊκού Κοινωνικού Ταμείου.